University of Pisa

Department of Information Engineering

Master's Thesis in
Telecommunication Engineering

Joint bit allocation and precoding for filterbank transceivers in NOFDM systems

Supervisors:

Prof. Filippo Giannetti

Ing. Vincenzo Lottici

Ing. Ivan Stupia

Ing. Adrian Kliks
Poznan University of Technology
(Poland)

Author:

Andrea Gregori

December 14^{th}, 2009

To those who were,
are and will be my family

Abstract

Recently, the *Non Orthogonal Frequency Division Multiplexing* (NOFDM) systems have attracted increased interest. They have several advantages over traditional OFDM systems such as higher bandwidth efficiency and a reduced sensitivity to carrier frequency offsets, oscillator phase noise and narrowband interference and a reduced intersymbol/intercarrier interference (ISI/ICI). In particular, low ISI/ICI will be important for future systems where Doppler frequencies will be larger (equivalently, channel variations will be faster) due to higher carrier frequencies and higher mobile velocities.

In this work the parallelism of the multicarrier systems with the Gabor frames is discussed and applied to the design of a *Generalized MultiCarrier* system based on a filterbank structure. The efficient polyphase implementation is also discussed.

In this thesis the channel *capacity* of a GMC systems is evaluated through the diagonalization of an equivalent matrix model where intersymbol and intercarrier interferences have been included. Exploiting the majorization theory, the mutual information can be represented as a Schur-concave function and it is maximized through a joint transceiver design adding a linear precoder at the transmitter and a LMMSE equalizer at the receiver. The capacity is derived by the eigenvalue decomposition of the global system matrix including the noise colored by the receiver filtering and employing a power allocation of the transmitted power according to the well-known *water-filling* solution.

This thesis investigates also the behaviour of the NOFDM systems when a power and bit allocation algorithm is employed in order to satisfy a certain QoS constraint. A comparison of the performances with OFDM systems is included.

Finally a simple application of the *cognitive radio* paradigm employing filterbank-based multicarrier systems is developed and some interesting results are showed.

Index terms

Multicarrier system, NOFDM, GMC, filterbank, Gabor theory, pulse design, majorization theory, transceiver design, bit loading, cognitive radio.

Contents

List of Tables

List of Figures

Acknowledgements

In English

I would like to express all my gratitude to Prof. Filippo Giannetti, Ing. Vincenzo Lottici and Ing. Adraian Kliks of Poznan University of Technology, for their helpfulness, their advices and their patience. I would also like to thank so much Ing. Ivan Stupia, without whom I wouldn't found the way to end successfully this long work. I wish him all the best and a long and brilliant career. He's got all the skills to make it, as he showed me during these last nine months. Thanks also to all the members of labs A-1-04 and A-1-05, in particular Riccardo and Paolo, who helped me with their advices and kept me up to date with their errors and problems. Thanks to all the university mates who I met during the last years: Davide, Gino, Gianluca, Alessandro, Mario and the others met during lectures and examinations. Thanks also to my "Livorno" friends: Alberto, Anna, Eleonora, Piercarlo, Irene and many others; they have always been ready to encourage me even in darkest and hardest moments.

I want to thank my family; first of all, thanks to my grandmother: it is thanks to her if I best began my school career and if now I achieve this important goal. Unfortunately she could not fully enjoy this moment but in my heart I will always be grateful to her. Thanks to my parents and to my brother, they always showed me the best way to follow with their patience, their helpfulness and their discreet but significant presence. They have given me the strength to go on. I hope I never let them down since they never did and I think they'll never do.

Finally I want to thank she whom I hope with all my heart will become my family, who was always by my side, supporting and encouraging me every single day since I met her. Thank you for your sympathy, your hugs, your presence to my problems. Thank you for your ability to amuse me or to bring the smile back on my face during the hardest moments. I hope one day I'll be able to do the same when you need it. Thank you Chiara!

In Italian

Vorrei esprimere tutta la mia gratitudine nei confronti del Prof. Filippo Giannetti, dell'Ing. Vincenzo Lottici e dell'Ing. Adrian Kliks della Poznan University of Technology, per la loro disponibilità, i loro consigli e la loro pazienza. Ringrazio infinitamente anche l'Ing. Ivan Stupia senza il quale non avrei mai potuto trovare la strada per concludere questo lungo lavoro di tesi. Gli auguro ogni bene e la possibilità di avere una carriera lunga e brillante in quanto ha tutte le capacità per far sì che ciò accada e me lo ha ampiamente dimostrato. Ringrazio i ragazzi dei laboratori A-1-04 e A-1-05, in particolar modo ci tengo a ringraziare Riccardo e Paolo che mi hanno aiutato con loro consigli e tenendomi sempre al corrente dei loro errori e problemi. Grazie ai miei compagni di avventure in questi lunghi anni di università: Davide, Gino, Gianluca, Alessandro, Mario e tutti i ragazzi incontrati durante i corsi e gli esami. Un grazie anche a tutti gli amici di Livorno: Alberto, Anna, Eleonora, Piercarlo e mille altri amici, sempre pronti a sostenermi anche nei momenti più bui.

Ringrazio coloro che sono la mia famiglia: dapprima la mia nonna, è grazie a lei se ho iniziato al meglio sin da piccolo, la mia "carriera" scolastica e se sono riuscito a raggiungere questo importante traguardo. Purtroppo non potrà mai godersi a pieno questo momento ma nel mio cuore le sarò sempre grato. Grazie ai miei genitori e al mio fratello che con la loro pazienza, la loro disponibilità e la loro presenza sempre discreta ma importante, mi hanno sempre indicato la via migliore da seguire e dato la forza per andare avanti. Spero di non averli mai delusi dato che loro non lo hanno mai fatto nei miei confronti e dubito mai lo faranno.

Infine ringrazio colei che spero con tutto il mio cuore diventi la "mia" famiglia, colei che mi è sempre stata accanto, sostenendomi e incoraggiandomi ogni singolo giorno da quando l'ho conosciuta. Grazie per la tua comprensione, per i tuoi abbracci, per la tua partecipazione ai miei problemi, per la tua capacità di distrarmi o di farmi tornare il sorriso nei momenti difficili. Spero un giorno di poter fare lo stesso quando sarai tu ad averne bisogno. Grazie Chiara!

Chapter 1

Introduction

The increasing demand for better spectral utilization and higher QoS requirements motivate the design of increasingly more intelligent and agile communication systems, able to adapt and adjust (in realtime) the transmission parameters based on the current link quality for the ultimate goal of reaching, to the degree possible, the inherent capacity of the underlying channel.

1.1 Non-Orthogonal Multi-Carrier Systems

The class of *Non Orthogonal Multicarrier Modulations* (NOMCM) was first introduced in 1998 by W. Kozek and A.F. Molisch [6] as a novel approach to multicarrier transmissions over doubly dispersive channels affected by both time-varying and frequency-selective fading phenomena. In such a kind of propagation scenarios, frequency-selectivity is caused by multipath, while time variations are due to the relative motion between transmitter and receiver. In the conventional OFDM scheme the data bit stream is divided into many (hundreds or thousands) of substreams, and each of these substreams modulates a different carrier. Since each of these substreams has a low data rate, the intersymbol interference (ISI) caused by the time dispersion effect of the propagation channel is greatly reduced with respect to the single-carrier (SC) case. However, such a big advantage comes at the expenses of interchannel interference (ICI), which arises when the propagation channel is also frequency dispersive and the energy from a subcarrier spills over into the adjacent ones. These two detrimental effects, i.e., ISI and ICI, are thus influenced by two factors:

1. the time dispersion (due to multipath propagation) and frequency dispersion (due to the Doppler effect) of the mobile radio channel;

2. the shape of the pulse that is used to transmit one symbol on one subcarrier.

Pulses that are well localized in the time domain (and thus cause little ISI) are widely spread out in the frequency domain (and thus cause more ICI), and vice versa.

The underlying idea of NOMCM consists in finding a pulse shape that gives minimum distortion for a given Doppler spread (denoted as D_f) and delay spread (denoted as spread τ_{spread}). In order to better clarify the question, let us consider again a conventional OFDM system, wherein each subcarrier is modulated by pulses having duration coincident with one symbol interval T and sinc-shaped spectrum. Under ideal propagation conditions, i.e., without ISI (e.g., thanks to the use of the cyclic prefix (CP)) and ICI, the pulse spectra on the subcarriers are orthogonal, as in AWGN conditions. However, when a time-varying propagation channel induces a frequency dispersion effect, the orthogonality condition does not hold true any longer, because the subcarrier frequencies do not coincide with the nulls of the sinc-shaped spectrum, thus causing ICI. In order to solve this problem, several pulse-shape optimization techniques have been proposed in the technical literature. For instance, some solutions proposed the use of Nyquist pulses [7], of the CP [8], of time-limited prolate spheroidal wave functions [9], and of Hermitian functions [10]. However, all of these proposals suffer from a severe limitation, as they assume that the pulses must be orthogonal, or that any deviation from orthogonality is a negligible effect. Actually, orthogonal functions are optimum basis functions only in AWGN channels, while in doubly dispersive channels other basis functions turn out to be optimal. The only requirement is that these basis functions form an (incomplete) Riesz basis.

To summarize, the key advantages of non-orthogonal systems (NOFDM) when compared to standard OFDM schemes are as follows:

- a modulation scheme based on incomplete Riesz bases tends to be more robust against frequency-selective fading;

- NOFDM systems lead to better bandwidth efficiency, because the underlying pulse can be chosen with sharper frequency domain decay than that of a comparable OFDM system (thus the spectral efficiency, defined as $\eta = \frac{\zeta}{TF} \left[\frac{\text{bit/s}}{\text{Hz}}\right]$ can

be maximized; in the equation above ζ denotes the number of bits per symbol and T and F are the time and frequency spacing, respectively);

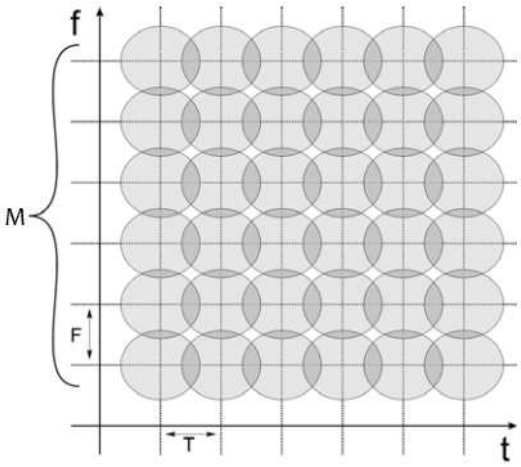

Figure 1.1: The time-frequency representation of the generic NOFDM signal

The NOFDM systems can be treated as a general representation of all multicarrier (MC) systems. In such an approach, the well-known OFDM technique is only a special case of the generic multi-carrier signalling. In OFDM systems the waveform is chosen to be rectangular and the consecutive pulses do not overlap each other in the time domain whereas in frequency domain they are spread over many adjacent subband spectra whilst do not affecting them. In general, the designed pulses used in an NOFDM system can overlap each other in time and/or in frequency domain. It is illustrated in Figure1.1, where one circle reflects the time-frequency representation of the non-orthogonal pulse used in the NOFDM system, T is the distance between consecutive pulses (atoms) in time domain and F denotes the distance between adjacent subcarriers in frequency domain. These pulses are called also *atoms* in the *time/frequency plane* because every signal can be built using the atom-waveform as the world is built with atoms.

FilterBank Multicarrier Modulation (FBMCM) was originally introduced in the scenario of high speed wired access networks [11] and in the standard for the return channel of terrestrial digital video broadcasting (DVB-RCT) [12]. FBMCM, which is a particular case of NOFDM, differs from conventional OFDM in that the data symbols are transmitted over the different subcarriers after proper pulse-shaping. The result

is that the spectra of the subcarriers are bandlimited, bringing forth a number of advantages, namely:

1. reduction of sensitivity to narrowband interferers;
2. frequency domain equalization without the need of the cyclic extension (thus avoiding the consequent efficiency loss);
3. more flexibility to allocate groups of subchannels to different users in the case of Orthogonal Frequency Division Multiple Access (OFDMA).

Moreover, similarly, as in the case of OFDM, the NOFDM transceivers can be also efficiently implemented using the fast Fourier transform (and its inverse) but followed by a polyphase filter.

1.2 Background of Adaptive techniques

Link adaptation to varying radio channel conditions is nowadays one of the key technologies for fulfilling the purpose of a 4G communication system, by efficiently making use of the available resort of the terminals. When a system does not adapt the transmission parameters to the actual channel conditions, the designer must consider a fixed link margin to maintain acceptable performance in the worst case channel conditions. As apparent, the more channel state get better, this strategy leads to a very inefficient utilization of the available resources. Of course, the basic premise for a proper link adaptation is the simultaneous knowledge of some sort of Channel State Information (CSI), by both the transmitter and the receiver, and this can be accomplished, as we will see in the sequel, with an estimate of the channel at the receiver and a feed back to the transmitter, of some link quality information based on that estimate. There are many parameters that can be adapted, according to the current channel status, such as:

- data rate;
- coding rate/scheme;
- power distribution among the subchannels;
- space-time coding.

In order to further improve the link performance, these adaptive techniques can be combined together, to design most powerful hybrid techniques which jointly adapt multiple system parameters.

1.2.1 Adaptive modulation

In variable-rate modulation, the data rate is varied with respect to the channel gain. This can be done by setting the symbol rate of the modulation and by using multiple modulation schemes or constellation sizes. In this work we consider variable rate QAM transmission, where the number of QAM levels is varied according to the channel status and the quality criteria which we intend to optimize [13]. When considering a GMC system, the process of varying the data rate of each subcarrier to obtain a certain global system performance (more in general, together with the Power allocation) is named *Bit loading*.

1.2.2 Power allocation

Another issue to face in adaptive transmitter design is how to distribute the available power across a set of subchannels. Among the diverse strategies that can be invoked, a very popular criterion is based on the maximization of the input-output mutual information. In the ideal case of parallel Gaussian channels, with Gaussian input distribution, the solution is given by the well-known water-filling policy [14]. Since practical systems usually operate far from the theoretical capacity, or when the target of a certain communication system does not involve directly the maximization of the mutual information, various alternative criteria could be used instead.

1.2.3 Adaptive coding

In adaptive coding different channel codes are used to provide different amounts of coding gain to the transmitted bits. A stronger error correction code may be used for harsh propagation conditions, while a weaker code could be more suitable for favorable channel conditions. The implementation of adaptive coding used in the system considered in this work, is called Rate-Compatible Punctured Convolutional (RCPC) codes [15], and it consists of a family of convolutional codes at different code rates r. The basic premise of RCPC codes is to have a single encoder and decoder, whose error correction capability can be modified by not transmitting certain coded

bits (e.g. by puncturing the code). Moreover, RCPC codes have a rate-compatibility constraint, so that, the coded bits associated with a high-rate (weaker protection) code are also used by all lower-rate (stronger protection) codes. Thus, in order to increase the error correction capability of the code, the coded bits of the weakest code are transmitted along with additional coded bits to achieve the desired level of error correction. The rate compatibility makes it very easy to adapt the error protection of the code, since the same encoder and decoder are used for all codes in the RCPC family, with puncturing at the transmitter to achieve the desired error correction. Decoding is performed by a Viterbi algorithm, operating on the trellis associated with the lowest rate code, with the puncturing incorporated into the branch metrics. In this thesis we do not consider any coding (uncoded system) but its implementation is straightforward. Adaptive coding, combined with adaptive modulation as a hybrid technique, takes the name of Adaptive Modulation and Coding (AMC).

1.3 Cognitive Radio

Cognitive radio [16] is a paradigm for wireless communication in which either a network or a wireless node changes its transmission or reception parameters to communicate efficiently avoiding interference with licensed or unlicensed users. This alteration of parameters is based on the active monitoring of several factors in the external and internal radio environment, such as radio frequency spectrum, user behaviour and network state. The idea of cognitive radio was first presented officially in an article by Joseph Mitola III and Gerald Q. Maguire, Jr in 1999 [17]. It was a novel approach in wireless communications that Mitola later described as:

> The point in which wireless personal digital assistants and the related networks are sufficiently computationally intelligent about radio resources and related computer-to-computer communications to detect user communications needs as a function of use context, and to provide radio resources and wireless services most appropriate to those needs.

It was thought of as an ideal goal towards which a software-defined radio platform should evolve: a fully reconfigurable wireless black-box that automatically changes its communication variables in response to network and user demands.

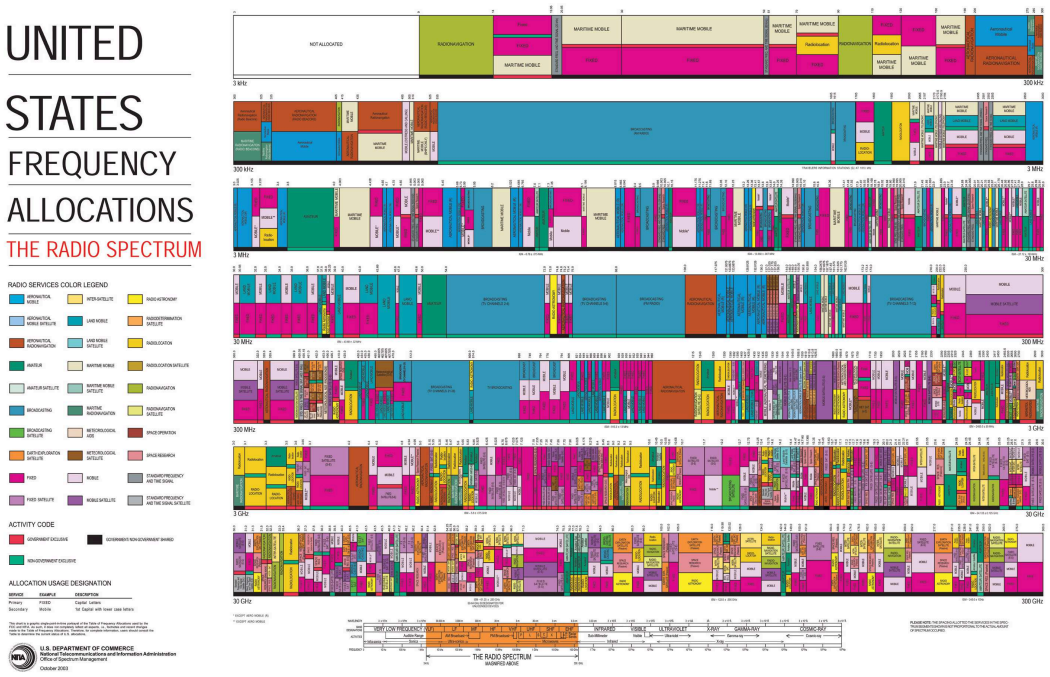

Figure 1.2: United States frequency allocations of the radio spectrum

Regulatory bodies in various countries (including the Federal Communications Commission in the United States, and Ofcom in the United Kingdom) found that most of the radio frequency spectrum was inefficiently utilized. For example, cellular network bands are overloaded in most parts of the world, but amateur radio and paging frequencies are not. Independent studies performed in some countries confirmed that observation [18], and concluded that spectrum utilization depends strongly on time and place. Moreover, fixed spectrum allocation prevents rarely used frequencies (those assigned to specific services) from being used by unlicensed users, even when their transmissions would not interfere at all with the assigned service. This was the reason for allowing unlicensed users to utilize licensed bands (see Figure 1.2) whenever it would not cause any interference (by avoiding them whenever legitimate user presence is sensed). This paradigm for wireless communication is known as *cognitive radio*.

Although cognitive radio was initially thought of as a *software-defined radio* extension (Full Cognitive Radio), most of the research work is currently focusing on Spectrum Sensing Cognitive Radio, particularly in the TV bands. The essential problem of Spectrum Sensing Cognitive Radio is in designing high quality spectrum sensing

devices and algorithms for exchanging spectrum sensing data between nodes. It has been shown that a simple energy detector cannot guarantee the accurate detection of signal presence, calling for more sophisticated spectrum sensing techniques and requiring information about spectrum sensing to be exchanged between nodes regularly. Increasing the number of cooperating sensing nodes decreases the probability of false detection [19].

Filling free radio frequency bands adaptively using OFDMA is a possible approach. Timo A. Weiss and Friedrich K. Jondral of the University of Karlsruhe proposed a *Spectrum Pooling* system [18] in which free bands sensed by nodes were immediately filled by OFDMA subbands.

Applications of Spectrum Sensing Cognitive Radio include emergency networks and WLAN higher throughput and transmission distance extensions.

Evolution of Cognitive Radio toward Cognitive Networks is under process, in which Cognitive Wireless Mesh Network (e.g. CogMesh) is considered as one of the enabling candidates aiming at realizing this paradigm change.

The main functions of Cognitive Radios are [20]:

Spectrum Sensing detecting the unused spectrum and sharing it without harmful interference with other users, it is an important requirement of the Cognitive Radio network to sense spectrum holes, detecting primary users is the most efficient way to detect spectrum holes. Spectrum sensing techniques can be classified into three categories:

Transmitter detection cognitive radios must have the capability to determine if a signal from a primary transmitter is locally present in a certain spectrum, there are several approaches proposed:

- matched filter detection
- energy detection
- cyclostationary feature detection

Cooperative detection refers to spectrum sensing methods where information from multiple Cognitive radio users are incorporated for primary user detection.

Interference based detection recently, a new model for measuring interference at the receiver, referred to as "interference temperature". Unlike

the other transmitter-centric approach, the interference temperature model manages interference at the receiver through the interference temperature limit, which is represented by the amount of new interference that the receiver could tolerate.

Spectrum Management capturing the best available spectrum to meet user communication requirements. Cognitive radios should decide on the best spectrum band to meet the Quality of service requirements over all available spectrum bands, therefore spectrum management functions are required for Cognitive radios, these management functions can be classified as:

- spectrum analysis
- spectrum decision

Spectrum Mobility is defined as the process when a cognitive radio user exchanges its frequency of operation. Cognitive radio networks target to use the spectrum in a dynamic manner by allowing the radio terminals to operate in the best available frequency band, maintaining seamless communication requirements during the transition to better spectrum

Spectrum Sharing providing the fair spectrum scheduling method, one of the major challenges in open spectrum usage is the spectrum sharing. It can be regarded to be similar to generic media access control MAC problems in existing systems

In last part of this thesis are introduced some aspect of cognitive radio paradigm in our filterbank systems and the advantages of the NOFDM systems compared to the OFDM systems will be discussed.

1.4 European research projects

This work is based on the work developed by two European projects, in particular on their theoretical work and this thesis presents some aspects in common with them. These two research projects are the URANUS and the PHYDYAS projects and they are funded by the European Commission. They try to overtake the OFDM limits as the lacks flexibility and its poor spectral resolution adopting a filterbank-based

multicarrier technique that offers high spectrum resolution and can provide independent subchannels, while maintaining or enhancing the high data rate capability. The filterbank-based system has the potential to fulfil the requirements of the new concepts, but a major research effort is necessary for full exploitation and optimization in all aspects of the radio context. The physical layer is the basis on which the networks are built and, with the numerous scenarios and environments, a complex and coherent set of techniques and algorithms has to be worked out. These are the scopes of both the projects. They have a strong academic participation, whose mission is to deliver the best methods and the most efficient algorithms. The industrial partners bring instead their experience in communication infrastructure design and deployment, in instrumentation and measurements and in circuit design. Non-profit research organizations facilitate the cooperation between academic and industry partners.

1.4.1 The URANUS project

The "Universal RAdio-link platform for efficieNt User-centric accesS" (URANUS) project it has been funded by the European Commission under the Framework Programme (FP) 6. It started on December 2005 and finished on December 2008. The partners of this project are the University of Oulu (Finland), the Poznan University of Technology (Poland), CEA LETI (France), STMicroelectronics (Swiss, France and Italy), Telefonica I+D (Spain), the Institute for Accelerating Systems and Applications (Greece) and the University of Kassel (Germany), of Kaiserslautern (Germany) and of Duisburg-Essen (Germany).

The objective of URANUS is the investigation and the design of a universal radio link platform as enabling technology for user-centric access in future wireless systems. The URANUS platform will grant access to existing proprietary as well as standardized wireless system in a unified way (single-mode operation), support simultaneous usage of links in different types of air interfaces (multi-mode operation) and, in particular, ease the introduction of future personalized communications (user-defined mode

operation) and reconfigurable air interfaces.

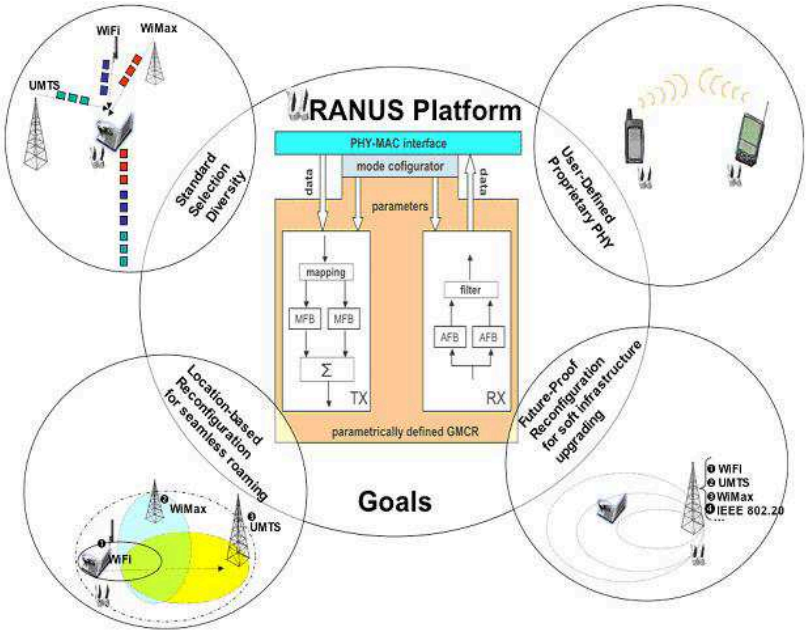

Figure 1.3: Goals of URANUS platform project

URANUS is based on a novel and efficient parametric approach to describe wireless transceivers (TRXs) in the complex baseband using a Generic Multicarrier representation (GMC), where a specific signalling format or mode is uniquely represented by a corresponding set of parameters. The approach is referred to as Canonical Parametric Description (CPD), since the proposed overall transceiver structure (unlike software-defined radio) is independent of the specific choice of the parameter set. The CPD can be used to describe any mode, given that the parameters are properly chosen, which in turn translates to corresponding TRX requirements. The anticipated benefits for the user include better coverage, adaptivity in different environments, and selection of air interfaces matching the user/service/cost requirements. The main motivation to choose a GMC for the CPD is the limited complexity of multi-carrier transceivers and the fact that recent wireless standardization proposals are already based on orthogonal multi-carrier signals. The baseband architecture of the CPD approach being inherently scalable with respect to the achievable data rate has been identified and implemented in software and hardware validation platforms. In order to quantify the system level benefits of multi-mode operation in relevant metrics such as spectrum

usage, coverage, throughput and load-balancing, the performance of the URANUS platform has been simulated at system level for a small number of predetermined scenarios. URANUS provided recommendations for standardization bodies in the area of broadband, wireless and mobile radio communications.

More information about URANUS project can be found on the official website `http://www.ist-uranus.org/`.

1.4.2 The PHYDYAS project

The "PHYsical layer for DYnamic spectrum AccesS and cognitive radio" (PHYDYAS) project has been started on January and it will end on June 2010. The members involved in this project are the Conservatoire National des Arts et Métiers (France), the Technishe Universität München (Germany), the Tampere University of Technology (Finland), the Université Catholique de Louvain (Belgium), SINTEF (Norway), the Centre Tecnologic de Telecomunicacions de Catalunya (Spain), the Research Academic Computer Technology Institute (Greece), the University of Napoli Federico II (Italy), CEA-LETI (France), Agilent (Belgium), Alcatel-Lucent (UK, Germany) and COMSIS (France).

The main objective is to propose FBMC (FilterBank Multi Carrier) physical layer for future radio systems that is more efficient than the present OFDM physical layer and better suited to the new concepts of DASM (Dynamic Access Spectrum Management) and cognitive radio.

PHYDYAS proposes an advanced physical layer, using filterbank-based multicarrier transmission, for the new concepts in radiocommunications: dynamic access spectrum management and cognitive radio. It shows that the performance and operational flexibility of systems are enhanced by exploiting the spectral efficiency of filter banks and the independence of subchannels. Combining with offset quadrature amplitude modulation (OQAM), no cyclic prefix is needed, all the radiated power is used

and gains in maximum throughput compared to OFDM are achieved. Robustness to the Doppler spread phenomenon and jammers is obtained and new functionalities are possible. The high resolution spectrum analysis capability is exploited for DASM and cognitive radio and a single device can do spectrum sensing and reception simultaneously.

Research in signal processing is carried out to complete the knowledge in filter banks for transmission and satisfy requirements of new radio systems: fast initialization, optimum transmit-receive processing for single and multiple antenna (MIMO) systems, scalability. Research in communications concerns dynamic access and cross-layer aspects, and compatibility with OFDM. In cognitive radio, research deals with radio scene analysis and channel identification and the impact of the independence of subchannels on transmit power control and dynamic spectrum management. A simulation software is developed for a typical WiMAX configuration and scenario and performance comparison with OFDM is carried out. A real time soft/hardware demonstrator is built to complete simulation results and show efficient architectures.

The expected impact of PHYDYAS is the migration of wireless systems to a physical layer that is more efficient and better responds to the needs of dynamic access and cognitive radio. The consortium consists of leading academic research groups across Europe, teamed with world leading companies in infrastructures, circuit design and instrumentation.

More information about PHYDYAS project can be found on the official website `http://www.ict-phydyas.org/`.

Chapter 2

The filterbank multicarrier systems

Some of today's common air interfaces adopt single carrier schemes, whereas others rely on multicarrier transmission. Conventional OFDM signals are generated by concatenating the outputs of IFFTs. A few parameters, including the number of subcarriers, the FFT and guard period lengths, and of course the subcarrier modulation scheme, completely define the OFDM modulation. Performing the IFFTs in signal windows with non-rectangular shapes leads to alternative, more general multicarrier modulation methods. Known as filterbank (FB)-based or generalized multicarrier (GMC) transmission, the freedom in the pulse design can be taken advantage of to reduce the vulnerability to phase noise or frequency-selective channels, for instance.

This multicarrier concept using arbitrary window functions is adopted to facilitate the representation of a wide range of modulation schemes. Conventional OFDM and alternative multicarrier signals can be represented by their window function in addition to the number of subchannels, etc., provided a regular grid-like spacing of the elementary pulses in the time-frequency plane. Single carrier signals can be viewed as a special case of multicarrier, with one subcarrier. The major advantage of multicarrier signalling is the narrowband character of the subcarriers, which simplifies dealing with multipath propagation. Employing a multicarrier approach in the receiver can be advantageous even if the actual signal to be decoded is single carrier. Moreover, appropriate signal expansion and processing in a time-frequency (TF) domain, rather than in frequency domain, facilitates simple channel estimation and demodulation similar as in OFDM receivers even when the channels are doubly dispersive.

We start our discussion from the mathematical framework that establishes the

basis for the development of the filterbank structure, i.e. the Gabor theory, both in a continuous time domain and in a sampled discrete domain for digital application [3].

2.1 Gabor Expansion and Weyl-Heisenberg Systems

The Gabor signal expansion is a special case of the more general frame signal expansion [21], [22] which refers to expressing an arbitrary signal $s(t) \in L^2$ (i.e. a function that is square integrable [23]) as

$$s(t) = \sum_{m\in\mathbb{Z}} \sum_{n\in\mathbb{Z}} c_{m,n} g_{m,n}(t) \tag{2.1.1}$$

where $(g_{m,n})$ is a sequence of functions in L^2, and $(c_{m,n})$ are the so called frame coefficients ($(c_{m,n}) \in l^2(\mathbb{Z}\times\mathbb{Z})$ i.e. they are square summable). The signal expansion (2.1.1) resembles the well-known signal expansion on a basis sequence. However, $(g_{m,n})$ consists, in general, of linearly depended components, with the property that they are complete in $L^2(\mathbb{R})$. The case of $(g_{m,n})$ being a basis can be considered as a special case of frame expansion.

A well known fact from frame theory is that an arbitrary system of functions $(g_{m,n})$ cannot constitute a frame, i.e., the functions in $(g_{m,n})$ are not complete in L^2. The formal definition of a sequence $(g_{m,n})$ to be a frame is that there exist two constants $0 < A \leq B < \infty$ such that [24]

$$A\|s\|^2 \leq \sum_{m,n\in\mathbb{Z}} |\langle s, g_{m,n}\rangle|^2 \leq B\|s\|^2 \tag{2.1.2}$$

where $\langle\cdot,\cdot\rangle$ denotes the inner product. If (2.1.2) holds then an arbitrary signal can be expressed as in (2.1.1) with a proper choice of coefficients $(c_{m,n})$. Constants A, B, are the frame bounds. For $A = B$ the frame is called tight, whereas for $A \approx B$ the frame is called snug. A major problem in frame theory is the specification of the frame coefficients $(c_{m,n})$. Since $(g_{m,n})$ consists of linearly dependent elements, $(c_{m,n})$ are not uniquely specified. One valid value for $(c_{m,n})$ is provided by the concept of the frame operator. The frame operator $\mathcal{F}$ of $(g_{m,n})$ is defined in terms of the operators

$$T : s \to \left(\langle s, g_{m,n}\rangle\right)_{m,n\in\mathbb{Z}} \tag{2.1.3}$$

called the analysis operator, and its conjugate

$$T^* : (c_{m,n}) \to \sum_{m,n\in\mathbb{Z}} c_{m,n} g_{m,n} \tag{2.1.4}$$

called the synthesis operator. The frame operator is defined as

$$\mathcal{F} = T^*T : s \to \mathcal{F}s = \sum_{m,n\in\mathbb{Z}} \langle s, g_{m,n}\rangle \, g_{m,n} \tag{2.1.5}$$

It can be shown that the frame operator is invertible and can be used to define the so called (canonical) dual frame sequence $(\gamma_{m,n}) = (\mathcal{F}^{-1} g_{m,n})$ with frame bounds B^{-1}, A^{-1}. Using the dual frame $(\gamma_{m,n})$, coefficients $(c_{m,n})$ can be found as

$$c_{m,n} = \langle s, \gamma_{m,n}\rangle \tag{2.1.6}$$

It can be shown that all valid $(c_{m,n})$ values can be produced by an inner product operation, as in (2.1.5), using any (non-unique) dual frame to $(c_{m,n})$. Using the canonical dual in (2.1.5) results in the minimum norm coefficients. It is also noted that the roles of $(g_{m,n})$ and $(\gamma_{m,n})$ can be exchanged, i.e.,

$$s(t) = \sum_{m\in\mathbb{Z}} \sum_{n\in\mathbb{Z}} \langle s, g_{m,n}\rangle \, \gamma_{m,n}(t) = \sum_{m\in\mathbb{Z}} \sum_{n\in\mathbb{Z}} \langle s, \gamma_{m,n}\rangle \, g_{m,n}(t) \tag{2.1.7}$$

The Gabor (frame) expansion of $s(t)$ has the same form as (2.1.1), with the functions of $(g_{m,n})$ having the special form [24], [25]

$$g_{m,n}(t) = g(t - nT)e^{j2\pi mF} \text{ with } m, n \in \mathbf{Z} \tag{2.1.8}$$

where $g \in L^2(\mathbb{R})$ is the prototype function or Gabor atom. This is called a Weyl-Heisenberg or Gabor system (frame) and, as can be seen, it is generated by shifting

the atom uniformly in time by T (time spacing) and in frequency by F (frequency spacing). This observation leads to the interpretation of the (Gabor) coefficients $(c_{m,n})$, as reflecting the signal's behavior in the time-frequency plane, at the regular grid defined by T, F, as shown in Figure 2.1 [25].

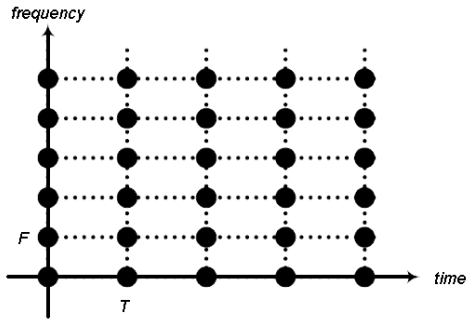

Figure 2.1: Gabor expansion sampling grid in the time-frequency plane [3]

The lattice size of the time/frequency grid, given by the product TF, plays a crucial role for the completeness and linear independence of the $(g_{m,n})$ [21]. The elements of $(g_{m,n})$ are complete in L^2 if and only if $TF \leq 1$. This constraint is only a necessary but not sufficient condition for $(g_{m,n})$ being a Gabor frame [21]. It can be shown that for $TF = 1$ (critical sampling), a Weyl-Heisenberg system is, in fact, a basis of L^2. In contrast, for $TF \leq 1$ (overcritical sampling) the elements of $(g_{m,n})$ become linearly dependent. A major result of Gabor frame theory is that for $TF = 1$, the atom γ cannot be well concentrated in time/frequency, e.g., a Gaussian γ cannot generate a complete Gabor frame in L^2. This is one of the major reasons for choosing overcritical Gabor representations, as well-localized atoms can be found in this case. In order to specify the Gabor coefficients $(c_{m,n})$, the dual frame $(\gamma_{m,n}) = (\mathcal{F}^{-1} g_{m,n})$ must be computed. It turns out that $(\gamma_{m,n})$ is actually a Gabor frame, generated by the atom $\gamma = \mathcal{F}^{-1} g$, i.e.,

$$\gamma_{m,n}(t) = \gamma(t - nT) e^{j2\pi mF} \text{ with } m, n \in \mathbb{Z} \tag{2.1.9}$$

with the same parameters T, F as $(g_{m,n})$. Function γ is often referred as the (canonical) dual atom of g. This is an important property of Gabor frames, since only the dual atom γ must be specified for the computation of the dual frame. For

the special case of tight frames, i.e., $A = B$, the dual atom can be shown to be readily specified as

$$\gamma(t) = c\, g(t) \tag{2.1.10}$$

where c is a normalization constant. It is noted that the canonical dual frame (2.1.9) is not the only choice of valid dual frames to $(g_{m,n})$. As a matter of fact, not every dual frame of $(g_{m,n})$ has the Weil-Heisenberg structure. The family of functions (atoms) that can be used to generate a valid dual Weil-Heisenberg frame (including the canonical dual atom) is specified by the so called Wexler-Raz identity [24].

2.2 Discrete Gabor Expansion as filterbank

In digital signal processing applications, the concept of Gabor expansion has to be translated to the discrete-time domain. The discrete Gabor expansion [26] of a signal $s[n] \in l^2(\mathbf{Z})$ refers to

$$s[k] = \sum_{n\in\mathbb{Z}} \sum_{m=0}^{M-1} c_{m,n} g_{m,n}[k] \tag{2.2.1}$$

where

$$c_{m,n} = \langle s, \gamma_{m,n} \rangle \tag{2.2.2}$$

are the Gabor coefficients of the signal and $(g_{m,n})$ and $(\gamma_{m,n})$ are dual (discrete-time) frames, obtained by uniform shifts in time and frequency of the (real valued) Gabor atoms $g[k]$ and $\gamma[k]$ respectively. Specifically,

$$g[k] = g[k - nN] e^{j2\pi km/M} \text{ with } n \in \mathbb{Z}, m = 0, \ldots, M-1 \tag{2.2.3}$$

and

$$\gamma[k] = \gamma[k - nN] e^{j2\pi km/M} \text{ with } n \in \mathbb{Z}, m = 0, \ldots, M-1 \tag{2.2.4}$$

where N and $2\pi/M$ are the time spacing and frequency spacing of the elementary functions, respectively. Similarly to the continuous-time Gabor expansion, the time-frequency lattice of the discrete Gabor expansion cannot be chosen arbitrary. A necessary requirement for completeness of the Gabor frames is

$$N \leq M \tag{2.2.5}$$

For $N = M$ the expansion corresponds to a critically sampled time-frequency plane, whereas $N < M$ corresponds to overcritical sampling. Although overcritical sampling results in a redundant signal expansion, i.e., the number of Gabor coefficients is greater than the number of signal samples, it is usually preferred since the Gabor atoms can be chosen with desirable properties such as good time-frequency localization, which is not possible in the case of critical sampling [25]. A significant advantage of the discrete Gabor transform is its efficient implementation. This can be seen by relating the Gabor transform to the concept of a perfect reconstruction (PR) Discrete Fourier Transform (DFT) filter bank [27] usually employed in signal processing sphere.

2.2.1 The biorthogonality property

In almost every signal processing application where filter bank is used, the PR property is mandatory. However, in order to achieve the PR property, $\gamma_m[k]$, $g_m[k]$, M, N must be properly selected, satisfying specific constraints [28]. Usually, the number of channels M and analysis filters $\gamma_m(f)$ are first selected according to some criterion depending on the specific application. Selection of the remaining filter bank parameters $(g_m[k], N)$ leading to PR of the input signal is done based on these. The problem of imposing the PR property (exactly or approximately) has been studied intensively in the signal processing literature (e.g., [29] and references therein) and is closely related to problem of filter design.

A fundamental condition leading to the PR property is the biorthogonality between the synthesis prototype pulse and the analysis one. The biorthogonality is equivalent to the completeness relation proved by Wexler and Raz in [30]:

$$\sum_{m\in\mathbb{Z}}\sum_{n\in\mathbb{Z}}\gamma^*_{m,n}[k']g_{m,n}[k] = \delta[k-k'] \tag{2.2.6}$$

Substituting (2.2.3) and (2.2.4) in (2.2.6), we obtain

$$\sum_{m\in\mathbb{Z}}\sum_{n\in\mathbb{Z}}\gamma^*[k'-nN]e^{-j2\pi mk'/M}g[k-nN]e^{j2\pi mk/M} = \delta[k-k'] \tag{2.2.7}$$

$$\sum_{m\in\mathbb{Z}}\sum_{n\in\mathbb{Z}}\gamma^*[k'-nN]g[k-nN]e^{j2\pi m(k-k')/M} = \delta[k-k'] \tag{2.2.8}$$

where $\delta[k]$ is the Kronecker delta operator, defined as

$$\delta[k] = \begin{cases} 1 & \text{if } k=0 \\ 0 & \text{otherwise} \end{cases} \tag{2.2.9}$$

Using the Poisson summation formula, (2.2.8) can be written as

$$\frac{1}{M}\sum_{m\in\mathbb{Z}}\sum_{n\in\mathbb{Z}}\gamma^*[k'-nN]g[k-nN]\delta[k-k'+mM] = \delta[k-k'] \tag{2.2.10}$$

$$\sum_{m\in\mathbb{Z}}\gamma^*[k-nN-mM]g[k-nN] = M\delta[n] \tag{2.2.11}$$

Formula (2.2.11) is the starting point to devise algorithms evaluating the dual prototype pulse $\gamma[k]$ used in the analysis filterbank. Two algorithms (one is fast version of the other) that allow to calculate the dual atom given the synthesis one, are discussed in Section 2.5.

2.2.2 DFT filterbank

A typical example of perfect reconstruction (PR) filterbank [29] is depicted in Figure 2.2. A (complex valued) signal $s[k]$ is input to M filters, possibly non-causal, whose frequency transform is denoted by $\Gamma_m(f)$. These filters can be either FIR or IIR and, in general, have passband characteristics. Ideally, their passband regions

do not overlap. Since the output sequence of $\Gamma_m(f)$ is frequency limited, it can be downsampled by a factor N. The cascade of filters $\Gamma_m(f)$ and the decimators constitute the analysis filterbank, with output sequences (subband signals) $c_m[k]$. Signal $s[k]$ is reconstructed by processing the subband signals by the subsequent synthesis filterbank. Each signal is first upsampled by a factor N and input to a filter $G_m(f)$, with passband frequency response. The M resulting output sequences are then summed in order to reconstruct the original signal $s[k]$. If the reconstructed signal has no distortion, i.e. $\hat{s}[k] = s[k]$, the structure of Figure 2.2 is referred to as perfect reconstruction (PR) filterbank.

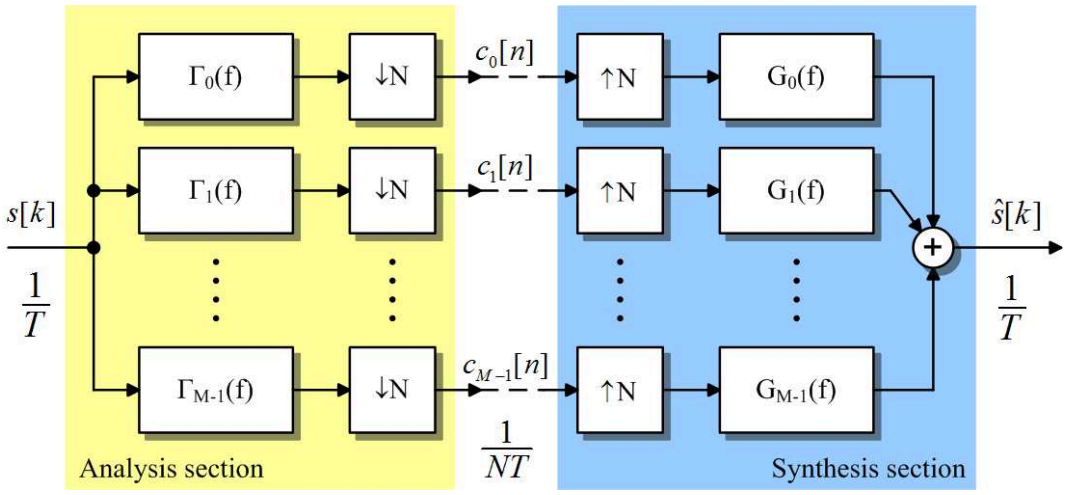

Figure 2.2: M-channel filter bank

By contrasting the operation of a PR filter bank, as described above, with the discrete Gabor expansion formula in (2.2.1), many commonalities can be readily identified. In both cases, the signal is analyzed to a set of coefficients which are combined in order to reconstruct the signal. In fact, as will be demonstrated in the following, a PR filter bank can actually be employed in order to efficiently implement the Gabor expansion.

A well known special case of PR filter bank is the DFT filter bank, which is obtained by selecting the analysis and synthesis filters as

$$\begin{aligned} \gamma_m[k] &= \gamma[k]e^{j2\pi km/M} \\ g_m[k] &= g[k]e^{j2\pi km/M} \end{aligned} \quad \text{with } m = 0, \ldots, M-1 \tag{2.2.12}$$

where $g[k]$, $\gamma[k]$ are the real-valued, prototype filters of finite duration (possibly non-causal) equal to L. It follows from (2.2.12) that

$$\begin{aligned} \Gamma_m(f) &= \Gamma\left(f - \frac{m}{M}\right) \\ & \qquad \text{with } m = 0, \ldots, M-1 \\ G_m(f) &= G\left(f - \frac{m}{M}\right) \end{aligned} \tag{2.2.13}$$

i.e., the filters are obtained as uniform shifts in frequency of the prototype filters. In general, due to the finite filter duration there is overlapping among the subbands but its effect is completely eliminated by an appropriate synthesis filter bank. However, the overlapping is an important aspect in data communication systems and it will be analyzed later (cfr. §2.3.1).

The subband signals generated by the DFT analysis filterbank are equal to

$$\begin{aligned} c_m[n] &= \sum_{k\in\mathbb{Z}} s[k]\gamma_m[nN-k] = \\ &= \sum_{k\in\mathbb{Z}} s[k]\gamma[nN-k]e^{-j2\pi m(nN-k)/M} \end{aligned} \tag{2.2.14}$$

and the reconstructed signal is

$$\begin{aligned} s[k] &= \sum_{m=0}^{M-1}\sum_{n\in\mathbb{Z}} c_m[n]g_m[n] = \\ &= \sum_{m=0}^{M-1}\sum_{n\in\mathbb{Z}} c_m[n]g[k-nN]e^{j2\pi m(k-nN)/M} \end{aligned} \tag{2.2.15}$$

Comparing (2.2.14), (2.2.15) to (2.2.1), (2.2.2) it follows that the DFT filterbank implements a Gabor expansion of the signal $s[n]$, employing the dual Gabor frame sequences

$$g_{m,n}[k] = g[k-nN]e^{j2\pi m(k-nN)/M} \text{ with } n \in \mathbb{Z}, m = 0, \ldots, M-1 \tag{2.2.16}$$

and

$$\gamma_{m,n}[k] = \gamma[-(k-nN)]e^{j2\pi m(k-nN)/M} \text{ with } n \in \mathbb{Z}, m = 0, \ldots, M-1 \qquad (2.2.17)$$

The frames of (2.2.16), (2.2.17) differ from the Gabor frame definition in (2.2.3), (2.2.4) by a multiplicative scalar, which is however irrelevant. Therefore, the Gabor expansion defines a DFT filterbank and viceversa, with the correspondences shown in Table 2.1 [31]. Of course, since non-causal filters can not be implemented in practice, delayed versions of the prototype filters are employed.

Gabor expansion	DFT filterbank
Gabor (synthesis) atom: $g[k]$	Synthesis prototype: $g[k]$
Gabor (analysis) atom: $\gamma[k]$	Analysis prototype: $\gamma[-k]$
Gabor coefficients: $(c_{m,n})$	Subband signals: $c_m[n]$
Time spacing: N	Downsampling factor: N
Frequency spacing: $2\pi/M$	Number of channels: M

Table 2.1: Parameter correspondence between Gabor expansion and DFT filter bank

The importance of identifying the Gabor expansion as a DFT filterbank is that the efficient implementation of DFT filterbanks can be employed to perform the expansion, resulting in significant computational gains compared to a straightforward implementation of (2.2.1), (2.2.2).

2.3 Multicarrier signaling with filterbank structure

Constraining the signal to be multicarrier in order to achieve mode flexibility is not a severe constraint. Actually, it is well known that multicarrier signals are optimal for broadband applications, where the channel is time invariant and introduces severe inter-symbol interference (ISI). This observation has led to the high utilization of OFDM signaling by current and future broadband standards. However, conventional multicarrier schemes are inferior, compared to other signaling formats (e.g., single carrier), in communication aspects such as transmission under channel with high

dynamics, peak to average power ratio and sensitivity to synchronization errors [32], [33].

A multicarrier communication system based on a filterbank structure is slightly different from the one show in Figure 2.2 used in signal processing. The main difference is that the order of the analysis and synthesis filterbanks has been interchanged from the subband coding arrangement discussed in Section 2.2.

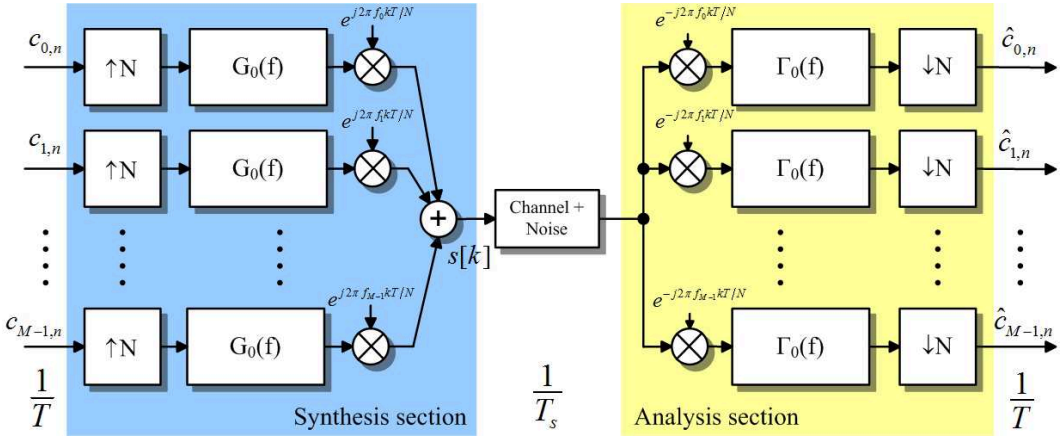

Figure 2.3: Direct realization of an M-band communication system using filterbank modulation

The analog multicarrier transmitted (baseband) signal is

$$s(t) = \sum_{n\in\mathbb{Z}} \sum_{m=0}^{M-1} c_{m,n} g(t - nT) e^{j2\pi mFt} \tag{2.3.1}$$

where T, F are respectively time and frequency shifts of Gabor atoms. In a data communication systems these parameters become the GMC symbol[1] interval and subcarriers spacing in frequency domain, respectively. Moreover $c_{m,n}$ are the source QAM symbols (at the rate $R_u = 1/T_u = 1/MT$), m is the index of the symbol within each block ($0 \leq k \leq M-1$) and n is generic block index. Each subcarrier is spectrally shaped with $G(f)$ filter and the center frequency of the mth subcarrier is mF.

It is well-known that the sampling of a continuous-time signal entails the origin of the repetitions of the spectrum of the analog signal translated in the frequency domain

[1]In this work we define a "GMC symbol" each block of N samples obtained by the filterbank modulation of M QAM symbols.

by the multiples of the sampling frequency. If the sampling frequency is badly chosen the spectrum repetitions can interfere with the original one (aliasing). According to the Nyquist sampling theorem the sampling frequency must be greater or equal than the overall bandwidth of the transmitted signal, i.e. $f_s \geq B_{TOT}$, in order to avoid any interference. The spectrum of an complex bandbased analog multicarrier signal is illustrated in Figure 2.4. In such example the overall bandwidth is about $B_{TOT} = 2$ MHz. The spectrum of the same sampled signal is shown in Figures 2.5 and 2.6. In the first on these two figures the repetitions (red lines) of the original spectrum (blue lines) are far from the bandbased spectrum because the sampling frequency has been chosen greater than the overall bandwidth, i.e. $f_s > B_{TOT}$. In Figure 2.6, instead the sampling frequency satisfies the Nyquist constraint with the equality and the spectrum repetitions are adjacent to the original one. In such case we can consider only the frequency $f \in [0, B_{TOT}]$ without any loss of information because the spectrum of the subcarriers is even.

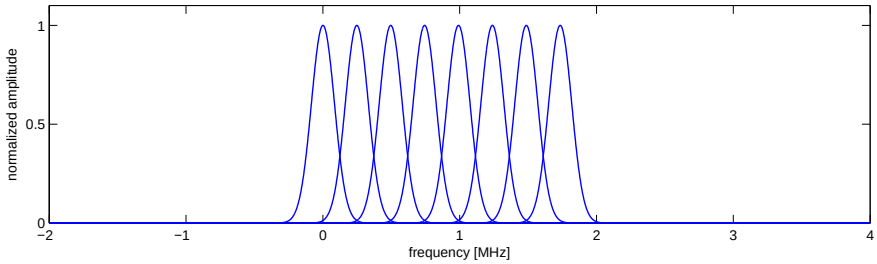

Figure 2.4: Spectrum of the analog multicarrier signal

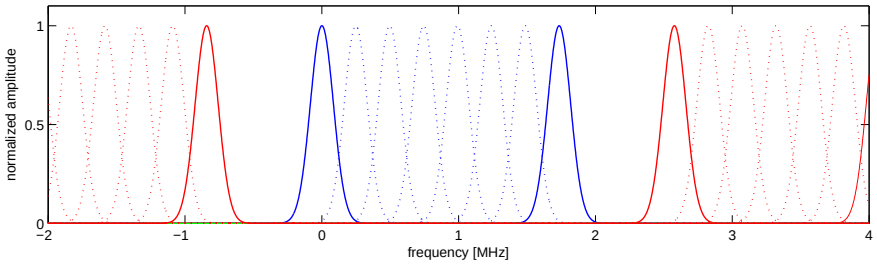

Figure 2.5: Spectrum of the digital multicarrier signal with $f_s > B_{TOT}$

In the remainder of this document we assume to work at Nyquist sampling fre-

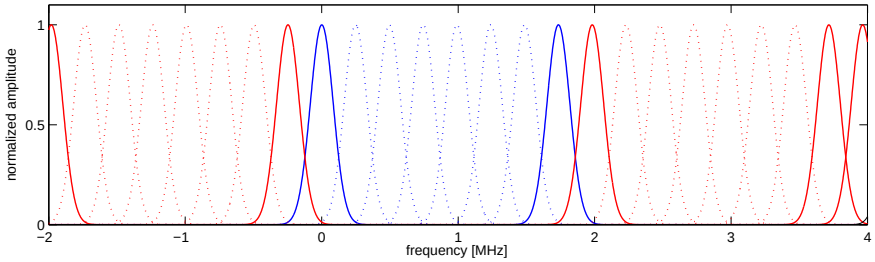

Figure 2.6: Spectrum of the digital multicarrier signal with $f_s = B_{TOT}$

quency and the presence of an anti-aliasing filter (i.e. a low-pass filter with bandwidth equal to the bandwidth of the analog signal) at the beginning of the receiver is assumed in order to avoid the aliasing and it will be no longer mentioned.

Thus assuming a sampling frequency equal to $f_s = 1/T_s$ and because every GMC symbol has to be composed by N samples according to the Gabor expansion (i.e. consecutive atoms are separated by N samples, see 2.2.3) the duration of each GMC symbol is $T = T_s \cdot N$. Consequently the overall bandwidth (and the sampling frequency) can be expressed as

$$f_s = B_{TOT} = \frac{N}{T} \tag{2.3.2}$$

Moreover the overall available bandwidth is divided equally into M subbands and hence the subcarrier spacing F results

$$F = \frac{B_{TOT}}{M} = \frac{N}{MT} \tag{2.3.3}$$

If $G(f)$ has limited bandwidth smaller than subcarrier spacing, i.e. $B_G < F$ (and hence there is no overlaping among the subcarriers in frequency domain), the signal will not be affected by inter-carrier interference (ICI). The digitalized signal is thus [34]

$$s\left(kT_S\right) = s\left(k\frac{T}{N}\right) = \sum_{n\in\mathbb{Z}}\sum_{m=0}^{M-1} c_{m,n}\, g\left(k\frac{T}{N} - nT\right) e^{j2\pi mFk(T/N)} =$$
$$= \sum_{n\in\mathbb{Z}}\sum_{m=0}^{M-1} c_{m,n}\, g\left[(k-nN)\frac{T}{N}\right] e^{j2\pi m(N/MT)k(T/N)} \quad (2.3.4)$$

Figure 2.3 shows an M-subchannel filterbank communication system, also referred to as a multicarrier communication system. The complex-valued modulation symbols $c_{m,n}$ with $m = 0, 1, \ldots, M-1$, chosen from a not necessarily identical QAM constellations, are provided at the GMC symbol rate $1/T$. After upsampling by a factor of N, indicated by the notation $\uparrow N$, each symbol stream is filtered by a baseband filter, referred to as a synthesis prototype filter, with frequency characteristic $G(f)$ and impulse response $g[k]$. The transmit signal $s[kT/N]$ is obtained at the transmission rate of N/T by adding the M filter-output signals properly shifted in frequency. At the receiver, the analysis prototype filter is chosen to be biorthogonal to the synthesis prototype filter and it is followed by subsampling by a factor of N, indicated by the notation $\downarrow N$.

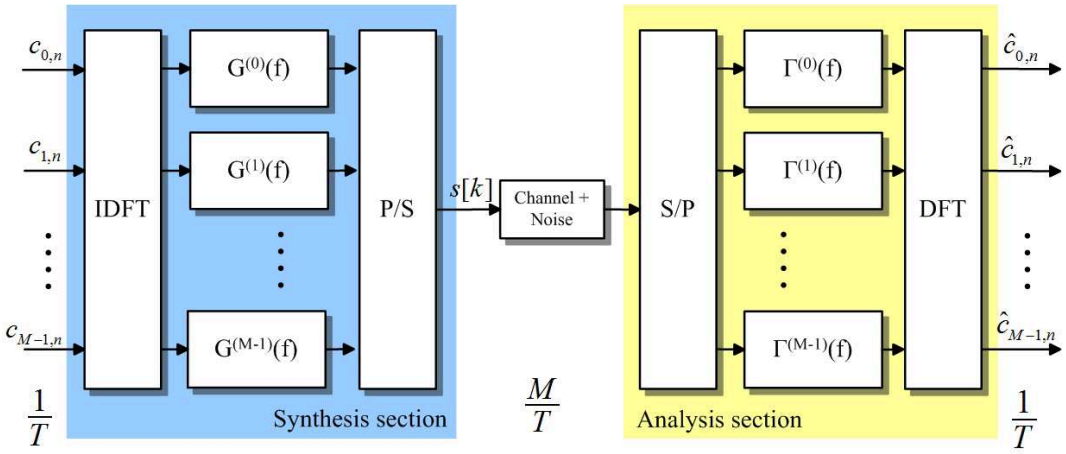

Figure 2.7: Efficient realization of the filterbank system for the case $N = M$

Bellanger et Al. [35] have shown that for the critically sampled case $N = M$ the filterbank transmitter and receiver can equivalently be realized as depicted in Figure 2.7. The M-branch filters with transfer functions $G^{(0)}(f), G^{(1)}(f), \ldots, G^{(M-1)}(f)$

and respective impulse responses $g^{(0)}[k], g^{(1)}[k], \ldots, g^{(M-1)}[k]$ are baseband filters that represent the M polyphase components of the synthesis prototype filter $G(f)$. Essentially, to obtain the impulse responses of the polyphase filter components, regularly T-spaced samples (or M-spaced for the discrete model) are extracted from the prototype filter impulse response $g[k]$ having T/M-spaced samples, i.e.

$$g^{(m)}[k] = g[kM + m] \text{ with } m = 0, \ldots, M-1 \tag{2.3.5}$$

Each polyphase filter component is then applied to a different time domain point of the IDFT output. The use of IDFT (and its fast version IFFT) is possible because, starting for (2.3.4),

$$\begin{aligned} s\left(k\frac{T}{N}\right) &= \sum_{n\in\mathbb{Z}}\sum_{m=0}^{M-1} c_{m,n} g\left[(k-nN)\frac{T}{N}\right] e^{j2\pi m(N/MT)k(T/N)} = \\ &= \sum_{n\in\mathbb{Z}} g\left[(k-nN)\frac{T}{N}\right] \underbrace{\sum_{m=0}^{M-1} c_{m,n} e^{j2\pi mk/M}}_{IDFT} \end{aligned} \tag{2.3.6}$$

This M-branch polyphase filterbank structure is attractive because the required filtering operations are performed at the symbol rate $1/T$ instead of the transmission rate M/T. It has been noted that a trade-off between processing speed and parallelism is generally allowed in systems where the filterbanks are employed.

Moreover, in this structure it can be used the (I)FFT algorithm in order to speed up the calculation of (I)DFT blocks output. The efficient polyphase implementation introduced by Bellanger et Al. can be also employed for the non-critically sampled case $N > M$. In that case the synthesis modulator is composed by N-branch filters represented by the N polyphase components of the synthesis prototype filter $G(f)$. Moreover, a further improved implementation will be discussed in Section 2.4.

The structure shows previously in Figure 2.3 represents a particular case of the filterbank structure. In fact the most general scheme for a multicarrier communication system based on filterbank modulation is depicted in Figure 2.8 [36].

The serial data stream $c[k]$ is first converted to M-parallel substreams $c_m[n] = c[nN+m]$ where $c_m[n]$ denotes the mth symbol in the nth block of M QAM symbols.

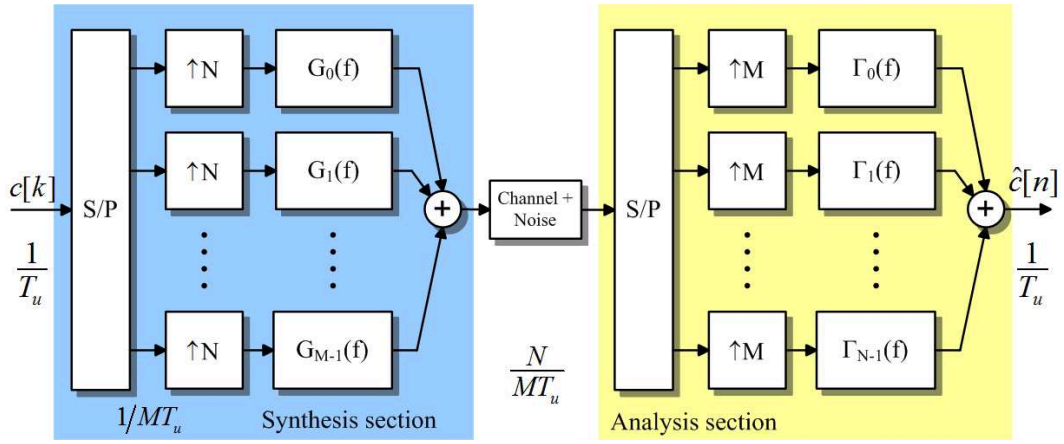

Figure 2.8: General multirate discrete-time filterbank system

With $N > M$, the ratio $(N-M)/N$ represents the amount of redundancy introduced per transmitted GMC symbol. At the receiver, the rate is reduced by the same amount such that the overall rate remains unchanged. From an input-output (I/O) point of view, our transmit filterbank takes size-M blocks of $c[k]$, filters them, and maps them to size-N at the end of the synthesis section. The QAM symbol rate in the serial data stream $c[k]$ is $1/T_u$ while the rate of the transmitted data is $1/T_s = (N/M)(1/T_u)$.

The generality of this scheme is given by the fact the every filter $G_m(f)$ and $\Gamma_m(f)$ can be arbitrarily choosen, each one independently from the others. In this case the usual Discrete Gabor Expansion is no longer enough to well describe the system and it is necessary to adopt a DGE improvement, such as the Discrete Multi-Gabor Expansion, introduced for the first time in [37]. In order to obtain the schemes analyzed previously and adopted in this work, we have to apply (2.2.12). Because the filters have all the same baseband frequency response (they differ only for the different frequency shift) the DGE is sufficient.

2.3.1 The overlapping factor β

Figure 2.9 illustrates how the parameters N, M and $1/T$ determine the spectral characteristic of the transmitted signal.

In the case illustrated in Figure 2.9 the subcarrier spacing is given by $F = N/MT$, as previously mentioned, while the bandwidth of every single subcarrier is determined by the GMC symbol interval T. By resorting to the non-critically sampled filterbanks,

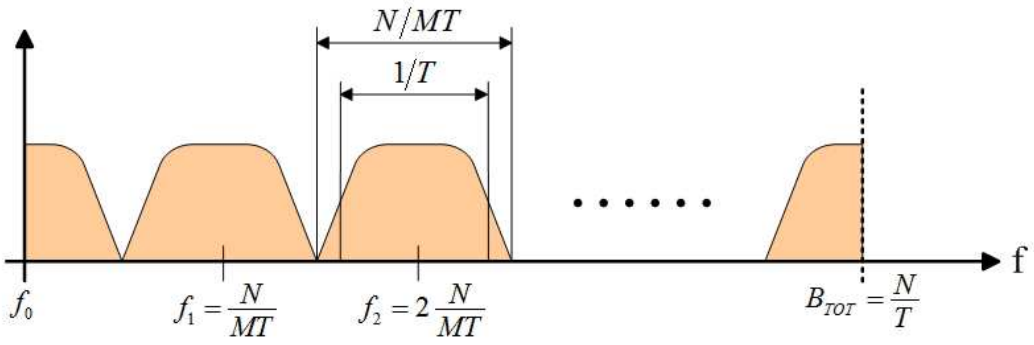

Figure 2.9: Transmit signal spectrum without subcarriers overlapping

the multicarrier modulation is feasible and ensures total spectral containment within a subchannel with an excess bandwidth of $\alpha = N/M - 1$. By letting $N \to M$, the penalty in bandwidth efficiency becomes vanishingly small ($\alpha \to 0$) at the price of an increased implementation complexity because the filters with increasingly sharper spectral roll-off must be realized in order to minimize ICI. Otherwise a certain level of overlapping between adjacent subcarriers must be tolerated and the level of inter-carrier interference affecting the transmitted signal will obviously increase as the overlapping grows. That situation is depicted instead in Figure 2.10.

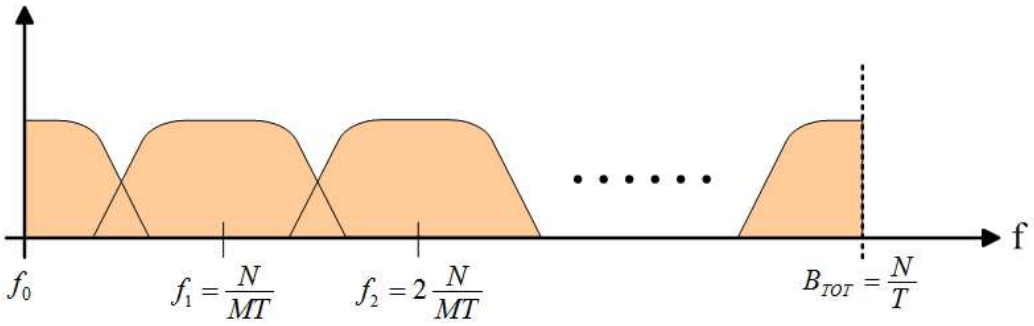

Figure 2.10: Transmit signal spectrum with subcarriers overlapping

In order to quantify this effect, we can define a new parameter β as

$$\beta \triangleq \frac{N}{M} \tag{2.3.7}$$

called *overlapping factor* or *oversampling factor* since it is the ratio between the

number of samples and the number of QAM symbols carried by every single GMC symbol. In order to vary the overlapping factor β, it is generally changed the number of samples per block N while the number of subcarriers M is usually given. Consequently even the duration of the GMC symbol is changed because $T = NT_s$ while the overall bandwidth remains constant. In fact it is given by $B_{TOT} = \frac{N}{T} = \frac{N}{NT_s} = 1/T_s$. So the subcarrier spacing can be expressed as

$$F = \frac{N}{MT} = \frac{\beta}{T} \tag{2.3.8}$$

Therefore in the spectrum of the transmitted signal, the bandwidth of each subcarrier changes whereas the subcarriers spacing is kept constant for each value of β. This fact can be easily understood looking Figure 2.10.

Thus the overlapping factor is a fundamental parameter because it determines the degree of the overlapping but also because it is the lattice size of the time/frequency grid, given by the product TF, that plays a crucial role in the discrete Gabor expansion. In fact, substituting (2.3.8) in the product TF, we obtain

$$TF = T\frac{N}{MT} = \frac{N}{M} = \beta \tag{2.3.9}$$

2.3.2 OFDM as particular FB polyphase case

Orthogonal Frequency Division Multiplexing (OFDM), the technology at the heart of digital broadcast television and radio, and also now accepted as the current generation standard for wireless LAN systems, solves the difficult inter-symbol interference problem encountered with high data rates across multipath channels. By dividing the bandwidth into many small orthogonal frequencies (efficiently achievable using the fast Fourier transform), the data can be transmitted across multiple narrowband channels, which suffer only from flat fading. We pay that in term of spectral efficiency caused by the introduction of the so-called *cyclic prefix* (CP), i.e. some redundancy in order to contrast ISI and ICI.

The block scheme of a general OFDM system is depicted in Figure 2.11.

In OFDM systems it was assumed that each symbol is transmitted by means of one rectangular pulse of length T so that the associated spectrum for one subcarrier is

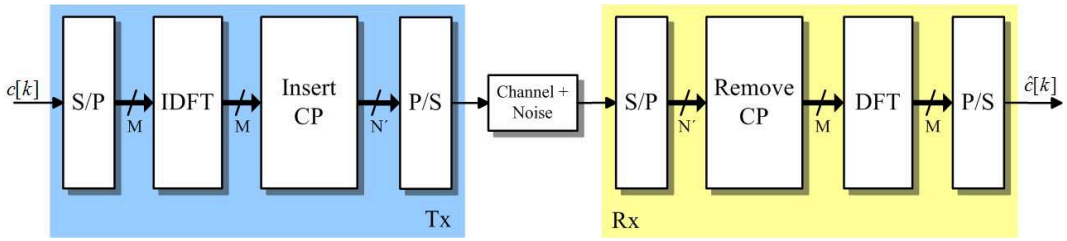

Figure 2.11: OFDM system

a sinc(f) function. The subcarriers are spaced $F = 1/T$ apart so that each subcarrier is in the zeros of the other subcarriers. This ensures that each bit-substream can be transmitted (over an ideal channel) without interference from the other subcarriers [8], i.e. that the subcarriers are orthogonal. So the absence of ICI is true only if $F = N/MT = \beta/T = 1/T$ that entails $N = M$ and $\beta = 1$.

Therefore, starting from the general form (2.3.4), the transmitted OFDM signal is

$$\begin{aligned} s[k] &= \sum_{n\in\mathbb{Z}} \sum_{m=0}^{M-1} c_m[n] g[k - nM] e^{j2\pi km/M} = \\ &= \frac{1}{\sqrt{M}} \sum_{n\in\mathbb{Z}} \sum_{m=0}^{M-1} c_m[n] e^{j2\pi km/M} \end{aligned} \tag{2.3.10}$$

where

$$g[k] = \begin{cases} 1/\sqrt{M} & \text{if } 0 \le k < M \\ 0 & \text{otherwise} \end{cases} \tag{2.3.11}$$

and it is illustrated in Figure 2.12. The analysis and synthesis filter banks reduce to DFT and IDFT operations (no polyphase filtering) up to a multiplicative constant. Figure 2.13 shows the spectral subchannel characteristics obtained with an OFDM system.

If $n = 0$, i.e. we consider only the first OFDM symbol, we obtain

$$s[k] = \frac{1}{\sqrt{N}} \sum_{m=0}^{M-1} c_m[0] e^{j2\pi km/M} \tag{2.3.12}$$

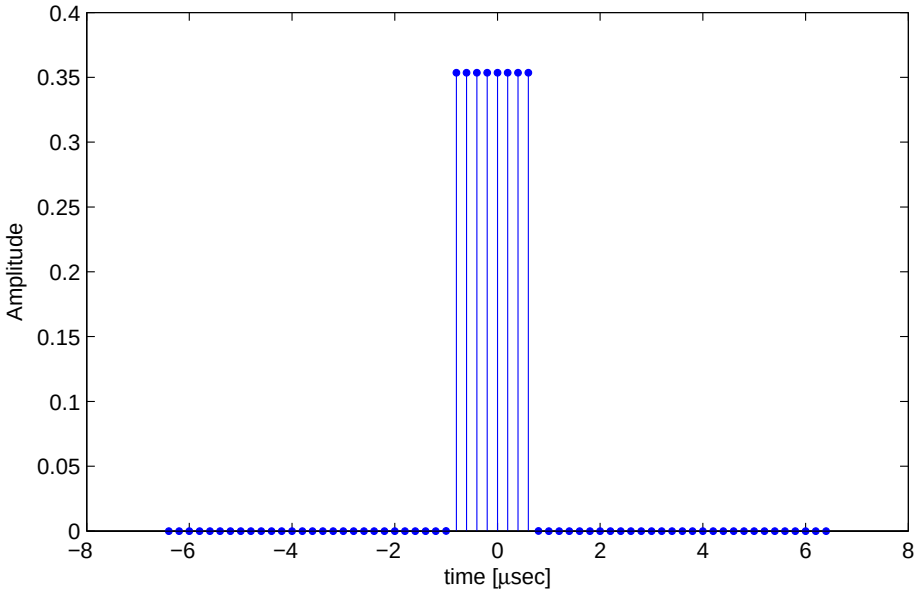

Figure 2.12: Prototype pulse for OFDM systems with M=8

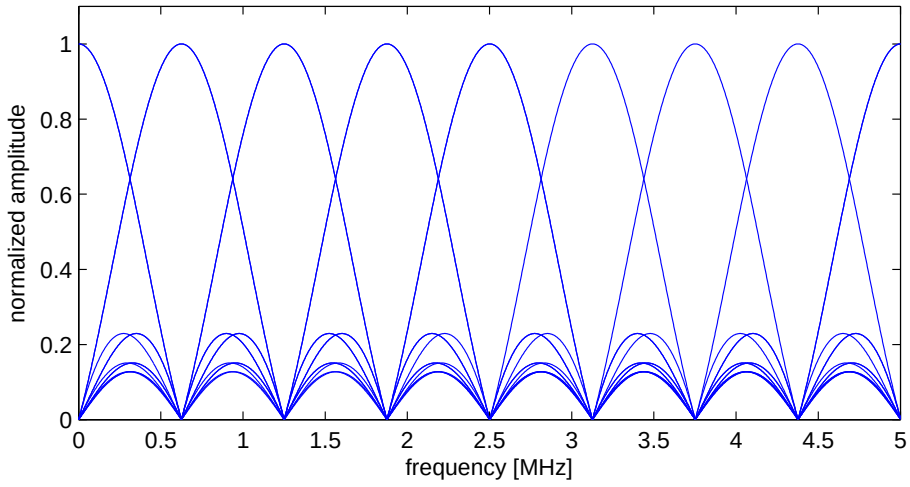

Figure 2.13: Subchannels frequency response for OFDM systems with M=8

that is the M-point inverse discrete Fourier transform of $c_m[0]$, $m = 0, \ldots, M-1$.

Let now discuss about the reasons why the cyclic prefix is introduced [38]. ISI arises from the fact that the channel performs a linear convolution of its impulse response with the time-domain waveform. By this time, the symbols have been mirrored, IFFT'd and concatenated. At the intersection of adjacent symbols, the linear convolution of the signal with the impulse response (whose support L_{ch} is assumed to be less than the symbol length but greater than unity) overlaps parts of both symbols. This means that independent symbols affect each other, i.e. one symbol "bleeds" into another. The addition of a prefix provides a buffer between symbols that prevents this.

ICI comes from the fact that the carrier frequencies for OFDM lose their orthogonality due to the frequency response of the channel. The frequency response of the channel has the effect of attenuating certain frequencies more than others, so each of the sincs is changed by a different amount. Since the inner product is a measure of the similarity of two vectors, two previously "completely dissimilar" sinc functions now have at least some degree of similarity, i.e they are no longer orthogonal. Without orthogonal carriers, the FFT cannot exactly recover the correct spectral coefficients. Cyclic padding solves this problem by turning the linear convolution of the channel impulse response with the signal into a *circular convolution*.

The addition of a cyclic prefix to each symbol solves both ISI and ICI. In our system, we assume the channel impulse response has a known length L_{ch}. The prefix consists simply of copying the last $L_{cp} = L_{ch} - 1$ values from each symbol and appending them in the same order to the front of the symbol. By having this buffer of essentially junk data in the front, the convolution of the impulse response with the signal at the end of a symbol does not affect any of the actual data at the beginning of the next symbol. In addition, by repeating the last elements at the beginning, the first real "data" elements of each symbol experience overlap with the "end" of the symbol, just as in cyclic convolution. This means the linear convolution of the channel impulse response with the concatenated symbols becomes concatenated cyclic convolutions of the impulse response with the individual symbols. Since cyclic convolution directly corresponds to multiplication in the frequency domain, this has great import with respect to equalization. After the time-domain signal passes through the channel, it is broken back into the parallel symbols and the prefix is simply discarded.

The cyclic prefix can so be considered as a kind of guard interval, so that the part of the received bit where the most ISI occurs is thrown away. This can be interpreted in the time/frequency plane by saying that we do not use a critical grid, where $TF = 1$, but an undercritical one ($TF > 1$). It is intuitively clear that such a grid is less sensitive to time dispersion [39], [40].

The introduction of the cyclic prefix of length L_{cp} gives a constant capacity loss, since the channel does no longer carry data for short periods of time. As such, one would like to minimize the length of the cyclic prefix, preferably maintaining performance. Common wisdom is to choose the cyclic prefix to be of roughly the same length as the channel (or system) impulse response, thus eliminating ISI and ICI.

One of the main advantage of filterbank systems is the capability to avoiding the cyclic prefix, in order to combat ISI and ICI, and the capacity loss. In fact with the filterbank-based modulation the GMC symbols transmitted can last less than OFDM symbols with CP, i.e. $N < M + L_{cp}$, and in spite of this the interferences are equally contrasted as the CP-OFDM systems do and any capacity loss appears. We discuss this aspects in next chapter.

2.3.3 Choice of β

Parameters T, F and β define the spacing of the sampling points of the TF plane (packing of the various shifts of the atom). Depending on this spacing, three different operating regions can be identified [41], each of them with different properties that affect waveform design [6].

Critical region. This region corresponds to a time and frequency spacing with the property $TF = \beta = 1$, i.e. $M = N$. For this choice of TF sampling, there exist pulse shapes that result in the set of functions of (2.1.8) and (2.2.3), in the continuous and discrete time domain respectively, constituting an orthogonal set for the space of time and bandlimited functions. Conventional multicarrier schemes (with no cyclic prefix) are actually based on an orthogonal Weyl-Heisenberg set derived from a rectangular pulse. Unfortunately, there do not exist pulses that are well localized in time and frequency in the critical region of the TF plane as established by the Balian-Low theorem [24]. Well localized pulses are preferable as they are more robust to doubly-selective channels compared to pulses

that are well-localized in frequency but not in time, as in OFDM. Moreover the Balian-Low theorem shows that in the case of critical sampling, "nice" Gabor windows do not have "nice" biorthogonal dual windows [42] and performances can be affected by computational and numerical problems.

Undercritical region. This region corresponds to a time and frequency spacing with the property $\beta > 1$. This sampling corresponds to a more distant placing of consecutive shifts of the atom in the time/frequency space. In this case there do not exist Weyl-Heisenberg sets that span the whole space of time and bandlimited functions (however, their elements may still be chosen to be orthogonal). This equivalently means that some portion of the available degrees of freedom is lost in transmission, i.e., smaller bandwidth utilization. However, one can find pulses with desirable properties that may outweigh the loss in efficiency. One such notable example is the cyclic prefixed OFDM where the original rectangular pulse is extended appropriately so that the effect of a linear time variant channel can be easily compensated at the receiver. However, as mentioned above this pulse choice is susceptible to channel variations. Therefore one can design the pulse in order to obtain robustness to channel variations [6]. A typical example is to design well localized pulses in order to reduce energy leakage to neighbour subcarriers due to time and frequency dispersion introduced by the channel.

Overcritical region. This region corresponds to a time and frequency spacing with the property $\beta < 1$. This sampling corresponds to a tight packing of the various time-frequency shifts of the atom in the time/frequency space. In this case the resulting Weyl-Heisenberg set spans the space of time and bandlimited functions, however, it is always composed of linearly dependent elements (also referred to as an overcomplete basis). Employing an overcomplete Weyl-Heisenberg set for data transmission should take into account the fact that loading independent data onto each elementary pulse will make the data retrieval at the receiver a singular problem. In fact, mapping M QAM symbols in the $N < M$ samples of the GMC symbol, will make impossible to recover the data transmitted at the receiver without adopting coding. Note that the pulse shape can also be optimized according to the channel conditions.

2.4 Efficient implementation of FB structure

Now we describe an efficient, fast-Fourier-transform (FFT)-based transmitter and receiver implementation of filterbank communication systems that employ noncritical sampling [11]. The general structure is illustrated in Figure 2.14 where the filtering elements $g^{(i)}[n]$ of the transmitter polyphase filterbank are given by polyphase components (with respect to N) of a synthesis prototype filter $g[n]$, while the filtering elements $\gamma^{(m)}[l]$ of the receiver polyphase filterbank are given by polyphase components (with respect to M) of a analysis prototype filter $\gamma[l]$.

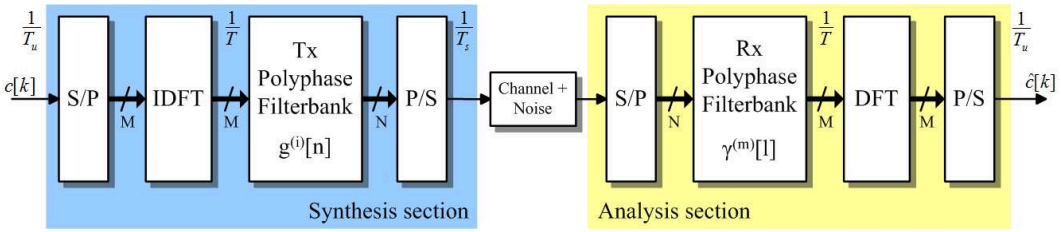

Figure 2.14: Efficient implementation of the polyphase filterbank system

At time kT/N, the signal input to the channel is given by (2.3.4)

$$s\left(k\frac{T}{N}\right) = \sum_{n\in\mathbb{Z}}\sum_{m=0}^{M-1} c_{m,n}\, g\left[k\frac{T}{N} - nT\right] e^{j2\pi m(N/MT)k(T/N)} \tag{2.4.1}$$

With the change of variables $k = lM + i$ with $i = 0, \ldots, M-1$, we get

$$\begin{aligned} s\left(lM\frac{T}{N} + i\frac{T}{N}\right) &= \sum_{n\in\mathbb{Z}}\sum_{m=0}^{M-1} c_{m,n}\, g\left(lM\frac{T}{N} + i\frac{T}{N} - nT\right) e^{j2\pi m(N/MT)i(T/N)} = \\ &= \sum_{n\in\mathbb{Z}} C_{i,n}\, g\left(lM\frac{T}{N} + i\frac{T}{N} - nT\right) \end{aligned} \tag{2.4.2}$$

where

$$C_i[n] \triangleq \sum_{m=0}^{M-1} c_{m,n} e^{j2\pi mi/M} \tag{2.4.3}$$

Clearly, $C_i[n]$, $i = 0, \ldots, M-1$ are obtained from $c_{m,n}$, via an inverse discrete Fourier transform (IDFT). Furthermore, by adopting the general expression for signal interpolation where a "filter index" $q = \lfloor (lM+i)/N \rfloor - n$, a "basepoint index" $\eta_{l,i} = \lfloor (lM+i)/N \rfloor$, and a "fractional index" $\nu_{l,i} = \lfloor (lM+i)/N \rfloor - \eta_{l,i}$ are introduced [43], the transmit signal can be expressed as

$$\begin{aligned} s\left(lM\frac{T}{N} + i\frac{T}{N}\right) &= \sum_{q=-\infty}^{\infty} C_i\left[\eta_{l,i} - q\right] g\left[(\nu_{l,i} + q)T\right] = \\ &= \sum_{q=-\infty}^{\infty} C_i\left[\eta_{l,i} - q\right] g^{(\nu_{l,i}N)}(qT) \\ &\quad \text{with } i = 0, \ldots, M-1 \end{aligned} \tag{2.4.4}$$

where $0 \leq \nu_{l,i} < 1$ and $\nu_{l,i}N = (lM+i) \bmod N$. Hence, it can be found that the transmit signal at time kT/N is computed by convolving the signal samples stored in the $(k \bmod M)$th delay line at the IDFT output with the $(k \bmod N)$th polyphase component (with respect to N) of the prototype filter. In other words, the integer number $\nu_{l,i}N$ provides the address of the polyphase component that needs to be applied at the $(k \bmod N)$th output of the IDFT to generate the transmitted signal $s(kT/N)$. Therefore, each element of the IDFT output frame is filtered by a periodically time-varying filter with period equal to $[\mathrm{lcm}(M,N)]T/N$, where $[\mathrm{lcm}(M,N)]$ denotes the least common multiple of M and N. This transmitter structure is depicted in Figure 2.15.

For a critically sampled system with $N = M$, the efficient realization shown in Figure 2.15 becomes equivalent to that obtained in Figure 2.7 [35]. In that case each element of the IDFT output frame is processed by a filter that is no longer periodically time varying.

We now turn to the efficient implementation of the filterbank demodulator, where it has been assumed for the received signals the same sampling rate as for the transmit signals. The received signal is, thus, denoted by $x(kT/N)$ and the filtering elements on the M branches are given by polyphase components (with respect to M) of a prototype filter $\gamma(kT/N)$ with T/N-spaced coefficients, defined as $\gamma^{(m)}[l] = \gamma^{(m)}[(MT/N)l] = \gamma[(lM+m)T/N]$, $m = 0, \ldots, M-1$, as illustrated in Figure 2.14. The ith output signal of the filterbank demodulator at time $n'T$ is given by

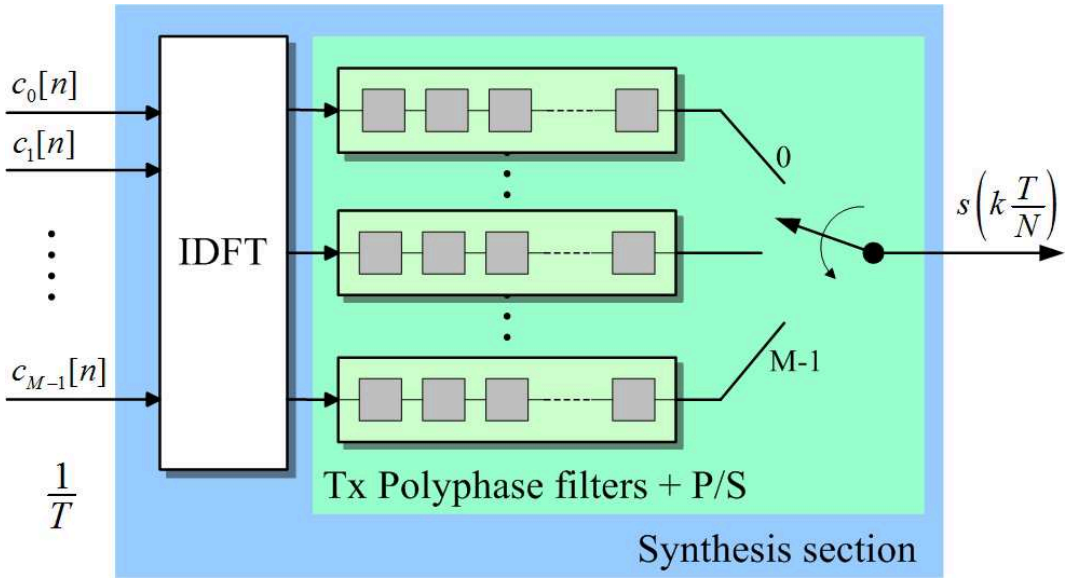

Figure 2.15: Efficient implementation of the polyphase filterbank modulator

$$\hat{c}_i\left(n'T\right) = \sum_{k=-\infty}^{\infty} x\left(k\frac{T}{N}\right)\gamma\left[(n'N-k)\frac{T}{N}\right]e^{-j2\pi i(N/MT)k(T/N)} \tag{2.4.5}$$

Letting $k = lM + m$ with $m = 0, \ldots, M-1$, we obtain

$$\hat{c}_i\left(n'T\right) = \sum_{m=0}^{M-1}\sum_{l=-\infty}^{\infty} x\left[(lM+m)\frac{T}{N}\right]\gamma\left[(n'N-lM-m)\frac{T}{N}\right]e^{-j2\pi im/M} \tag{2.4.6}$$

which can be expressed as

$$\hat{c}_i\left(n'T\right) = \sum_{m=0}^{M-1} u_m\left(n'T\right)e^{-j2\pi im/M} \tag{2.4.7}$$

where

$$u_m\left(n'T\right) \triangleq \sum_{l=-\infty}^{\infty} x\left[(lM+m)\frac{T}{N}\right]\gamma\left[(n'N-lM-m)\frac{T}{N}\right] \tag{2.4.8}$$

Clearly, $\hat{c}_i(n'T)$ with $i = 0, \ldots, M-1$, are obtained from $u_m(n'T)$ with $m = 0, \ldots, M-1$, via a discrete Fourier transform (DFT). Furthermore, if we define the polyphase components (with respect to M) of the received signal as $x^{(m)}[l(MT/N)] = x[(lM+m)T/N]$, $m = 0, \ldots, M-1$ and introduce a "filter index" $q' = \lfloor (n'N - m)/M \rfloor - l$, a "basepoint index" $\eta'_{n',m} = \lfloor (n'N-m)/M \rfloor$, and a "fractional index" $\nu'_{n',m} = \lfloor (n'N-m)/M \rfloor - \eta'_{n',m}$, we obtain

$$u_m\left(n'T\right) \triangleq \sum_{q'=-\infty}^{\infty} x^{(m)}\left[(\eta'_{n',m} - q')\frac{MT}{N}\right] \gamma^{(\nu'_{n',m}M)}\left[q'\frac{MT}{N}\right] \tag{2.4.9}$$

In general, a new DFT output frame at time kT/N is obtained by the following method (see Figure 2.16): the commutator is circularly rotated N steps from its position at time $(n'-1)/T$, allowing a set N of consecutive received signals $x(kT/N)$ to be input into the M delay lines. The content of each delay line is then convolved with a polyphase component (with respect to M) of the receive prototype filter. The integer number $\nu'_{n',m}M$ provides the address of the polyphase component that needs to be applied at the mth branch. The resulting signals are then input to the DFT to finally yield the signals $\hat{c}_i(n'T)$, $i = 0, \ldots, M-1$. Note that the DFT output frames are obtained at the rate of $1/T$.

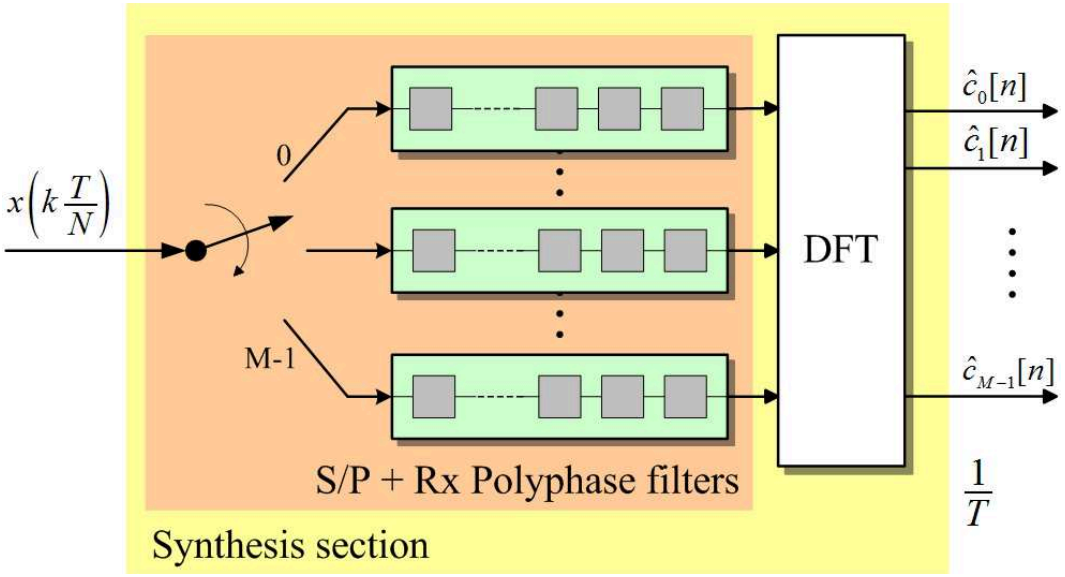

Figure 2.16: Efficient implementation of the polyphase filterbank demodulator

We consider in this work linear-phase FIR prototype pulses of length $L = N \cdot N_f^{(Tx)}$ (i.e., $g[k] = 0$ for $k < 0$ and $k > L-1$). Hence, at the transmitter, each of the N polyphase filter components has $N_f^{(Tx)}$ coefficients, while at the receiver each of the M polyphase filter components has $N_f^{(Rx)}$ coefficients. So

$$L = N \cdot N_f^{(Tx)} = M \cdot \beta \cdot N_f^{(Tx)} = M \cdot N_f^{(Rx)} \tag{2.4.10}$$

and

$$N_f^{(Rx)} = \beta \cdot N_f^{(Tx)} \tag{2.4.11}$$

Moreover $N_f^{(Tx)}$, $N_f^{(Rx)}$ represent respectively the number of points in the time/frequency grid along the time axis and the number of samples in the TF grid between two adjacent atoms in the frequency domain. In general, greater values of $N_f^{(Tx)}$, $N_f^{(Rx)}$ allow a better approximation of pulses with transfer function that exhibit sharp spectral roll-off (and so impulse responses longer in time domain) and high attenuation of out-of-band energy, but lead to an increase in system latency. The choice of prototype filter allows various trade-offs between number of subchannels, level of spectral containment, signal latency, transmission efficiency, and system complexity.

2.5 Finding the dual prototype pulse

In literature many algorithms have been proposed with the intent to find the dual analysis window $\gamma[k]$ for a given synthesis prototype pulse $g[k]$. In order to verify the duality property, i.e. the biorthogonality between the synthesis and the analysis prototype pulses, (2.2.5) should hold true. Unfortunately we work in the critical or undercritical region, i.e. with $\beta \geq 1$. Hence, the biorthogonality cannot perfectly be verified but only partially, as mentioned previously in Section 2.3.3.

Now we discuss the mathematical procedure to find dual pulse and then we present a fast-version algorithm that simplifies and speeds up the calculation of the synthesis window introduced for the first time by Pritz in [42].

Since the detailed derivation has appeared elsewhere [44], only the final formulas will be reviewed here. For a given synthesis window $g[k]$ with length L, the discrete

Gabor transform (2.5.1), and the discrete Gabor expansion (2.5.2), of the discrete-time signal $s[k]$ are defined in the same way as before as

$$c_{m,n} = \sum_{k=0}^{\infty} s[k]\gamma^*[k - nN]e^{-j2\pi mk/M} \tag{2.5.1}$$

$$s[k] = \sum_{m=0}^{M-1} \sum_{n=-(\frac{L}{N}-1)}^{\infty} c_{m,n}g[k - nN]e^{j2\pi mk/M} \tag{2.5.2}$$

where $\frac{L}{N} = N_f^{(Tx)}$ (see 2.4.10). In all this work the synthesis window $g[k]$ is assumed to be normalized and it has unit energy. If the length of the analysis window $\gamma[k]$ is defined to be L, then $\gamma[k]$ is a solution of a linear system given by

$$\sum_{k=0}^{L-1} \bar{g}[k + nM]e^{-j2\pi mk/N}\gamma^*[k] = \delta_n\delta_m \tag{2.5.3}$$

where $\bar{g}[k]$ is a periodic sequence constructed by the synthesis window $g[k]$ with zero-padding, i.e.

$$\bar{g}[k] = \begin{cases} g[k] & 0 \le k < L \\ 0 & L \le k < 2L - M \end{cases} \tag{2.5.4}$$

For the sake of simplicity, (2.5.3) often is written in the matrix form

$$\mathbf{G}_{q\times L}\,\bar{\gamma}^* = \bar{\mu} \tag{2.5.5}$$

where

$$\bar{\mu} = \begin{bmatrix} 1 & 0 & 0 & \cdots & 0 \end{bmatrix}^T \tag{2.5.6}$$

where the number of rows $q = N(\frac{2L}{M} - 1)$. The matrix $\mathbf{G}$ is constructed by

$$\mathbf{G}_{nN+m,k} = \bar{g}[k + nM]e^{-j2\pi mk/N} \tag{2.5.7}$$
$$\text{with } 0 \le n < \tfrac{2L}{M} - 1,\ 0 \le m < N,\ 0 \le k < L$$

From elementary matrix analysis, the existence of solution of (2.5.5) depends on whether the vector $\bar{\mu}$ belongs to the range of the matrix $\mathbf{G}$, that is the span of columns of the matrix $\mathbf{G}$. If so, and the rank of $\mathbf{G}$ is less than the number of columns, the system described by (2.5.5) could have an infinite number of solutions. In this case, it has been suggested finding the analysis window that is most similar to the given synthesis window, in the sense of least square error (LSE) and it has been called the "canonical" dual pulse:

$$\mathbf{\Gamma} = \min_{\bar{\gamma}:\mathbf{G}\bar{\gamma}^*=\bar{\mu}} \left\| \frac{\gamma[k]}{\|\gamma[k]\|} - g[k] \right\|^2 \tag{2.5.8}$$

where $g[k]$ is normalized. When $\gamma[k]$ is closer to $g[k]$, the Gabor expansion has a form similar to an orthonormal representation though the elementary functions $g_{m,n}[k]$ even are not linear independent, i.e.

$$s[k] \approx \alpha \sum_{n=-\left(\frac{L}{N}-1\right)}^{\infty} \sum_{m=0}^{M-1} \left\{ \sum_{i=0}^{\infty} s[i] g^*_{m,n}[i] \right\} g_{m,n}[k] \tag{2.5.9}$$
$$\alpha = \|\gamma[k]\|$$

In this case, the Gabor coefficient could be considered as the measure of similarity between the sequence $s[k]$ and the individual elementary function $g_{m,n}[k]$. Consequently, Gabor coefficients well reflect signal local behaviours as long as the synthesis window $g[k]$ is well-localized. The resulting expansion was named the orthogonal-like discrete Gabor expansion [45]. If the matrix has a full row rank, the solution of (2.5.8) is

$$\bar{\gamma}^* = \mathbf{G}^T \left(\mathbf{G}\mathbf{G}^T\right)^{-1} \bar{\mu} \tag{2.5.10}$$

Digressing the above subject, it has pointed out that a main topic in implementing the Gabor expansion is to have both the synthesis function and the Gabor coefficients localized. The Zak transform approach [46] presents many interesting features, but

generally it is not known to what extent the resulting coefficients represent the analyzed signal. $c_{m,n}$ evaluated by the iteration approach originally proposed by Gabor may also lead to the orthogonal-like representation (if the initial window is properly selected), but the convergence of the iteration is not always guaranteed [47].

In real applications, the synthesis window matrix $\mathbf{G}$ is not always of full row rank. In some applications one may intentionally seek $\gamma[k]$ that differs from $g[k]$. A more general method to find the biorthogonal analysis window function is discussed in [45]

2.5.1 Efficient algorithm to find biorthogonal pulses

In the following sections, we discuss a different method to determine the dual window $\gamma[k]$ from a given pulse $g[k]$. It has been shown that the computational effort of such algorithm mainly depends on the structure and size of the sampling set $\mathbf{G}$. We assume that $\mathbf{G}$ has full rank and that the synthesis window $g[k]$ is considered to be L-periodic[2], i.e., if the index exceeds N, the vector is defined as $g[k] = g[k + L]$ for all $n \in \mathbb{Z}$. This algorithm was proposed for the first time by Pritz in [42].

In this section we have to define two new operator: the time shift operator $\mathcal{T}_n$, $n \in \mathbb{Z}$ and the frequency shift operator $\mathcal{M}_m$, $m \in \mathbb{Z}$, defined as

$$\begin{aligned} \mathcal{T}_n(\mathbf{x}) &= \mathcal{T}_n(x[0], \ldots, x[L-1]) \\ &\triangleq [x[n], x[n+1], \ldots, x[L+n-1]] \end{aligned} \tag{2.5.11}$$

$$\mathcal{M}_n(\mathbf{x}) \triangleq \left[x[0], x[1]e^{j2\pi m/L}, \ldots, x[L-1]e^{j2\pi m(L-1)/L}\right] \tag{2.5.12}$$

With this notation our synthesis matrix $\mathbf{G}$ becomes

[2]Note that in this case the starting prototype pulse $g[k]$ is no zero-padded unlike previous mathematical procedure.

$$\mathbf{G} = \begin{pmatrix} \mathcal{M}_{m_0}\mathcal{T}_{n_0}g \\ \mathcal{M}_{m_1}\mathcal{T}_{n_1}g \\ \vdots \\ \mathcal{M}_{m_{q-1}}\mathcal{T}_{n_{q-1}}g \end{pmatrix} \tag{2.5.13}$$

$$\begin{aligned} & m \in \{0, N_f^{(Rx)}, 2N_f^{(Rx)}, \ldots, L - N_f^{(Rx)}\} \\ & n \in \{0, N, 2N, \ldots, L - N\} \end{aligned} \tag{2.5.14}$$

where q is the number of sampling points on the time/frequency grid and it is defined as $q = M \cdot N_f^{(Tx)}$. Let $\mathcal{F}$ be the Fourier matrix of size $(M \times M)$, i.e. $\mathcal{F}_{m,n} = e^{-j2\pi mn/M}$. The $(q \times q)$ matrix $\mathbf{F}$ is defined as

$$\mathbf{F} = \begin{pmatrix} \mathcal{F} & 0 & \cdots & 0 \\ 0 & \mathcal{F} & \ddots & \vdots \\ \vdots & \ddots & \ddots & 0 \\ 0 & \ldots & 0 & \mathcal{F} \end{pmatrix} \tag{2.5.15}$$

Let the matrix $\mathbf{B}$ be defined as $\mathbf{B} = \mathbf{FG}$, and $\mathbf{G}^M$ denotes a $(M \times L)$ matrix containing the first M rows of $\mathbf{G}$. Since the matrix $\mathbf{F}$ is block diagonal (with blocksize M), we examine the first M rows of $\mathbf{B}$ separately:

$$\begin{aligned} \mathbf{B}_{m,n} &= \left\{\mathcal{F}\mathbf{G}^M\right\}_{m,n} \qquad \text{for } m = 0, \ldots, M-1 \\ &= \sum_{i=0}^{M-1} e^{-j2\pi inM} e^{j2\pi imM} g[m] = \\ &= \sum_{i=0}^{M-1} e^{j2\pi i(m-n)M} g[m] = \\ &= \begin{cases} Mg[m] & \text{if } (m-n) \text{ is a divisor of } M \\ 0 & \text{otherwise} \end{cases} \end{aligned} \tag{2.5.16}$$

The next M rows of $\mathbf{B}$ differ from the first ones in the way that only the non-vanishing values are different. Here, the mth entry of $\mathbf{B}_{m,n}$ is not just $Mg[m]$, but

the index m is decreased by N, which is the time-shift gap. This leads to the general result for the matrix $\mathbf{B}$:

$$\mathbf{B}_{m,n} = \begin{cases} Mg\left[m - N\left\lfloor \frac{n}{M} \right\rfloor\right] & \text{if } (m-n) \text{ is a divisor of } M \\ 0 & \text{otherwise} \end{cases} \tag{2.5.17}$$

where $\left\lfloor \frac{n}{M} \right\rfloor$ denotes the greatest integer not greater than n/M. More precisely, $\mathbf{B}$ looks as in (2.5.18).

$$\mathbf{B} = M \begin{pmatrix} g[0] & 0 & \cdots & 0 & g[M] & 0 & \cdots & g[L-M] \\ 0 & g[1] & \ddots & \vdots & 0 & g[M+1] & & \\ \vdots & \ddots & \ddots & 0 & \vdots & & & \\ 0 & \cdots & 0 & g[M-1] & 0 & & & \\ g[L-N] & 0 & \cdots & 0 & g[M-N] & & & \\ 0 & & & & & g[M-N+1] & & \\ \vdots & & & & & & \ddots & \\ g[N] & & & & & & & g[N-M] \end{pmatrix} \tag{2.5.18}$$

To make use of the sparse structure of $\mathbf{B}$, we need two permutation matrices: $\mathcal{P}_r$ is a $(q \times q)$ matrix that rearranges the rows of a $(q \times \cdot)$ matrix in the following order[3]:

$$\begin{aligned} &\mathcal{P}_r \{0, 1, \ldots, q-1\} \rightarrow \\ &\quad \left\{0, N_f^{(Tx)}, 2N_f^{(Tx)}, \ldots, (M-1)N_f^{(Tx)}, 1, N_f^{(Tx)}+1, \ldots, N_f^{(Tx)}M\right\} \end{aligned} \tag{2.5.19}$$

and $\mathcal{P}_c$, is a $(L \times L)$ matrix that rearranges the columns of a $(\cdot \times L)$ matrix in the following order:

$$\begin{aligned} &\mathcal{P}_c \{0, 1, \ldots, L-1\} \rightarrow \\ &\quad \left\{0, M, 2M, \ldots, (N_f^{(Rx)}-1)M, 1, M+1, \ldots, L-N_f^{(Rx)}-1, L-1\right\} \end{aligned} \tag{2.5.20}$$

Multiplying the matrix $\mathbf{B}$ from the left and the right side by $\mathcal{P}_r$, and $\mathcal{P}_c$, rearranges the rows and columns and results in a blockdiagonal matrix $\mathbf{W}$

[3]The meaning of (2.5.19) is the following: row #0 becomes row #0, row $\#N_f^{(Tx)}$ becomes row #1, row $\#2N_f^{(Tx)}$ becomes row #2, ... etc.

$$\mathbf{W} = \mathcal{P}_r \mathbf{B} \mathcal{P}_c = \mathcal{P}_r \mathbf{F}\mathbf{G} \mathcal{P}_c = \begin{pmatrix} \mathbf{W}_0 & 0 & \cdots & 0 \\ 0 & \mathbf{W}_1 & \ddots & \vdots \\ \vdots & \ddots & \ddots & 0 \\ 0 & \dots & 0 & \mathbf{W}_{M-1} \end{pmatrix} \tag{2.5.21}$$

where

$$\mathbf{W}_i = M \begin{pmatrix} g[i] & g[i+M] & \cdots & g[i+L-M] \\ g[i-N] & g[i+M-N] & \cdots & g[i+L-M-N] \\ \vdots & & & \vdots \\ g[i-(L-N)] & g[i-(L-N)+M] & \cdots & g[i+N-M] \end{pmatrix} \tag{2.5.22}$$

Now we use the two following matrix properties:

Lemma 1 *If* $\mathbf{Q}$ *is an unitary matrix, then the following formula holds true for every matrix* $\mathbf{A}$[4]*:*

$$(\mathbf{A}\mathbf{Q})^\dagger = \mathbf{Q}^H \mathbf{A}^\dagger \tag{2.5.23}$$

Lemma 2 *If* $\mathbf{W}$ *is a blockdiagonal matrix, then the pseudoinverse* $\mathbf{W}^\dagger$ *is also blockdiagonal in the following way:*

$$\begin{aligned} \mathbf{W}^\dagger &= \begin{pmatrix} \mathbf{W}_1 & 0 & \cdots & 0 \\ 0 & \mathbf{W}_2 & \ddots & \vdots \\ \vdots & \ddots & \ddots & 0 \\ 0 & \cdots & 0 & \mathbf{W}_n \end{pmatrix}^\dagger \\ &= \begin{pmatrix} {\mathbf{W}_1}^\dagger & 0 & \cdots & 0 \\ 0 & {\mathbf{W}_2}^\dagger & \ddots & \vdots \\ \vdots & \ddots & \ddots & 0 \\ 0 & \cdots & 0 & {\mathbf{W}_n}^\dagger \end{pmatrix} \end{aligned} \tag{2.5.24}$$

[4] $\mathbf{A}^\dagger$ denotes the pseudoinverse of matrix $\mathbf{A}$

For a proof of these two lemmata, see, e.g., [48]. Since the matrices $\mathcal{P}_r$, $\mathcal{P}_c$, and $\mathbf{F}$ are unitary and $\mathbf{W}$ is block diagonal, the pseudoinverse of $\mathbf{G}$, is easily calculated:

$$\begin{aligned} \mathbf{W} &= \mathcal{P}_r \mathbf{F} \mathbf{G} \mathcal{P}_c \\ &\Updownarrow \\ \mathbf{G} &= \mathbf{F}^H \mathcal{P}_r^H \mathbf{W} \mathcal{P}_c^H \\ &\Updownarrow \\ \mathbf{G}^\dagger &= \mathcal{P}_c \mathbf{W}^\dagger \mathbf{F} \mathcal{P}_r \end{aligned} \tag{2.5.25}$$

Substituting the window function g in (2.5.25) by the dual window function $\gamma[k]$ gives

$$\mathbf{\Gamma} = \mathbf{F}^H \mathcal{P}_r^H \widetilde{\mathbf{W}} \mathcal{P}_c^H \tag{2.5.26}$$

where $\widetilde{\mathbf{W}}$ is similar to $\mathbf{W}$ in (2.5.21) and (2.5.22), replacing the $g[k]$ by $\gamma[k]$. Now we exploit the following theorem discussed and proofed in [49] and [50].

Theorem 1 *Let* $\mathbf{G}$*, be a Gabor frame matrix defined as in (2.5.13); then, there is a so-called dual Gabor frame matrix* $\mathbf{\Gamma}$ *satisfying*

$$x = x\, \mathbf{\Gamma}^H \mathbf{G} \quad \textit{for all} \quad x \in \mathbb{C}^L \tag{2.5.27}$$

which is of the same structure as $\mathbf{G}$*, i.e.* $\mathbf{\Gamma} = \{\mathcal{M}_m \mathcal{T}_n \gamma\}_{m,n}$

From Theorem 1, it is easy entails that $\mathbf{G}^\dagger = \mathbf{\Gamma}^H$, which implies that

$$\begin{aligned} \mathbf{\Gamma}^H &= \mathcal{P}_c \widetilde{\mathbf{W}}^H \mathcal{P}_r \mathbf{F} = \mathcal{P}_c \mathbf{W}^\dagger \mathcal{P}_r \mathbf{F} = \mathbf{G}^\dagger \\ &\Rightarrow \quad \widetilde{\mathbf{W}}^H = \mathbf{W}^\dagger \end{aligned} \tag{2.5.28}$$

The calculation of the dual Gabor window is thus reduced to the calculation of the pseudoinverse of the blockdiagonal matrix $\mathbf{W}$. This is, according to Lemma 2, the calculation of the pseudoinverses of M matrices of size $(N_f^{(Tx)} \times N_f^{(Rx)})$. Equation (2.5.22) shows that every element of the matrix $\mathbf{W}_i$, uniquely determines one element of the vector $g[k]$. Theorem 1 and (2.5.28) lead to the fact that every element of $\gamma[k]$ is uniquely represented by a matrix $\mathbf{W}_i^\dagger$ (for some i). Therefore, the number of matrices $\mathbf{W}_i$ for which we have to calculate the

pseudoinverse depends on the number of different matrices $\mathbf{W}_i$ necessary to represent each element of the window function $g[k]$ at least once. The following proposition shows that this number is given by the greatest common divisor of (N,M).

Proposition 1 *Let $\mathbf{W}_0, \mathbf{W}_1, \ldots, \mathbf{W}_(N_f^{(Rx)} - l)$ be the family of matrices as defined in (2.5.22). The minimal number of $\mathbf{W}_i$, required to recover the window $g[k]$ is given by the greatest common divisor (gcd) of (N,M).*

Proof: According to (2.5.22), each element of the matrix $\mathbf{W}_i$, can be represented in the following way:

$$\mathbf{W}_i(n,m) = g[i + mM - nN] \tag{2.5.29}$$

where (n,m) denotes the row-column position. It has been shown how many different indices $(i + mM - nN)$ of $g[k]$ in the $\mathbf{W}_i$, are possible for given L, N, $N_f^{(Rx)}$. Since $g[k]$ is L-periodic (or finite), any index i equals an index q if $q = i + dL$ for some $d \in \mathbb{Z}$. In our notation, we will write $q =_L i$. Let c be the greatest common divisor of (N,M). Then

$$\begin{array}{rrcl} & g[i + m_1M - n_1N] & = & g[i + m_2M - n_2N] \\ \Rightarrow & i + m_1M - n_1N & =_L & i + m_2M - n_2N \\ \Rightarrow & (n_1 - n_2) & =_L & (m_1 - m_2)\frac{M}{c} \big/ \frac{N}{c} \end{array} \tag{2.5.30}$$

This leads to the fact that $(m_1 - m_2)$ is a multiple of $\frac{N}{c}$, and $(n_1 - n_2)$ is a multiple of $\frac{M}{c}$. Hence, there are $m = \frac{N}{c}$ columns (or $m = \frac{M}{c}$ rows), where each two elements out of these columns (or rows) are pointwise different, i.e.,

$$\begin{gathered} \mathbf{W}_i(n_1,m_1) \neq \mathbf{W}_i(n_2,m_2) \\ \text{for all } n_1, n_2 \in \{0,1,\ldots,N_f^{(Tx)}\} \text{ if } |m_1 - m_2| \leq \frac{N}{c}, \\ \mathbf{W}_i(n_1,m_1) \neq \mathbf{W}_i(n_2,m_2) \\ \text{for all } m_1, m_2 \in \{0,1,\ldots,N_f^{(Rx)}\} \text{ if } |n_1 - n_2| \leq \frac{M}{c}. \end{gathered}$$

If the size of $\mathbf{W}_i$, is greater or equal to $(\frac{M}{c} \times \frac{N}{c})$, i.e.

$$\frac{L}{N} \geq \frac{M}{c} \quad \text{and} \quad N_f^{(Rx)} \geq \frac{N}{c} \tag{2.5.31}$$

every matrix $\mathbf{W}_i$, contains $\frac{L}{N}\frac{N}{c} = N_f^{(Rx)}\frac{M}{c} = \frac{L}{c}$ mutual different elements. Hence, we need c matrices to represent an L-dimensional vector. Finally, it has been shown that inequality (2.5.31) always holds true:

$$\begin{aligned} \frac{L}{N} \geq \frac{N}{c} \qquad &\Rightarrow \qquad Lc \geq MN \\ \frac{L}{M} = N_f^{(Rx)} \geq \frac{N}{c} \qquad &\Rightarrow \qquad Lc \geq MN \\ L \geq \tfrac{M}{c} N \end{aligned} \tag{2.5.32}$$

If $\prod_{q \in Q} p_q$ is the prime factorization of L, then N and $\frac{M}{c}$ can be uniquely represented by a product of these p_q's. Since N and $\frac{M}{c}$ are relative prime, no prime number p_q can be a part of the prime factorization of N and $\frac{M}{c}$. This proves inequality (2.5.32).

Summing up, the calculation of the dual Gabor window can be obtained by calculating the pseudoinverses of $\gcd(N, M)$ matrices of size $(N_f^{(Tx)} \times N_f^{(Rx)})$.

At the end of the algorithm, the dual prototype pulse is normalized in order to be with unit energy because the filtering have to be passive. That normalization will entail an attenuation of the demodulated signal (the energy of the not-normalized dual pulse is usually greater than 1) and consequently a decrease of the signal-to-noise ratio because the noise does not experience this attenuation. This behavior is equivalent to the increase of the noise power caused by the not-normalized analysis filterbank in the receiver. In fact in this case the not-unit energy of the dual pulse amplifies the noise increasing its power and decreasing the signal-to-noise ratio.

Finally the algorithm scheme is exposed in Table 2.2. Note that in the algorithm is present a check in order to guarantee that $N_f^{(Rx)}$, $N_f^{(Tx)}$ are natural numbers, otherwise the algorithm cannot work. If the check failed, the algorithm exits and the parameters M,N or the length of synthesis prototype window $g[k]$ must be changed.

2.6 Prototype pulses

The pulse shape $g[k]$ is of critical importance in every linear modulation scheme. It has a major impact on essential properties of the transmitted signal such as bandwidth and complexity of signal construction but also affects overall system performance (robustness to channel impairments, ISI and ICI level, timing errors, etc.) [51]. Designing an appropriate pulse is therefore a crucial procedure for every successful communication scheme. However, although transmitted signal properties can be easily accomplished by a variety of pulse shapes, designing a pulse shape that allows for good performance under a wide range of channel conditions is a difficult (if not impossible) task. The typical example is the pulse employed by OFDM. It is well known that OFDM employs a long rectangular pulse (possibly slightly smoothed for spectral sidelobe reduction). This type of pulse is actually optimal for transmission under a channel with large delay spread. Ideally, the pulse length is large enough so

EFFICIENT ALGORITHM

Input: $g[k]$,M,N
Output: $\gamma[k]$

1. **Set** $L = \text{length}(g[k])$;
2. **Compute** $N_f^{(Tx)} = \frac{L}{N}$;
3. **Compute** $N_f^{(Rx)} = \frac{L}{M}$;
4. **If** $N_f^{(Rx)}, N_f^{(Tx)} \notin \mathbb{N}$, then **Exit**;
5. **For** $i = 0$ to $(\gcd(N, M) - 1)$;
6. **For** $n = 0$ to $(N_f^{(Tx)} - 1)$;
7. **For** $m = 0$ to $(N_f^{(Rx)} - 1)$;
8. **Set** $\mathbf{W}(n, m) = g[i + mM - nN]$;
9. **end**;
10. **end**;
11. **Compute** $\widetilde{\mathbf{W}} = \frac{1}{M} \left(\mathbf{W}^{\dagger}\right)^{H}$;
12. **For** $n = 0$ to $(N_f^{(Tx)} - 1)$;
13. **For** $m = 0$ to $(N_f^{(Rx)} - 1)$;
14. **Set** $\gamma[i + mM - nN]$ equal to $\widetilde{\mathbf{W}}(n, m)$;
15. **end**;
16. **end**;
17. **end**;
18. **Normalize** $\gamma[k]$;

Table 2.2: Efficient algorithm to calculate the dual Gabor window

that ISI is negligible. However, when the channel is varying during the pulse duration, or there are nonlinearities present in transmission, e.g., phase noise, OFDM waveform severely suffers from increased ISI/ICI [32], [33]. A robust pulse shape that would allow for acceptable performance in a larger range of channel dynamics is certainly desirable.

In this section we talk about the performance with three different type of pulses:

- Root Raised Cosine pulse
- Gaussian pulse
- Hermite pulse

For each one of these pulses, it will be shown how the pulse shape and the performance can change for the different values of the particular parameter chosen and the relative biorthogonal pulse[5]. In the last subsection we will briefly discuss about optimization techniques in order to minimize some objective functions and hence improve the performances.

2.6.1 Root raised cosine pulse

The raised cosine (RC) [52] filter is a filter frequently used for pulse-shaping in digital modulation due to its ability to minimize inter-symbol interference (ISI). Its name stems from the fact that the non-zero portion of the frequency spectrum of its simplest form ($\alpha = 1$) is a cosine function, 'raised' up to sit above the f axis. The root raise cosine (RRC) is simply the square root (in frequency domain) of the raised cosine pulse. Hence we start our discussion talking about this last pulse.

The raised cosine filter is an implementation of a low-pass Nyquist filter, i.e., one that has the property of vestigial symmetry. This means that its spectrum exhibits odd symmetry about $\frac{1}{2T}$, where T is the symbol period of the communications system.

Its frequency-domain description is a piecewise function, given by

$$G_{rc}(f) = \begin{cases} T, & |f| \leq \frac{1-\alpha}{2T} \\ \frac{T}{2}\left[1 + \cos\left(\frac{\pi T}{\alpha}\left[|f| - \frac{1-\alpha}{2T}\right]\right)\right], & \frac{1-\alpha}{2T} < |f| \leq \frac{1+\alpha}{2T}\ 0 \leq \alpha \leq 1 \\ 0, & \text{otherwise} \end{cases} \tag{2.6.1}$$

and characterized by two values α, the roll-off factor, and T, the reciprocal of the symbol rate. As mentioned before, the description in frequency domain of the root raised cosine pulse is the square root of the frequency response of the raised cosine filter [53], i.e.

$$G_{RC}(f) = G_{RRC}(f) \cdot G_{RRC}(f) \tag{2.6.2}$$

[5]All analysis prototype pulses are found with fast algorithm described in Section 2.5.1.

or, equivalently,

$$|G_{RRC}(f)| = \sqrt{|G_{RC}(f)|} \tag{2.6.3}$$

The impulse response of raised cosine filter is given by

$$g(t) = \text{sinc}\left(\frac{t}{T}\right)\frac{\cos\left(\frac{\pi\alpha t}{T}\right)}{1-\frac{4\alpha^2t^2}{T^2}} \tag{2.6.4}$$

in terms of the normalized sinc function. The impulse response of root raised cosine filter instead is

$$g(t) = \begin{cases} 1-\alpha+4\dfrac{\alpha}{\pi}, & t=0 \\ \dfrac{\alpha}{\sqrt{2}}\left[\left(1+\dfrac{2}{\pi}\right)\sin\left(\dfrac{\pi}{4\alpha}\right)+\left(1-\dfrac{2}{\pi}\right)\cos\left(\dfrac{\pi}{4\alpha}\right)\right], & t=\pm\dfrac{T}{4\alpha} \\ \dfrac{\sin\left[\pi\dfrac{t}{T}(1-\alpha)\right]+4\alpha\dfrac{t}{T}\cos\left[\pi\dfrac{t}{T}(1+\alpha)\right]}{\pi\dfrac{t}{T}\left[1-\left(4\alpha\dfrac{t}{T}\right)^2\right]}, & \text{otherwise} \end{cases} \tag{2.6.5}$$

The roll-off factor, α, is a measure of the excess bandwidth of the filter, i.e. the bandwidth occupied beyond the Nyquist bandwidth of $\frac{1}{2T}$. If we denote the excess bandwidth as Δf, then:

$$\alpha = \frac{\Delta f}{\left(\frac{1}{2T}\right)} = \frac{\Delta f}{R/2} = 2T\Delta f \tag{2.6.6}$$

where $R = \frac{1}{T}$ is the symbol-rate.

Figure 2.18 shows the amplitude frequency response when the roll-off factor α is between 0.1 and 0.5, while their relative impulse responses[6] are depicted in Figure 2.17. As we can see, the time-domain ripple level increases as α decreases.

This shows that the excess bandwidth of the filter can be reduced, but only at the expense of an elongated impulse response. The overall bandwidth of a raised cosine filter is most commonly defined as the width of the non-zero portion of its spectrum, i.e.:

$$B = \frac{1+\alpha}{T} \tag{2.6.7}$$

[6]Remember that all the prototype pulses are normalized, i.e. they have unit energy.

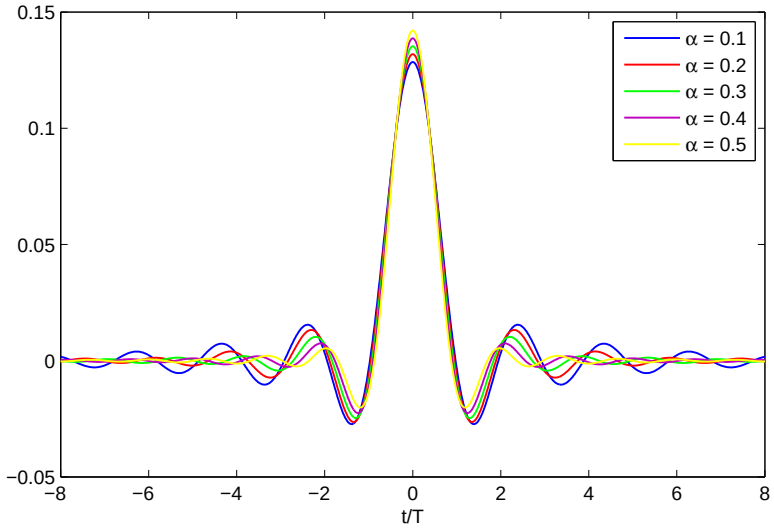

Figure 2.17: Root raised cosine pulses in time domain for different α values

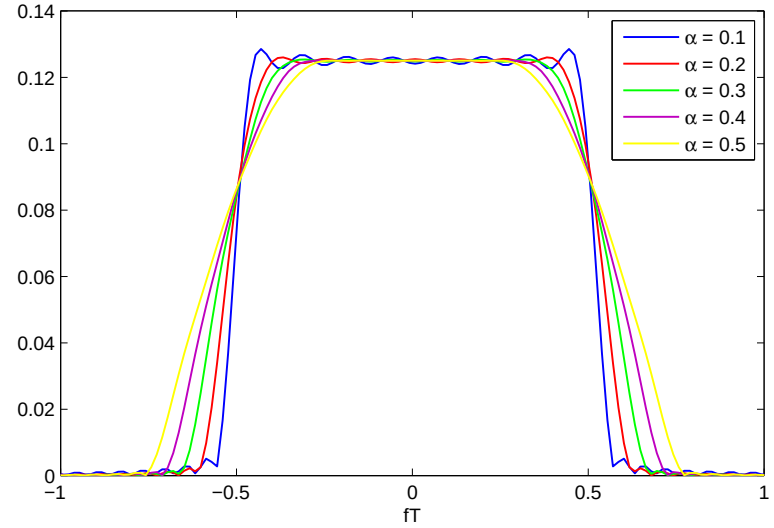

Figure 2.18: Amplitude of root raised cosine pulses in frequency domain for different α values

As α approaches 0, the roll-off zone becomes infinitesimally narrow, hence $\lim_{\alpha\to 0} G(f) = \text{rect}(fT)$, where $\text{rect}(\cdot)$ is the rectangular function, so the impulse response approaches $\text{sinc}\left(\frac{t}{T}\right)$. Hence, it converges to an ideal rectangular filter in this case. When $\alpha = 1$, the non-zero portion of the spectrum is a pure raised cosine.

In an ideal RRC filter, there should not be any ripple in the amplitude frequency response while the pulses depicted in Figure 2.18 show some ripple due to the truncation of the impulse responses in time domain. In fact, these frequency response have been compute by FFT of RRC pulses lasting $16T$, i.e. $N_f^{(Tx)} = 16$.

Obviously the main feature that make RRC pulses desirable is the limited bandwidth that make ICI weaker than other pulses. We can even guarantee the absence of interference between adjacent subcarriers if we impose no overlapping. Under this constraint, the subcarriers spacing, i.e. $\frac{\beta}{T}$, must be greater than subcarriers bandwidth $\frac{1+\alpha}{T}$, thus the ICI-absence constraint become

$$\beta \geq \alpha + 1 \tag{2.6.8}$$

The partially frequency response of two transmitted signal are illustrated in Figure 2.19. They are obtained with two different β values with the same roll-off factor. The other parameters are set to $M = 64$, $N_f^{(Tx)} = 16$, $T_s = 50$ nsec and $\alpha = 0.25$. In 2.19(b) $\beta = 1 + \alpha = 1.25$ and we obtain no overlapping among the subcarriers, while in 2.19(a) we choose $\beta = 1$ (critical sampling) and the overlapping is maximum.

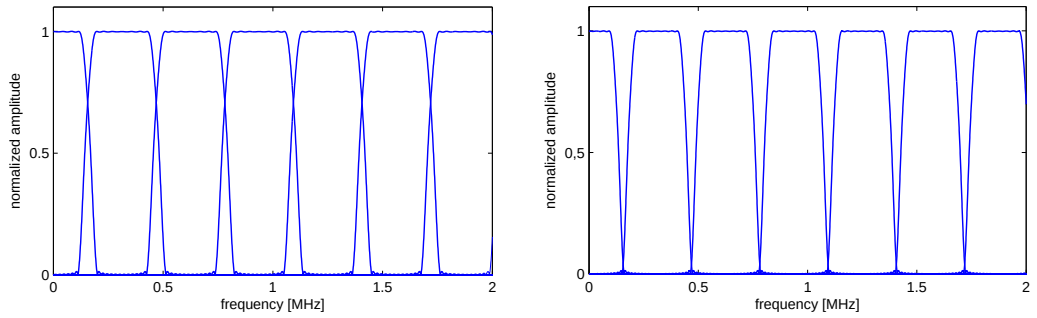

(a) (b)

Figure 2.19: Amplitude of frequency response for different β values

From a biorthogonal point of view, if there is no overlapping, then the analysis prototype pulse becomes equal to the synthesis one. The synthesis and relative analysis pulse for four different β values are depicted in Figure 2.20. It can be notice that when $\beta = 1$, we have

many spikes in the dual pulse, caused by the critical sampling.

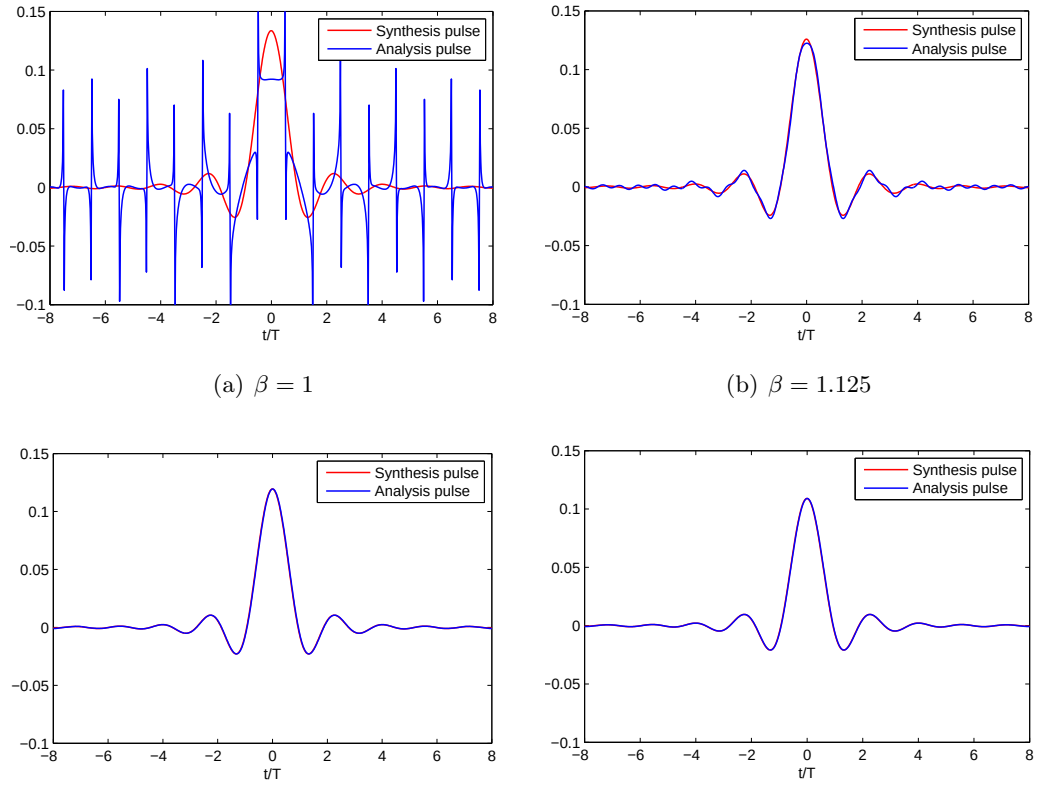

(a) $\beta = 1$ (b) $\beta = 1.125$

(c) $\beta = 1.25$ (d) $\beta = 1.5$

Figure 2.20: RRC synthesis and analysis prototype pulse for different β values

Now we can show how perfect biorthogonality is not achieved for $\beta \geq 1$. According to (2.2.7), the biorthogonality property can be represented by a matrix $\mathbf{R}_{BIO}$ where row and column indices are the k an k' indices of the left-hand side of the expression (2.2.7). If (2.2.7) holds true then the matrix must be an identity matrix $\mathbf{I}_L$ of size $(L \times L)$ according to the right-hand side of the expression (2.2.7). In Figure 2.21 the biorthogonality matrices are shown for the same four β values used previously in Figure 2.20[7].

We can observe that the biorthogonality matrix $\mathbf{R}_{BIO}$ is very similarly to the identity matrix only for critical sampling even if there are small spikes out of the diagonal caused by the not-so-perfect biorthogonalization of the synthesis window. This effect increases with the growth of β. The dual window and the biorthogonality matrix for a value of β smaller than 1, i.e. $\beta = 0.875$, are depicted in Figure 2.22. In this case the biorthogonality is fully checked

[7]The matrices depict in this thesis have the element $(0, 0)$ in the bottom left corner.

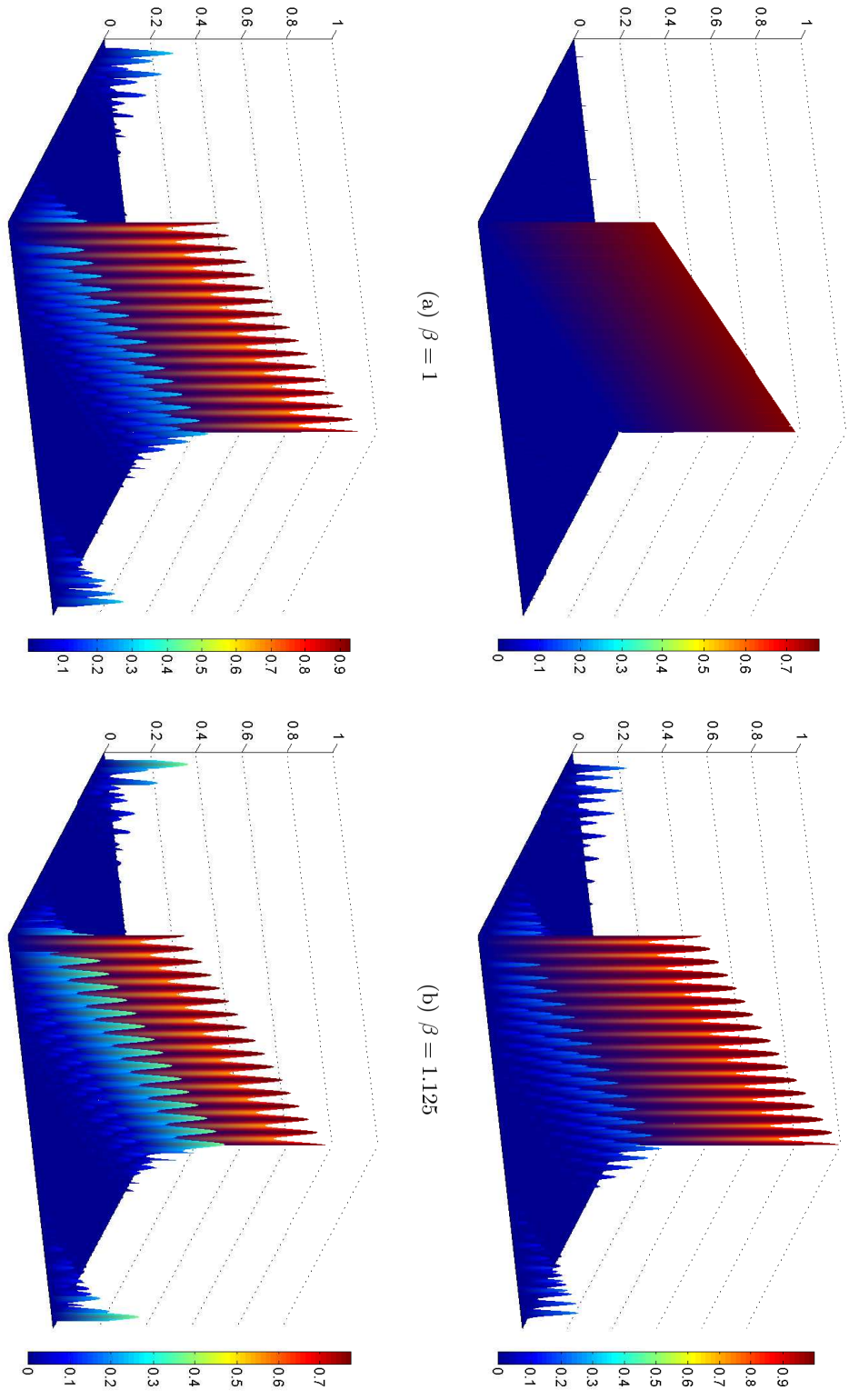

(a) $\beta = 1$ (b) $\beta = 1.125$ (c) $\beta = 1.25$ (d) $\beta = 1.5$

Figure 2.21: Biorthogonality matrices for different β values with RRC pulses

and the matrix is almost[8] equal to the identity matrix but we cannot transmit any data.

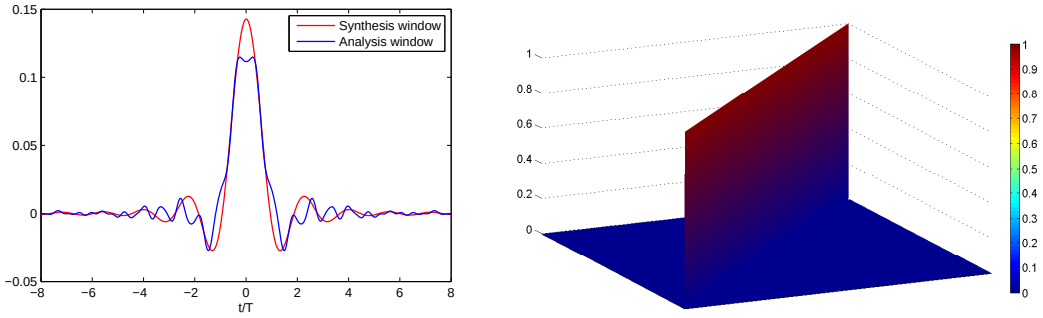

(a) (b)

Figure 2.22: Synthesis and analysis pulse and biorthogonality matrix for $\beta = 0.875$

The BER and MSE values of a 4-QAM mapping employing different β values are shown in Table 2.3. These values have been obtained under ideal channel conditions, i.e. with no fading and no noise. The other system parameters are $M = 64$, $N_f^{(Tx)} = 16$, $T_s = 50$ ns and $\alpha = 0.25$.

β	Biorthogonality (%)	BER	MSE
0.500	99.5692	0.493307	0.103174
0.750	99.7203	0.495805	0.102357
0.875	99.7456	0.493988	0.116789
1.000	99.5101	1.11898e-05	0.0586892
1.125	88.6939	0	3.86745e-05
1.250	79.8482	0	1.36359e-05
1.500	66.5717	0	2.65725e-06
1.750	57.0786	0	1.89101e-06
2.000	49.9539	0	1.70430e-06

Table 2.3: Performances with ideal channel for different values of β

As expected, for $\beta < 1$, the data transmission is impossible and the BER is always about 1/2, while, when $\beta > 1$, we have no errors. Only for critical sampling ($\beta = 1$) we have some errors caused by the dual window (see Figure 2.20(a)) that, as mentioned in previous chapter,

[8]The "almost" is due to the pulse truncation in time domain.

is not so "nice", i.e. it presents many spikes that worsen the performances. This effect is vanishing as the number of subcarriers grows and the prototype pulse is sampled thickly. The "Biorthogonality" parameter is calculated as

$$\text{Biorthogonality } (\%) = \frac{1}{L^2} \sum_{k=0}^{L-1} \sum_{k'=1}^{L-1} \left| \{\mathbf{I}_L - \mathbf{R_{BIO}}\}_{k,k'} \right|^2 \cdot 100 \tag{2.6.9}$$

where $\{\mathbf{A}\}_{m,n}$ denotes the element of mth row and nth column of matrix $\mathbf{A}$. This parameter represents the mean square error between the identity matrix $\mathbf{I}_L$ and the biorthogonality matrix $\mathbf{R}_{BIO}$. It can be notice from the table 2.3 that the biorthogonality is almost perfect for $\beta \leq 1$, while it decreases as the overlapping factor β increases. This is in keeping with what we have seen in Figure 2.21. In spite of this growing lack of biorthogonality, the BER still be equal to zero.

In order to choose the better value of the roll-off factor α we can make reference to the curves in Figure 2.23. These curves have been obtained with an AWGN channel for $E_b/N_0 = 10dB$. When α is chosen, such that $\beta > 1 + \alpha$, we have better performances because we have no overlapping among the subcarriers. However this good performances are limited by the truncation of the prototype pulse. In fact, the number of errors caused by truncation increases as the roll-off factor decreases. We can avoid this phenomenon choosing a prototype pulses longer than before. This entails an increase of the system complexity. When the α value increases, the BER raises because of the normalization of the dual pulse. In fact, the energy of the not-normalized dual pulses grows as α increases. Hence the data signal suffers an attenuation as stronger as the roll-off factor increases.

2.6.2 Gaussian pulse

The FIR Gaussian pulse-shaping filter design is done by truncating a sampled version of the continuous-time impulse response of the Gaussian filter which is given by:

$$g(t) = \frac{\sqrt{\pi}}{\alpha} e^{-\frac{\pi^2 t^2}{\alpha^2}} \tag{2.6.10}$$

The parameter α is related to 3dB bandwidth-symbol time product ($B{\cdot}T$) of the Gaussian filter as given by:

$$\alpha = \frac{1}{BT} \sqrt{\frac{\log 2}{2}} \tag{2.6.11}$$

There are two approximation errors in the design: a truncation error and a sampling error. The truncation error is due to a finite-time (FIR) approximation of the theoretically

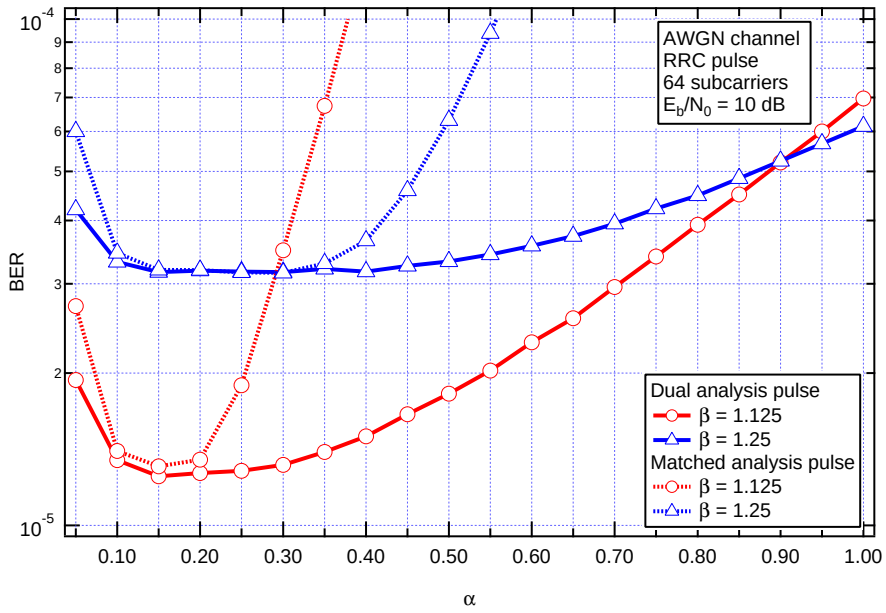

Figure 2.23: BER curves with RRC pulse for different β values in function of roll-off factor α

infinite impulse response[9] of the ideal Gaussian filter. The sampling error (aliasing) is due to the fact that a Gaussian frequency response is not really band-limited in a strict sense (i.e. the energy of the Gaussian signal beyond a certain frequency is not exactly zero). This can be noted looking at the transfer function of the continuous-time Gaussian filter (that is still a Gaussian function), which is given as below:

$$G(f) = e^{-\alpha^2 f^2}$$

As f increases, the frequency response tends to zero, but never is exactly zero, which means that it cannot be sampled without some aliasing occurring.

Hence the main parameter of these pulses is BT that determines his behaviour in time and frequency domain. As we can see in Figure 2.24, when BT increases his value, then the function decays quicker and the truncation error can be neglected. The respective amplitude frequency response of the curves illustrated in Figure 2.24, are depicted in Figure 2.25. Obviously they have the opposite trend than in time domain, i.e. the spectra decays quicker when BT is smaller.

From a time/frequency point of view, we have to choose an optimal value for BT given

[9]Even the RRC and Hermite pulses suffer this approximation.

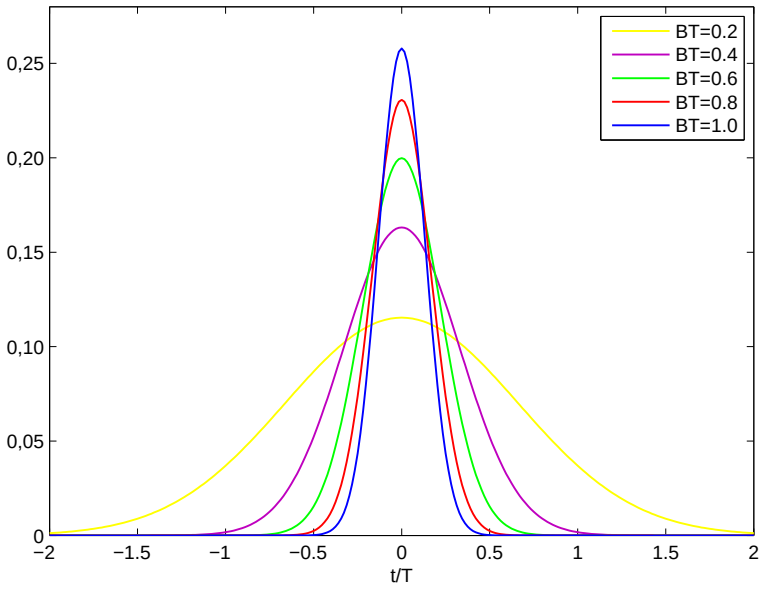

Figure 2.24: Gaussian pulses in time domain for different BT values

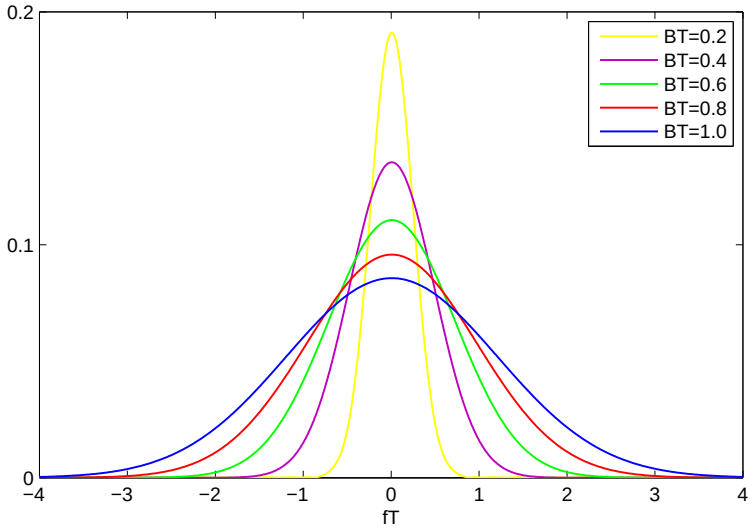

Figure 2.25: Gaussian pulses in frequency domain for different BT values

by the trade-off of ICI and ISI level. In fact the greatest BT values generate narrow pulses in time domain (small ISI) and large spectra (great ICI), while the smallest BT values entail pulses narrow in frequency domain (small ICI) but large in time domain (great ISI). Moreover this trade-off is affected by β value. A first advantage of the Gaussian pulses against the RRC ones is the smallest extension of pulses in time domain because of its rapidly decay. In fact the curves in Figure 2.24 go from $-2T$ to $2T$ while for the RRC pulse time axis goes from $-8T$ to $8T$ and it entails that with the Gaussian pulses $N_f^{(Tx)}$ can be choose smaller than the RRC pulses, i.e. the filters are shorter in the filterbank modulator and demodulator. A second advantage is the good localization of the base functions in the sense of a small dispersion, i.e. the product of frequency dispersion ΔW and time dispersion ΔT, necessary to avoid that the symbol energy "smears out" over the dispersive channel. In general the dispersion product is lower bounded by the uncertainty principle:

$$\Delta W \Delta T \geq \frac{1}{4\pi} \tag{2.6.12}$$

which is satisfied with equality just only for the Gaussian pulse.

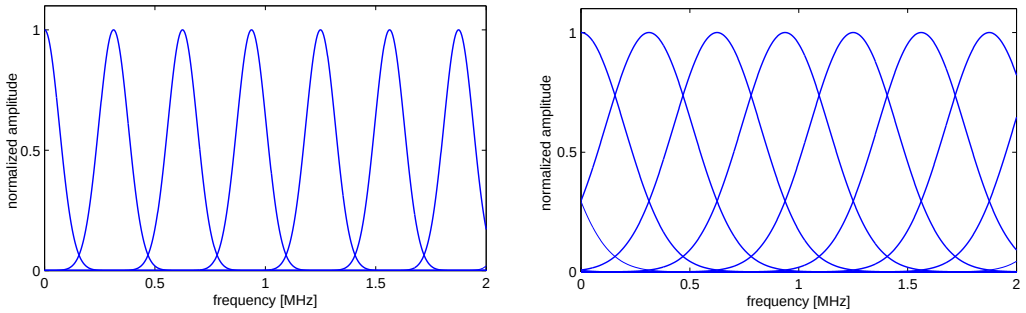

(a) (b)

Figure 2.26: Amplitude of frequency response for different BT values with $\beta = 1.125$

The partial amplitude frequency response of two transmitted signals are illustrated in Figure 2.26. They have been obtained using two different BT values for a given β. The other parameters are set to $M = 64$, $N_f^{(Tx)} = 4$ and $T_s = 50$ ns. We will now repeat the same biorthogonality analysis made for the RRC pulse. Let see first the dual windows with various β values and $BT = 0.5$ in Figure 2.27. Even for the Gaussian pulse some spikes appear at critical sampling. The relative biorthogonality matrices are illustrated in Figure 2.28.

In confirmation of perfect biorthogonality when $\beta < 1$ we show the dual window of a Gaussian pulse and their biorthogonality matrix when $\beta = 0.875$ in Figure 2.29.

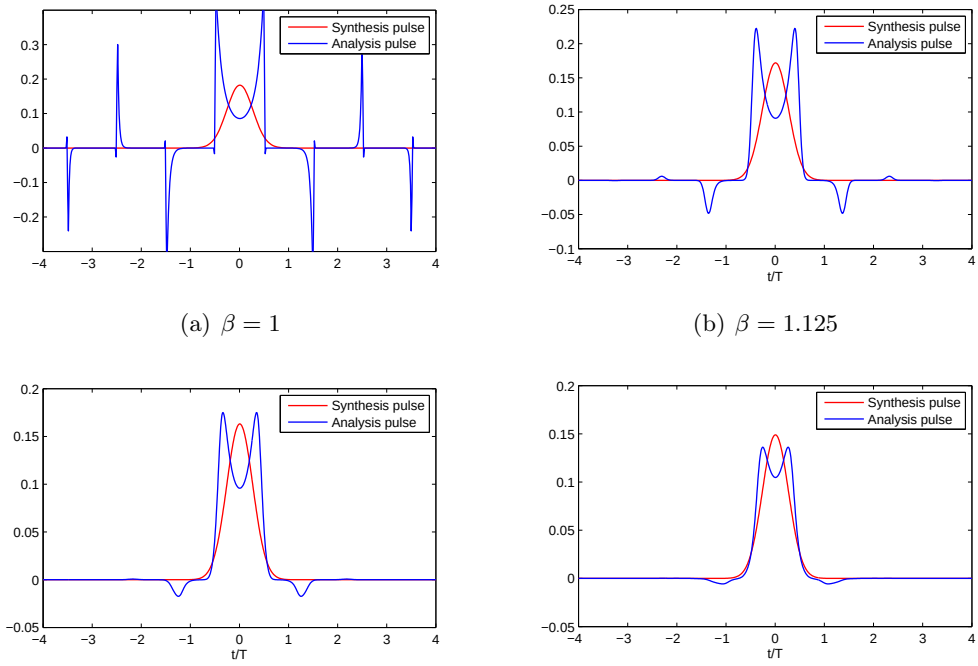

(a) $\beta = 1$

(b) $\beta = 1.125$

(c) $\beta = 1.25$

(d) $\beta = 1.5$

Figure 2.27: Gaussian synthesis and analysis prototype pulse for different β values

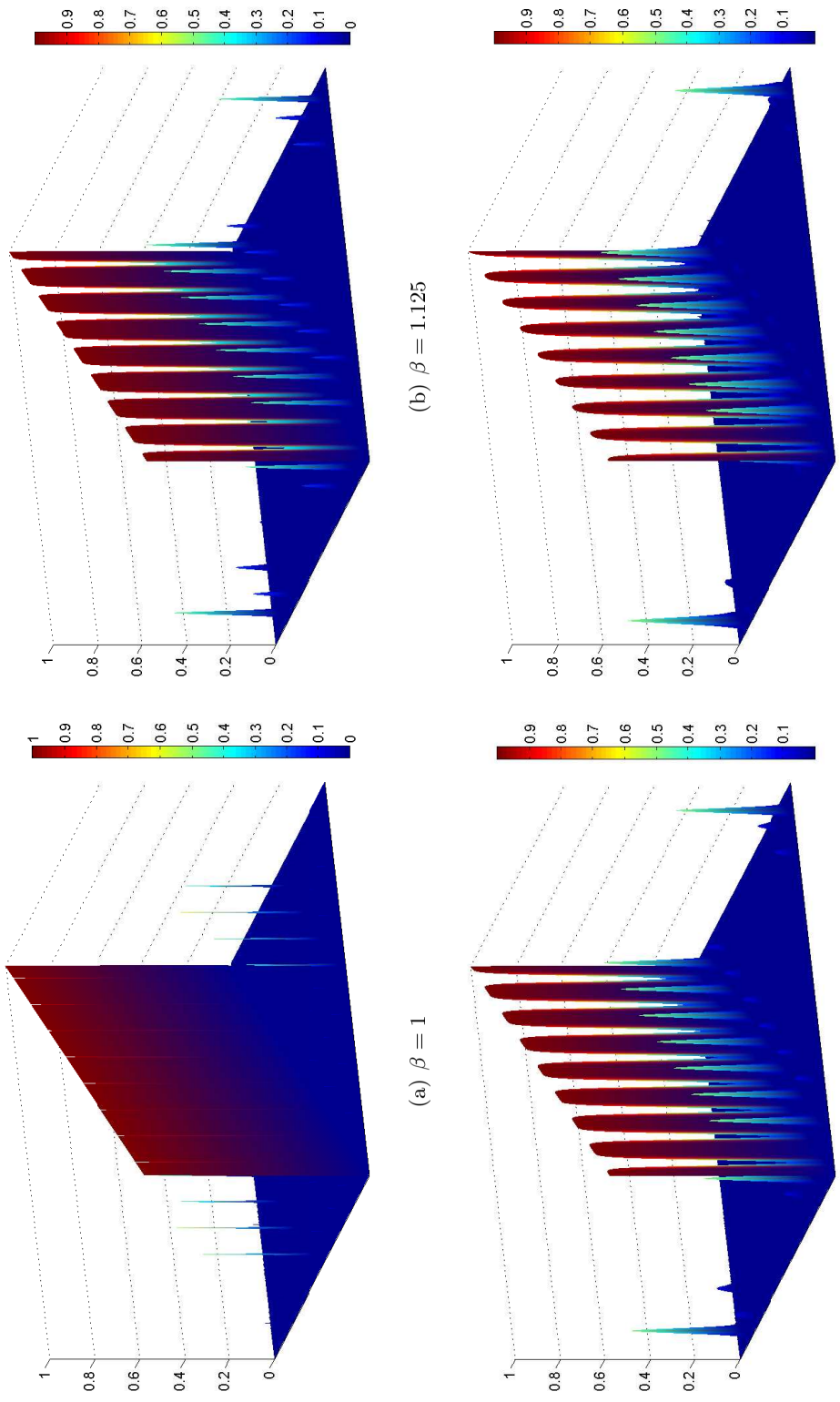

(a) $\beta = 1$ (b) $\beta = 1.125$

(c) $\beta = 1.25$ (d) $\beta = 1.5$

Figure 2.28: Biorthogonality matrices for different β values with Gaussian pulses

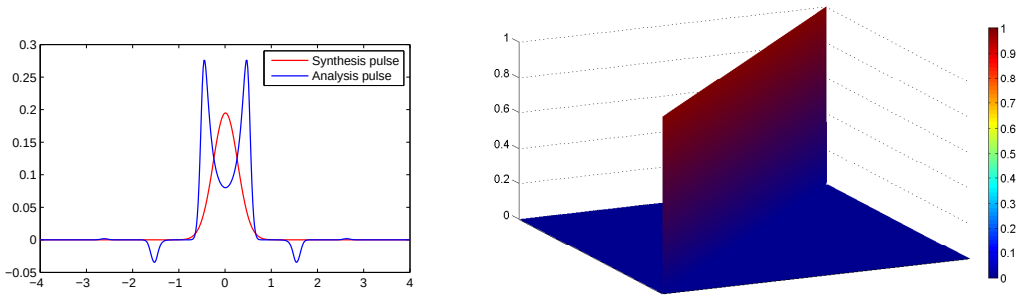

(a) (b)

Figure 2.29: Synthesis and analysis pulse and biorthogonality matrix for $\beta = 0.875$

Some atoms on the time/frequency grid for different values of β and BT are depicted in Figure 2.30 in order to show how these two parameters affect the transmitted signal on the TF grid. The other parameters are set to $M = 64$, $N_f^{(Tx)} = 8$ and $T_s = 50$ ns. The atoms depicted in the figure are the first three in time ($n = 0, 1, 2$) and the subcarriers $m = 7, 8, 9$ in frequency domain.

The BER and MSE results obtained for 4-QAM mapping with different β values are shown in Table 2.4. The channel is assumed ideal such as we have previously made for the RRC pulse. The other system parameters are $M = 256$, $N_f^{(Tx)} = 8$, $T_s = 50$ ns and $BT = 1$.

β	Biorthogonality (%)	BER	MSE
0.500	100.0000	0.492908	0.734708
0.750	100.0000	0.494303	0.852269
0.875	100.0000	0.498421	0.908879
1.000	99.0723	0	0.010150
1.125	88.8889	0	1.53349e-21
1.250	80.0000	0	1.83885e-21
1.500	66.6667	0	2.66238e-21
1.750	57.1429	0	3.71179e-21
2.000	50.0000	0	4.91300e-21

Table 2.4: Performances with ideal channel for different values of β

As for the RRC pulse, when $\beta < 1$, the data transmission is impossible and the BER is always about 1/2, while, when $\beta > 1$, we have no errors. For critical sampling ($\beta = 1$) we

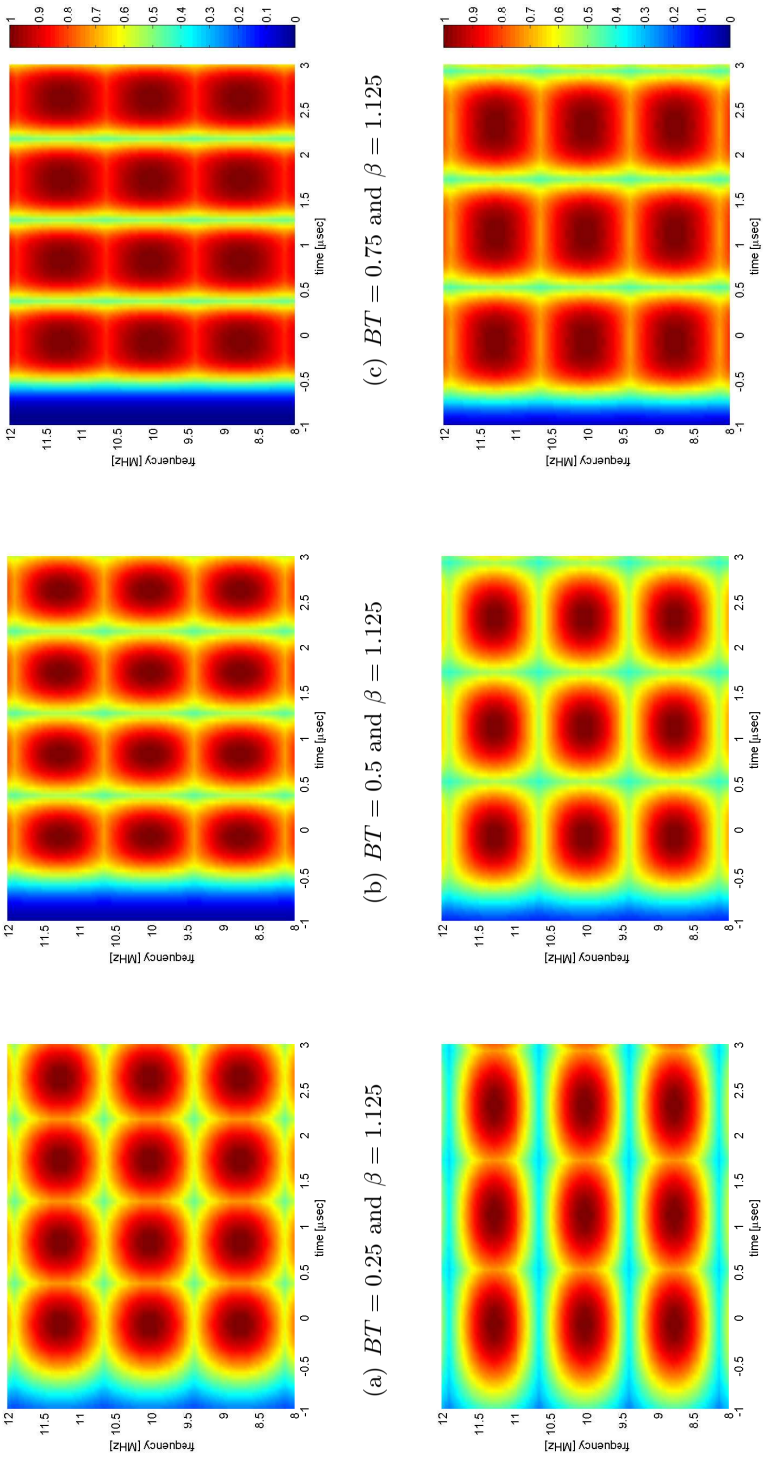

(a) $BT = 0.25$ and $\beta = 1.125$ (b) $BT = 0.5$ and $\beta = 1.125$ (c) $BT = 0.75$ and $\beta = 1.125$

(d) $BT = 0.25$ and $\beta = 1.5$ (e) $BT = 0.5$ and $\beta = 1.5$ (f) $BT = 0.75$ and $\beta = 1.5$

Figure 2.30: Gaussian atoms on TF grid for different β and BT values

have no errors too even if the dual window presents the spikes. This fact is caused by the high number of subcarriers and by the negligible truncation of the Gaussian pulse. This is confirmed be the MSE values that are lower than RRC pulse.

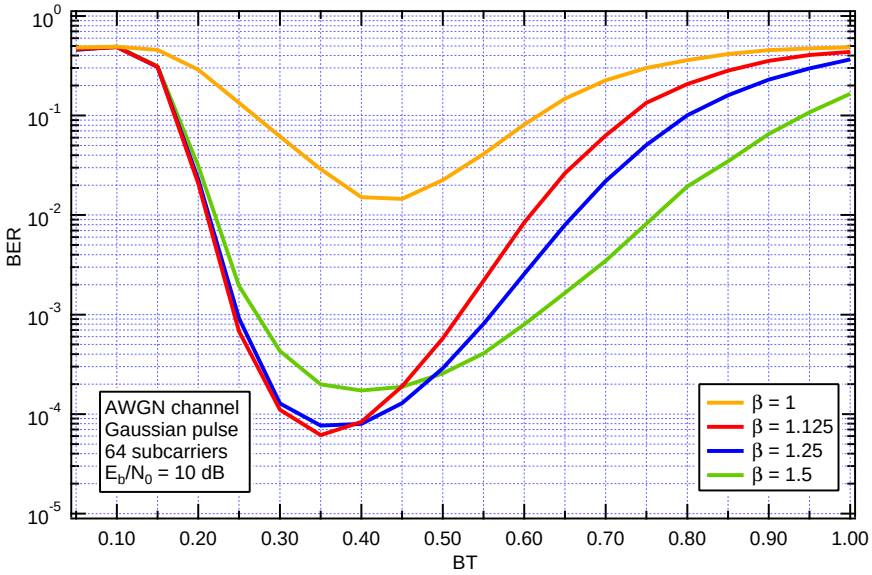

Figure 2.31: BER curves with Gaussian pulse for different β values in function of BT

In order to choose the better BT value we can look at Figure 2.31. These curves have been obtained with an AWGN channel and an $E_b/N_0 = 10dB$. As stated before, when the BT value decreases, the ISI is dominating and the dual prototype pulse increases its energy in order to contrast the interference. Thus the data signal suffers attenuation and BER grows. When the BT increases, the interference decreases and BER improves until the ICI comes out worsening the performances. The optimum value is obviously depending from β.

2.6.3 Hermite pulse

Another approach is to adopt an Hermite pulse [1]. This pulse is obtained combining Hermite functions, i.e.

$$g(t) = \sum_k a_k \phi_k(t) \tag{2.6.13}$$

where $\phi_k(t)$ is the kth Hermite function. The main motivation behind employing Hermite functions is that the first Hermite function is the Gaussian function given by (2.6.10) and kth Hermite function is the kth best localized function that is orthogonal to the Gaussian

and $k-1$ other Hermite functions. In [1], Kurt et Al. tried to optimize the coefficients' set $\{a_k\}$ by brute force approach, using exhaustive search in order to maximize the localization. There are three main results that are obtained from the simulations:

- The coefficients $\{a_k\}$ decrease exponentially with increasing k, hence only 5 coefficients were satisfactory for convergence.
- Only the Hermite functions whose frequency transforms are the same as themselves, hence time-frequency symmetric Hermite functions give good localization performance. These Hermite functions are the ones where $k(\text{mod } 4) = 0$.
- When we set $a_0 = 1$, all other coefficients $\{a_k\}$ should be real. In general all complex coefficients must have the same phase for optimum localization with the exception of a 180 degree phase shift.

Keeping these conditions in mind, the Hermite functions that are employed are given by [54]

$$\phi_k(t) = \frac{1}{\sqrt{n!\,2^k\sqrt{\pi}}}\,\mathrm{e}^{-t^2/2}H_k(t) = g_G(t)H_k\left(\frac{t}{\sigma}\right), \quad k = 0, 4, 8, 12, 16 \tag{2.6.14}$$

where *sigma* is derived from (2.6.11) as $\sigma = \frac{\alpha}{\sqrt{2\pi}}$, $g_G(t)$ is given by (2.6.10) and $H_k(x)$ are the Hermite (physicists) polynomials employed

$$\begin{aligned}
H_0(t) &= 1 \\
H_4(t) &= 16t^4 - 48t^2 + 12 \\
H_8(t) &= 256t^8 - 3584t^6 + 13440t^4 - 13440t^2 + 1680 \\
H_{12}(t) &= 4096t^{12} - 135168t^{10} + 1520640t^8 - 7096320t^6 + \\
&\qquad +13305600t^4 - 7983360t^2 + 665280 \\
H_{16}(t) &= 65536t^{16} - 3932160t^{14} + 89456640t^{12} - 984023040t^{10} + \\
&\qquad +5535129600t^8 - 15498362880t^6 + 19372953600t^4 - \\
&\qquad -8302694400t^2 + 518918400
\end{aligned} \tag{2.6.15}$$

The optimum coefficients of these functions are given in Table 2.5. Instead in [2], the set of coefficients used are different in order to satisfy other design criteria involving the ambiguity function and they are shown in Table 2.6.

The synthesis and the relative analysis Hermite pulses are depicted in Figure 2.32. In 2.32(a) it has been used the coefficients set in Table 2.5 proposed by Kurt et Al. in [1], while

a_k	
a_0	1
a_4	$-1.5 \cdot 10^{-3}$
a_8	$-3 \cdot 10^{-6}$
a_{12}	$-2 \cdot 10^{-10}$
a_{14}	$-2 \cdot 10^{-13}$

Table 2.5: Coefficient used for Hermite pulse in [1]

a_k	
a_0	1.1850899
a_4	$-1.9324881 \cdot 10^{-3}$
a_8	$-7.3110588 \cdot 10^{-6}$
a_{12}	$-3.1542096 \cdot 10^{-9}$
a_{14}	$9.6634138 \cdot 10^{-13}$

Table 2.6: Coefficient used for Hermite pulse in [2]

in 2.32(b) it has been used the coefficients set in Table 2.6 proposed by Haas et Al. in [2]. This pulses have been obtained for $BT = 0.35$, $\beta = 1.125$ and $N_f^{(Tx)} = 8$.

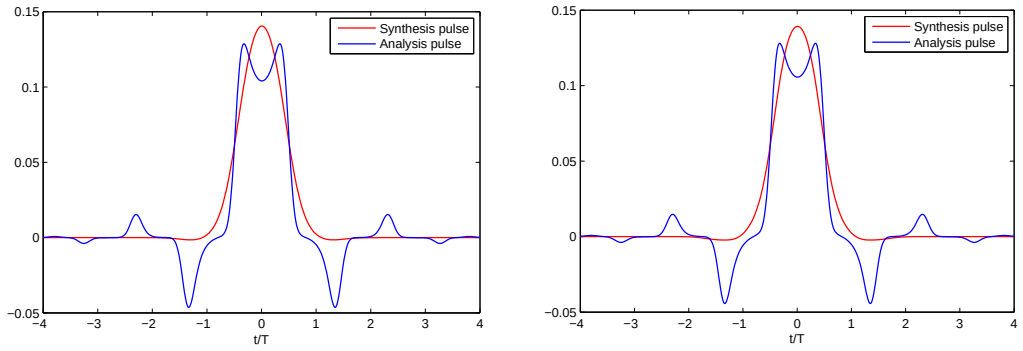

(a) (b)

Figure 2.32: Synthesis and relative analysis pulses with Hermite pulses

The two pulses seem identical but it can be notice the differences looking at the Figure

2.33 where it have been used a log scale for y-axis.

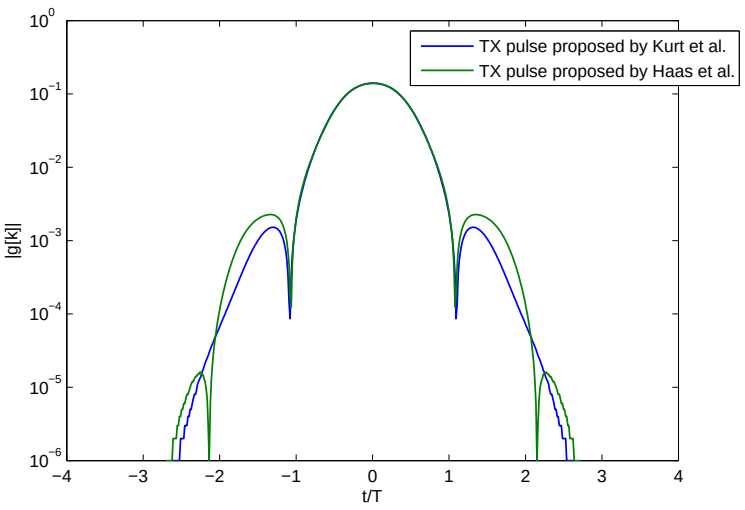

Figure 2.33: Comparison between the two different coefficients' sets $\{a_k\}$

2.6.4 Numerical pulse optimization

In this subsection we will discuss about some numerical criteria in order to optimize the analysis and/or the synthesis pulses according to a particular objective function that has to be minimized or maximized subject to some constraints in the form of equality constraints and/or inequality constraints.

In PHYDYAS project [55], the researchers adopt three well-known design criteria, i.e. least-squares (LS), minimax, and peak-constrained least-squares (PCLS) criteria. For this purpose the magnitude response of the real-valued prototype filter is divided into three types of regions: the passband region is $[0, \omega_p]$, the stopband region is $[\omega_p, \pi]$, and the gap between these two is called as the transition band. $G\left(e^{j\omega}\right)$ represents the transfer function of the prototype filter.

- The goal of the LS criterion is to minimize the stopband energy of the prototype filter. The objective function can be written as follows

$$F(x) = \int_{\omega_s}^{\pi} \left|G\left(e^{j\omega}\right)\right|^2 \, d\omega \tag{2.6.16}$$

The magnitude response of the resulting filter is shaped in such a manner that the attenuation increases steadily when going further from the stopband edge. The attenuation is rather low at the stopband edge, but it increases very rapidly to the level of the first stopband ripple.

- The goal of the minimax criterion is to minimize the maximum stopband ripple instead of the stopband energy. In minimax design, the objective function is

$$F(x) = \max_{\omega \in [\omega_s, \pi]} \left| G\left(e^{j\omega}\right) \right| \tag{2.6.17}$$

  The magnitude response of the resulting filter is shaped in such a manner that the attenuation is equiripple on the overall stopband region. The attenuation at the stopband edge is much higher than in the case of LS criterion, but this results in significantly increased total stopband energy.

- The PCLS criterion offers a trade-off between the LS and minimax criteria. The objective function is the stopband energy subject to maximum stopband ripple that is less than or equal to some prescribed value δ, i.e.,

$$F(x) = \int_{\omega_s}^{\pi} \left| G\left(e^{j\omega}\right) \right|^2 \, d\omega \text{ s.t. } \left| G\left(e^{j\omega}\right) \right| \leq \delta \text{ for } \omega \in [\omega_s, \pi] \tag{2.6.18}$$

  If δ is large enough, then this criterion reduces to the LS criterion. When decreasing δ, this criterion approaches the minimax criterion. Logically, this additional constraint increases total stopband energy.

Now, we discuss in detail a pulse optimization procedure that aim at low global interference and capitalizes on the design freedom existing for redundant MC systems. This pulse procedure optimization has been presented for the first time by Matz et Al. in [56] and it has been designed for filterbank-based multicarrier systems that transmit over doubly dispersive fading channels. This algorithm uses the mean intersymbol and intercarrier interference power as a cost function and thus performs an explicit minimization of ISI/ICI.

For low ISI/ICI, a multicarrier system should be almost orthogonal and use pulses that are jointly well localized in time and frequency. In [56], Matz et Al. demonstrate that for $\beta > 1$ there are other biorthogonal receive pulses besides the canonical one that can be found with the efficient algorithm described in Section 2.5.1. The pulse optimization procedure exploits this design freedom to improve on the canonical biorthogonal receive pulse in terms of ISI/ICI. The symbol period T and subcarrier spacing F will be assumed fixed. Parts of the results below have previously been obtained in [6]. The pulse optimization method uses a prescribed transmit pulse $g^{(0)}(t)$ and calculates the receive pulse $\gamma(t)$ minimizing the ISI/ICI power σ_I^2 subject to the biorthogonality condition. Fixed $g^{(0)}(t)$ and $TF = \beta > 1$, any biorthogonal receive pulse $\gamma(t)$ can be written as [57]

$$\gamma(t) = \gamma^{(0)}(t) + \psi(t) \tag{2.6.19}$$

Here, $\gamma^{(0)}(t)$ is the canonical biorthogonal pulse associated to $g^{(0)}(t)$ and $\psi(t)$ is an arbitrary element of the orthogonal complement space $\mathcal{G}^{\perp}$ of $\mathcal{G} = \text{span}(g^{(0)}_{m,n}(t))$, i.e. $\left\langle \psi, g^{(0)}_{m,n} \right\rangle = 0$ for all m,n. Hence, $\psi(t)$ can be written as

$$\psi(t) = \sum_i c_i u_i(t) \tag{2.6.20}$$

where $u_i(t)$ is an orthonormal basis of $\mathcal{G}^{\perp}$ and $c_i = \langle \psi, u_i \rangle$ denotes the corresponding coefficient of $\psi(t)$. Using (2.6.19), the minimization of σ_I^2 with respect to $\gamma(t)$ under the biorthogonality constraint can be formulated as an unconstrained minimization with respect to the coefficients c_i.

In this subsection the channel is assumed to satisfy the wide-sense stationary uncorrelated scattering (WSSUS) property and can be modeled as a random time-varying system $\mathbb{H}$ with time-varying impulse response $h(t,\tau)$. The second-order statistics of $\mathbb{H}$ can alternatively be described by the scattering function defined as

$$C_{\mathbb{H}}(\tau,\nu) = \int_{\Delta t} R_{\mathbb{H}}(\Delta t,\tau) e^{-j2\pi\nu\Delta t}\, d\Delta t \tag{2.6.21}$$

where ν denotes Doppler frequency and $R\mathbb{H}(t,\tau)$ is the time-delay correlation function of the channel. It will be convenient to use the following expression for power of the global interference σ_I^2 (see [6], [56])

$$\sigma_I^2 = \int_{\tau}\int_{\nu} Q^{(0)}_{\mathbb{H}}(\tau,\nu)\, |A_{\gamma,g}(\tau,\nu)|^2 \; d\tau \; d\nu \tag{2.6.22}$$

where $A_{\gamma,g}(\tau,\nu)$ is the cross-ambiguity fuction (CAF) of the synthesis and the analysis prototype pulses that is defined as

$$A_{\gamma,g}(\tau,\nu) \stackrel{\Delta}{=} \int_t \gamma(t) g^*(t-\tau) e^{-j2\pi\nu t}\, dt \tag{2.6.23}$$

and

$$Q^{(0)}_{\mathbb{H}}(\tau,\nu) \stackrel{\Delta}{=} \sum_{m,n\neq(0,0)} C_{\mathbb{H}}(\tau - nT, \nu - mF) \tag{2.6.24}$$

is a periodized version of $C_{\mathbb{H}}(\tau,\nu)$ with the term at the origin suppressed. Inserting (2.6.19) in (2.6.22), it is seen that σ_I^2 depends quadratically on the coefficients c_i. The (unconstrained) minimization of σ_I^2 with respect to the c_i then amounts to solving the linear equation $\mathbf{Bc} = -\mathbf{b}$ with $\{\mathbf{c}\}_i = c_i$ and

$$\{\mathbf{B}\}_{i,k} = \int_\tau \int_\nu Q_{\mathbb{H}}^{(0)}(\tau,\nu) A^*_{u_i,g^{(0)}}(\tau,\nu) A_{u_k,g^{(0)}}(\tau,\nu)\, d\tau\, d\nu \tag{2.6.25}$$

$$\{\mathbf{b}\}_{i} = \int_\tau \int_\nu Q_{\mathbb{H}}^{(0)}(\tau,\nu) A^*_{u_i,g^{(0)}}(\tau,\nu) A_{\gamma^{(0)},g^{(0)}}(\tau,\nu)\, d\tau\, d\nu \tag{2.6.26}$$

Thus the optimal biorthogonal receive pulse associated to the given transmit pulse $g^{(0)}(t)$ is obtained as

$$\gamma^{\text{opt}}(t) = \gamma^{(0)}(t) + \sum^{i} c_i^{\text{opt}} u_i(t) \quad \text{with } \mathbf{c}^{\text{opt}} = -\mathbf{B}^{-1}\mathbf{b} \tag{2.6.27}$$

The same approach can be used to optimize the transmit pulse $g(t)$ for a prescribed receive pulse $\gamma^{(0)}(t)$. The linear optimization method discussed above has the drawback that one of the two pulses must be chosen beforehand and is not optimized. Therefore, Matz et Al. propose a joint optimization of $g(t)$ and $\gamma(t)$. As a cost function, they use the reciprocal of the signal-to-interference ratio (SIR) σ_D^2/σ_I^2 given by [56]

$$J(g,\gamma) \triangleq \frac{\sigma_D^2}{\sigma_I^2} = \frac{\int_\tau \int_\nu Q_{\mathbb{H}}^{(0)}(\tau,\nu) \left|A_{\gamma,g}(\tau,\nu)\right|^2 \, d\tau\, d\nu}{\int_\tau \int_\nu C_{\mathbb{H}}(\tau,\nu) \left|A_{\gamma,g}(\tau,\nu)\right|^2 \, d\tau\, d\nu} \tag{2.6.28}$$

The goal is to minimize $J(g,\gamma)$ simultaneously with respect to $g(t)$ and $\gamma(t)$. For the sake of increased design freedom, this minimization is performed without the biorthogonality constraint. Thus, the resulting pulses are not necessarily exactly biorthogonal. While this allows for lower ISI/ICI power in the case of dispersive channels, there will be some residual ISI/ICI (typically below the noise level) for an ideal (nondispersive) channel. However, this is not a problem because an ideal channel rarely occurs in practice. Moreover, it is observed that the jointly optimized pulses tend to be almost biorthogonal (in fact, almost orthogonal). The minimization of $J(g,\gamma)$ has to be done by means of numerical techniques. In general, the resulting pulses correspond to a local minimum of $J(g,\gamma)$ and they depend on the pulses used for initializing the minimization procedure.

Chapter 3

Joint Tx-Rx transceivers design

The presence of the frequency-selective fading channel destroys the biorthogonality between synthesis and the analysis prototype pulses of the transmitter and the receiver filterbank and it introduces correlation among the "atoms" of the transmitted signal. Hence the performances suffer the multipath channel and they consequently worsen. Through a joint transceiver design and exploiting the majorization theory and a new equivalent model, we are able to contrast the channel effects and improve the performance of a NOFDM system.

In next section, hence we have to introduce the new equivalent model in order to describe the global interference affecting the system based on the model developed by Matz et al. in [56]. We will define a new equivalent channel matrix **H** including the channel and the transmitter and receiver filterbanks. Thanks to this new model we will be able to calculate the mutual information and to provide a procedure to evaluate the capacity of a filterbank-based communication system. Finally we will present and discuss the joint transceiver design that improves the system performances.

3.1 The equivalent system model

The complete block scheme of the communication system chain in presence of blockfading channels is depicted in Figure 3.1. The blocks "Precoder" and "Equalizer" will be considered in Section 3.3 and they are ignored for the moment. The remainder of the scheme is the same presented in Section 4.1.1 but the presence of the multipath channel generating the frequency-selective fading.

Now we concentrated our attention on signals involved in filterbank modulation, fading and filterbank demodulation. According to the scheme depicted in Figure 3.2 and the systems discussed in Chapter 2, the transmitted signal is

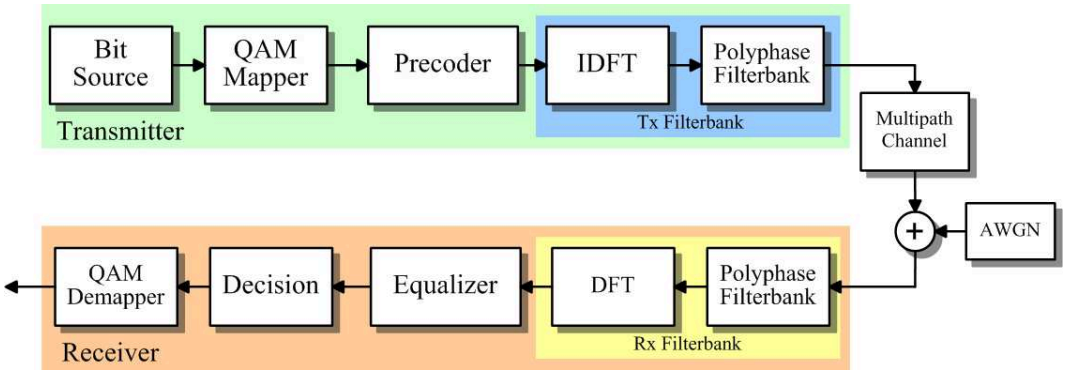

Figure 3.1: Block scheme for the filterbank communication system in presence of fading channel

$$\begin{aligned} s[k] &= \sum_{n=0}^{L/N-1} \sum_{m=0}^{M-1} c_{m,n} g_{m,n}[k] = \\ &= \sum_{n=0}^{L/N-1} \sum_{m=0}^{M-1} c_{m,n} g[k-nN] e^{j2\pi km/M} \end{aligned} \tag{3.1.1}$$

where

$$g_{m,n}[k] = g[k-nN] e^{j2\pi km/M} \tag{3.1.2}$$

is the (m,n)th atom on the TF grid and $m \in \{0,1,\ldots,M-1\}$ is the index in frequency domain while $n \in \{0,1,\ldots,L/N-1\}$ is the index in time domain. $c_{m,n}$ is the QAM symbol at the IDFT input transmitted on (m,n)th atom. M and N are the number of subcarriers and the time gap in samples between adjacent atoms, respectively. L is the total length of the prototype pulse. From now on we assume frames composed by $N_{GMC} = L/N = N_f^{(Tx)}$ consecutive GMC symbols (see 2.4.10).

The received signal is given by[1]

$$x[k] = s[k] \otimes h[k] + n[k] \tag{3.1.3}$$

[1]The operator $\otimes$ represents the convolution operator.

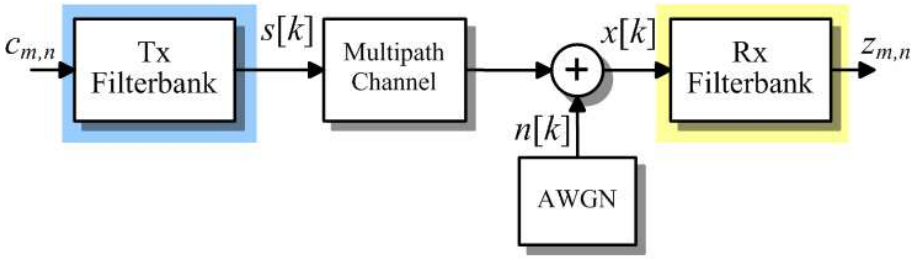

Figure 3.2: Core of filterbank system communication with fading channels and additive noise

where $h[k]$ is a $(L_{ch}+1)$-dimensional vector representing the channel impulse response sampled at Nyquist frequency $f_s = N/T$ and $n[k]$ is the zero-mean additive white gaussian noise (AWGN) with variance σ^2 defined in (4.1.1). Thus, exploiting (3.1.1) we obtain

$$\begin{aligned} x[k] &= s[k] \otimes h[k] + n[k] \\ &= \sum_{l=0}^{L_{ch}} s[k-l]h_l[k] = \\ &= \sum_{n=0}^{L/N-1} \sum_{m=0}^{M-1} c_{m,n} \left[\sum_{l=0}^{L_{ch}} g[k-l-nN]h_l[k]e^{j2\pi(k-l)m/M} \right] + n[k] = \\ &= \sum_{n=0}^{L/N-1} \sum_{m=0}^{M-1} c_{m,n}\eta_{m,n}[k] + n[k] \end{aligned} \tag{3.1.4}$$

where

$$\eta_{m,n}[k] = \sum_{l=0}^{L_{ch}} g[k-l-nN]h_l[k]e^{j2\pi(k-l)m/M} \tag{3.1.5}$$

and $h_l[k]$ denotes the lth sample of channel impulse response at time k. In this thesis we assume blockfading, i.e. the channel is static long all the frame. Hence $h_l[k] \to h_l$. After the filtering made by receiver filterbank, with substitution (3.1.1), we have the soft symbols

$$
\begin{aligned}
z_{m,n} &= \sum_k x[k]\gamma^*_{m,n}[k] = \\
&= \sum_k x[k]\gamma^*[k-nN]e^{-j2\pi km/M} = \\
&= \sum_k \left[\sum_{n'=0}^{L/N-1}\sum_{m'=0}^{M-1} c_{m',n'}\eta_{m',n'}[k]\right]\gamma^*[k-nN]e^{-j2\pi km/M} + w_{m,n} \\
&= \sum_{n'=0}^{L/N-1}\sum_{m'=0}^{M-1} c_{m',n'}\left[\sum_k \eta_{m',n'}[k]\gamma^*[k-nN]e^{-j2\pi km/M}\right] + w_{m,n} = \\
&= \sum_{n'=0}^{L/N-1}\sum_{m'=0}^{M-1} c_{m',n'}\left[\sum_k \eta_{m',n'}[k]\gamma^*_{m,n}[k]\right] + w_{m,n}
\end{aligned} \tag{3.1.6}
$$

where $\{w_{m,n}\}$ are the noise samples on (m,n)th received atom. After the filtering, the noise is no more white but colored, i.e. the noise samples are now dependent each other. So the system is affected by additive colored gaussian noise (ACGN). They are defined as

$$
w_{m,n} = \sum_k n[k]\gamma^*[k-nN]e^{-j2\pi km/M} \tag{3.1.7}
$$

From (3.1.6) we can define the tensor

$$
\begin{aligned}
\{\mathbf{H}(\mathbf{g},\gamma,\mathbf{h})\}_{m,n,m',n'} &= \left\langle \eta_{m',n'}, \gamma^*_{m,n}\right\rangle = \sum_k \eta_{m',n'}[k]\gamma^*_{m,n}[k] \\
&= \sum_{l=0}^{L_{ch}} h_l \left[\sum_k g[k-l-n'N]\gamma^*[k-nN]e^{j2\pi k(m'-m)/M}\right] e^{-j2\pi lm'/M}
\end{aligned} \tag{3.1.8}
$$

and (3.1.6) can be rewritten as

$$
z_{m,n} = \sum_{n'=0}^{L/N-1}\sum_{m'=0}^{M-1} c_{m',n'}\{\mathbf{H}\}_{m,n,m',n'} + w_{m,n} \tag{3.1.9}
$$

Now, letting

$$
\begin{cases} \mu = nM + m \\ \mu' = n'M + m' \end{cases} \tag{3.1.10}
$$

we can map the original tensor into a $(\frac{L}{N}M \times \frac{L}{N}M)$-dimensional matrix denoted by $\mathbf{H}$. Thus

$$z_\mu = \sum_{\mu'=0}^{\frac{L}{N}M-1} c_{\mu'} H_{\mu,\mu'} + w_\mu \tag{3.1.11}$$

where $H_{\mu,\mu'}$ denotes the generic element of the matrix $\mathbf{H}$ in μth row and μ'th column. For the sake of simplicity, (3.1.11) can be written in the matrix form

$$\mathbf{z} = \mathbf{Hc} + \mathbf{w} \tag{3.1.12}$$

We have so defined a new matrix $\mathbf{H}$ that connects the QAM soft symbols $\{z_{m,n}\}$ received after the filterbank filtering with the transmitted QAM symbols $\{c_{m,n}\}$. Figure 3.3 outlines a simple procedure to evaluate the equivalent channel matrix $\mathbf{H}$.

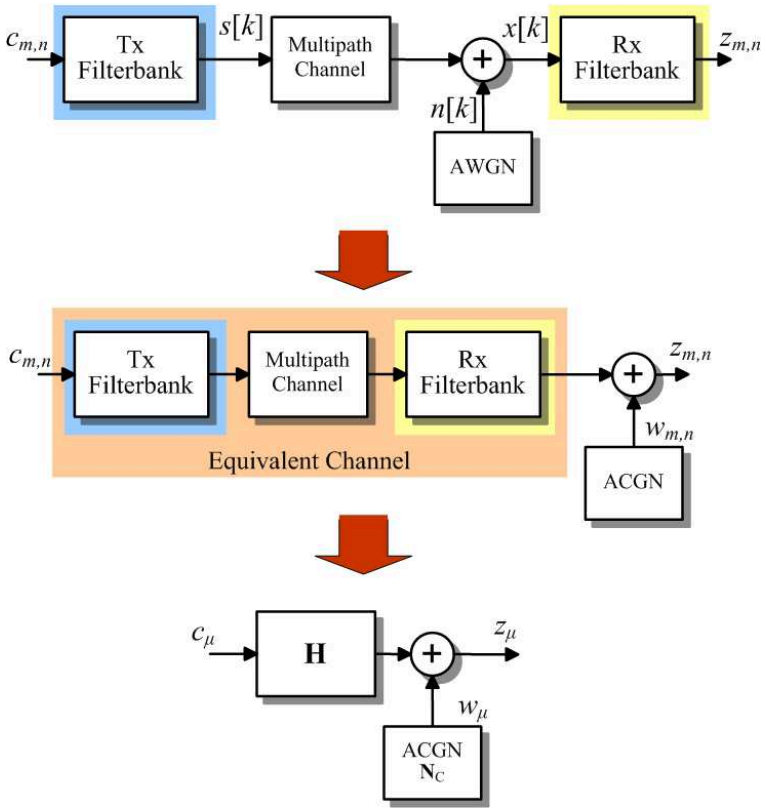

Figure 3.3: Procedure to derivation of equivalent channel matrix $\mathbf{H}$

Now, let us analyze the equation (3.1.12) by re-writing it as

$$z_\mu = \underbrace{c_\mu H_{\mu,\mu}}_{\text{Data}} + \underbrace{\sum_{\substack{\mu'=0 \\ \mu' \neq \mu}}^{\frac{L}{N}M-1} c_{\mu'} H_{\mu,\mu'}}_{\text{Interference}} + \underbrace{w_\mu}_{\text{ACGN}} \tag{3.1.13}$$

The soft channel symbols $z_\mu = z_{m,n}$ are given by the summation of the relevant transmitted symbol $c_\mu = c_{m,n}$ multiplied by the μth element on the diagonal of the equivalent channel matrix $\mathbf{H}$, plus the colored noise w_μ and an interference contribution. The latter is given by the sum of all the symbols of the transmitted frame (except the μth) element-wise multiplied by the μth row (obviously except the μth element) of matrix $\mathbf{H}$. So we can state that all the elements of equivalent channel matrix out of the diagonal determine the quantity of interference affecting the whole frame.

Let us note that with an AWGN channel, the tensor $\mathbf{H}_{m,n,m',n'}$ can be mapped into a diagonal matrix of size $(\frac{L}{N}M \times \frac{L}{N}M)$ if and only if the synthesis and analysis pulses are calculated according to the biorthogonal condition (even not perfectly).

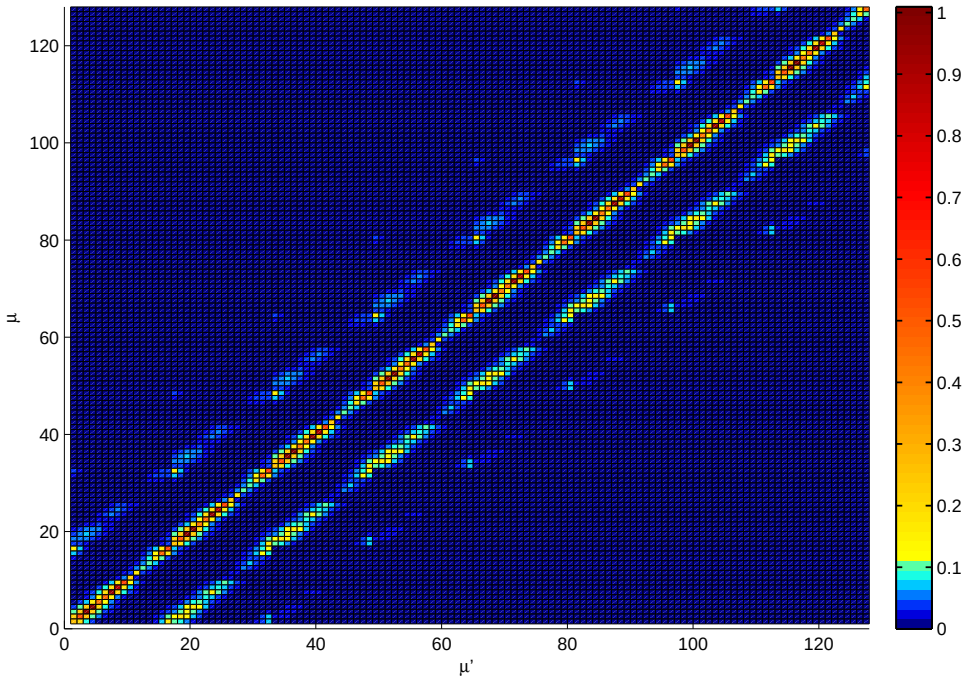

Figure 3.4: Example of equivalent channel matrix $\mathbf{H}$

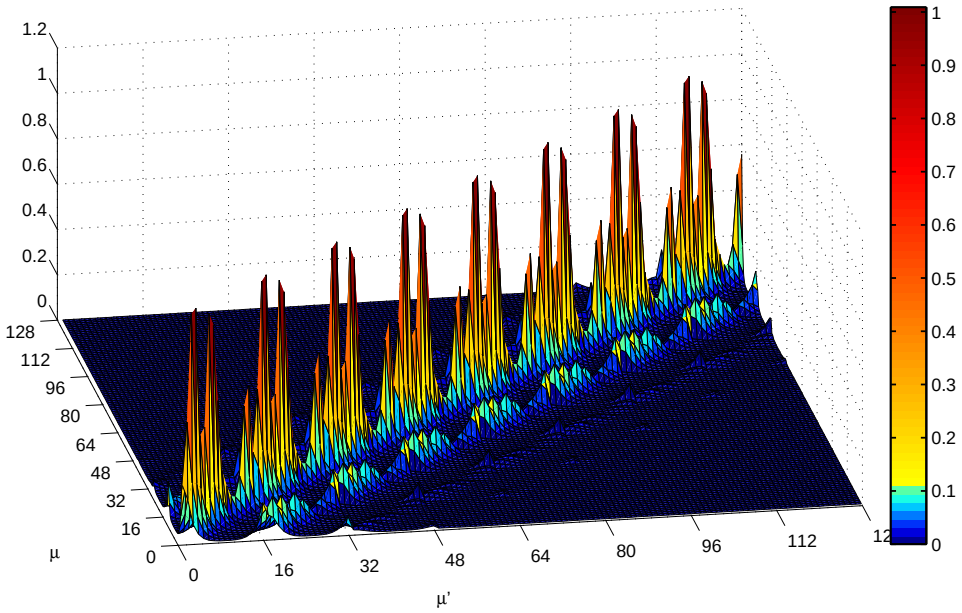

Figure 3.5: 3D version of the equivalent channel matrix **H**

We now discuss the structure of matrix **H** determined by the mapping (3.1.10). An example of equivalent channel matrix obtained with gaussian pulse ($BT = 0.5$) is illustrated in Figure 3.4 where the indices (μ, μ') are respectively the row and the column indices. The system parameters are $M = 16$, $\beta = 1.125$, $N_f^{(Tx)} = 8$ and $T_s = 50$ ns. A 3D version of the matrix is also illustrated in Figure 3.5.

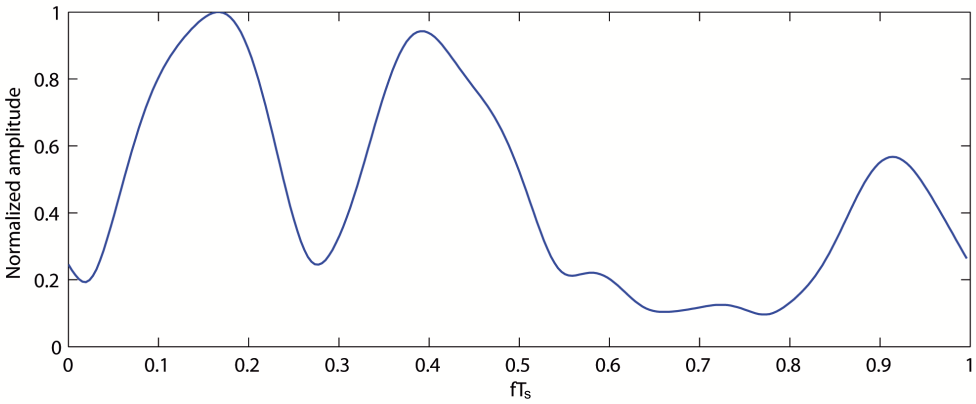

Figure 3.6: Normalized amplitude of the channel realization's frequency response

The amplitude frequency response of the channel realization affecting matrix depicted in Figures 3.4 and 3.5 is shown in Figure 3.6.

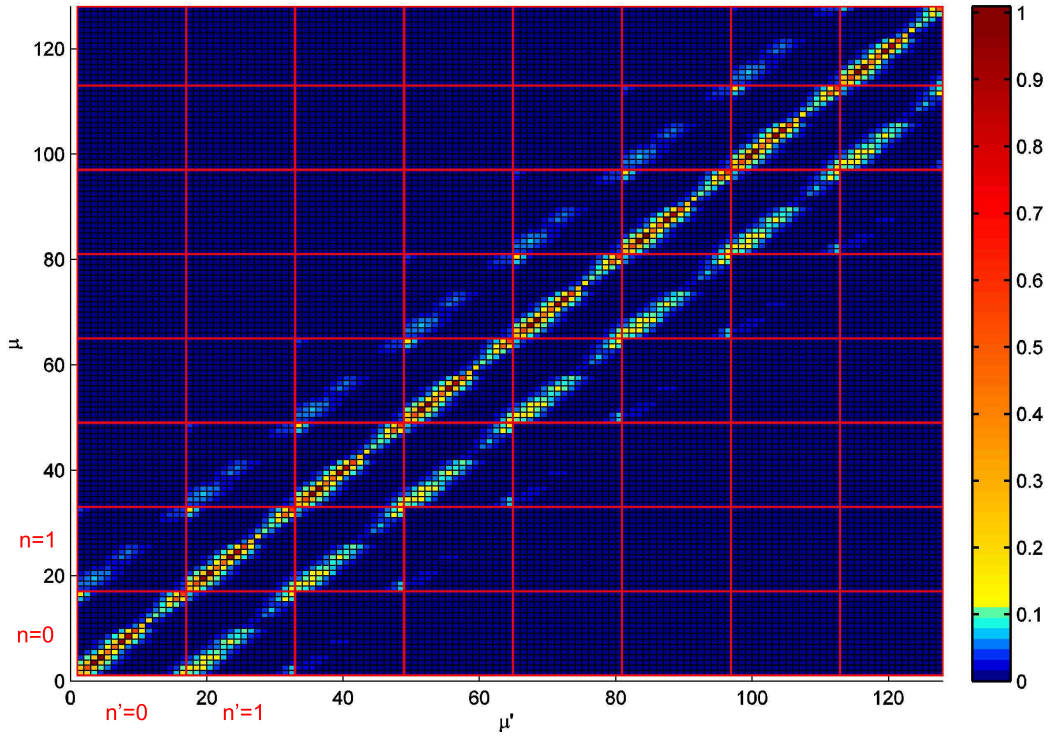

Figure 3.7: Blocks division of equivalent channel matrix $\mathbf{H}$

It can be notice that $\mathbf{H}$ is a not-symmetric Toeplitz block matrix, i.e. the blocks are the same on every diagonal block of the matrix. So it can be represented as

$$\mathbf{H}_{\mu,\mu'} = \begin{pmatrix} \mathbf{H}_0 & \mathbf{H}_1 & \cdots & \mathbf{H}_{N_f^{(Tx)}} \\ \mathbf{H}_{-1} & \mathbf{H}_0 & \ddots & \vdots \\ \vdots & \ddots & \ddots & \mathbf{H}_1 \\ \mathbf{H}_{-N_f^{(Tx)}} & \cdots & \mathbf{H}_{-1} & \mathbf{H}_0 \end{pmatrix} \tag{3.1.14}$$

The block division of the matrix in Figure 3.4 is shown in Figure 3.7. Each block on the diagonal represents a different GMC symbol of the frame and they are pointed out by the index $n = 0, 1, \ldots, \frac{L}{N}M - 1$. Considering the nth block on the diagonal, the blocks on the same row on its left represent the interference suffered by the nth GMC symbols caused by previous GMC symbols while these blocks on its right represent the interference brought by

the GMC symbols after the nth. In other words we can say that blocks out of the diagonal on the nth row carry information about ISI suffered by nth GMC symbol of the frame under analysis. All the blocks are square matrices of size $(M \times M)$ and elements inside every diagonal block represent the ICI between the mth subcarrier and the m'th one inside a same GMC symbol. Broadening the discussion to the whole matrix $\mathbf{H}$ we can say that μ'th element is the interference affecting the μth QAM symbol $c_\mu = c_{m,n}$, i.e. the symbol carried by the mth subcarrier of the nth GMC symbol caused by the the μ'th QAM symbol $c'_\mu = c_{m',n'}$ carried by the m'th subcarrier of the n'th GMC symbol of the same frame.

Looking at the Figure 3.5, we can notice that the profile of the main diagonal of matrix $\mathbf{H}$ is just the frequency response of the channel repeated in each diagonal block $\frac{L}{N}$ times, i.e. the number of GMC symbols in the frame.

The channel matrix can be approximated considering only the interference caused by the neighboring atoms both in frequency and time domain. In this case the only non-null elements of approximated equivalent matrix $\tilde{\mathbf{H}}$ are $\tilde{H}_{\mu,\mu'} = \{\mathbf{H}\}_{m,n,m',n'}$ with $|m'-m| \leq 1$ and $|n'-n| \leq 1$, i.e.

$$\tilde{H}_{\mu,\mu'} = \begin{cases} \{\mathbf{H}\}_{m,n,m',n'} & \text{if } \begin{cases} |m'-m| \leq 1 \\ |n'-n| \leq 1 \end{cases} \\ 0 & \text{otherwise} \end{cases} \tag{3.1.15}$$

In this case $\tilde{\mathbf{H}}$ is a tridiagonal block matrix and each block becomes a tridiagonal matrix. The approximated version of $\mathbf{H}$ depicted in Figure 3.4 is shown in Figure 3.8. The mean square error between $\mathbf{H}_{APPROX}$ and $\mathbf{H}$ is about $10^{-3} \div 10^{-4}$.

In presence of flat fading channel, the channel impulse response is $h_l = h_0 = 1$ and the tensor $\mathbf{H}$ becomes

$$\begin{aligned} \mathbf{H}_{m,n,m',n'} &= \sum_k g[k - n'N]\gamma^*[k - nN]e^{j2\pi k(m'-m)/M} \\ &\Downarrow \\ \mathbf{H}_{\mu,\mu'} &= \chi \mathbf{I}_{\frac{L}{N}M} \end{aligned} \tag{3.1.16}$$

where

$$\chi = \sum_k g[k]\gamma^*[k] \tag{3.1.17}$$

In this case we obtain the absence of any interference, i.e. (3.1.13) becomes

$$\mathbf{z}_\mu = \mathbf{c}_\mu \mathbf{H}_{\mu,\mu} + \mathbf{w}_\mu \tag{3.1.18}$$

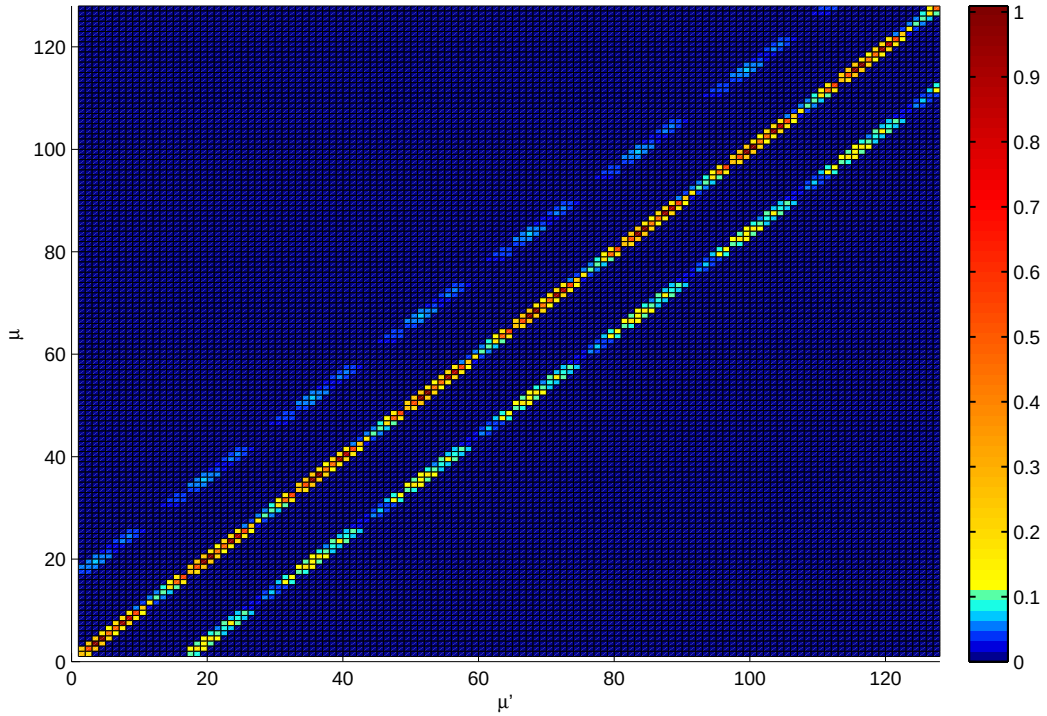

Figure 3.8: Approximated version of **H** shown in Figure 3.4 according to (3.1.15)

It means that elements out of diagonal of equivalent matrix are all zeros. Finally we show the equivalent matrix channel **H** in presence of an ideal flat channel in Figure 3.9. The system's parameters are the same of previous example. The absence of interference is clearly visible coherently with what have been stated in (3.1.18) and (3.1.16).

In this situation every atom is independent of other atoms, i.e. $z_{m,n}$ is only given by the right $c_{m',n'} = c_{m,n}$ transmitted QAM symbol, and the parallelization of the channels is allowed. Moreover it can be notice that the maximum of the matrix is not unitary because the dual pulse at the receiver is normalized. Without the normalization we exactly obtain the identity matrix. In Section 3.3 we will discuss about a technique used to transform any equivalent matrix **H** affected by frequency-selective fading into an ideal identity matrix and thus clear all the interference affecting the frame. In this way we can calculate the capacity of a filterbank-base communication system and evaluate the benefits of these systems compared with OFDM systems.

Finally we show how biorthogonality between synthesis and analysis is mandatory. In

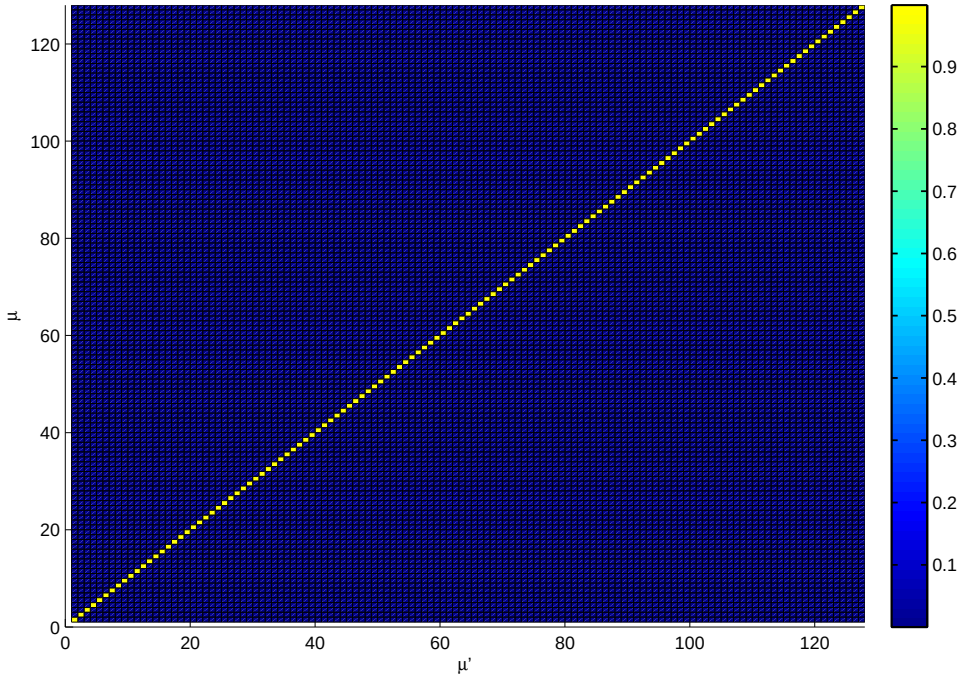

Figure 3.9: Equivalent channel matrix **H** with ideal channel

Figure 3.10 is illustrated the equivalent matrix **H** under ideal channel assumption for a filterbank system that uses the same prototype pulse both at the transmitter and at the receiver, i.e. $g[k] = \gamma[k]$. The pulse chosen is a Gaussian one with $BT = 0.5$. It is evident from Figure 3.10 that the absence of biorthogonality creates both ISI and ICI even without frequency-selective fading channel.

3.1.1 Colored noise covariance matrix

In order to complete the presentation of the new equivalent channel model, we have to describe the covariance matrix $\mathbf{N}_C$ of the colored noise $w[k]$. The covariance matrix of AWGN $n[k]$ is simply $\mathbf{N}_W = \sigma^2 \mathbf{I}_{\frac{L}{N}M}$, i.e. it is a diagonal matrix with elements on the diagonal σ^2

$$\mathbf{N}_W = \begin{pmatrix} \sigma^2 & & 0 \\ & \sigma^2 & \\ & & \ddots \\ 0 & & \sigma^2 \end{pmatrix} \tag{3.1.19}$$

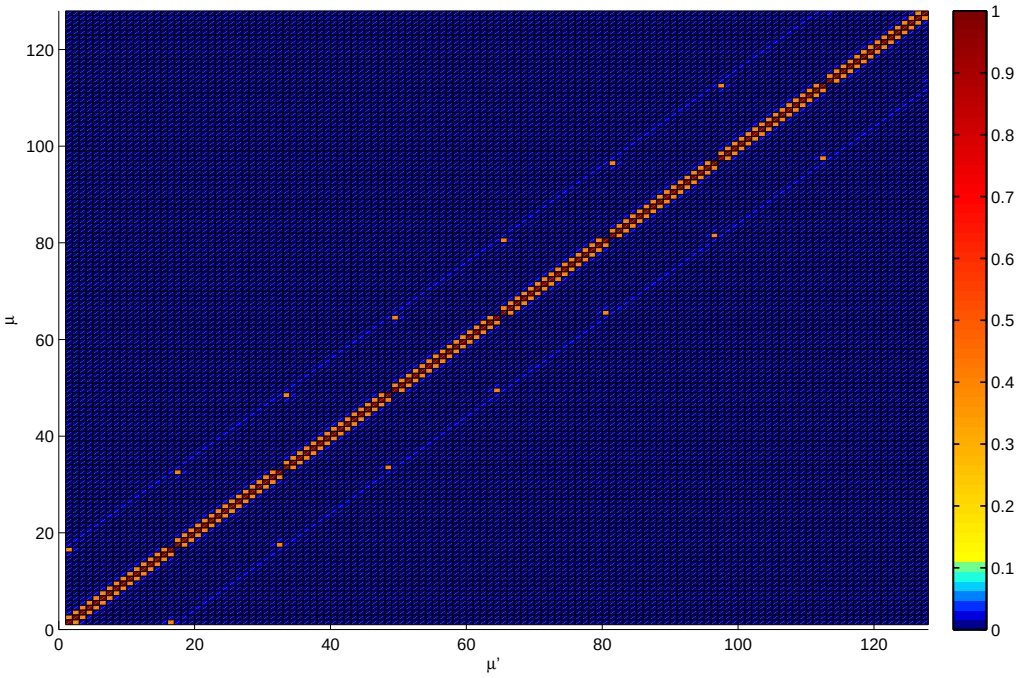

Figure 3.10: Equivalent matrix with flat channel and $g[k] = \gamma[k]$

For the calculation of $\mathbf{N}_C$ we apply the definition of the covariance matrix

$$\{\mathbf{N}_C\}_{\mu,\mu'} = E\{w_\mu w^*_{\mu'}\} \tag{3.1.20}$$

Substituting (3.1.7) in (3.1.20) we obtain

$$\begin{aligned} E\{w_\mu w^*_{\mu'}\} &= E\{w_{m,n} w^*_{m',n'}\} = \\ &= E\left\{\sum_{k=0}^{q-1} n[k]\gamma^*[k-nN]e^{-j2\pi km/M} \sum_{k'=0}^{q-1} n^*[k']\gamma[k'-n'N]e^{j2\pi k'm'/M}\right\} = \\ &= \sum_{k=0}^{q-1}\sum_{k'=0}^{q-1} E\{n[k]n^*[k']\}\gamma^*[k-nN]\gamma[k'-n'N]e^{-j2\pi km/M}e^{j2\pi k'm'/M} \end{aligned} \tag{3.1.21}$$

where $q = \frac{L}{N}M$ is the size of the square matrix and $E\{n[k]n^*[k']\}$ represents the covariance between the two white noise sample $n[k]$ and $n[k']$. Thus, recalling that

$$E\{n[k]n^*[k']\} = \sigma^2\delta[k-k'] = \begin{cases} \sigma^2 & \text{if } k = k' \\ 0 & \text{otherwise} \end{cases} \tag{3.1.22}$$

and substituting (3.1.22) into (3.1.21) we have

$$\mathbf{N}_{C\,m,n,m',n'} = \sigma^2 \sum_{k=0}^{q-1} \gamma^*[k-nN]\gamma[k-n'N]e^{j2\pi k(m'-m)/M} \tag{3.1.23}$$

We can observe from equation (3.1.23) that the covariance matrix $\mathbf{N}_C$ depends only from analysis prototype pulse. An example of covariance noise matrix normalized to σ^2 is shown in Figure 3.11. The system parameters are $M = 16$, $\beta = 1.125$, $N_f^{(Tx)} = 8$ and $T_s = 50$ ns as before. The prototype pulse is a Gaussian pulse with $BT = 0.5$ and the channel realization is the same of Figure 3.6.

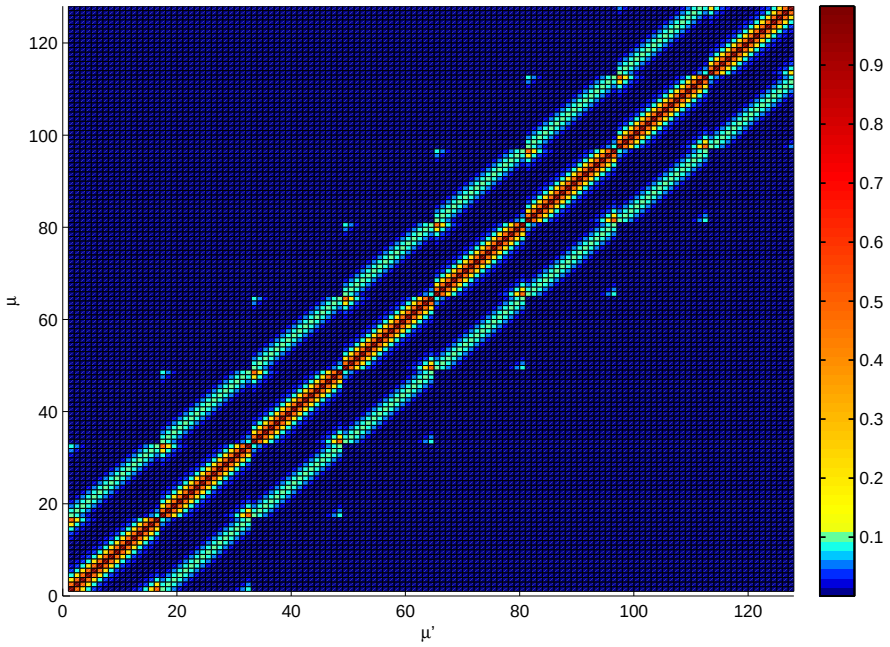

Figure 3.11: Normalized covariance matrix of colored noise $w[k]$

It can be notice that the matrix $\mathbf{N}_C$ has a symmetric block diagonal Toeplitz structure whose relevant blocks presents a symmetric diagonal Toeplitz structure again.

3.1.2 OFDM systems with equivalent model

This model is suitable even for OFDM systems. Assuming the cyclic prefix longer than the maximum delay of the channel impulse response (i.e. $L_{cp} \geq L_{ch}$) and remembering that $g[k]$ and $\gamma[k]$ are rectangular pulses with length equal to M, the product $g[k-l-n'N]\gamma^*[k-nN]$ in (3.1.8) is non-null only if[2] $n' = n$. Moreover $\sum_k e^{j2\pi k(m'-m)} = \delta[m'-m]$ because of the orthogonality condition. Thus (3.1.8) becomes

$$H^{(O)}_{\mu,\mu'} = \mathbf{H}_{m,n,m',n'} = \begin{cases} \sum_{l=0}^{L_{ch}} h_l e^{-j2\pi lm/M} & \text{if } m = m' \text{ and } n = n' \\ 0 & \text{otherwise} \end{cases} \tag{3.1.24}$$

that is the DFT of the channel impulse response. So the structure of the equivalent channel matrix is strongly simplified by the time-limited prototype pulses and by the orthogonality condition that assures $\mathbf{H}^{(O)}$ to be diagonal. In this way the absence of interference in OFDM systems adopting CP is confirmed. In Figure 3.12 is depicted $\mathbf{H}^{(O)}$ in presence of the channel realization in Figure 3.6.

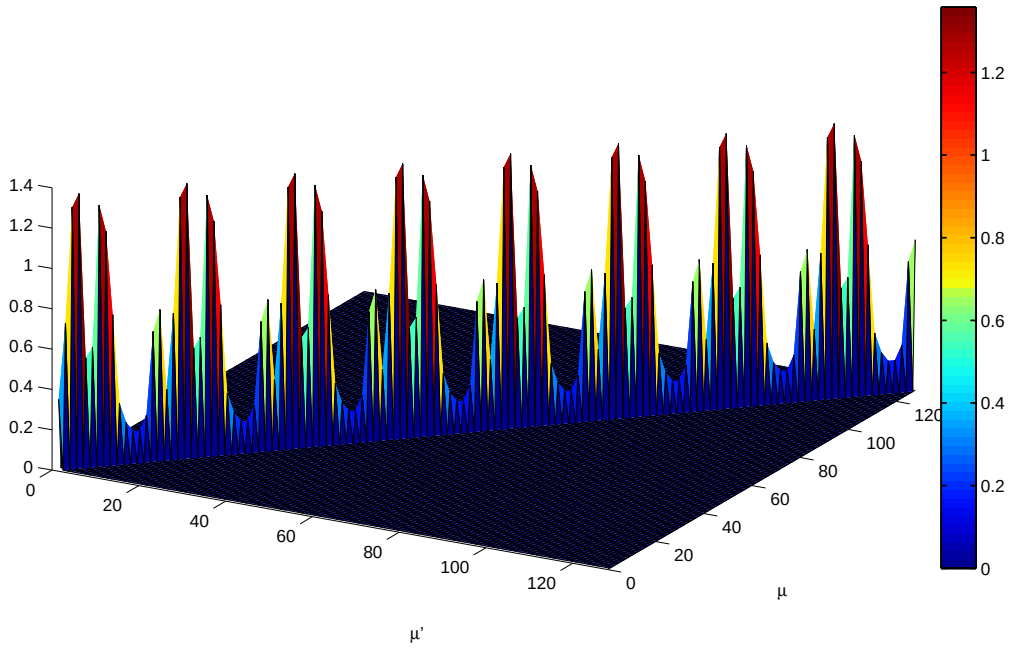

Figure 3.12: Equivalent channel matrix for an OFDM system

For an OFDM communication system the noise does not suffer the receiver filterbank

[2]In this case N is given by $M + L_{cp}$.

filtering and it preserves its AWGN characteristics. This fact can be easily understand looking at (3.1.23) and making the same considerations made previously in the derivation of the matrix $\mathbf{H}^{(O)}$.

3.2 Mutual information evaluation

Once a simplified input-output relationship for the GMC system has been defined, in this section, we follow the procedure described in [14] to evaluate the input-output mutual information.

The mutual information between the output symbols $\mathbf{z} = \{z_\mu\}_0^{q-1}$ and the input symbols $\mathbf{c} = \{c_\mu\}_0^{q-1}$ is given by [14]

$$I_M(\mathbf{c};\mathbf{z}) = h(\mathbf{z}) - h(\mathbf{w}) \tag{3.2.1}$$

where $q = \frac{L}{N}M = N_{GMC}M$ is the number of the QAM symbols and of the atoms into the whole frame and $h(\mathbf{z})$ is the entropy of the symbols $\{z_\mu\}$ while $h(\mathbf{w})$ is the entropy of the colored noise samples. In case of Gaussian sources, this two values are equal to[3] [58]

$$h(\mathbf{z}) = \log_2\left((\pi e)^q |\mathbf{R}_Z|\right) \tag{3.2.2}$$

$$h(\mathbf{w}) = \log_2\left((\pi e)^q |\mathbf{R}_C|\right) \tag{3.2.3}$$

where $\mathbf{R}_C = \mathbf{N}_C$ is the covariance matrix of the noise (in this case colored) and $\mathbf{R}_Z$ is the covariance matrix of the output symbols $\{z_\mu\}$. Since $\{x_\mu\}$ and the noise samples are independent, the covariance of the output is $\mathbf{R}_Z = \mathbf{R}_X + \mathbf{N}_C$. In order to determine $\mathbf{R}_X$, we can apply the definition of the covariance matrix, i.e.

$$\begin{aligned}
\mathbf{R}_X &= E\{\mathbf{x}\mathbf{x}^H\} = \\
&= E\{\mathbf{H}\mathbf{c}\mathbf{c}^H\mathbf{H}^H\} = \\
&= \mathbf{H}E\{\mathbf{c}\mathbf{c}^H\}\mathbf{H}^H = \\
&= \mathbf{H}\mathbf{R}_C\mathbf{H}^H
\end{aligned} \tag{3.2.4}$$

where $\mathbf{R}_C$ is the covariance matrix of the input symbols $\{x_\mu\}$. Since they are independent and with zero-mean and unit variance, we have $\mathbf{R}_C = \mathbf{I}_q$. Thus (3.2.4) becomes

[3] The notation $|\mathbf{A}|$ represents the determinant of matrix $\mathbf{A}$.

$$\mathbf{R}_X = \mathbf{H}\mathbf{H}^H \tag{3.2.5}$$

Now we can write the mutual information $I_M(\mathbf{c};\mathbf{z})$ as

$$\begin{aligned} I_M(\mathbf{c};\mathbf{z}) &= \log_2\left((\pi e)^q |\mathbf{R}_Z|\right) - \log_2\left((\pi e)^q |\mathbf{N}_C|\right) = \\ &= \log_2\left(\frac{(\pi e)^q |\mathbf{R}_Z|}{(\pi e)^q |\mathbf{N}_C|}\right) = \\ &= \log_2\left(\frac{|\mathbf{N}_C + \mathbf{R}_X|}{|\mathbf{N}_C|}\right) = \\ &= \log_2\left(\frac{\left|\mathbf{N}_C + \mathbf{H}\mathbf{H}^H\right|}{|\mathbf{N}_C|}\right) = \\ &= \log_2\left(\left|\mathbf{I} + \mathbf{H}\mathbf{N}_C^{-1}\mathbf{H}^H\right|\right) \qquad [\text{bits}] \end{aligned} \tag{3.2.6}$$

In order to make fair comparison with OFDM systems we normalized the mutual information with respect to the overall bandwidth B_{TOT} and the GMC symbol interval T. Since the mutual information is calculated on the entire frame we will normalized even with respect to the number of GMC symbols per frame N_{GMC}. Thus, we obtain the normalize mutual information as

$$\begin{aligned} \overline{I}_M &= \frac{I_M(\mathbf{c};\mathbf{z})}{B_{TOT}\cdot T\cdot N_{GMC}} = \\ &= \frac{I_M(\mathbf{c};\mathbf{z})\cdot T_s}{T_s\cdot N\cdot N_{GMC}} = \\ &= \frac{I_M(\mathbf{c};\mathbf{z})}{N_{GMC}\cdot N} = \\ &= \frac{1}{N_{GMC}\cdot N}\log_2\left(\left|\mathbf{I} + \mathbf{H}\mathbf{N}_C^{-1}\mathbf{H}^H\right|\right) \qquad \left[\frac{\text{bit/s}}{\text{Hz}}\right] \end{aligned} \tag{3.2.7}$$

The calculation of the mutual information of an OFDM system is simplified by the diagonal structures of the matrices $\mathbf{H}^{OFDM}$ and $\mathbf{N}_C$. In fact considering (3.1.24) and the fact that $\mathbf{R}_N = \sigma^2\mathbf{I}$, (3.2.6) becomes

$$
\begin{aligned}
I_M^{(O)} &= \log_2\left(\left|\mathbf{I}+\mathbf{H}^{(O)}\mathbf{R}_C^{-1}{\mathbf{H}^{(O)}}^H\right|\right) \\
&= \log_2\left(\left|\mathbf{I}+\frac{1}{\sigma^2}\mathbf{H}^{(O)}{\mathbf{H}^{(O)}}^H\right|\right) = \\
&= \log_2\left(\prod_{\mu=0}^{q-1}\left(1+\frac{\rho_\mu^2}{\sigma^2}\right)\right) = \\
&= \sum_{\mu=0}^{q-1}\log_2\left(1+\frac{\rho_\mu^2}{\sigma^2}\right) \qquad [\text{bits}]
\end{aligned} \tag{3.2.8}
$$

where $\rho_k^2 = \left|\left\{\mathbf{H}^{(O)}\right\}_{\mu,\mu}\right|^2$ is the square modulus of the μth element on the diagonal of $\mathbf{H}^{(O)}$. This time the normalization has to consider the length of cyclic prefix. Thus the normalized mutual information is

$$
\overline{I}_M^{(O)} = \frac{1}{N_{GMC}(M+L_{cp})}\sum_{\mu=0}^{q-1}\log_2\left(1+\frac{\rho_\mu^2}{\sigma^2}\right) \qquad \left[\frac{\text{bit/s}}{\text{Hz}}\right] \tag{3.2.9}
$$

In Figure 3.13 are depicted the normalized mutual information curves with different β values employing a Gaussian pulse ($BT = 0.5$). It is shown even the normalized mutual information of an OFDM system (black line). It is evident how the mutual information grows as β decreases. This is caused by the fact that the duration of a GMC symbol decreases with the overlapping factor β at a given value of overall bandwidth. Regarding the OFDM system, its mutual information has been evaluated employing a cyclic prefix 4 samples[4]. Hence for $M = 16$, the length of the OFDM symbols is 20 samples. In that case, the OFDM system has the same spectral efficiency of a NOFDM system with the overlapping factor set to $\beta = 1.25$. Comparing the normalized mutual information curves of these two system, it can be notice that the OFDM system works better than NOFDM one because of the orthogonality condition and the presence of the cyclic prefix. But for $\beta < \frac{M+L_{cp}}{M} = 1.25$ the FB-based systems overtake the OFDM one. Hence we can state that a filterbank-based multicarrier system allows to receive more information bits than an OFDM system using less time. In fact we can decrease the duration of the GMC symbols and avoid the employment of the cyclic prefix that worsens the spectral efficiency of the system. Unfortunately the gain of the mutual information given by the decreased redundancy does not automatically entail an improvement of the performances. In order to obtain satisfactory performances we have to take account of the introduction of further data processing through a better design of both the transmitter and the receiver.

[4]When $T_s = 200$ ns the channel impulse response lasts 4 samples.

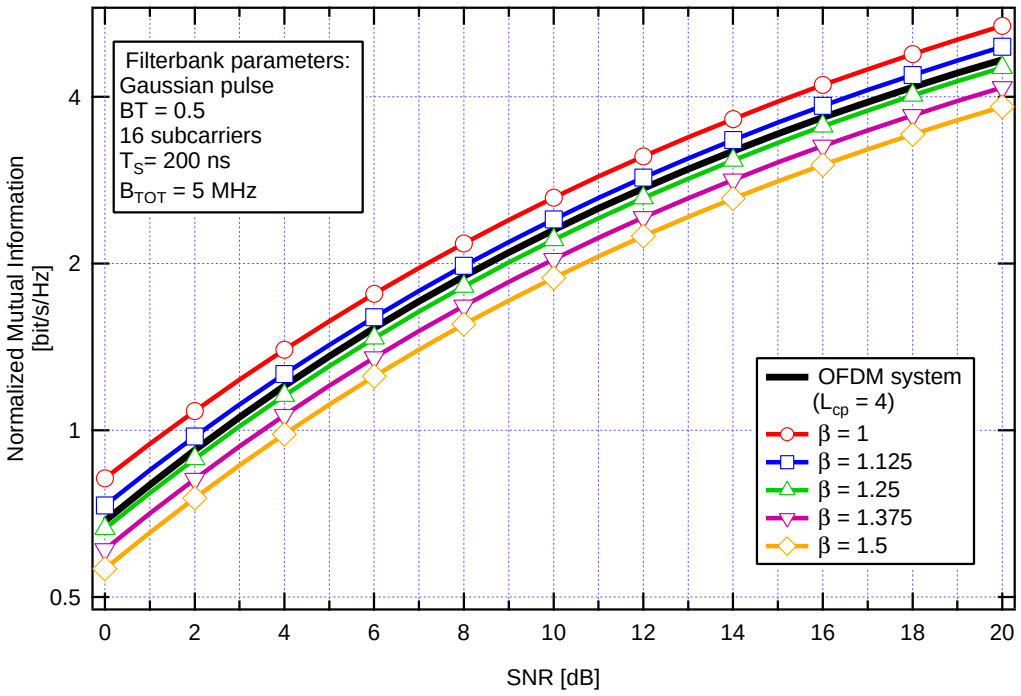

Figure 3.13: Normalized mutual information curves for different β values with gaussian pulse

In Figure 3.14 we show the normalized mutual information for a NOFDM system employing a Gaussian pulse with different values of BT and $\beta = 1.125$. We can observe that the mutual information gain given by decrease of the signaling interval can be easily lost if the BT is not wisely chosen. In fact a wrong choice of BT can entail a huge increase of the interference (in practice it decreases the signal-to-noise ratio) yielding to the lost of received information.

3.3 Capacity evaluation with diagonalization

In [36], Scaglione et Al. present a procedure to the determination of the synthesis and analysis filterbanks in order to achieve the maximization of the mutual information. They assume that the number of samples into a GMC symbol N satisfies the constraint $N = M + L_{ch}$, i.e. that the channel impulse response affects only a GMC symbol at once. In this way the interference between adjacent symbols is avoided. Moreover the algorithm developed by Scaglione et Al., entails different filters onto each branch of the filterbanks. Thus the polyphase implementation is not possible and the complexity of the modulator and the de-

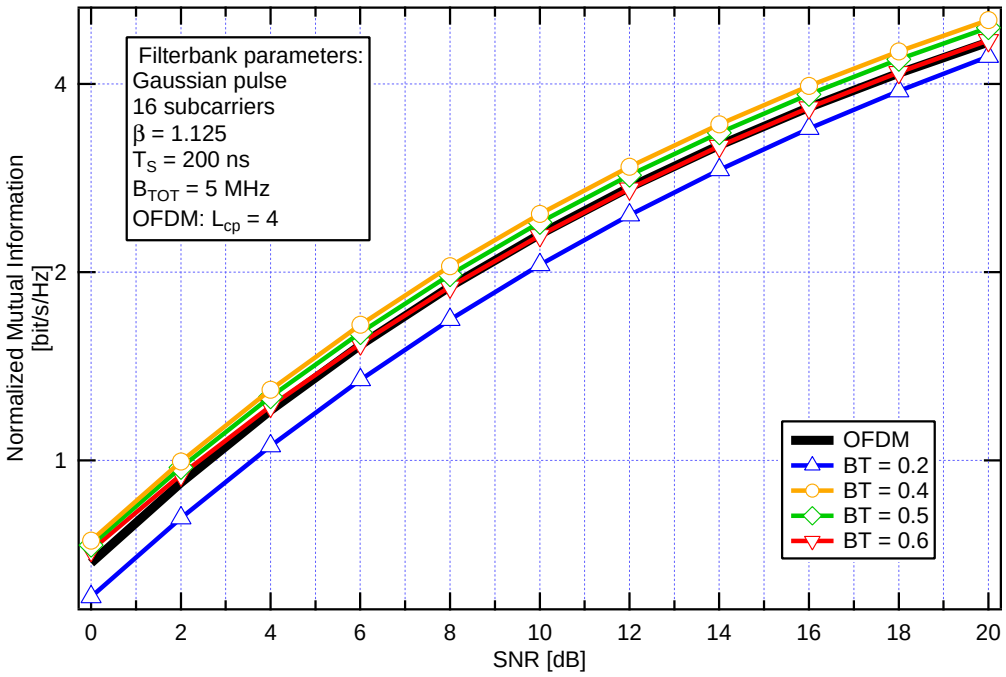

Figure 3.14: Normalized mutual information curves for different BT values with gaussian pulse

modulator considerably increases. In this work we do not assume the constraint on N in order to do not limit β to a narrow range depending on the channel selectivity. Moreover, as we will discuss, the introduction of a precoder out of the modulator and of an equalizer out of the demodulator allows to employ the efficient polyphase implementation.

The technique presented in this section, allows to decompose the channel into a certain number of parallel AWGN channels. Since the equivalent model can be considered similar to a MIMO model we can exploit the joint tx-rx beamforming design for multicarrier MIMO systems discussed by Palomar et Al. in [59]. In this article, the joint design adds a linear precoder at the transmitter and an equalizer at the receiver. The authors of [59] consider different design criteria based on optimizing the MSE, the SINR, and also the BER directly. Instead of considering each design criterion in a separate way, Palomar et Al. develop a unifying framework and generalize the existing results by considering two families of objective functions that embrace most reasonable criteria to design a communication system: Schur-concave and Schur-convex functions that arise in majorization theory [60]. For Schur-concave objective functions, the channel-diagonalizing structure is always optimal, whereas for Schur-convex functions, an optimal solution diagonalizes the channel only after a very specific rotation of the transmitted symbols. One of the main goal of this thesis is the capacity

evaluation, i.e. the mutual information maximization through an MSE-based optimization criteria.

According to the Hadamard's inequality [14], (3.2.7) is maximized when the matrix $\mathbf{I} + \mathbf{H}\mathbf{N}_C^{-1}\mathbf{H}^H$ is diagonal. In order to realize that we have to introduce the "Precoder $\mathbf{B}$" and the "Equalizer $\mathbf{A}^H$" as depicted in Figure 3.1. Hence the equivalent model becomes that depicted in Figure 3.15.

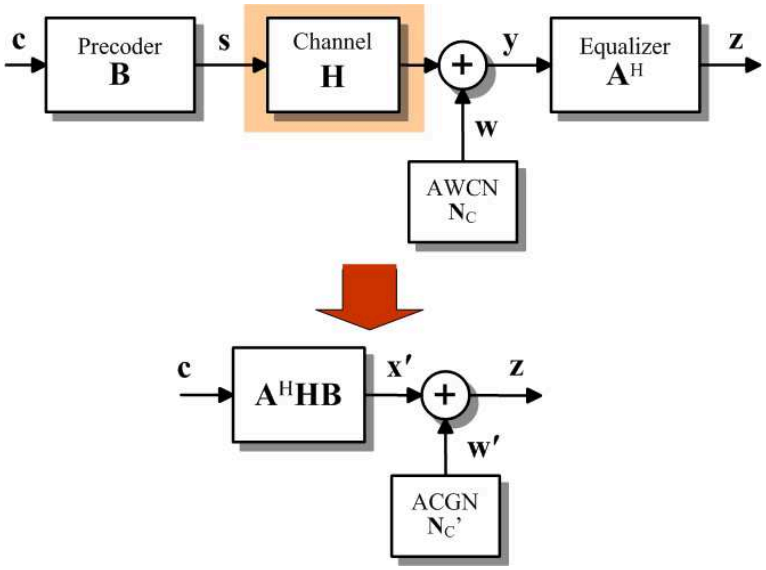

Figure 3.15: Equivalent capacity-achieving model with introduction of $\mathbf{B}$ and $\mathbf{A}^H$

The vector $\mathbf{s}$ is given by the processed vector $\mathbf{c}$ through the precoder $\mathbf{B}$, i.e. $\mathbf{s} = \mathbf{B}\mathbf{c}$. Then it experiences the transmitter filterbank, the fading channel and the receiver filterbank. The received vector $\mathbf{y}$ (containing the colored additive noise $\mathbf{w}$) is finally equalized by matrix $\mathbf{A}^H$ in order to return the vector $\mathbf{z}$.

This time we will use the new equivalent matrix $\mathbf{H}_{TOT} = \mathbf{A}^H\mathbf{H}\mathbf{B}$ given by the chain composed by the precoder, the channel (with the filterbanks) and the equalizer. These two matrices are square of same size ($q \times q$). As stated before, the mutual information is maximized when this new matrix is diagonal. Now our goal is to determine the matrices $\mathbf{A}^H$ and $\mathbf{B}$ realizing the diagonalization.

In order to design the system, we first derive the optimum receive matrix $\mathbf{A}$, assuming the transmit precoder $\mathbf{B}$ fixed, and then deal with the difficult part, which is the derivation of the optimal transmit matrix $\mathbf{B}$. The MSE matrix is defined as the covariance matrix of the error vector (given by $\mathbf{e} \triangleq \mathbf{z} - \mathbf{c}$)

$$\begin{aligned}\mathbf{E}(\mathbf{B},\mathbf{A}) &\triangleq E\{(\mathbf{z}-\mathbf{c})(\mathbf{z}-\mathbf{c})^H\} = \\ &= \mathbf{A}^H\mathbf{R}_y\mathbf{A}+\mathbf{I}-\mathbf{A}^H\mathbf{H}\mathbf{B}-\mathbf{B}^H\mathbf{H}^H\mathbf{A} \qquad (3.3.1)\end{aligned}$$

where $\mathbf{R}_y \triangleq E\{\mathbf{y}\mathbf{y}^H\} = \mathbf{H}\mathbf{B}\mathbf{B}^H\mathbf{H}^H + \mathbf{N}_C$ is the covariance matrix of the received symbols $\mathbf{y}$. The MSE of the μth atom is the μth diagonal element of $\mathbf{E}$, i.e.,

$$\begin{aligned}\mathrm{MSE}_\mu(\mathbf{B},\mathbf{a}_\mu) &= \{\mathbf{E}\}_{\mu,\mu} = \qquad (3.3.2)\\ &= \mathbf{a}_\mu^H\mathbf{R}_y\mathbf{a}_\mu+\mathbf{I}-\mathbf{a}_\mu^H\mathbf{H}\mathbf{b}_\mu-\mathbf{b}_\mu^H\mathbf{H}^H\mathbf{a}_\mu \qquad (3.3.3)\end{aligned}$$

where $\mathbf{a}_\mu$ (respectively $\mathbf{b}_\mu$) is the μth column of $\mathbf{A}$ (respectively $\mathbf{B}$). Expression (3.3.2) is mathematically intractable since it is nonconvex in $(\mathbf{B},\mathbf{a}_\mu)$. However, for a given $\mathbf{B}$, MSE_μ is convex in $\mathbf{a}_\mu$ and independent of the other columns of $\mathbf{A}$ and of the other atoms, which means that each $\mathbf{a}_\mu$ can be independently optimized. To obtain the optimal receive matrix $\mathbf{A}^{\mathrm{opt}}$ in a more direct way, it suffices to find $\mathbf{A}$ such that the diagonal elements of $\mathbf{E}$ are minimized. Alternatively, we can obtain $\mathbf{A}^{\mathrm{opt}}$ so that $\mathbf{E}(\mathbf{B},\mathbf{A}^{\mathrm{opt}}) \leq \mathbf{E}(\mathbf{B},\mathbf{A})$, which in particular implies that the diagonal elements are minimized (in fact, both criteria are equivalent as shown in [61]). In other words, we want to solve

$$\min_{\mathbf{A}^*}\ \mathbf{c}^H\mathbf{E}(\mathbf{B},\mathbf{A})\mathbf{c}, \qquad \forall\mathbf{c} \qquad (3.3.4)$$

Setting the gradient of[5] $\mathbf{c}^H\mathbf{E}\mathbf{c} = \mathrm{Tr}(\mathbf{E}\mathbf{c}\mathbf{c}^H)$ to zero

$$\nabla_{\mathbf{A}^*}\mathrm{Tr}(\mathbf{E}\mathbf{c}\mathbf{c}^H) = \mathbf{R}_y\mathbf{A}\mathbf{c}\mathbf{c}^H - \mathbf{H}\mathbf{B}\mathbf{c}\mathbf{c}^H = 0, \qquad \forall\mathbf{c} \qquad (3.3.5)$$

and particularizing $\mathbf{c}$ for all the vectors of the canonical base, it follows that

$$\mathbf{A}^{\mathrm{opt}} = \left(\mathbf{H}\mathbf{B}\mathbf{B}^H\mathbf{H}^H + \mathbf{N}_C\right)^{-1}\mathbf{H}\mathbf{B} \qquad (3.3.6)$$

Formula (3.3.6) is the linear minimum MSE (LMMSE) receiver. Later we will express $\mathbf{A}^{(ZF)}$ for a zero-forcing receiver. Using the optimal receive matrix $\mathbf{A}^{\mathrm{opt}}$, we obtain the following concentrated error matrix

[5]The function $\mathrm{Tr}(\mathbf{A})$ denotes the trace of matrix $\mathbf{A}$.

$$\begin{aligned}\mathbf{E}(\mathbf{B}) &= \mathbf{E}(\mathbf{B},\mathbf{A}^{\text{opt}}) = \\ &= \mathbf{I}-\mathbf{B}^H\mathbf{H}^H\left(\mathbf{H}\mathbf{B}\mathbf{B}^H\mathbf{H}^H+\mathbf{N}_C\right)^{-1}\mathbf{H}\mathbf{B} = \\ &= \left(\mathbf{I}+\mathbf{B}^H\mathbf{R}_\mathbf{H}\mathbf{B}\right)^{-1} \end{aligned} \tag{3.3.7}$$

where we have used the matrix inversion lemma[6], and we have defined $\mathbf{R}_\mathbf{H} \triangleq \mathbf{H}\mathbf{N}_C^{-1}\mathbf{H}^H$ (note that the eigenvectors and eigenvalues of $\mathbf{R}_\mathbf{H}$ are the right singular vectors and the squared singular values, respectively, of the whitened channel ${\mathbf{R}_\mathbf{H}}^{-1/2}\mathbf{H}$).

To obtain the transmit matrix $\mathbf{B}$, we now consider the minimization of an arbitrary objective function f_0 of the diagonal elements of (3.3.7) using a theorem proposed by Palomar (for the proof see [59])

Theorem 2 *Consider the following constrained optimization problem*

$$\begin{aligned}&\min_{\mathbf{B}}\ f_0\left(\mathbf{d}\left(\mathbf{E}\left(\mathbf{B}\right)\right)\right)\\ &s.t.\ \text{Tr}\left(\mathbf{B}\mathbf{B}^H\right)\leq P_{\text{TOT}}\end{aligned} \tag{3.3.8}$$

where $\mathbf{d}\left(\mathbf{E}\left(\mathbf{B}\right)\right)$ *is the vector of diagonal elements*[7] *of the MSE matrix* $\mathbf{E}(\mathbf{B}) = \left(\mathbf{I}+\mathbf{B}^H\mathbf{R}_\mathbf{H}\mathbf{B}\right)^{-1}$, *the matrix* $\mathbf{B}\in\mathbb{C}^{q\times q}$ *is the optimization variable,* $\mathbf{R}_\mathbf{H}\in\mathbb{C}^{q\times q}$ *is a positive semidefinite Hermitian matrix, and* $f_0:\mathbb{R}^q\longrightarrow\mathbb{R}$ *is an arbitrary objective function (increasing in each variable). It then follows that there is an optimal solution* $\mathbf{B}$ *of at most rank* $p\triangleq\min(q,\text{rank}(\mathbf{R}_\mathbf{H}))$ *with the following structure*

- *if* f_0 *is Schur-concave, then*

  $$\mathbf{B}=\mathbf{U}_\mathbf{H}\mathbf{\Sigma}_\mathbf{B} \tag{3.3.9}$$

  where $\mathbf{U}_\mathbf{H}\in\mathbb{C}^{q\times p}$ *has as columns the eigenvectors of* $\mathbf{R}_\mathbf{H}$ *corresponding to the* p *largest eigenvalues in increasing order, and* $\mathbf{\Sigma}_\mathbf{B}=[\mathbf{0}\ \ \text{diag}(\{\delta_\mu\})]\in\mathbb{C}^{p\times q}$ *has zero elements, except along the rightmost main diagonal (which can be assumed real w.l.o.g.).*

- *if* f_0 *is Schur-convex, then*

  $$\mathbf{B}=\mathbf{U}_\mathbf{H}\mathbf{\Sigma}_\mathbf{B}{\mathbf{V}_\mathbf{B}}^H \tag{3.3.10}$$

  where $\mathbf{U}_\mathbf{H}$ *and* $\mathbf{\Sigma}_\mathbf{B}$ *are defined as before, and* $\mathbf{V}_\mathbf{B}\in\mathbb{C}^{q\times q}$ *is a unitary matrix such that* $\left(\mathbf{I}+\mathbf{B}^H\mathbf{R}_\mathbf{H}\mathbf{B}\right)^{-1}$ *has identical diagonal elements. This rotation can be computed using the algorithm given in [62] or with any rotation matrix* $\mathbf{Q}$ *that satisfies* $\left|\{\mathbf{Q}\}_{i,k}\right| = \left|\{\mathbf{Q}\}_{i,l}\right|, \forall i,k,l$ *such as the discrete Fourier transform (DFT) matrix or the Hadamard matrix.*

[6] $(\mathbf{A}+\mathbf{BCD})^{-1}=\mathbf{A}^{-1}-\mathbf{A}^{-1}\mathbf{B}\left(\mathbf{D}\mathbf{A}^{-1}\mathbf{B}+\mathbf{C}^{-1}\right)^{-1}\mathbf{D}\mathbf{A}^{-1}$

[7] The diagonal elements of $\mathbf{E}\left(\mathbf{B}\right)$ are assumed in decreasing order without loss of generality (w.l.o.g.).

P_{TOT} is the power in units of energy per frame and $P_{\mathrm{TOT}} = P \cdot q = q$.

For Schur-concave objective functions (as the mutual information), the global communication process including pre- and post-processing $\mathbf{A}^H\mathbf{HB}$ is fully diagonalized as well as the MSE matrix. Among the atoms, only p are associated to nonzero channel eigenvalues, whereas the remainder are associated with zero eigenvalues. But in our case p is always equal to q because of the diagonal structure of the matrices $\mathbf{H}$ and $\mathbf{N}_C$ (they are always full rank matrices) and all the eigenvalues are nonzero.

So the global communication process is[8]

$$\mathbf{z} = \left(\mathbf{I} + \mathbf{\Sigma}_\mathbf{B}^H \mathbf{D}_\mathbf{H} \mathbf{\Sigma}_\mathbf{B}\right)^{-1} \mathbf{\Sigma}_\mathbf{B}^H \mathbf{D}_\mathbf{H}^{1/2} \left(\mathbf{D}_\mathbf{H}^{1/2} \mathbf{\Sigma}_\mathbf{B} \mathbf{c} + \overline{\mathbf{w}}\right) \tag{3.3.11}$$

where $\mathbf{D_H} = \mathrm{diag}(\lambda_{\mathbf{H},\mu})$, $\lambda_{\mathbf{H},\mu}$ are the eigenvalues of $\mathbf{R_H}$ in increasing order and $\overline{\mathbf{w}}$ is the normalized equivalent noise. The eigenvalues and the eigenvector can be calculated from $\mathbf{R_H}$ with one of the many numerical techniques discussed in literature.

Now it is left to determine the set $\{\delta_\mu\}$. In order to do that we have to choose the mutual information function as objective function f_0. With the introduction of $\mathbf{B}$ and $\mathbf{A}$ the mutual information of the system (3.2.6) becomes (see Figure 3.15)

$$c = \max_{\mathbf{B}} I_M = \log_2 \left(\left| \mathbf{I} + \mathbf{H}_{TOT} \mathbf{N'}_C^{-1} \mathbf{H}_{TOT}^H \right| \right) \qquad \text{[bits]} \tag{3.3.12}$$

where $\mathbf{N'}_C = \mathbf{A}\mathbf{N}_C\mathbf{A}^H$ is the covariance matrix of the colored noise $\mathbf{w'}$ resulting from the filtering made by the equalizer on noise vector $\mathbf{w}$. (3.3.12) can be rewritten as [59], [14]

$$c = \max_{\mathbf{R}_s} I_M = \log_2 \left(\left| \mathbf{I} + \mathbf{N}_C^{-1} \mathbf{H} \mathbf{R}_s \mathbf{H}^H \right| \right) \qquad \text{[bits]} \tag{3.3.13}$$

where $\mathbf{R}_s$ is the the transmit covariance matrix. Using the fact that $\mathbf{R}_s = \mathbf{B}\mathbf{B}^H$ (remember that $\mathbf{s} = \mathbf{B}\mathbf{c}$) and that $|\mathbf{I} + \mathbf{X}\mathbf{Y}| = |\mathbf{I} + \mathbf{Y}\mathbf{X}|$, the mutual information can be expressed (see [61] for detailed connections between the mutual information and the MSE matrix) as

$$\max_{\mathbf{R}_s} I_M = -\log_2 \left(|\mathbf{E}| \right) \tag{3.3.14}$$

and therefore, the maximization of I_M is equivalent to the minimization of $|\mathbf{E}|$. The minimization of the determinant of the MSE matrix was considered in [63]. Using the fact that[9] $\mathbf{X} \geq \mathbf{Y} \Rightarrow |\mathbf{X}| \geq |\mathbf{Y}|$, it follows that $|\mathbf{E}|$ is minimized for the choice of the receive matrix

[8] Note that $\mathbf{A} = \left(\mathbf{H}\mathbf{B}\mathbf{B}^H\mathbf{H}^H + \mathbf{N}_C\right)^{-1}\mathbf{H}\mathbf{B} = \mathbf{N}_C^{-1}\mathbf{H}\mathbf{B}\left(\mathbf{I} + \mathbf{B}^H\mathbf{H}^H\mathbf{N}_C^{-1}\mathbf{H}\mathbf{B}\right)^{-1}$

[9] By $\mathbf{A} \geq \mathbf{B}$, we mean that $\mathbf{A} - \mathbf{B}$ is positive semidefinite.

given by (3.3.6). From (3.3.7), it is clear that $|\mathbf{E}|$ does not change if the transmit matrix $\mathbf{B}$ is post-multiplied by a unitary matrix (a rotation). Therefore, we can always choose a rotation matrix so that $\mathbf{E}$ is diagonal without loss of optimality (as we already knew from [63]), and then

$$|\mathbf{E}| = \prod_k \{\mathbf{E}\}_{j,j} \tag{3.3.15}$$

Therefore, the minimization of $|\mathbf{E}|$ is equivalent to the minimization of the product of the MSE. This problem has a water-filling solution (from the Karush-Kuhn-Tucker (KKT) optimality conditions). Hence, the minimization of the product of the MSE, the minimization of the determinant of the MSE matrix and the maximization of the mutual information are all equivalent criteria with the same solution given by a channel-diagonalizing structure and the classical capacity-achieving water-filling solution for the power allocation[10] [59], i.e.

$$\delta_\mu^2 = \left(K - \lambda_{\mathbf{H},\mu}^{-1}\right)^+ \tag{3.3.16}$$

where K is the water-level chosen to satisfy the power constraint with equality. The term *"water-filling"* (or, equivalently, *water-pouring*) seems to have been coined by Fano [64]. Its interpretation is straightforward, in fact, looking at Figure 3.16, the PSD of the noise represents the profile of the base of a 2D vessel, and the total average power of the transmitted signal plays the role of the water which is poured into that shaped vessel, up to reach the level K.

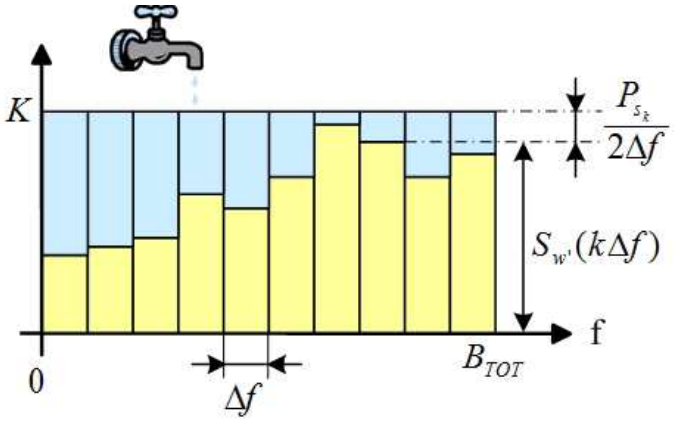

Figure 3.16: Water-filling

[10] The notation $(x)^+$ represents $\max(0, x)$

Following this criterion, in order to get the maximum input-output mutual information from a system composed of q parallel Gaussian channels, we should allocate on each subchannel an amount of power, such that, the received signal be frequency-flat, with PSD equal to K.

It is clear that the channels wherein the noise level is low will be allocated a bigger amount of power than those more noisy. And it is also possible that, sometimes because of the scarce transmission power, the water level K be lower than the PSD of the noise of some subchannels, as shown in Figure 3.17. In this situation, no power will be allocated on such subchannels and subsequently they will not be used for the transmission.

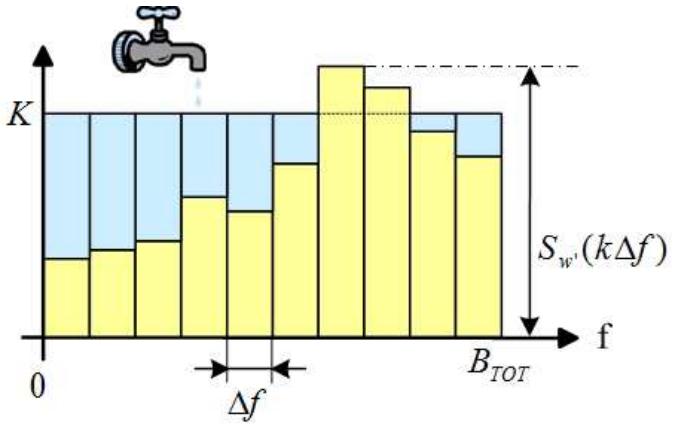

Figure 3.17: Water-filling - bad channel.

Once the power is allocated following the water-filling policy, the capacity would be achieved by transmitting on the active atoms while no bits will be transmitted on the subchannels with no power allocated.

In Table 3.1 the procedure to diagonalize the filterbank-based system is summed up. It is important to highlight that is necessary the knowledge of the channel state information (CSI) at both ends of the link, i.e. both at the transmitter and at the receiver.

The global matrices $\mathbf{H}_{TOT}$ after the diagonalization with (3.18(b)) and without (3.18(a)) the water-filling process are showed in Figure 3.18. In the latter case we must set $\mathbf{\Sigma_B} = \mathbf{I}$. The diagonalization is anyway guaranteed but not the mutual information maximization. In both cases the starting channel matrix is illustrated in Figure 3.4. Comparing the two matrices we can see how the water-filling turn off the last atoms, i.e. those suffering the strongest noise due to deepest notch in the frequency response of the channel realization (the eigenvalue decrease sorting puts the worst atoms at the end of the diagonal of the matrix).

The channel capacity curves are depicted in Figure 3.19. These curves have been obtained from the diagonalized system with 16 subcarriers shaped with a gaussian pulse and using the

DIAGONALIZATION

Input: $g[k]$, $\gamma[k]$, h_l
Output: $\mathbf{A}$, $\mathbf{B}$

1. **Calculate** the equivalent channel model $\mathbf{H}$;
2. **Calculate** the covariance matrix $\mathbf{N}_C$ of the colored noise;
3. **Find** the eigenvalues $\{\lambda_{\mathbf{H},\mu}\}$ and the eigenvectors of the matrix $\mathbf{H}\mathbf{N}_C^{-1}\mathbf{H}^H$;
4. **Sort** eigenvalues in decreasing order and the eigenvector consistently (in matrix $\mathbf{U_H}$);
5. **Evaluate** the water-level K according to power constraint;
6. **Calculate** the power $\left\{\delta_\mu^2\right\}$ according to the water-filling criterion;
7. **Make** the matrix $\mathbf{\Sigma_B} = \mathrm{diag}\left(\{\delta_\mu\}\right)$;
8. **Calculate** the precoder matrix as $\mathbf{B} = \mathbf{U_H}\mathbf{\Sigma_B}$;
9. **Calculate** the optimum LMMSE equalizer as $\mathbf{A} = \left(\mathbf{H}\mathbf{B}\mathbf{B}^H\mathbf{H}^H + \mathbf{N}_C\right)^{-1}\mathbf{H}\mathbf{B}$;

Table 3.1: Capacity-achieving procedure for filterbank systems

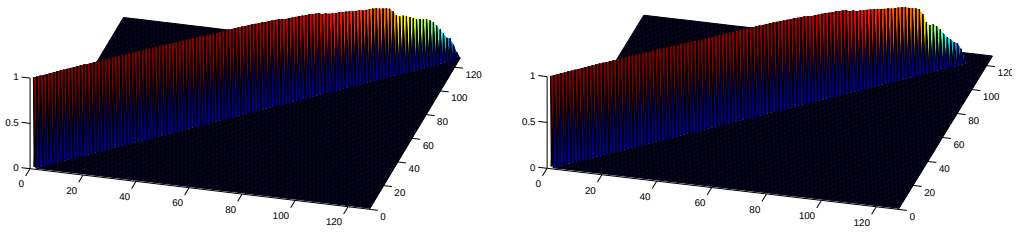

(a) (b)

Figure 3.18: Matrices $\mathbf{H}_{TOT}$ after the diagonalization with (b) and without (a) the water-filling process

water-filling power allocation solution as described in this section. The capacity curves can be compared with the relative mutual information curves before the diagonalization of the NOFDM system (dashed lines).

As we can see, the mutual information evaluated with the diagonalization and the water-filling increases compared to the case without diagonalization. At high signal-to-noise ratio the mutual information curves approach the relative capacity curves. It can be notice that even for the capacity, the relationship among the curves relative to different β values and the OFDM system are similar to the ones relative to the mutual information evaluated without the diagonalization, i.e. until $\beta < \frac{M+L_{cp}}{M}$ the filterbank capacity overtakes the OFDM capacity.

The channel capacity curves for a GMC system with RRC pulse are showed in Figure 3.20. The previous remarks are valid for the RRC pulse too. It can be notice that the capacity of a GMC system with $\beta = 1.25$ and the capacity of an OFDM system are almost the same because in this case $\beta = 1.25 = 1 + \alpha$ and hence there is no overlapping among the subcarriers. Hence the orthogonality constraint is satisfied even for the GMC system and the capacities achieved by the two systems are identical.

As said before, it is possible to use a zero-forcing equalizer instead of a MMSE one. In this case, we lose the MSE optimality but we can contrast the interference in a better manner. The disadvantage of this technique is obviously the strong amplification of the noise that every ZF equalizer suffers. Moreover the water-filling process cannot be used in order to obtain the channel diagonalization. Thus the equalizer matrix becomes

$$\mathbf{A}^{(ZF)} = \left(\mathbf{H}\mathbf{B}\mathbf{B}^H\mathbf{H}^H\right)^{-1}\mathbf{H}\mathbf{B} \tag{3.3.17}$$

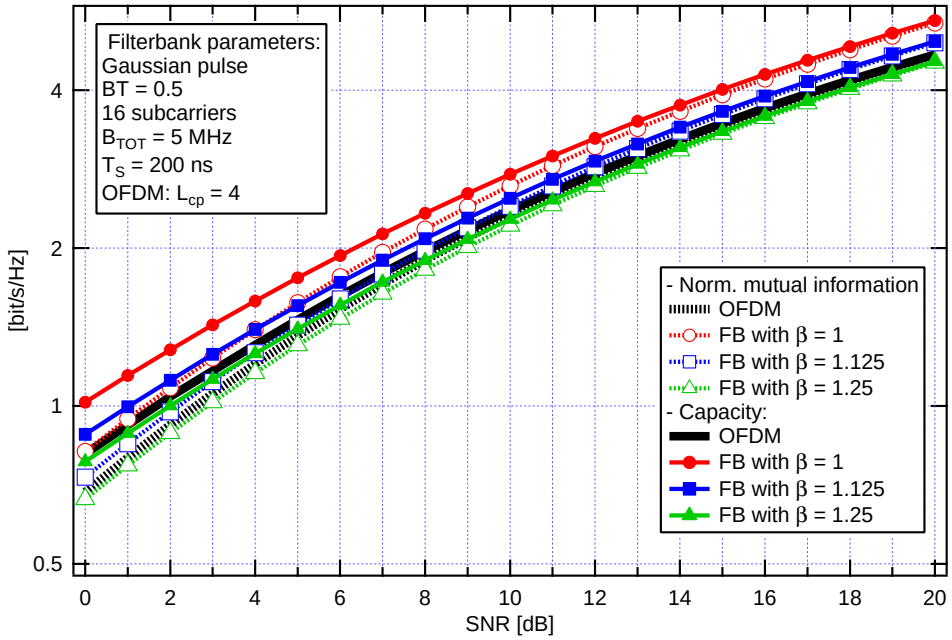

Figure 3.19: Capacity and normalized mutual information curves for different β values with gaussian pulse

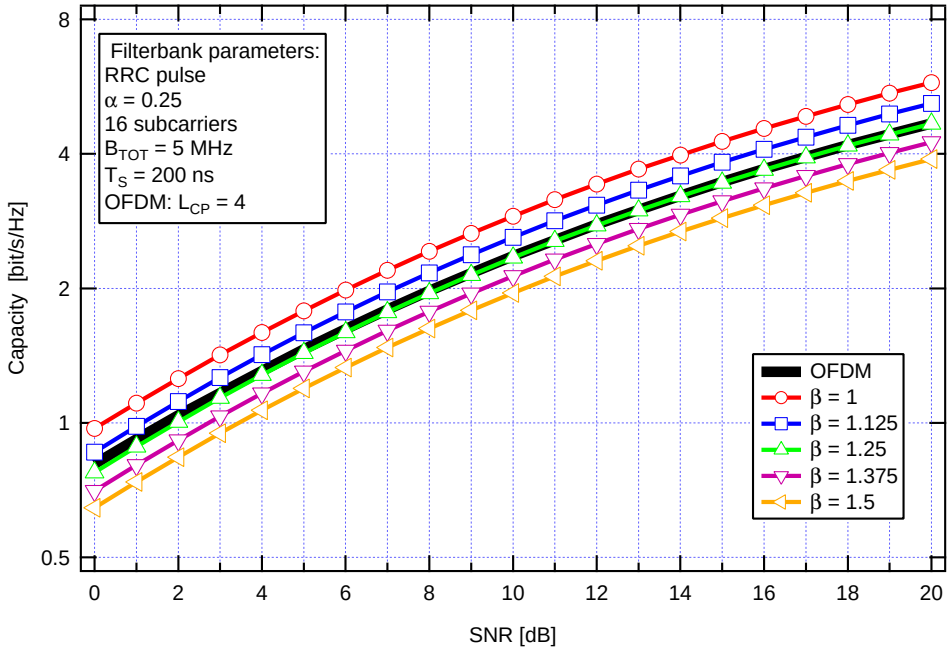

Figure 3.20: Capacity curves for different β values with RRC pulse

In this case the matrix resulting from diagonalization of the matrix illustrated in Figure 3.4, is shown in Figure 3.21. The perfect compensation of the interference is clear, in fact using (3.3.17) we obtain

$$\mathbf{H}_{TOT}^{(ZF)} = \mathbf{A}^{(ZF)^H}\mathbf{HB} = \mathbf{I} \tag{3.3.18}$$

Thus the symbols returned by the equalizer are

$$\mathbf{z} = \mathbf{H}_{TOT}^{(ZF)}\mathbf{c} + \mathbf{A}^{(ZF)^H}\mathbf{w} = \mathbf{c} + \mathbf{w}' \tag{3.3.19}$$

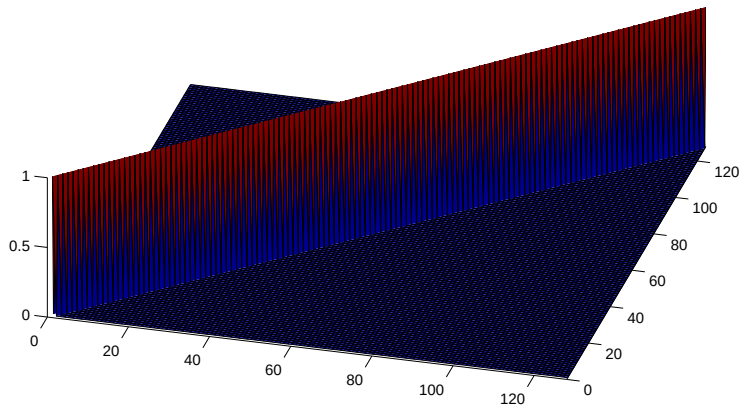

Figure 3.21: Global system matrix $\mathbf{H}_{TOT}$ with zero-forcing equalization

We can make some different approximations in order to simplify the signals processing, in particular the equalization. First of all we can use only the diagonal elements of the matrix $\mathbf{H}$. So the matrix $\mathbf{A}$ becomes diagonal and we can consider only its diagonal as a vector $\mathbf{a}$

$$\mathrm{diag}(\mathbf{A}^{(diag)}) = \mathbf{a}^{(diag)} \tag{3.3.20}$$

and the μth element of $\mathbf{a}^{(diag)}$ is given by

$$\left\{\mathbf{a}^{(diag)}\right\}_{\mu} = \frac{\mathbf{H}_{\mu,\mu}}{|\mathbf{H}_{\mu,\mu}|^2 + \sigma^2} \tag{3.3.21}$$

This is the canonical single-tap equalization technique used by the OFDM systems. It is clear that this equalizer does not take in count the interference generated by the frequency-selective channel. Hence we can approximate the interference as an additive gaussian noise with variance σ_I^2. As mentioned previously the interference affecting the μth symbol is given by the whole μth row of equivalent matrix $\mathbf{H}$. So the interference power on the μth symbol (that is the μth element of equalizer vector) can be calculated as

$$\sigma_I^2 = \sum_{\substack{\mu'=0 \\ \mu' \neq \mu}}^{q} \left|\mathbf{H}_{\mu,\mu'}\right|^2 \tag{3.3.22}$$

The equivalent interference noise is independent from the thermal noise affecting the system, so the variance of the global disturb is $\sigma_I^2 + \sigma^2$. Thus the new equalizer is given by

$$\left\{\mathbf{a}^{(int)}\right\}_\mu = \frac{\mathbf{H}_{\mu,\mu}}{\left|\mathbf{H}_{\mu,\mu}\right|^2 + \sigma^2 + \sigma_I^2} \tag{3.3.23}$$

With these two approximation the receiver can avoid the calculation of the entire matrix $\mathbf{H}$ because its main diagonal is just the frequency response of the channel repeated $\frac{L}{N}$ times, i.e. the number of GMC symbols in the frame, as previously said. The MSE curves obtained for the different approximations discussed are depicted in Figure 3.22. Moreover are shown the MSE curve obtained with the optimum equalizer $\mathbf{A}^{\text{opt}}$ (blue curve) and two different MSE curves gotten without the diagonalization, i.e. without employing any precoding at the transmitter. These two curves are calculated the first assuming the perfect knowledge of CSI (red curve) and the other with an estimation of the channel through a preamble made by the first GMC symbol of every transmitted frame (orange curve).

As we can see, the worst performance are obtained with the CSI estimated without diagonalization because the symbol used as preamble is affected by interference which make difficult the recover of the channel impulse response. The approximations made with the diagonalization give similar results except at high E_b/N_0 values, where the noise is weaker and the interference approximation as additive noise gives better results. The best performance are obviously given by the optimum equalizer. We pay this improvement with an high system complexity caused by the calculation of an high number of matrices, each one composed by $(M \cdot N_{GMC})^2$ complex numbers.

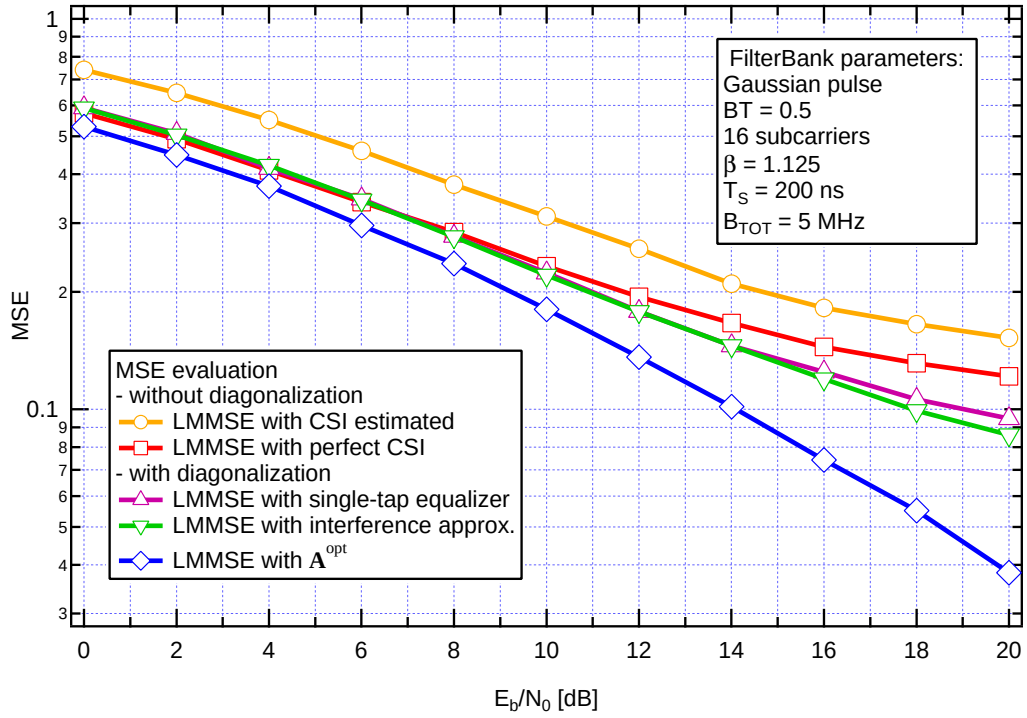

Figure 3.22: MSE evaluation with different approximations

Chapter 4

Performances on gaussian channels

In this chapter, we will present the results obtained from the simulations. We will assume to work with a fixed number of subcarriers M and with fixed overall bandwidth B_{TOT}, i.e. assuming the same sampling interval T_s. We will observe the behavior of the system for different values of the overlapping factor β. Hence the data-rate R_b will change with β because the GMC symbol interval changes with β. In fact the data-rate can be expressed as the ratio between the number of bits carried by a GMC symbol and the duration of the GMC symbol in sec, i.e.

$$R_b = \frac{M \ \log_2 M_{QAM}}{T} = \frac{M \ \log_2 M_{QAM}}{T_s \ M \ \beta} = \frac{\log_2 M_{QAM}}{T_s \ \beta} \qquad \left[\frac{\text{bit}}{\text{s}}\right] \tag{4.0.1}$$

where $T = 50$ ns is the duration of a GMC symbol and $M_{QAM} = 2^m$ is the order of the QAM modulation and it usually is a power of 2. In this chapter we will show performances for a 4-QAM modulation. The performances will be analyzed for GMC systems employing the three different pulses previously discussed in Section 2.6. We will first discuss the results for a white noisy Gaussian channel and then for a frequency-selective channel caused by the multipath plus Gaussian noise.

4.1 AWGN channel

4.1.1 Model description

With reference to the block diagram depicted in Figure 4.1, N_b independent information bits $\{b_j\}$ are Gray mapped onto $N_{QAM} = N_b/M_{QAM}$ QAM symbols $\{c_k\}$, where $M_{QAM} = 2^m$ is the order of the QAM modulation and it usually is a power of 2. Then they are transmitted through N_{GMC} consecutive GMC symbols which form a GMC frame (or block) after that

they have been modulated by transmitter filterbank onto M subcarriers. Each GMC symbols is made up by N samples for every block of M QAM symbols as known.

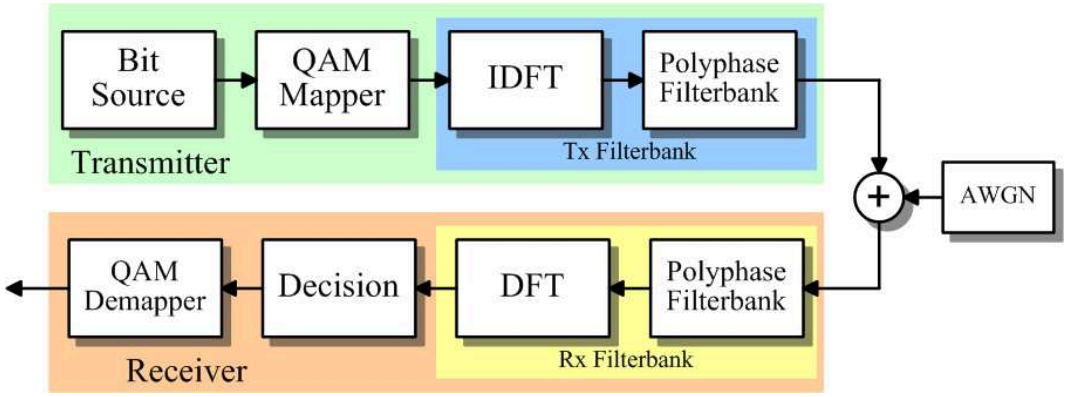

Figure 4.1: Complete FB-based system model with AWGN channel

At the receiver, the signal received $x[k]$ is given by the signal transmitted $s[k]$ plus white noise (AWGN) $w[k]$ with zero-mean and variance σ^2. The variance is calculated as a function of the SNR (Signal-to-Noise Ratio) E_b/N_0 where $E_b = E_s/M_{QAM} = 1/M_{QAM}$ is the energy per bit[1] and E_s is the energy per symbol. Thus

$$\sigma^2 = \frac{P \cdot \beta}{\log_2 M_{QAM} \cdot E_b/N_0} \tag{4.1.1}$$

where P represents the amount of power allocated on each atom in case of uniform distribution. In this chapter we assume $P = 1$. It can be notice that the noise power increases with the overlapping factor β because the duration of the GMC symbols increases and hence every GMC symbol contains more samples affected by the noise. The receiver demodulates the signal $x[k]$ through the receiver filterbank. Then, the soft-demodulated metrics are hard-decoded by a classic QAM threshold decisor in order to obtain the estimated QAM symbols $\{\hat{c}_k\}$. Finally, the ML estimation of the information bits, $\{\hat{b}_j\}$, are obtained from the QAM symbols by the QAM demapper.

4.1.2 Performances

In Figure 4.5, the BER is evaluated for a filterbank system employing a RRC pulse with roll-off factor $\alpha = 0.25$ and $M = 64$ subcarriers. The BER curves have been obtained for different values of the overlapping factor β. The theoretical AWGN performance of a single carrier 4-QAM system is depicted for comparison.

[1] $E_s = 1$ because the considered prototype pulses are all normalized and with unit energy.

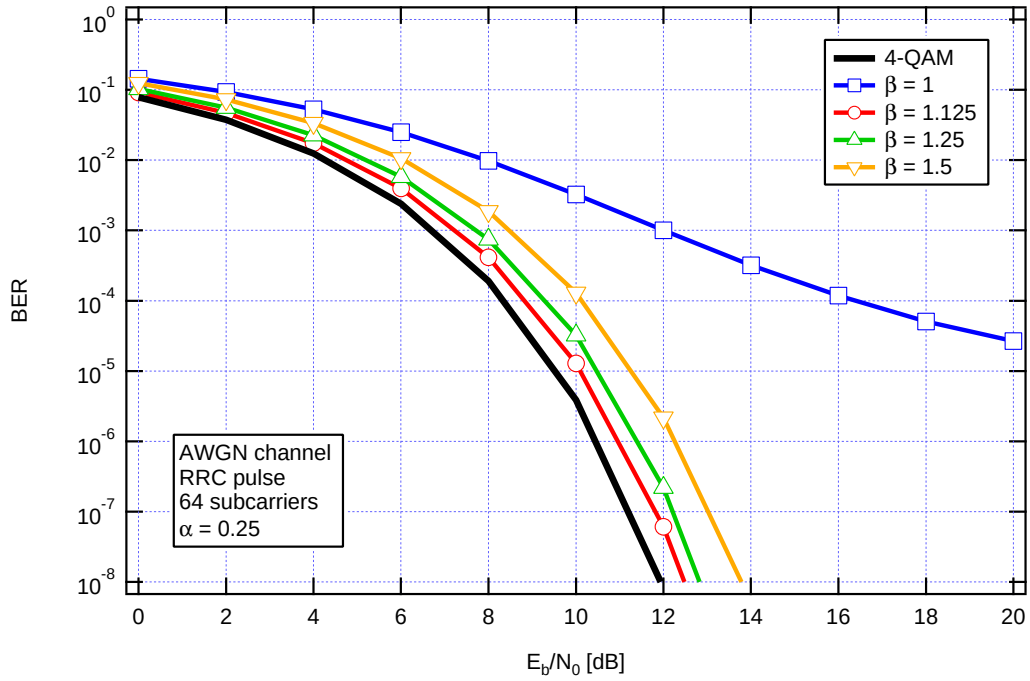

Figure 4.2: BER curves with RRC pulses for different β values

It can be notice the poor performances of the critical sampling $\beta = 1$ caused by the presence of the spikes in the normalized dual prototype window. These spikes decrease significantly the signal-to-noise ratio worsening the performances because they increase significantly the energy of the not-normalized dual pulses. As stated in Chapter 2.5.1 the normalization of the analysis pulse at the receiver will entail an attenuation of the demodulated signal and consequently a decrease of the signal-to-noise ratio because the noise does not experience this attenuation. When β is chosen greater than 1, then the spikes disappear and the BER curves improve approaching (but not reaching) the theoretical performance given by the single carrier system. When the β grows, the performances worsen because of the noise power σ^2 increases with β according to Formula (4.1.1).

The BER curves in Figure 4.3 have been obtained with a RRC pulse for different values of the roll-off factor α. The other parameters of the filterbank system are $M = 64$ subcarriers, overlapping factor $\beta = 1.125$ and $N_f^{(Tx)} = 16$. The theoretical AWGN performance of a single carrier 4-QAM system is depicted for comparison.

It can be notice that the BER curves are poorly influenced by the changing of the roll-off factor. As said in Section 2.6.1, the SNR decreases as the roll-off factor grows because the energy of the not-normalized dual pulse increases. But this increase of the energy is in the order of $10^{-3} \div 10^{-4}$ and hence the BER curves are poorly affected by the worsening of the

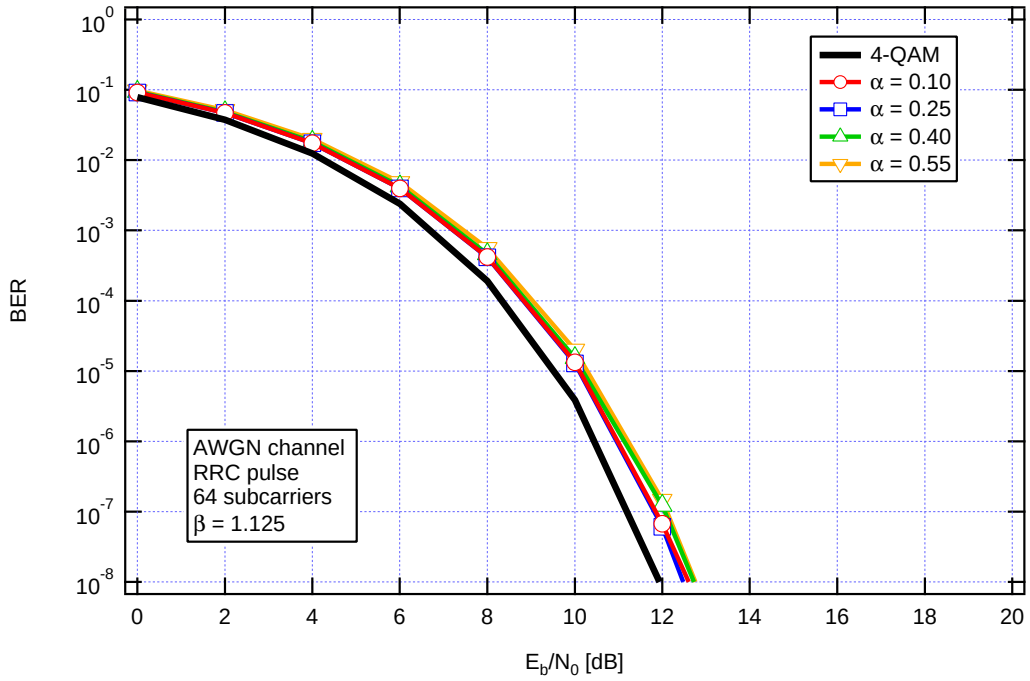

Figure 4.3: BER curves with RRC pulses with different α values

signal-to-noise ratio.

Now, we will discuss the performances of a filterbank-based system employing a Gaussian prototype pulse. The performances obtained for $\beta = 1.125$ and different BT values are depicted in Figure 4.4.

It can be notice how much the choice of the BT influences the performances of the systems. In fact the BT value determines the amount of the interference affecting the atoms on the TF grid. The ICI is dominating when the BT is high while the ISI replaces the ICI when the BT is low. As stated in Section 2.6.2, the energy of the biorthogonal pulse increases with respect to the amount of the interference in order to contrast it. Thus even the noise power grows with respect to the amount of the interference worsening the performances. In fact the worst results are obtained for high and low BT values. The best performances are obtained when the BT is chosen about $0.3 \div 0.5$ according to Figure 2.31.

The BER curves obtained for two BT values (0.35 and 0.50) at different β values are depicted in Figure 4.5.

It can be notice that with the critical sampling the performances are very poor because when $\beta = 1$, the not normalized dual pulse has a very large energy and the decrease of the SNR due by the pulse normalization is very strong. Moreover when $BT = 0.35$ a performance floor appears because the synthesis and analysis pulses are too short and they are not able

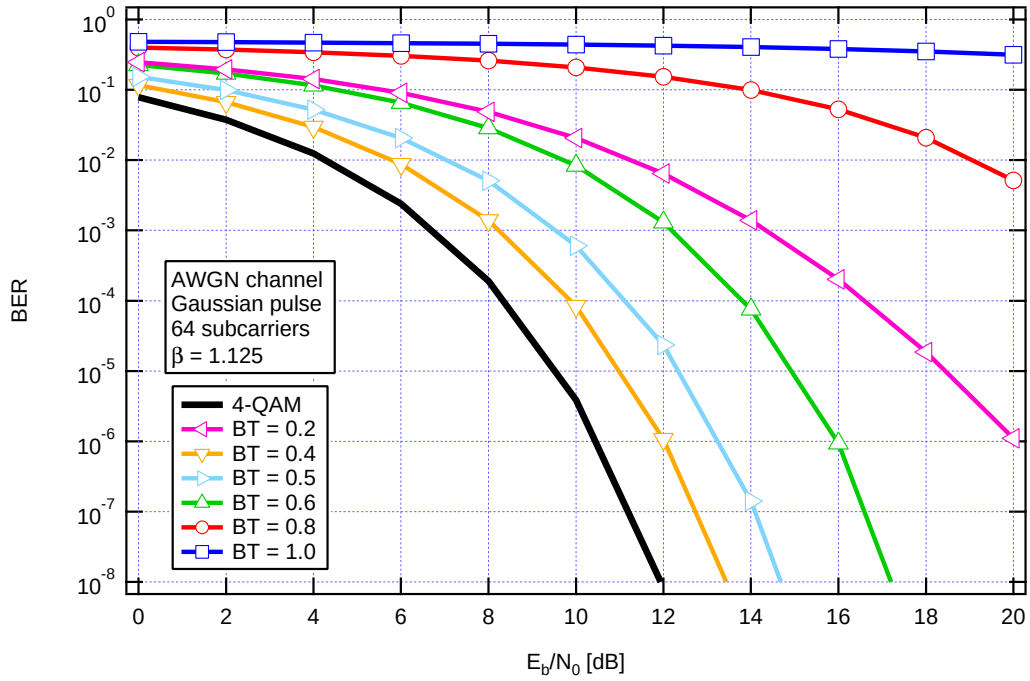

Figure 4.4: BER curves with Gaussian pulses with different BT values

to compensate all the interferences.

In other cases we can observe how the performances depend on the joint choice of the β and the BT. In fact for $BT = 0.35$ the best performance is obtained when $\beta = 1.125$ while for $BT = 0.50$ we can obtain the best performance when $\beta = 1.25$. When we choose $BT = 0.50$ and $\beta = 1.125$ the performances worsen because the increase of the ICI is stronger than the decrease of the power noise caused by a β lower. It can be even notice that the performances given by $\beta = 1.125$ and $\beta = 1.25$ are almost identical when $BT = 0.35$. In this case the increase of noise power is almost fully absorbed by the decrease of the ICI caused by the less overlapping between the adjacent subcarriers.

Thus we can observe the importance of the investigation of a trade-off between the β and the BT, i.e. between the increase of the noise power (caused by high β values) and the amount of interference (given by the BT) in order to reach the best performances.

In Figure 4.6 the BER curves obtained with Hermite pulses are showed for different values of the overlapping factor β. The BT value of the Gaussian pulse employed in order to get the Hermite pulse is 0.35. The dashed lines have been achieved with the Hermite prototype pulse proposed by Kurt et Al. in [1], while the continuous lines have been obtained with the Hermite prototype pulse with the coefficients proposed by Haas et Al. in [2]. It can be notice that the latter pulse gives slightly better performances, especially when β value is

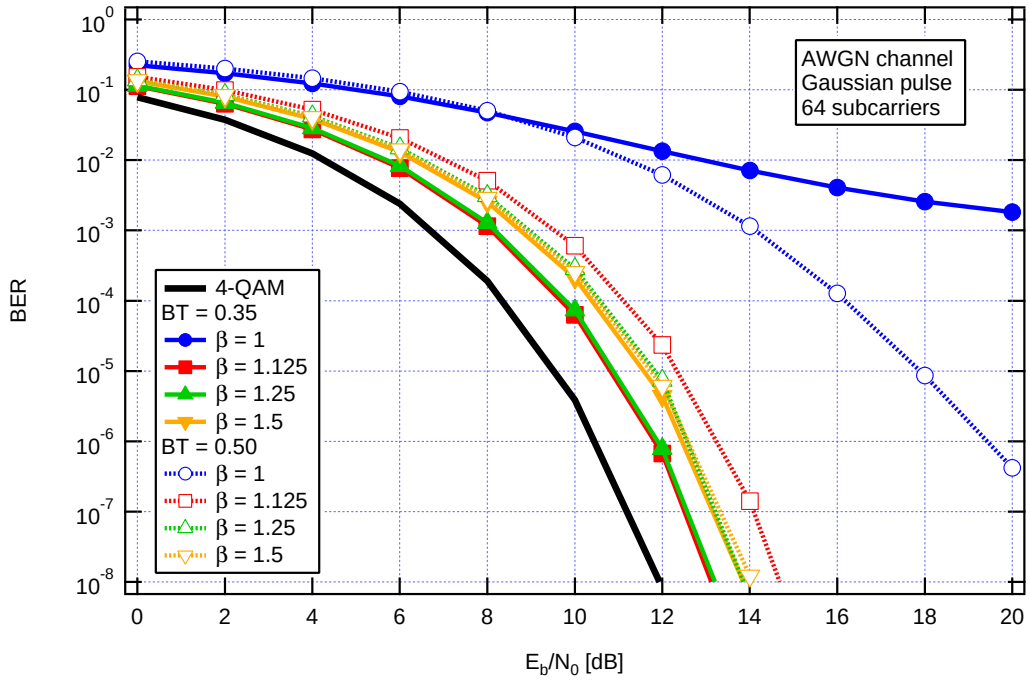

Figure 4.5: BER curves with Gaussian pulses for different β values

low. Moreover we can observe that the best performances are given when $\beta = 1.125$ like the performances obtained with the Gaussian pulse.

Finally we can observe a comparison of the performance obtained with the different pulses discussed up to now in Figure 4.7. In Figure 4.7(a) the overlapping factor is set to $\beta = 1.125$, in Figure 4.7(b) it is $\beta = 1.25$ and in Figure 4.7(c) it is $\beta = 1.5$. The critical sampling case is not discussed because of the too poor performances. The Hermite pulse used is given by the Haas coefficients [2] with $BT = 0.35$.

We can observe the best performances have been reached when the RRC prototype pulse is employed, while Hermite pulse gives better performances than the Gaussian one. As the overlapping factor β increases, the performances of the three pulses approach to be the same.

4.2 Fading channel

4.2.1 Model description

The model used to obtain the simulations is depicted in Figure 4.8. In this section the precoder, the multipath channel and the equalizer are introduced. Thus the whole frame is linearly precoded before it is modulated by the transmitter filterbank. Uniform bit and power

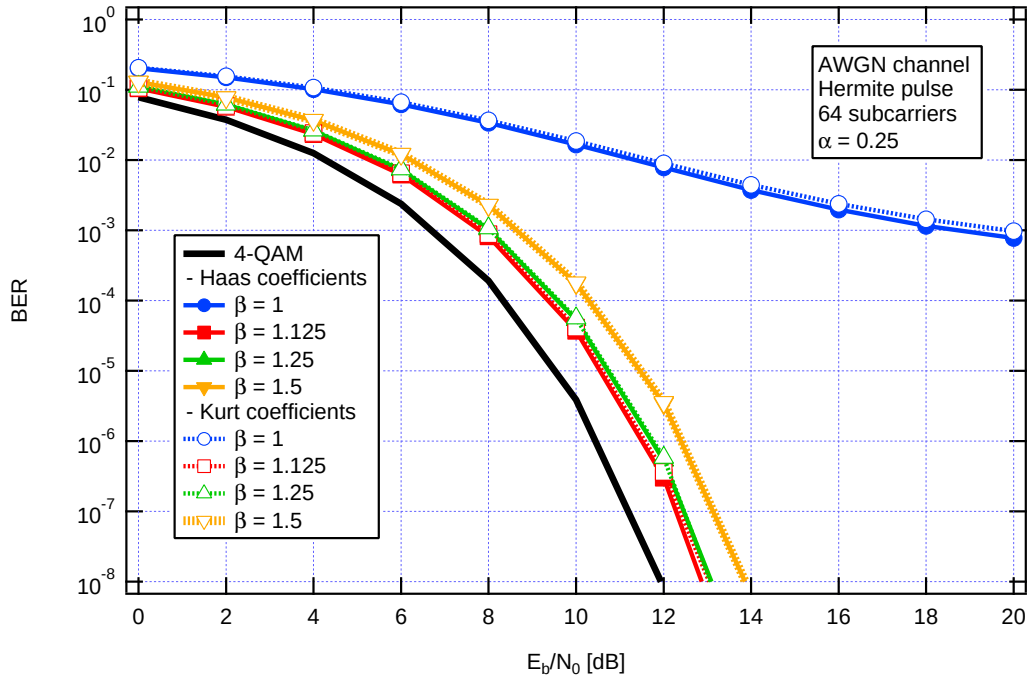

Figure 4.6: BER curves with Hermite pulses for different β values

allocation is assumed in this section, i.e. $\mathbf{\Sigma_B} = \mathbf{I}$.

The transmitted GMC signal experiences a frequency-selective fading channel which will be assumed stationary for whole frame duration, i.e. *blockfading* is considered [65], [66], [67], [68].

Path	Delay [ns]	Relative Power [dB]
1	0	-3.3
2	50	0
3	100	-0.99
4	200	-1.5
5	250	-3
6	600	-9.40

Table 4.1: Delays and power channel profiles values

Each multipath channel realization is modeled as a 6-taps independent Rayleigh RVs and it will be assumed stationary for the whole frame duration. The power and delay profiles

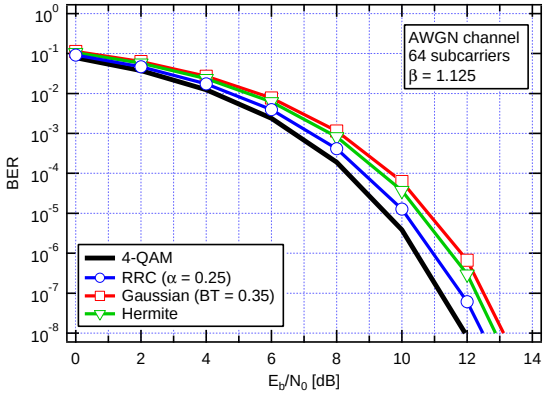

(a) $\beta = 1.125$

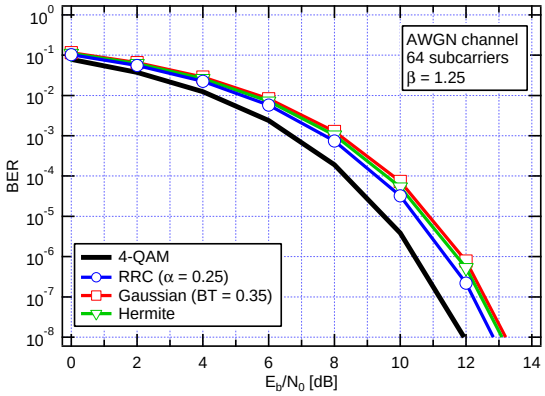

(b) $\beta = 1.25$

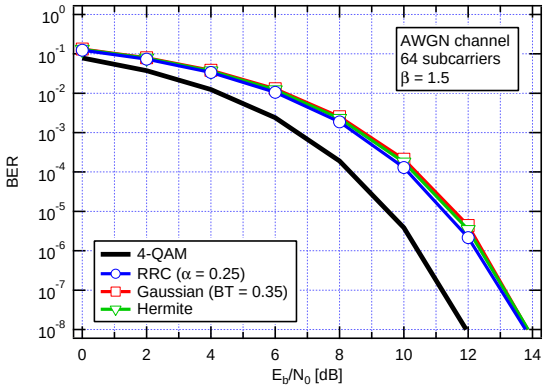

(c) $\beta = 1.5$

Figure 4.7: Performance comparison with different prototype pulses and different β values

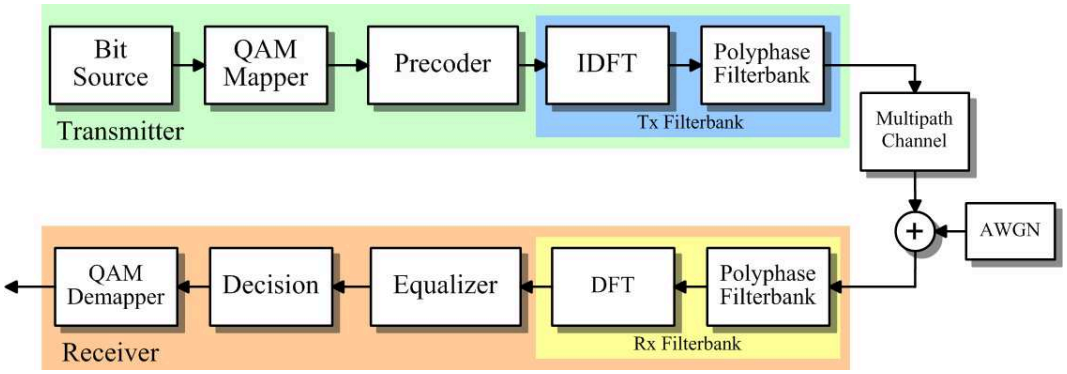

Figure 4.8: Block scheme for the filterbank communication system in presence of fading channel

are presented in Table 4.1 and depicted in Figure 4.9. The coherence bandwidth, i.e. the bandwidth where the frequency response can be assumed flat, defined as $B_C = 1/(10 \cdot \tau_{\max})$, is about $B_C = 166.7$ kHz.

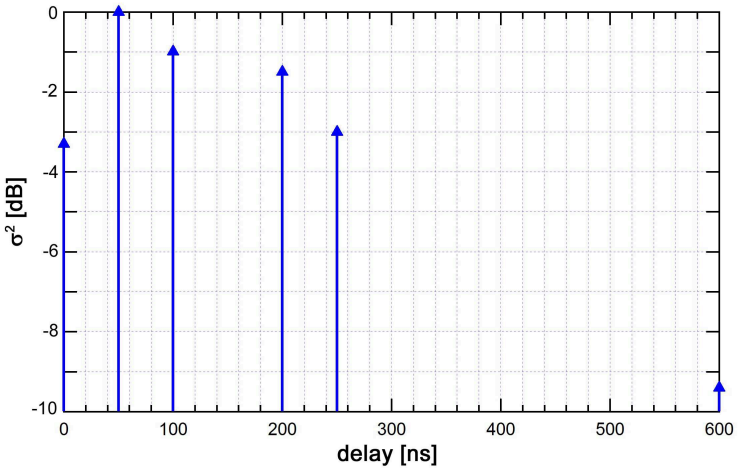

Figure 4.9: Channel profile used in simulations

Before the demodulation, the white Gaussian noise is added to the signal filtered by the frequency selective-channel. Thus the signal received is demodulated by the receiver filterbank and then post-processed by the equalizer.

4.2.2 Results

The BER curves depicted in Figure 4.10 are given by a filterbank-based system employing a RRC pulse and its dual as synthesis and analysis prototype pulse, respectively and they are evaluated with different values of the overlapping factor β. The other parameters of the filterbank system are $M = 64$ subcarriers, the roll-off factor $\alpha = 1.125$ and $N_f^{(Tx)} = 16$. The performance of a CP-OFDM system is shown as comparison (black line). The latter employs a cyclic prefix lasting $L_{cp} = 13$ samples in order to completely avoid the ISI generated by the frequency-selective channel. In the cases presented, the performances are poor because the system is uncoded.

It can be notice that the diagonalized NOFDM system give better performances than OFDM system when the signal-to-noise ratio is lower than 14 dB. The performances are almost the same for all the three β values employed. Moreover we can observe that with the diagonalization the performances with the critical sampling, i.e. $\beta = 1$ are no longer poor such as in the AWGN case and it can be take in count as a valid β value. This achievement holds true for all the pulses discussed so far.

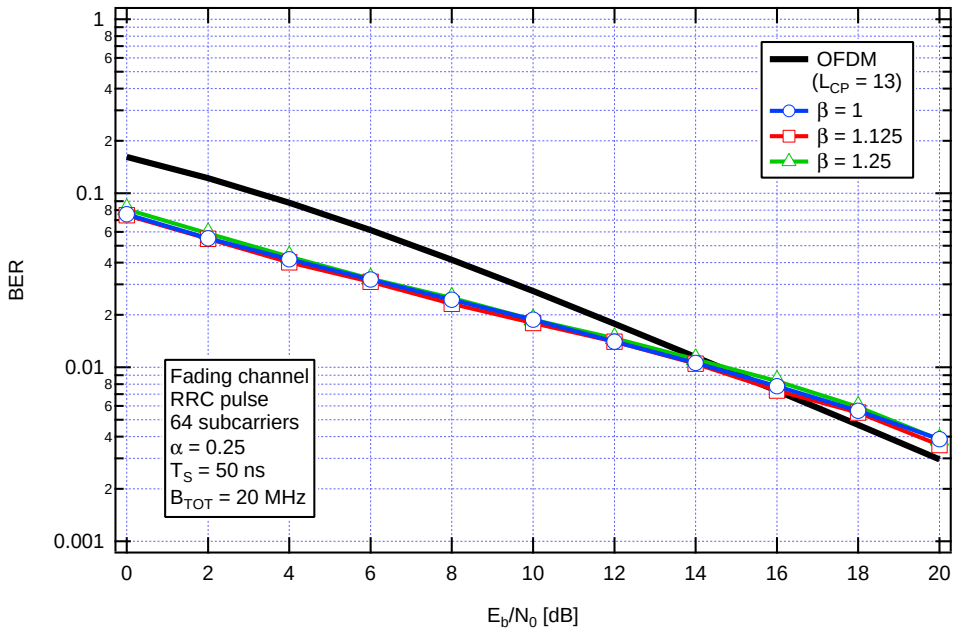

Figure 4.10: BER curves with RRC pulses for different β values

The BER curves obtained with a filterbank-based system employing a Gaussian pulse are depicted in Figure 4.11 for different BT values. As in the AWGN case the performance are strongly influenced by the BT chosen and the performances become poor when the BT is chosen too low or too high because of the decrease of the SNR.

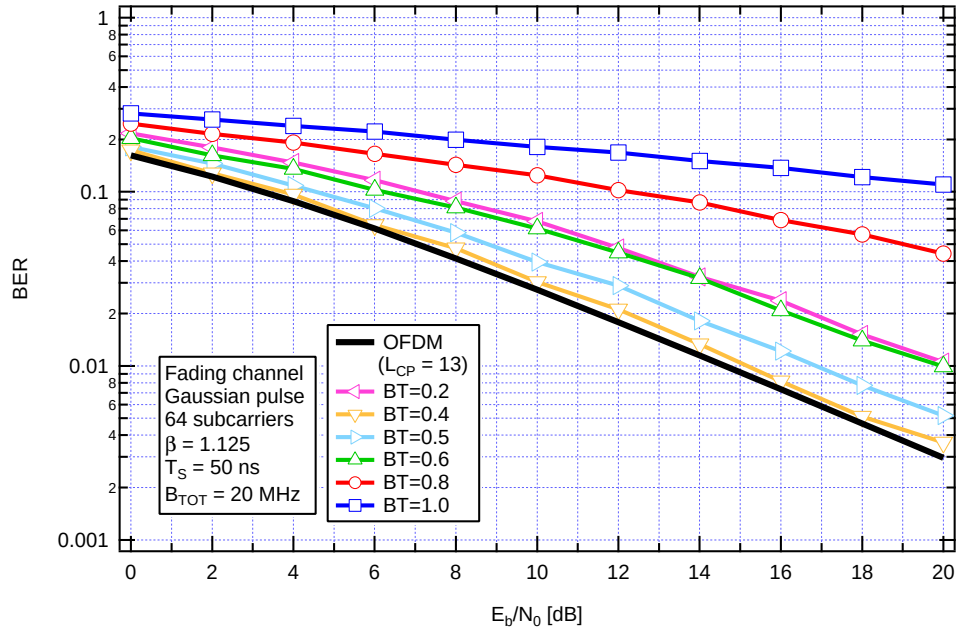

Figure 4.11: BER curves with Gaussian pulses for different BT values

The BER curves for different β values with the Gaussian pulse are showed in Figure 4.12. Unlike the RRC pulse, the performances with the Gaussian pulse do not reach the CP-OFDM performances. Obviously the optimum value of the overlapping factor β giving the best performances, depends on the value of the BT chosen. As previously stated, the critical sampling is no longer poor as in the AWGN case and the performances are satisfactory. Moreover this time the performances are more influenced by the value of the overlapping factor β chosen than the RRC pulse.

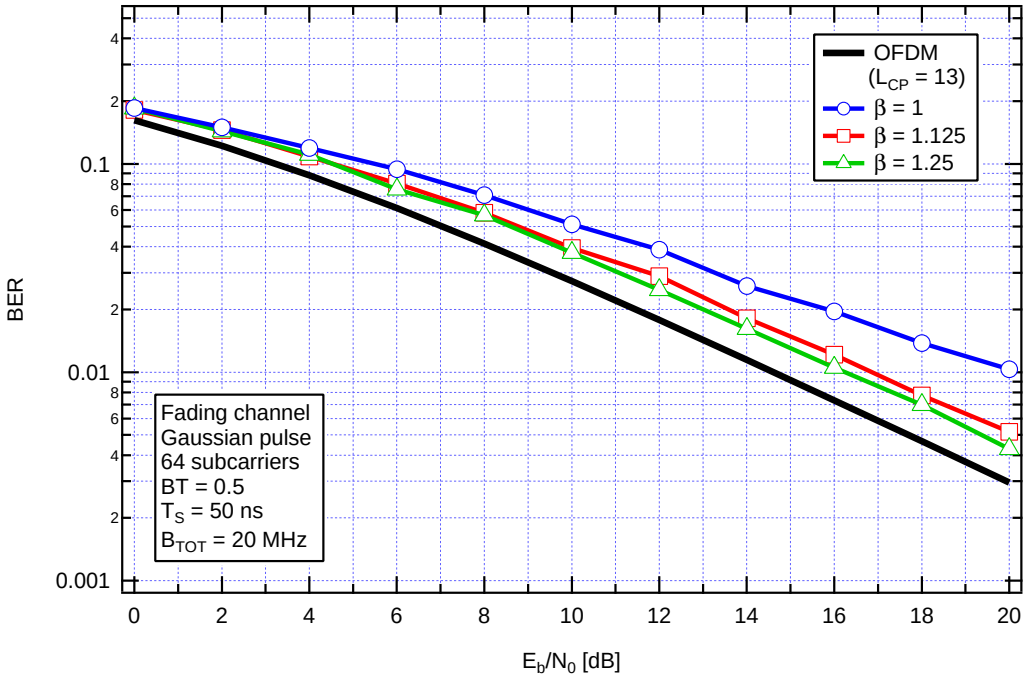

Figure 4.12: BER curves with Gaussian pulses for different β values

Chapter 5

Bit and power allocation strategies

In last years various techniques for wisely allocating *bits* and *powers* among a set of parallel frequency-flat channels have been studied. The way we will manage this process, which is called in general *bit loading*, is directed at the optimization of a certain objective function. This criterion was also used in IEEE 801.11a wireless LAN, to adaptively select the best physical layer mode, and it is meaningful in all the applications (like data file transmission) where in the end, all the bits must be received correctly.

However, in many power constrained communication systems, other optimization strategies are commonly used, for instance:

- the maximization of the bit rate under a bit error rate (BER) constraint;
- the minimization of the BER under a bit rate constraint;
- the maximization of the input-output mutual information.

These strategies are appropriate for applications like speech or video transmissions which do not require a null BER due to the user's limited sensitivity [69].

In this chapter we will review and analyze some solutions proposed in the literature for the bit loading problem and the implementation problems that arise when the theory is applied to actual communication systems like Asymmetric Digital Subscriber Line (ADSL) or in our filterbank-based multicarrier systems.

Then, in Sections 5.2 and 5.3, two greedy algorithms based on the water-filling policy, for allocating bits and power under different constraints are analyzed: the *Hughes-Hartogs algorithm* [70] and the *Campello algorithm* [71], [72]. About the last algorithm, there has been obtained the closed-form expression for some iterative formulas involved in the procedure.

5.1 The "SNR gap" concept

The water-filling solution found in Chapter 3 is the optimal solution to the problem of allocating a constrained average power among a set of parallel independent Gaussian channels in order to get the maximum of the input-output mutual information of the system. In Chapter 3, we evaluate the capacity of our filterbank-based system and it is given by

$$\begin{aligned} c &= \log_2\left(\left|\mathbf{I}+\mathbf{N}_C^{-1}\mathbf{H}\mathbf{B}\mathbf{B}^H\mathbf{H}^H\right|\right) \\ &= \sum_{\mu}\log_2\left(1+\mathrm{SNR}_\mu\right) \qquad\qquad [\text{bits}] \end{aligned} \tag{5.1.1}$$

where SNR_μ is the μth diagonal element of the matrix $\mathbf{N}_C^{-1}\mathbf{H}\mathbf{B}\mathbf{B}^H\mathbf{H}^H$ and it represents the signal-to-noise ratio experienced by the μth transmitted symbol. The matrix $\mathbf{B}=\mathbf{U_H}\mathbf{\Sigma_B}$ is the precoder introduced to diagonalize the system and maximize the mutual information. The matrix $\mathbf{\Sigma_B}$ is a diagonal matrix whose element on the diagonal $\{\delta_\mu\}$ are given by the water-filling solution (3.3.16). Hence $c_\mu=\log_2\left(1+\mathrm{SNR}_\mu\right)$ is the Shannon capacity of the μth stream. In our system we have $\mu=0,1,\ldots,q$ with $q=\frac{L}{N}M$ parallel subchannel and the average power allocated on the μth channel P is assumed unitary.

The water-filling solution is optimum from a mutual information standpoint, but it is actually a tough task to be realized in practice, because the (5.1.1) requires the input signal to be Gaussian, which can never be realized in practice. Rather, the inputs are usually drawn from discrete constellations (often with very limited peak-to-average ratios), which may significantly depart from the Gaussian idealization [64]. For specific coding schemes, or even in the absence of coding, the allocation of power (and bits) in order to maximize the throughput with discrete constellations at some target error probability is tackled with a heuristic strategy which consists of applying the water-filling policy, except with the gain of each channel reduced by a gap Γ that quantifies the deficit of the corresponding class of constellations (e.g., m-QAM) with respect to a Gaussian signal operating at the same rate [64].

Hence, the SNR gap takes into account the fact that, the Shannon capacity is the theoretic upper limit of achievable data rate, for a channel with BER that tends to zero. In practical analysis, the BER of a communication system can never be zero; instead, we expect an acceptable BER at some practical data rate [73]. The Shannon capacity formula including the SNR gap is the following

$$c_\mu=\log_2\left(1+\frac{\mathrm{SNR}_\mu}{\Gamma}\right) \qquad [\text{bits}] \tag{5.1.2}$$

with $\mu = 0, 1, \ldots, q$. When $\Gamma = 1$ (0 dB), c_μ becomes the channel capacity. The selection of Γ depends on the BER and coding scheme. Higher BER requires larger Γ. Complex coding scheme that guarantees reliable transmission can reduce the Γ. For the two-dimensional QAM system with BER $= 10^{-7}$, the gap Γ is computed using the following formula [73], [74]

$$\Gamma = 9.8 + \gamma_m + \gamma_c \qquad [\text{dB}] \tag{5.1.3}$$

where γ_m is the performance margin and γ_c is the coding gain. For an uncoded system, as in our case, ($\gamma_c = 0$ dB) with the performance margin equal to 0 dB, the gap is 9.8 dB.

At the end of this section it is worth pointing out that, (3.3.16) regarding the power allocation, and (5.1.1) or in case (5.1.2) concerning the bit allocation, are the chief criterions which all of the practical bit loading algorithms, whose objective function involves somehow the input-output mutual information, are based on. The next sections of the chapter are proper dedicated to two of these procedures, very popular especially for the ADSL systems and suitable for our system. The output of the algorithms is the vector of the allocation power on the subchannels $\mathbf{p} = \{p_\mu\}$. The elements of this vector will be used to determine the elements of the matrix $\mathbf{\Sigma_B}$ as $\delta_\mu = \sqrt{p_\mu}$. Hence, with the power allocation the transmitted signal is given by

$$s[k] = \sum_m \sum_n \sqrt{p_{m,n}} c_{m,n} g_{m,n}[k] = \sum_\mu \delta_\mu c_\mu g_\mu[k] \tag{5.1.4}$$

where $\mu = nM + m$ as stated in previous chapter. The QAM symbols $\{c_{m,n}\}$ are assumed with unit energy. Thus the total transmitted power is given by $P_{\text{TOT}} = \sum_\mu p_\mu$ and it is assumed to be equal to the number of atoms into the frame ($P_{\text{TOT}} = q$) because the average power on the μth atom of the frame is unitary.

5.2 The Hughes-Hartogs algorithm

A finite-granularity constellation size, iterative, greedy algorithm for variably allocating data and power among a set of parallel channels, in order to compensate the equivalent noise and to maximize the data rate is presented in this section. It was proposed as an approximation to the water-pouring solution and achieves the optimal solution for the discrete problem [72].

The "greedy principle" underlying the procedure claims that: at every iteration, every incremental power to transmit one or more additional bit(s) must be allocated to the subchannel that can use it most economically [73] The *Hughes-Hartogs* algorithm was first invented for voice-band modem in 1987, [70], but unfortunately for the modern DSL systems,

the number of subchannels is usually much larger than the voice-band modems. The slow convergence rate of Hughes-Hartogs algorithm and some other constraints, such as the fixed SNR assumption, make this algorithm impractical in DSL systems. But it is still a good starting point for later improved algorithms.

5.2.1 Description of the algorithm

Assuming to deal with a system composed of q parallel subchannels, such as the OFDM, where in each subchannel it is possible to allocate a number of bits

$$m \in \left\{0, 2^{\beta}, 2 \cdot 2^{\beta}, ..., k \cdot 2^{\beta}\right\}, \qquad k, \beta \in \mathbb{N} \tag{5.2.1}$$

Considering for example a scheme which includes a set of m-QAM constellations together with 0

$$m \in \{0, 2, 4, 6\} \tag{5.2.2}$$

In this case $k = 3$ and $\beta = 1$, as for m-QAM constellations.

Let us assume to have the knowledge, thanks to the aid of a return channel for example, of the equivalent power of the noises all over the subchannels

$$[\sigma_1^2, \sigma_2^2, ..., \sigma_q^2] \tag{5.2.3}$$

the following procedure claims to allocate bits and powers to the various subchannels in order to maximize the overall data transmission rate.

Carrying forward our example, let us imagine to have a multicarrier system with $q = 3$ and that the vector of the equivalent noises be

$$\left[\sigma_1^2, \sigma_2^2, \sigma_3^2\right] = [2.51\ (4\ dBW),\ 0.16\ (-8\ dBW),\ 1\ (0\ dBW)]$$

The maximum power which can be allocated among the subchannels, P, is constrained. If we want to maintain the BER of the system below a specified level, we could use the concept of the "SNR gap" previously introduced, and consider the equivalent noise over all the subchannels equals to

$$[\Gamma\sigma_1^2, \Gamma\sigma_2^2, ..., \Gamma\sigma_q^2], \tag{5.2.4}$$

with Γ accurately calculated in order to guarantee a determined performance.

In the example we want to maintain the BER under the value $\overline{\text{BER}} = 10^{-5}$, thus we introduce an SNR gap $\Gamma|_{dB} = 3$, so that

$$\left[\Gamma\sigma_1^2, \Gamma\sigma_2^2, \Gamma\sigma_3^2\right] = [5.02\ (7\ dBW),\ 0.32\ (-5\ dBW),\ 2\ (3\ dBW)]$$

Given the set of the transmission constellation, it is possible to pre-calculate, the value of the SNRs needed to maintain a certain the BER level, under a value $\overline{BER}$. We call such SNRs

$$[\gamma_1, \gamma_2, ..., \gamma_k]. \tag{5.2.5}$$

In the example

$$[\gamma_1, \gamma_2, \gamma_3, \gamma_4] = [0,\ 6.31\ (8\ dBW),\ 25.12\ (14\ dBW),\ 316.23\ (25\ dBW)].$$

The 0 corresponds to the no transmission.

Then, we multiply each SNR for the equivalent noise (including the gap) of each μth subchannels, obtaining the powers required for transmitting all the possible data rates over all the subchannels

$$p_j^{(\mu)} = \gamma_j^{(\mu)} \cdot \Gamma\sigma_\mu^2, \qquad j = 1, 2, ..., k, \quad \mu = 1, 2, ..., q \tag{5.2.6}$$

obtaining:

$$[p_1^{(\mu)}, p_2^{(\mu)}, ..., p_k^{(\mu)}], \qquad \mu = 1, 2, ..., q \tag{5.2.7}$$

It is convenient saving all this power levels in a table, like in the example (see Table 5.1).

	Sub 1	**Sub 2**	**Sub 3**
0 bits/sub	0	0	0
2 bits/sub	31.62 (15 dBW)	2 (3 dBW)	12.59 (11 dBW)
4 bits/sub	125.89 (21 dBW)	7.94 (9 dBW)	50.12 (17 dBW)
6 bits/sub	1584.89 (32 dBW)	100 (20 dBW)	630.96 (28 dBW)

Table 5.1: H.H. Powers

From this power levels, the *marginal* required power levels to increase the data rate complexity over each subchannels of one unit, for every possible data rate, are determined.

This levels are the difference in transmission power, divided by the difference between the constellation complexity involved. If the data rate of the lth subchannel is b bits, and this is obtained by transmitting a power $p_b^{(l)}$, the marginal power required to increase the data rate to its closest element in complexity is

$$\Delta p_{b+2^\beta}^{(l)} = \frac{p_{b+2^\beta}^{(l)} - p_b^{(l)}}{2^\beta} \tag{5.2.8}$$

As before, we can save all this marginal power values and their respective data rates, in a new table, which can be obtained from the previous, simply subtracting two rows and dividing from the difference between the corresponding data rates.

In the example (see Table 5.2), it is showed the table corresponding to the marginal powers multiplied by the difference between the constellation sizes. This will help for the implementation of the follows algorithm.

	Sub 1	**Sub 2**	**Sub 3**
0-2 bits/sub	31.62 (15 dB)	2 (3 dB)	12.59 (11 dB)
2-4 bits/sub	94.27 (19.74 dB)	5.95 (7.74 dB)	37.53 (15.74 dB)
4-6 bits/sub	1459 (31.64 dB)	92.06 (19.64 dB)	580.84 (27.64 dB)

Table 5.2: H.H. Marginal powers

At this point in time, the preliminary operations have been concluded and the iterative greedy algorithm works this way: starting from the null bit and power configuration, it allocates, at each iteration 2^β bits and the required amount of power, on the subchannel corresponding to the minimum marginal powers, until the available power P is not exceeded.

Let us assume in the example, to have a total available transmitting power $P = 200$ (23 dBW), with the help of the Table 5.2, the sequence of step is:

1. Allocate 2 bits and a marginal power of 2 (3 dB) on the 2nd subcarrier,
   the allocated power is $P_a = 2 < 200$,
   save the configuration [0, 2, 0];
   go to step 2;

2. Allocate 2 bits and a marginal power of 5.95 (7.74 dB) on the 2nd subcarrier, the allocated power is $P_a = 7.95 < 200$,
   save the configuration [0, 4, 0];
   go to step 3;

3. Allocate 2 bits and a marginal power of 12.59 (11 dB) on the 3rd subcarrier,
   the allocated power is $P_a = 20.54 < 200$,
   save the configuration [0, 4, 2];
   go to step 4;

4. Allocate 2 bits and a marginal power of 31.62 (15 dB) on the 1st subcarrier,
   the allocated power is $P_a = 52.16 < 200$,
   save the configuration [2, 4, 2];
   go to step 5;

5. Allocate 2 bits and a marginal power of 37.53 (15.74 dB) on the 3rd subcarrier,
   the allocated power is $P_a = 89.69 < 200$,
   save the configuration [2, 4, 4];
   go to step 6;

6. Allocate 2 bits and a marginal power of 92.06 (19.64 dB) on the 2nd subcarrier,
   the allocated power is $P_a = 181.75 < 200$,
   save the configuration [2, 6, 4];
   go to step 7;

7. Allocate 2 bits and a marginal power of 94.27 (19.74 dB) on the 1st subcarrier,
   the allocated power is $P_a = 276.02 > 200$,
   Exit and return the configuration at the previous step.

Given this configuration, with the help of Table 5.1, it is possible to determine the vector of the powers associated. In the example it is [31.62 100 50.12]. In this case, part of the available transmitting power ($P_{na} = 18.25$) has not been allocated, and this fact very often happens in practice, due to the integer bits constellations.

The process described leads to the *optimum* bit loading, in the sense that the overall bit rate, under the BER and power P constraint, is maximized, whether for each cth subchannel stands the following condition:

$$\Delta p_s^{(c)} > \Delta p_t^{(c)}, \qquad \forall s > t \tag{5.2.9}$$

The above condition means that, the marginal power needed to switch between two more complex constellation, must be bigger than the marginal power required to step up two less complex constellation, on an arbitrary subchannel subject to a certain noise level.

Before analyzing the algorithm, it is worth focusing on the *"greedy choice"* that has been made step by step. In fact, at every iteration, two incremental bits and an amount of power have been allocated on the subchannel which required the less cost in term of power. This choice left the largest amount of available power for the next allocation.

The complexity of the algorithm is quite high, in fact it requires $O(q \log q)$ steps in order to sort all the marginal power levels into monotonically increasing order, plus $O(q)$ operations for scanning these ordered values. This running times leads the Hughes-Hartogs algorithm to be too slow [74], also for applications like ADSL, where a large number of bits (in the range of 400 to 2000+) will be contained in each modulated symbol and transmitted over a large number of subchannels (typically 256).

5.3 The Campello algorithm

In the last section of the chapter, an efficient bit loading algorithm for multicarrier modulation will be described, the "Campello algorithm". This procedure is based on the aforementioned water-filling principle, but as ever, it must take into account the fact that the bit rate assignments are constrained to be integer. This optimization method is suitable to be used in the Discrete MultiTone (DMT), the modulation scheme selected by the American National Standardization Institute (ANSI), for a number of Digital Subscriber Line (DSL) [72]. Depending on the kind of traffic that must be conveyed, different optimization strategies can be employed, for example, for the voice, the constraint has represented by the delay, which must be minimized; while for other application like the Pay-Per-View, the demanding requirement to be respected is a certain Quality of Service, which can be a BER constraint. This algorithm is suitable even for our GMC filterbank-based multicarrier system in order to guarantee a certain QoS.

Hereafter, we will introduce a couple of problem of interest: the first one concerns the maximization of the overall bit rate to be transmitted among a set of parallel subchannel, given a fixed amount of power P, while the second one aims to minimize the total power, required to transmit a determined number of bits B. For the latter problem we will see how the Campello algorithm works.

5.3.1 Problem formulation

In this work, we will use the gap concept (see Section 5.1) to approximate the performance of the coding scheme in use on an AWGN Channel. For a gap Γ, corresponding to the target probability of error and the coding scheme in use, the number of bits that can be transmitted on a given subchannel as a function of the normalized power, $p_\mu = \delta_\mu^2$, allocated to that subchannel, for example using m-QAM modulation, is given approximately by

$$b_\mu = \log_2\left(1 + \frac{p_\mu P \left|\alpha_\mu\right|^2}{\Gamma \sigma_\mu^2}\right) \qquad \left[\frac{bit}{symb}\right], \tag{5.3.1}$$

where α_μ is the complex scalar gain of the μth subchannel, P is the portion of power allocated on the μth channel, when the total available transmitting power, qP, is uniformly distributed among the q parallel subchannels, and $\Gamma\sigma^2$ represent the equivalent noise power. In the application discussed in this thesis, the square of the complex scalar gain are the eigenvalues of the matrix $\mathbf{R_H} \triangleq \mathbf{H}\mathbf{N}_C^{-1}\mathbf{H}^H$, i.e. $|\alpha_\mu|^2 = |\lambda_\mu|$. The eigenvalues include the noise power on the subchannels and the σ_μ^2 must be removed from (5.3.1). In order to be avoid cumbersome notation in the sequel, we will define

$$\gamma_\mu = \frac{|\lambda_\mu|}{\Gamma} \tag{5.3.2}$$

as the signal to noise ratio (SNR) (with the gap incorporated), when the normalized power allocation is uniform ($p_\mu = 1,\ \mu = 1, 2, ..., q$).

Hence, we can write

$$b_\mu = \log_2(1 + p_\mu\gamma_\mu) \qquad \left[\frac{bit}{symb}\right]. \tag{5.3.3}$$

Given the γ_μ for all the q subchannels, the two problems of interest to be solved will be addressed as "the Bit Rate (or Throughput) Maximization Problem (BRMP)" and the "Margin Maximization Problem (MMP)".

Bit Rate Maximization Problem (BRMP)

The goal is to distribute a fixed amount of power, among a set of subchannels, such that the overall bit rate is maximized. The optimal solution to the problem as stated will invariably lead to a non-integer bit allocation. However, in practice we are restricted to integer allocations, and furthermore, we are always limited to a maximum number of bits, $\overline{b}$, per subchannel. Introducing the following notation: $\mathbb{Z}_a = \{0, 1, ..., a-1\}$ being a set of integer value from "0" to "$a-1$", and $\mathbf{b} \in \mathbb{Z}_{\overline{b}+1}^M$ representing any possible bit allocation vector with each element in $\mathbb{Z}_{\overline{b}+1}^q$, the BRMP is stated as

$$\mathbf{b_{BRM}} = \underset{\mathbf{b}\in\mathbb{Z}_{\overline{b}+1}^q}{\arg\max} \left\{ \sum_{\mu=1}^{q} b_\mu \right\}, \tag{5.3.4}$$

s.t.

$$\frac{1}{q}\sum_{\mu=1}^{q} p_\mu \leq 1. \tag{5.3.5}$$

Margin Maximization Problem (MMP)

This time, the problem requires to transmit a total number of bits among the subcarriers fixed and equal to the integer B. The goal is to determine (when possible, because the problem is innately power constrained) the bit allocation that requires the least amount of power, leaving the maximum amount of power for system margin, which may be wisely redistributed to strengthen the transmission system. The MMP is stated as follows

$$\mathbf{b_{MM}} = \underset{\mathbf{b}\in\mathbb{Z}^1_{\bar{b}+1}}{\arg\min} \left\{ \sum_{\mu=1}^{1} p_\mu \right\}, \tag{5.3.6}$$

s.t.

$$\sum_{\mu=1}^{q} b_\mu = B. \tag{5.3.7}$$

The two problems above and several variations of them (e.g. by limiting the amount of power allocated to each subchannels) can be solved by similar algorithms. In what follows, we will concentrate on the MMP, but the algorithms presented can be readily modified to solve the BRMP and the variations of both problems [72].

5.3.2 Description of the algorithm for the MMP

It was postulated in [71], that for a discrete bit allocation $\mathbf{b} \in \mathbb{Z}^M_{\bar{b}+1}$ satisfying (5.3.7) to be a solution to the MMP optimization problem, it must satisfy

$$\Delta p_{s_\mu} > \Delta p_{t_\mu}, \quad \forall s_\mu > t_\mu, \ \ \forall \mu \in 1, 2, ..., q \tag{5.3.8}$$

where, likewise in Section 5.2.1, we have defined

$$\Delta p_{b_\mu + 2^\beta} = \frac{p_{b_\mu + 2^\beta} - p_{b_\mu}}{2^\beta} \tag{5.3.9}$$

and p_{b_μ} is the power that must be allocated on the μth subchannel in order to transmit b_μ bit/symb at a certain target BER (determined by Γ), using the chosen coding scheme.

As stated in [71], discrete bit allocations satisfying (5.3.8) are called *efficient* and allocations satisfying (5.3.7) are called *B-tight*.

For the problem we are considering, by inverting (5.3.3), we obtain for each subchannel

$$p_{b_\mu} = \frac{\left(2^{b_\mu} - 1\right)}{\gamma_\mu} \tag{5.3.10}$$

and then, by using $\delta = 2^{\beta}$

$$\Delta p_{b_\mu} = \frac{2^{\beta b_\mu}}{\gamma_\mu} = \frac{\delta^{b_\mu}}{\gamma_\mu}. \tag{5.3.11}$$

Now, before stating the two theorems which are at the base of the low complexity optimum discrete bit loading algorithm, let us introduce a few of notations. We will call $b_\mu(i)$ the number of bits allocated on the μth subchannel at a certain iteration $i \in \mathbb{Z}$, where "i" can assume also negative values. Moreover, we will denote as $\mathbf{b}(i)$ an arbitrary discrete bit allocation at the iteration "i" and with $|\mathbf{b}(i)| = \sum_{\mu=1}^{q} b_\mu(i)$. Eventually, we will define

$$[x]_a^b = \begin{cases} b & \text{if } x > b \\ x & \text{if } a \leq x \leq b \\ a & \text{if } x < a \end{cases}$$

Theorem 3 *The discrete bit allocation,* $\mathbf{b}(i)$*, given by*

$$b_\mu(i) = [\lfloor \log_\delta \gamma_\mu \rfloor + i]_0^{\overline{b}}, \mu = 1, 2, ..., q \tag{5.3.12}$$

is efficient for all $i \in \mathbb{Z}$*.*

Hence, assuming that $0 < B < q\overline{b}$, what we have to do is to find a value of i, such that the resulting allocation be as tight as possible, that is

$$i_B = \max\{i \in \mathbb{Z} : |\mathbf{b}(i)| \leq B\} \tag{5.3.13}$$

Theorem 4 *The solution to the MMP satisfies* $\mathbf{b}(i_B) \leq \mathbf{b_{MM}} \leq \mathbf{b}(i_B + 1)$*, where the inequalities must be intended component-wise.*

The proof of both the theorems is stated in [72]. The problem now is to find an efficient method for determining i_B.

We could come up with the idea of starting with some value, for instance $i = 0$, and go on incrementing (or decrementing) i until i_B is found. But, as we will see shortly, this method turns out to be too computationally expensive because for each i tested, we have to perform $O(q)$ operations. So, even an efficient binary search would be too expensive, resulting in an $O(qlogq)$ algorithm.

The efficient procedure for determining i_B, starts by drawing attention at theorem 3, and noticing that two or more channels corresponding to the same $\lfloor \log_\delta \gamma_\mu \rfloor$, will always be

allocated the same amount of bits. Such a subchannels can be gathered together, so the entire set of subchannels can be divided into L groups ($L < q$) with the same bit allocation. Let us define

$$\pi_k = \{\mu \in \{1, 2, ..., q\} : \lfloor \log_\delta \gamma_\mu \rfloor = k\}, \quad k = 0, 1, 2, ..., L-1 \tag{5.3.14}$$

and let $N_k = |\pi_k|$, the $|\mathbf{b}(i)|$ values can be calculated thanks to the following iterative equation

$$|\mathbf{b}(i)| = |\mathbf{b}(i-1)| + S_i, \tag{5.3.15}$$

where

$$\text{if } \overline{b} \leq L:$$

$$S_i = \begin{cases} S_{i-1} + N_{i-1} & ,1-L \leq i \leq \overline{b}+1-L \\ S_{i-1} + N_{i-1} - N_{\overline{b}+1-i} & ,\overline{b}+1-L < i \leq 1 \\ S_{i-1} - N_{\overline{b}+1-i} & ,1 < i < \overline{b} \\ 0 & ,\overline{b} < i \end{cases} \tag{5.3.16}$$

$$\text{else if } \overline{b} > L:$$

$$S_i = \begin{cases} S_{i-1} + N_{i-1} & ,1-L \leq i \leq 1 \\ S_{i-1} & ,1 < i \leq \overline{b}+1-L \\ S_{i-1} - N_{\overline{b}+1-i} & ,\overline{b}+1-L < i < \overline{b} \\ 0 & ,\overline{b} < i \end{cases} \tag{5.3.17}$$

with the initial condition

$$S_{1-L} = |\mathbf{b}(1-L)| = 0.$$

Hence, starting from $i = 2 - L$ we go through incrementing i until $|\mathbf{b}(i)| > B$ and then by setting $i_B = i - 1$. Finally, in order to obtain a bit rate equal to B, we have to increment the group of subchannels that have not yet reached $\overline{b}$, which corresponds to the smallest incremental power $\Delta p_{b_\mu(i)+2^\beta}$. This last step corresponds to the selection of the minimum, from a set of N elements, in the worst case, so it requires $O(q)$ complexity. In total, since the first part of the algorithm requires $O(q)$ operations to find the $M_k's$ and a constant number

of operations, as $3L+\overline{b}-2$, the total running time of the Campello algorithm for solving the MMP has $O(q)$ complexity.

The algorithm presented here has also the advantage of only using simple operations. With the exception of the log_{δ}, calculation the algorithm only uses additions (most of the time simple increments), compares and index swapping.

Anyway, looking at the iterative form of (5.3.16) which makes use of (5.3.16) and (5.3.17), in order to properly perform the algorithm, we are obliged to starting from the index $i=2-L$, and go incrementing i until $|\mathbf{b}(i)|>B$.

The following "closed form" of (5.3.15) will instead allow to start from any index $i=2-L,3-L,...,\overline{b}$.

if $\overline{b}\leq L$:

$$|\mathbf{b}(i)|=\begin{cases}\sum\limits_{u=1}^{i+L-1}u\cdot N_{u-1} & ,1-L\leq i\leq 1-L+\overline{b}\\ \sum\limits_{u=1}^{i+L-1}u\cdot N_{u-1}-\sum\limits_{u=1}^{(i-\overline{b})+L-1}u\cdot N_{u-(i-\overline{b})} & ,1-L+\overline{b}\leq i\leq 1\\ \sum\limits_{u=1}^{L}u\cdot N_{u-1}-\sum\limits_{u=1}^{L-\overline{b}}u\cdot N_{u-1+\overline{b}}+\sum\limits_{v=1}^{i-1}\cdot\sum\limits_{u=0}^{\overline{b}-1-v}N_u & ,1\leq i\leq\overline{b}\end{cases} \tag{5.3.18}$$

else if $\overline{b}>L$:

$$|\mathbf{b}(i)|=\begin{cases}\sum\limits_{u=1}^{i+L-1}u\cdot N_{u-1} & ,1-L\leq i\leq 1\\ \sum\limits_{u=1}^{L}u\cdot N_{u-1}-(i-1)\sum\limits_{u=0}^{L-1}N_u & ,1\leq i\leq\overline{b}+1-L\\ \sum\limits_{u=1}^{L}u\cdot N_{u-1}+\left(\overline{b}-L\right)\sum\limits_{u=0}^{L-1}N_u+\sum\limits_{v=1}^{i-\left(\overline{b}+1-L\right)}\cdot\sum\limits_{u=0}^{L-1-v}N_u & ,\overline{b}+1-L\leq i\leq\overline{b}\end{cases} \tag{5.3.19}$$

It is clear that the cost of a single iteration, by using one of the latter expression is higher compared to the cost of an iteration using (5.3.15), (5.3.16), (5.3.17), but the fact that we could start from any index we want, does not forbid the possibility of shortening the number of iteration, for example by selecting a starting index as a function of the channel gains. However, we have only derived the "closed form expression" from the respective iterative ones by induction; the issue of how to use them has only been supposed and it has not been faced in this thesis.

5.4 Concluding remarks

It is important to emphasize how the water-filling principle play a fundamental role in the design of a bit and power allocation strategy. Its greedy principle of "loading more" those channel which are in a better condition concerning the level of the noise, in order to maximize the mutual information, is often the core issue also when the objective function changes.

Furthermore, it is worth stressing the theoretical aspect of the water-filling, which, aiming at obtaining the Shannon capacity of a multichannel system, it assumes Gaussian inputs and error probability tending to zero, both *infeasible* requirements. Anyway, by introducing an SNR gap, as seen in Section 5.1, we were able to slightly modify the initial problem in order to, approximately, take into account the real conditions of integer input constellations and finite BER.

An optimal solution to the problem of the input distribution differing from the Gaussian, when wanting the power allocation policy that maximizes the mutual information over parallel channels, is the *mercury/waterfilling* [64], [75]. However, its coverage is wide, complicated and it uses tools, like the nonlinear input-output estimation MMSE [76], which would need more than a chapter for their description.

Instead, we have preferred focusing on two practical techniques: the Hughes-Hartogs algorithm and the Campello algorithm, which, although they are both too slow for modern wireless mobile communication systems.

Chapter 6

Campello algorithm with cognitive implementation

With the increase in the demand for radio frequency (RF) spectrum, and with the non-availability of "prime" spectrum, the expansion of the existing services or the allocation of spectrum for additional services was an important technical challenge identified by the scientific community. The traditional spectrum allocation techniques rely on segmenting the available spectrum and assigning the fixed blocks to the licensed users. In such a spectrum allocation scenario, unlicensed users are not permitted to access the already licensed bands since strict regulations are imposed on their access. As a result of the prohibition on the unlicensed access to licensed spectrum, heavily populated and highly interference-prone frequency bands have to be accessed. Clearly, this results in reduced system performance.

Nowadays most of the radio frequency spectrum is mainly inefficiently used and we can exploit the fact that at any given time and place, a significant part of spectrum is unused by existing legacy systems. For example, channel occupancy measurements in the range 30MHz - 3GHz conducted in 2005 at six locations in USA revealed an average occupancy rate of only 5.2% [77]. The measured average occupancy rate ranges from 1% at Radio Astronomy site to 13.1% in New York City.

Figure 6.1 shows a measurement campaign conducted at the Information Technology and Telecommunications Center (ITTC) on 8/31/2005 [4]. The spectral occupancy from 9 kHz to 1 GHz is shown. From this figure, it is observed that there are several spectral white spaces in the licensed portions of the spectrum demonstrating that allocated spectrum is under-utilized. Thus, what was basically thought of, as an apparent scarcity of spectrum is actually the result of the under-utilization caused by existing spectrum allocation policies. Hence, the need for a novel spectrum allocation policy has been identified.

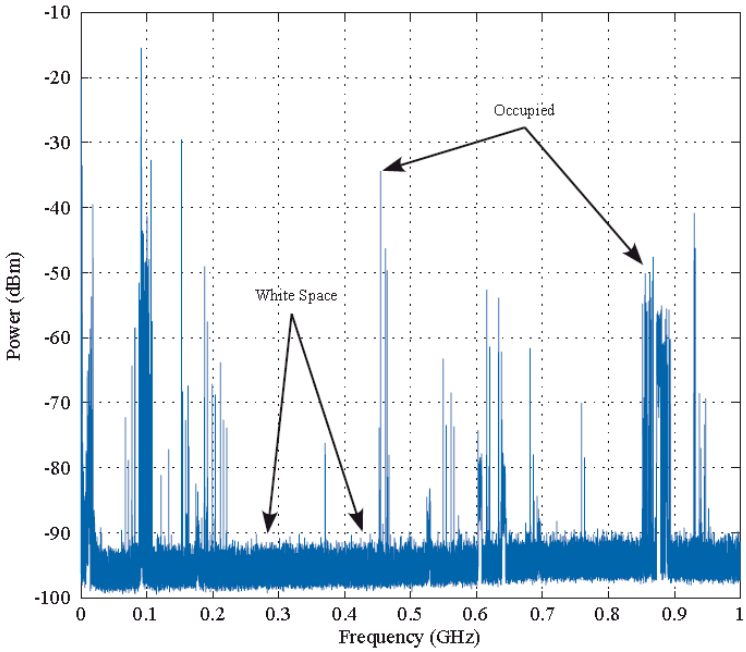

Figure 6.1: Spectrum occupancy measurements from 9 kHz to 1 GHz (8/31/2005, Lawrence, KS, USA) [4]

The basic objective of the recent spectrum allocation policy is the promotion of secondary utilization of unused portions of the spectrum in the form of *spectrum pooling*, wherein, unlicensed users rent licensed portions of the spectrum from a common pool of spectral resources from different owners [18]. This improves the utilization of the spectral resources while potentially generating additional revenue to the licensed users. However, the implementation of a spectrum pooling system raises many technological, economic and political questions, that need to be answered for the successful coexistence of the legacy[1] and rental systems. Efficient pooling of the radio spectrum is achieved by using a *cognitive radio*, which is a multi-band, spectrally agile radio that employs flexible communication techniques and detects the presence of primary user transmissions over different spectral ranges to avoid interference to the licensed users.

Thus these white spaces can change in time their position in frequency spectrum and their width. In Figure 6.2 we can see primary users (dark colors) transmitting in a discontinuous manner according to their needs. So the secondary user can take advantage by the parts of

[1]The terms *legacy systems* and *primary systems* are used to refer to the licensed owners of the RF spectrum whereas the terms *rental systems* and *secondary systems* are used to refer to the users that utilize the idle licensed portions of the spectrum.

the spectrum left free by primary users in order to increase its bandwidth and to establish transmissions at an increased data-rate. In this chapter we will consider transmissions with constant data-rate. Hence we will assume that the number of subcarriers and the duration of the multicarrier symbol are given parameters.

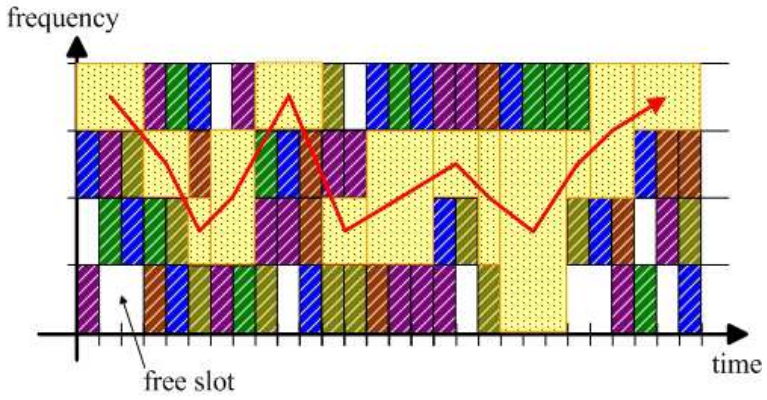

Figure 6.2: Application of cognitive radio paradigm

A filterbank-based cognitive system must continually sense the spectrum in order to detect the free parts of the spectrum and it must set its transmission parameters (as the number of subcarriers and/or the overlapping factor) according to the bandwidth availability in the current time slot to avoid or minimize the interference with active transmissions in adjacent spectrum.

When the OFDM technique is employed by cognitive radio systems, new challenges appear, raising recently interesting research topics [5]. One of the main challenges in OFDM cognitive radio systems is spectrum shaping. In OFDM-based systems, spectrum shaping means determining the subcarriers to be used by the OFDM system while keeping the interference to and from primary users at a negligible level. Once spectrum sensing information is acquired, this knowledge should be utilized to select the subcarriers to be used by the secondary/cognitive users. This problem is addressed in [78] by using energy detectors over each subcarrier. Moreover, a detection criterion is used to determine used subcarriers. Spectrum sensing is directly related to the sensing problem for spectrum hole identification. However, cognitive radio might prefer to skip some opportunities depending on the power and network traffic requirements.

Moreover OFDM system can adjust its waveform by turning off some subcarriers in order to exploit the available spectrum holes. The receiver, however, should be informed about subcarriers that are deactivated and that are to be used. Signaling of this information should be performed carefully in order to prevent interference to primary users while keeping the bandwidth loss at minimum. Detection of those unused subcarriers can also be performed

blindly. However, to the best knowledge of the authors, no work in this area has been done yet. One method to reduce the overhead due to signaling is proposed in [79]. The activation/deactivation of subcarriers is performed over a block of subcarriers instead of each individual subcarrier. Hence, the signaling overhead can be reduced by a factor of each blockŠs size. Moreover, depending on the channel quality and available resources, parameters like FFT size, CP size, etc. can be changed and this information should also be conveyed to the receiver.

Synchronization is another important issue that needs to be addressed in OFDM system design. With the introduction of cognitive radio, new aspects are introduced to the problem. The narrow band interference, which can interfere with the preamble, is one of the problems [80]. Furthermore, the incomplete subcarrier set might be an issue for preambles, and pilots might fall into unused subcarriers if used. Moreover, if multiple user accessing is employed, the subcarriers can be assigned to different users. To keep the orthogonality between subcarriers and avoid interference, all users should be synchronized to the receiver as illustrated in Figure 6.3(a) where the subcarriers of the primary users are plotted with blue lines while the subcarriers of the cognitive system are plotted with red lines. If the synchronization fails (see Figure 6.3(b)) then the orthogonality condition does not hold true any longer, because the subcarrier frequencies of the secondary users do not coincide with the nulls of the sinc-shaped spectrum of the primary users and the mutual interference appears. A zoomed version of spectrum depicted in Figure 6.3 are shown in Figure 6.4 in order to appreciate the differences between the spectrum obtained with and without the frequency synchronization. In [80], it is shown that longer preambles are needed in CR-OFDM systems as compared to conventional systems. Moreover, new preamble structures are introduced and their performance for time and frequency synchronization is investigated.

Finally the mutual interference between the secondary user and the primary ones should be carefully considered when designing cognitive radio systems. The side lobes of modulated OFDM subcarriers are known to be large as shown in Figure 6.5. As a result, there will be power leakage from used subcarriers to nulled subcarriers which causes interference to the licensed users. Various methods are proposed in the literature to reduce this leakage and to enable co-existence of cognitive-OFDM systems with primary license owner systems. One method is to make the sinc function (see 6.5) decay faster by windowing the time domain OFDM samples [81]. Similar techniques have already been investigated to reduce ICI and out-of-band radiation in OFDM systems [82], [83]. In [81], a raised-cosine window is applied. By changing the roll-off factor of the raised-cosine window, interference reduction of up to 6 dB has been achieved. The drawback of this method is the reduction of system throughput due to the temporal extension of time domain signal to maintain orthogonality. Another method for reducing the interference is to adaptively deactivate the subcarriers that are adjacent to the subcarriers occupied by licensed users [81]. This way the interference can be

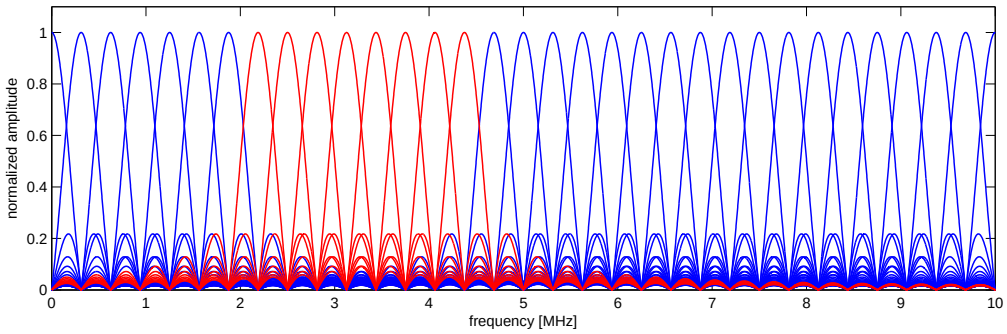

(a) Perfect frequency synchronization with primary user

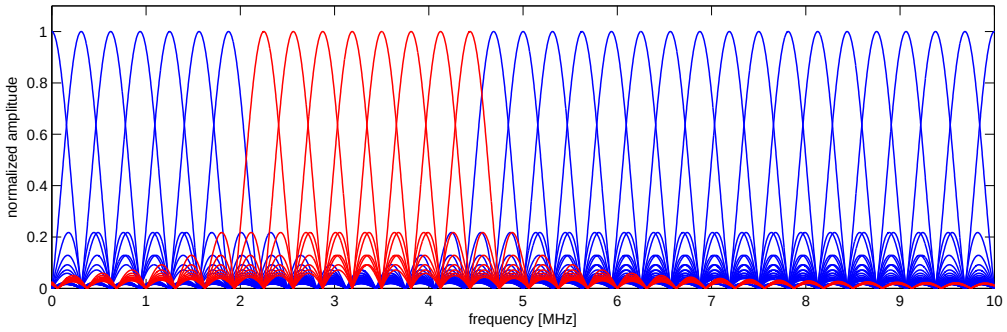

(b) Lack of frequency synchronization with primary user

Figure 6.3: Cognitive OFDM system

greatly reduced as most of the interference comes from the neighboring subcarriers. However, the obvious disadvantage of this method is the reduction of spectral efficiency. Instead of deactivating the neighboring subcarriers, their values can be determined actively in order to cancel the interference in the deactivated bands. This technique is proposed in [84], [85] and referred to as active interference cancellation and cancellation carriers, respectively. It is shown that the performance can be improved, however, determination of the values for cancellation subcarriers is complex as it requires optimization. One last method for reducing the interference to and from the narrowband primary users is subcarrier weighting [86], [87]. In this method, the subcarrier weights are determined in such a way that the sidelobes of the transmission signal are minimized according to an optimization algorithm which allows several optimization constraints. This way, more than 10 dB reduction in the sidelobes of OFDM signal can be achieved. Note that subcarrier weighting requires constant envelope modulation such as BPSK or QPSK. Moreover, the receiver does not need to know the weighting sequence as the phase information is not changed. In addition to the aforementioned challenges, there

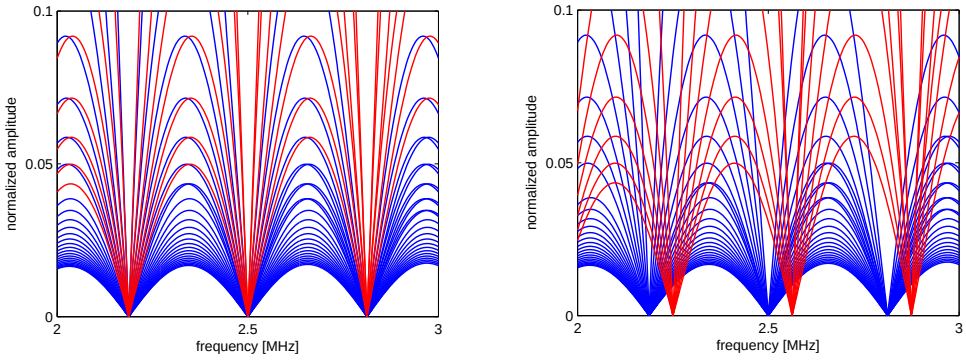

(a) Perfect frequency synchronization (b) Lack of frequency synchronization

Figure 6.4: Cognitive OFDM system (zoom)

are other issues for practical implementation of OFDM cognitive radio systems.

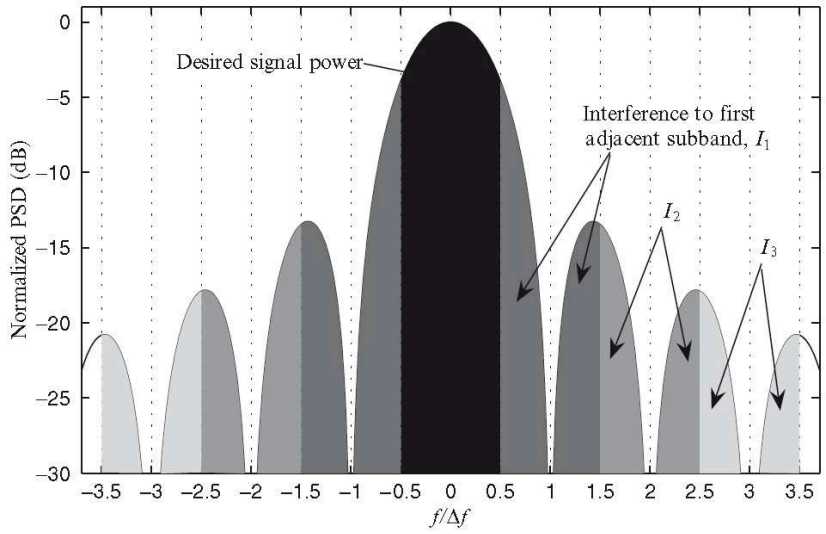

Figure 6.5: Power spectrum density of a single OFDM subcarrier [5]

Some of the challenges just mentioned can be avoided adopting a NOFDM modulation scheme such as the synchronization with the licensed users because the orthogonality constraint must no longer satisfied. Employing a NOFDM system we can shape the subcarriers in order to decrease or even avoid any interference with primary users choosing pulses with very low (or null) out-of-band sidelobe levels such as the RRC or the Gaussian pulse. An other advantage of adopting the filterbank-based NOFDM systems relies on its flexibility.

These systems can wisely adapt the transmitted signal shrinking the subcarriers, i.e. changing simply the overlapping factor according to the available bandwidth. OFDM systems cannot shrink the subcarriers because of the orthogonality constraint. In Figure 6.6 we can observe the behavior of a cognitive NOFDM system. In Figure 6.6(a) the available bandwidth is about $B_{\max} = 2$ MHz and the overlapping is maximum according to the given signaling interval, i.e. $\beta = 1$. In Figure 6.6(b), the available bandwidth is instead about $B_{\max} = 4$ MHz. Thus the GMC system is able to relax the overlapping among the subcarriers and β is increased.

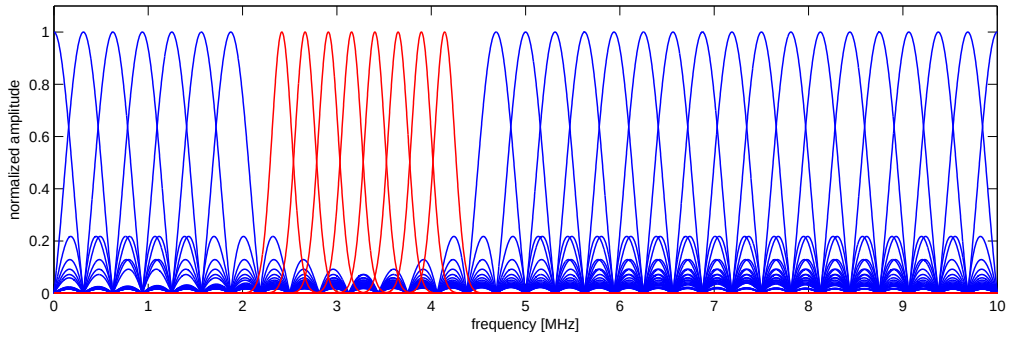

(a) $B_{\max} \approx 2$ MHz

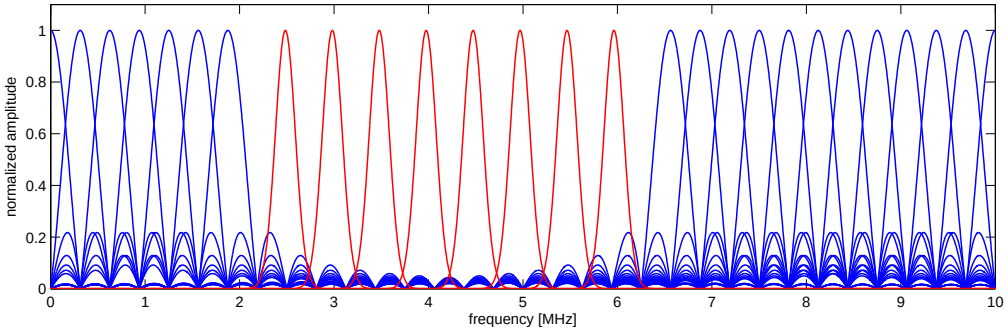

(b) $B_{\max} \approx 4$ MHz

Figure 6.6: Cognitive NOFDM system adopting gaussian shaping with two different values of available bandwidth

Unfortunately the NOFDM technique presents even some drawbacks such as the high amount of computational complexity

6.1 Cognitive algorithm for filterbank-based systems

We will presents a very simple procedure that varies only the overlapping factor β while the number of subcarriers is kept constant. As said before, the other given parameters are the GMC symbol duration T and the length (in signalling intervals) of the prototype pulses $N_f^{(Tx)}$. In this way the data-rate is kept constant. First of all we calculate the starting sampling interval as $T_{s\min} = \frac{1}{B_{\max}}$. This value is even the minimum sampling interval that we can employ according the available bandwidth and the Nyquist theorem. At the first iteration of the algorithm we set $T_s = T_{s\min}$. Then we have to determine the number of samples per GMC symbol according to the given GMC symbol duration. Thus

$$N = N = \left\lfloor \frac{T}{T_s} \right\rfloor \tag{6.1.1}$$

The floor operator[2] guarantees that $N \in \mathbb{N}$ and the overall bandwidth constraint is checked. Then we can determine the overlapping factor $\beta = \frac{N}{M}$. However this value must satisfy two constraints at the same time: the first one is that β must be equal or greater than 1 (otherwise the data transmission is impossible); the second constraint allows the efficient filterbank implementation, i.e.

$$\begin{cases} L = kN & \text{with } k \in \mathbb{N} \\ L = iM & \text{with } i \in \mathbb{N} \end{cases} \tag{6.1.2}$$

where L is the length (in samples) of the synthesis and analysis prototype pulses. The constraint (6.1.2) means that the length of prototype pulse must be divisible both for the number of subcarriers M and the number of samples per GMC symbols N. According to (6.1.1, the constraint on N is automatically verified. Moreover because of $L = \beta \cdot M \cdot N_f^{(Tx)} = N \cdot N_f^{(Tx)}$, (6.1.2) becomes

$$\beta \cdot N_f^{(Tx)} \in \mathbb{N} \tag{6.1.3}$$

If $\beta < 1$ the algorithm fails because the constraints are "too strong". It means that the starting parameters are ill-posed in particular T (too small) and/or $T_{s\min}$ (too big), i.e. the available bandwidth is not enough to put the M subcarriers with fixed bandwidth $1/T$. In this case the starting parameters have to be change in order to transmit. If the constraint (6.1.3) is not checked, we have to decrease N of an unit and the new β value is re-calculate until the constraint is checked.

This algorithm is summed up in Table 6.1.

[2]The floor operator $\lfloor \cdot \rfloor$ maps a real number to the next smallest integer.

COGNITIVE ALGORITHM

Input: $B_{\max}$, M, T, $N_f^{(Tx)}$
Output: β

1. **Calculate** the sampling interval $T_s = 1/B_{\max}$;
2. **Calculate** the number of samples per GMC symbol as $N = \lfloor T/T_s \rfloor$;
3. **Calculate** the overlapping factor $\beta = N/M$;
4. **If** $\beta < 1$, then "Error: constraints too strong";
5. **If** $\beta \cdot N_f^{(Tx)} \in \mathbb{N}$, then **Exit**;
6. **else**
7. $N - -$;
8. Go to point 3;

Table 6.1: Cognitive algorithm for the choose of β

6.2 Simulations and results

In this section we will show the results obtained with a filterbank-based GMC system adopting the Campello algorithm as bit and power allocation algorithm and the cognitive implementation in order to choose the β according to the available bandwidth. The Campello algorithm works according to the Margin Maximization Problem (MMP) (see Section 5.3.2). Hence these results will be compared with OFDM performances and with a NOFDM system adopting an uniform bit allocation algorithm.

The simulations have been obtained with a filterbank-based multicarrier system with $M = 16$ subcarriers and a Gaussian pulse and its dual as synthesis and analysis prototype pulse. The pulse duration (in signaling interval) and the number of GMC symbols in each frame is $N_{GMC} = N_f^{(Tx)} = 8$. The GMC symbol last 4μsec because the simulations are compared to an 16-subcarrier OFDM system working with a cyclic prefix of 4 samples and

a sampling interval of $T_s = 200$ nsec. Thus the minimum bandwidth required by the (CP-)OFDM system is equal to 5 MHz. The frame duration of both the NOFDM and OFDM system is consequently 32μsec. The SNR gap is set to $\Gamma = 2.5$ dB in order to obtain a BER constraint equal to $\overline{\text{BER}} = 10^{-2}$. The data-rate is set to 8 Mbit/s and hence the uniform bit loading allocates 2 bits per each atom.

Two different approximations of the channel state information will be considered:

Partial CSI TX and full CSI RX. In this case the LMMSE equalizer $\mathbf{A}$ is calculated using all the equivalent matrices $\mathbf{H}$ and $\mathbf{N}_C$, while at the transmitter the precoder $\mathbf{B}$ is calculated employing only the main diagonal of the matrices $\mathbf{H}$ and $\mathbf{N}_C$. With this approximation the transmitter does not consider the interference affecting the received frames when it has to calculate the allocation of the transmitted power.

Partial CSI TX/RX. Both the LMMSE equalizer $\mathbf{A}$ and the precoder $\mathbf{B}$ are calculated using only the main diagonal of the matrices $\mathbf{H}$ and $\mathbf{N}_C$. This time both the transmitter and the receiver do not consider the interference.

In Figures 6.7, 6.8 and 6.9, the normalized average required transmitted power and the BER curves are depicted when the overall available bandwidth $B_{\max}$ is 5 MHz, 4.5 MHz and 4 MHz, respectively. The dashed lines refer to the simulations employing the uniform bit loading algorithm, while the dashed black line is obtained with the OFDM system employing the Campello algorithm and the minimum bandwidth. The overlapping factors β chosen by the cognitive algorithm are shown in Table 6.2 for the different values of available bandwidth.

$B_{\max}$	β
5 MHz	1.25
4.5 MHz	1.125
4 MHz	1

Table 6.2: The overlapping factors β chosen by the cognitive algorithm

The normalized average required transmitted power is the power required to satisfy the BER constraint and the margin maximization and it is normalized with respect to the power transmitted when any power allocation algorithm is employed, i.e. $P_{\text{TOT}} = q$.

Looking at the Figures 6.7(a), 6.8(a) and 6.9(a), it can be notice that the BER constraint is always checked except when the "Partial CSI TX/RX" approximation is assumed (green lines). The loss of performances is mainly caused by the suboptimal LMMSE receiver that is not able to perfectly compensate the interference affecting the received signal and it generates more errors than other approximation where optimum equalization is assumed. When the

available bandwidth decreases such as in Figures 6.8(a) and 6.9(a), the overlapping factor is decreased by the cognitive algorithm and the subcarriers are compressed. Hence the global interference grows and the performances given by suboptimal LMMSE equalizer worst.

The normalized average transmitted powers are depicted in Figure 6.7(b) when the available bandwidth is $B_{\max} = 5$ MHz. We can observe that the optimal assumption, i.e. full CSI at the transmitter and at the receiver, the transmit power allocated is the same as the OFDM system. When the "partial CSI TX" assumption is adopted (red and green lines) the required power increases of about 1 dB because of the lack of information about the interference during the bit allocation at the transmitter. Moreover the uniform bit allocation requires about 10 dB more than Campello bit allocation. As stated previously, when the the available bandwidth decreases such as in Figures 6.8(a) and 6.9(a) the interference increases. Hence even the required power increases when the suboptimal bit allocation is adopted. In fact when the maximum available bandwidth is $B_{\max} = 4$ MHz, the transmitted power is about 4 dB greater than the optimum case.

In spite of that, the optimum bit allocation and the optimum equalizer (blue line) guarantee at any value of available bandwidth the same performances and the same required transmitted power as the OFDM system, even when the available bandwidth is 20% less than the minimum bandwidth required by the OFDM system.

In this scenario, the NOFDM system is no longer able to transmit when the available bandwidth is less than 4 MHz, because the overlapping factor becomes smaller than 1. In such a case we have to relax the constraint on the duration of the GMC symbol in order to transmit.

Thus we can say that the NOFDM system is able to guarantee the same performances of an OFDM system assuming the perfect knowledge of the channel state both at the transmitter and at the receiver saving bandwidth and increasing the spectral efficiency according to the spectrum occupancy. Moreover in a cognitive application where the available bandwidth can change with time, this flexibility becomes a strong benefit compared to the OFDM systems.

In order to keep the BER constraint holding true when the "Partial CSI TX/RX" approximation is assumed we have to increase the SNR gap Γ. Hence the required transmitted power increases in order to compensate the interference and the BER constraint holds true. It can be notice, from Figure 6.10, that the SNR gap, employed to obtain $\overline{\mathrm{BER}} = 10^{-2}$ when the available bandwidth is $B_{\max} = 4.5$ MHz, becomes 3.8 dB. Instead, when $B_{\max} = 4$ MHz, the SNR gap required is $\Gamma = 7.5$ dB (see Figure 6.11).

The results of the simulation depicted in Figures 6.12, 6.13 and 6.14 have been obtained using a RRC prototype pulse with the roll-off factor $\alpha = 0.25$ and $N_f^{(Tx)} = N_{GMC} = 16$ GMC symbols per frame and assuming the available bandwidth equal respectively to 5 MHz, 4.5 MHz and 4 MHz. We can observe that the performances with the RRC pulse are better than the performances obtained with the Gaussian pulse. The required transmitter power

does not increase both when the available bandwidth decrease and when the approximations on the channel state information are assumed. It can be notice only a slightly worsening of the BER obtained when the available bandwidth decreases. We can compensate this loss of performances given by the suboptimal bit allocation with an increase of the SNR gap.

In order to keep the BER constraint holding true when the "Partial CSI TX/RX" approximation we have to increase the SNR gap to $\Gamma = 3.3$ dB when the overall available bandwidth is $B_{\max} = 4$ MHz (see Figure 6.15). Hence the RRC pulse is able to satisfy the BER constraint transmitting less power than the Gaussian pulse when the "Partial CSI TX/RX" approximation is assumed. The drawbacks are an higher computational complexity than Gaussian pulse given by the increased length of the prototype pulse and consequently an higher global latency of the system given by the doubled length of the frames.

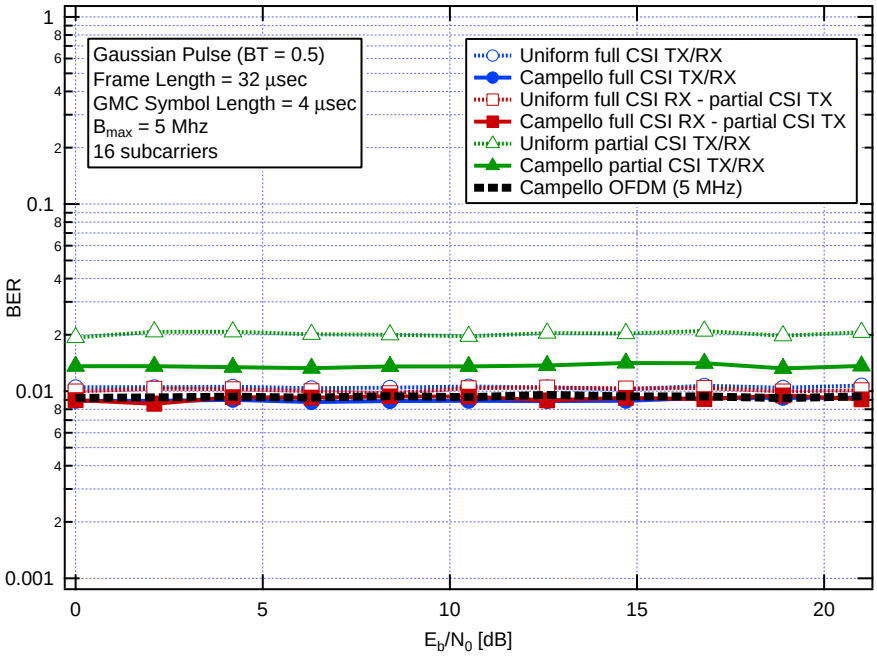

(a)

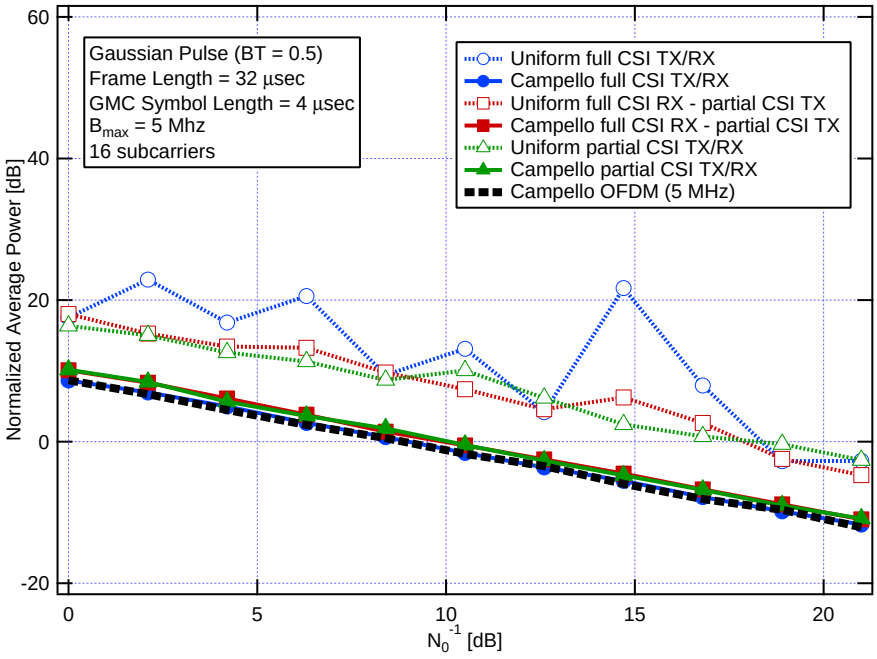

(b)

Figure 6.7: Normalized average transmitted power and BER when the available bandwidth is $B_{\max} = 5$ MHz and comparison with OFDM performances - *Gaussian pulse*

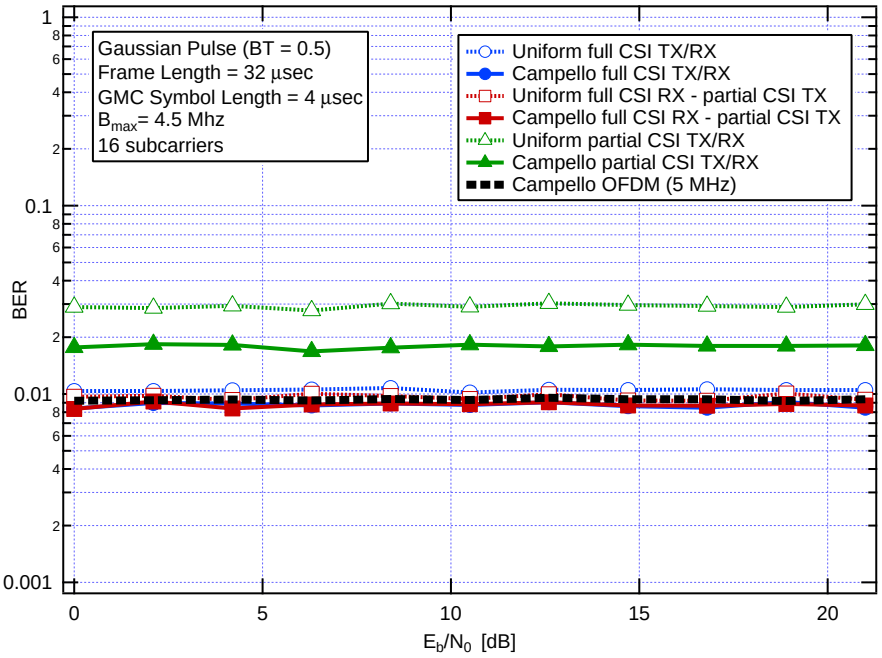

(a)

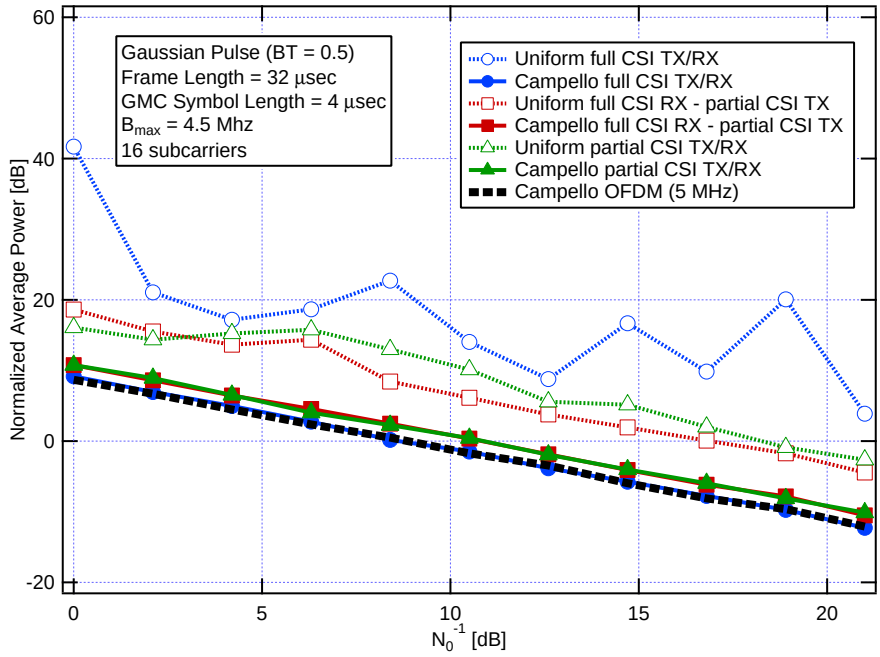

(b)

Figure 6.8: Normalized average transmitted power and BER when the available bandwidth is $B_{\max} = 4.5$ MHz and comparison with OFDM performances - *Gaussian pulse*

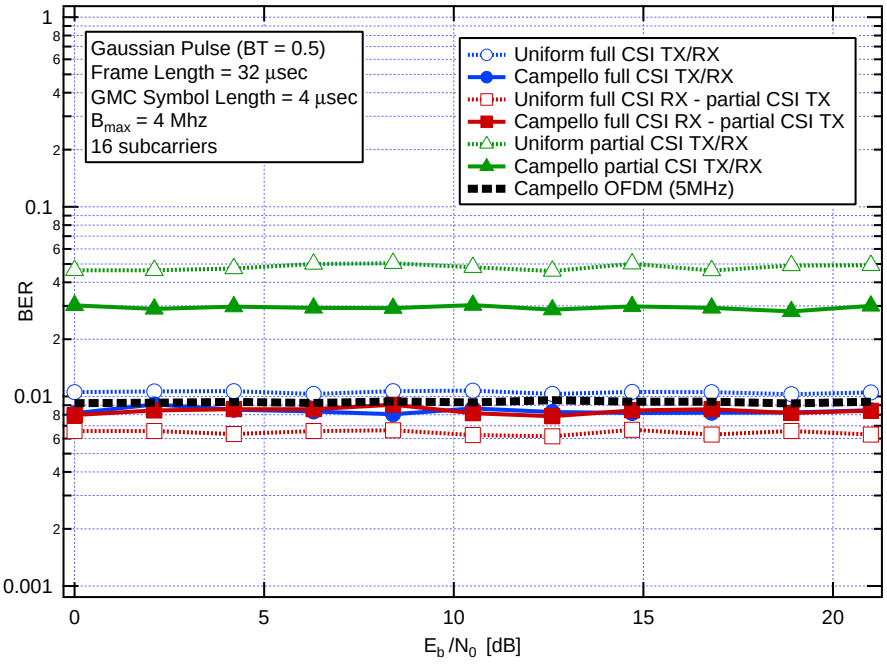

(a)

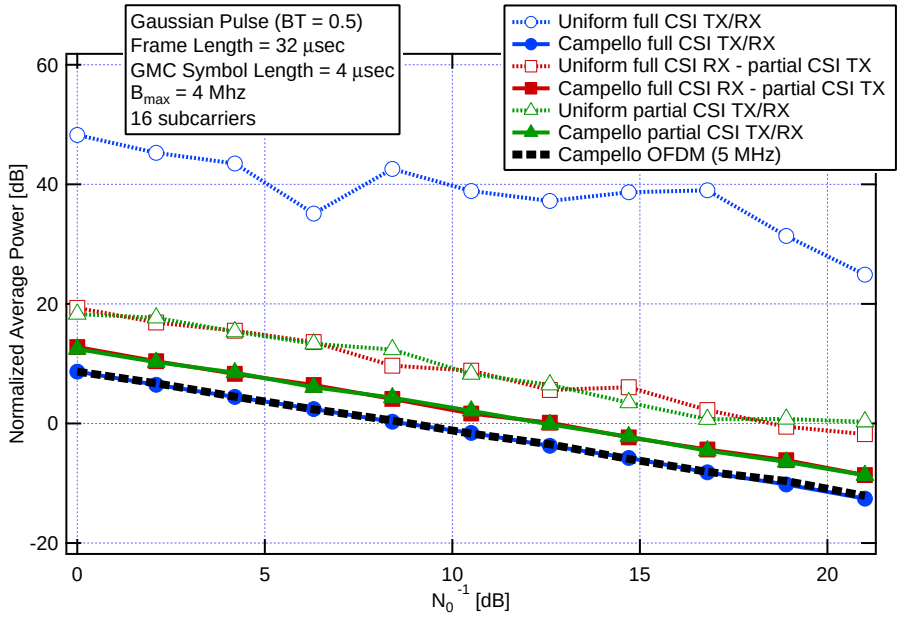

(b)

Figure 6.9: Normalized average transmitted power and BER when the available bandwidth is $B_{\max} = 4$ MHz and comparison with OFDM performances - *Gaussian pulse*

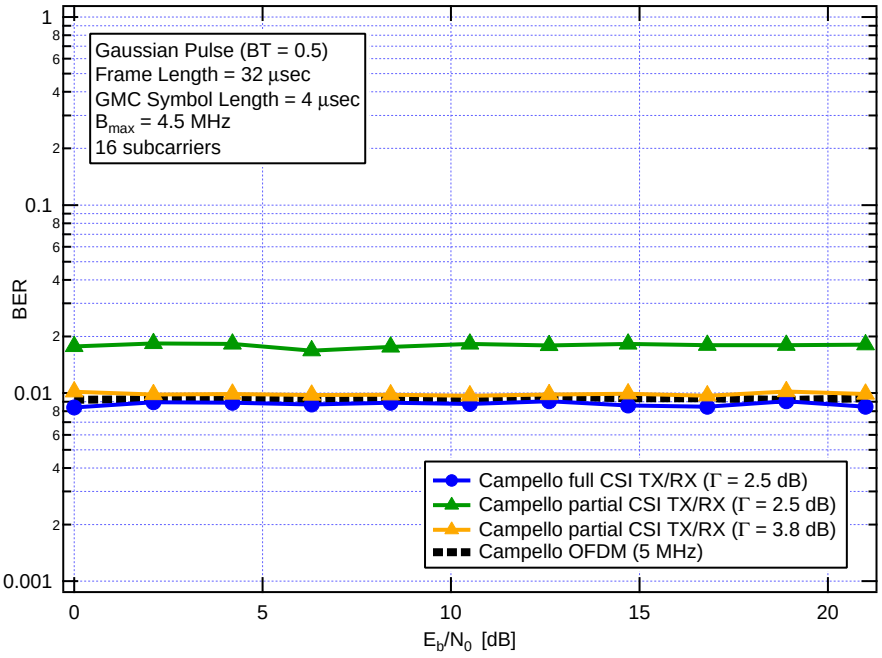

(a)

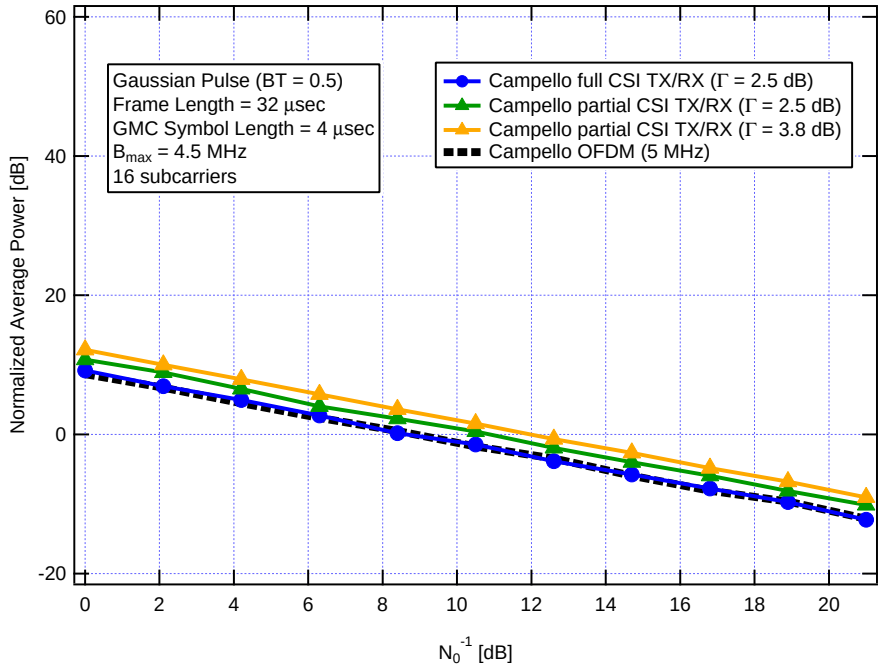

(b)

Figure 6.10: SNR gap increase - *Gaussian pulse*

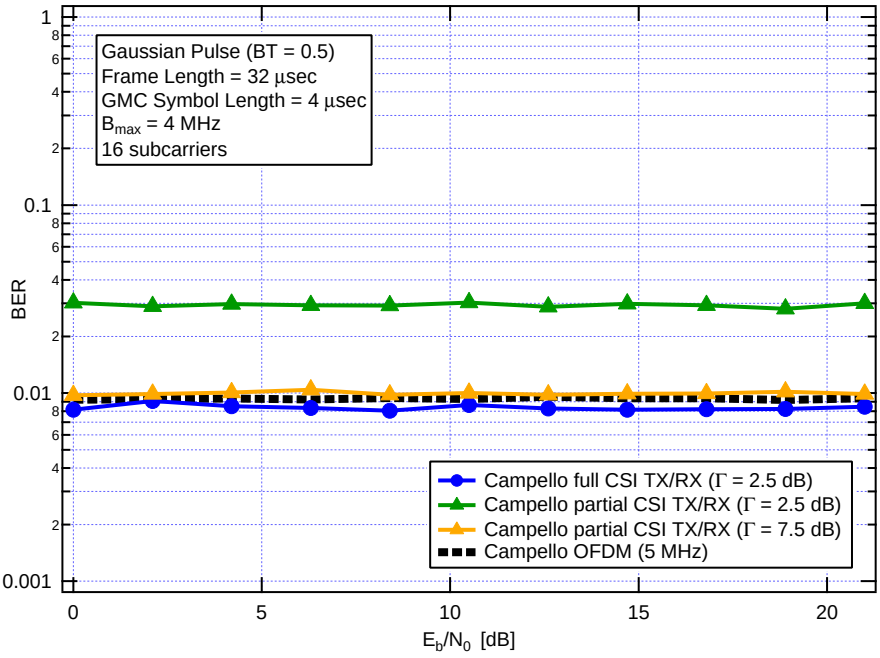

(a)

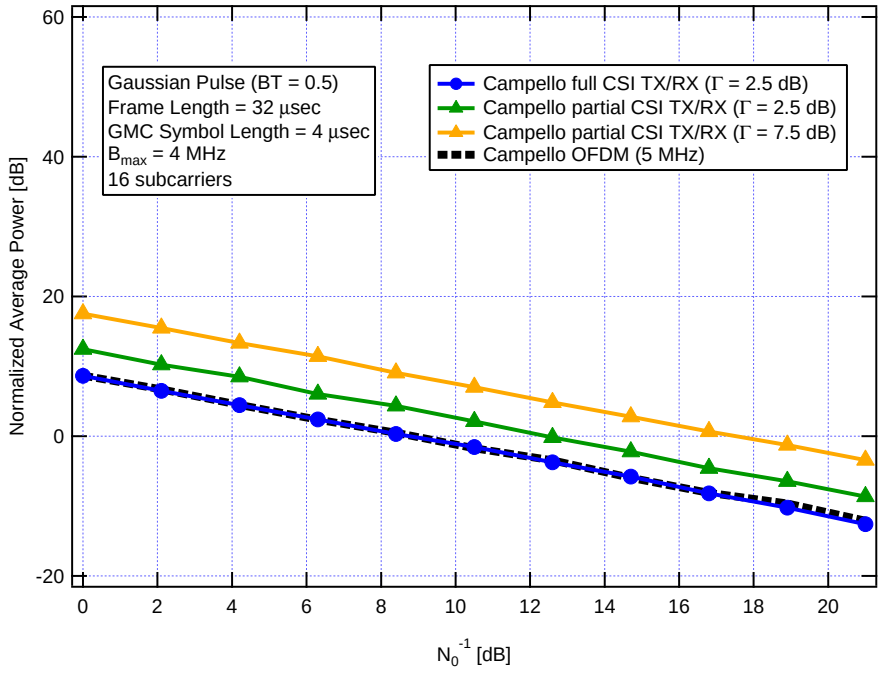

(b)

Figure 6.11: SNR gap increase - *Gaussian pulse*

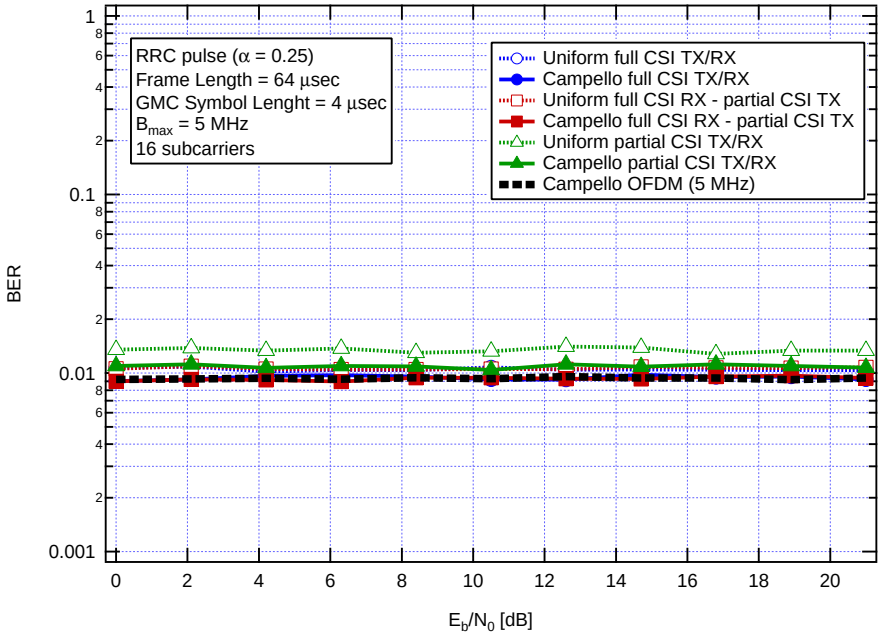

(a)

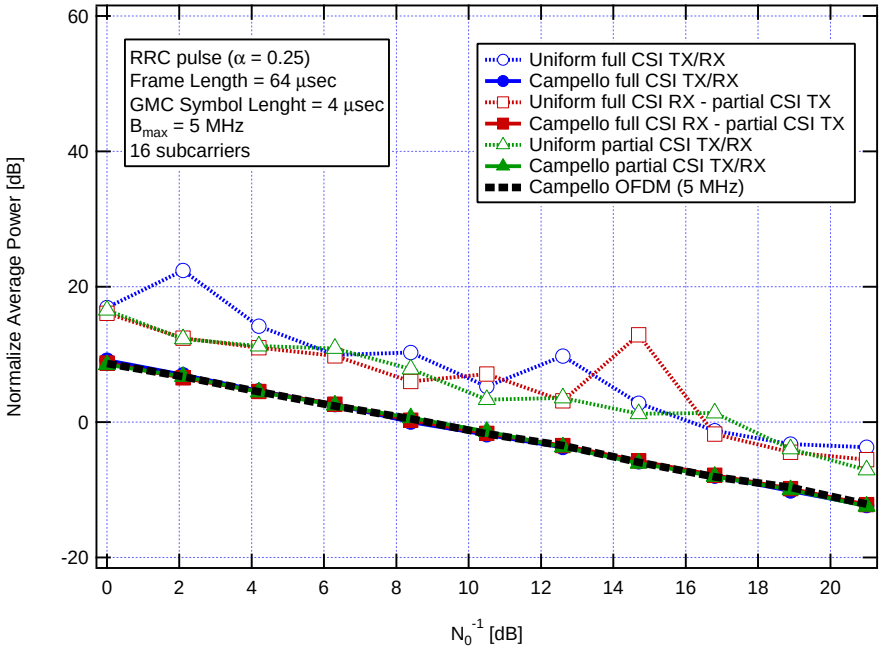

(b)

Figure 6.12: Normalized average transmitted power and BER when the available bandwidth is $B_{\max} = 5$ MHz and comparison with OFDM performances - *RRC pulse*

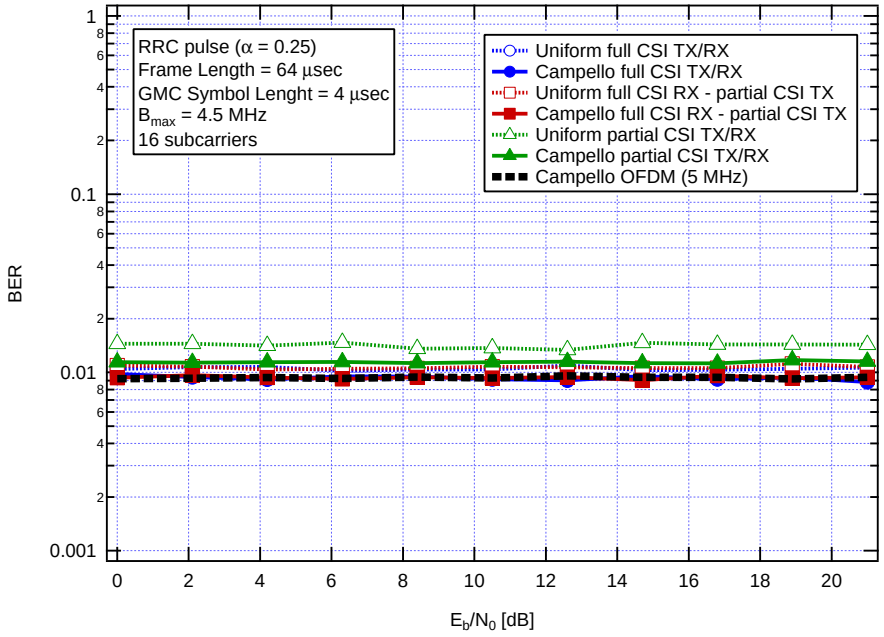

(a)

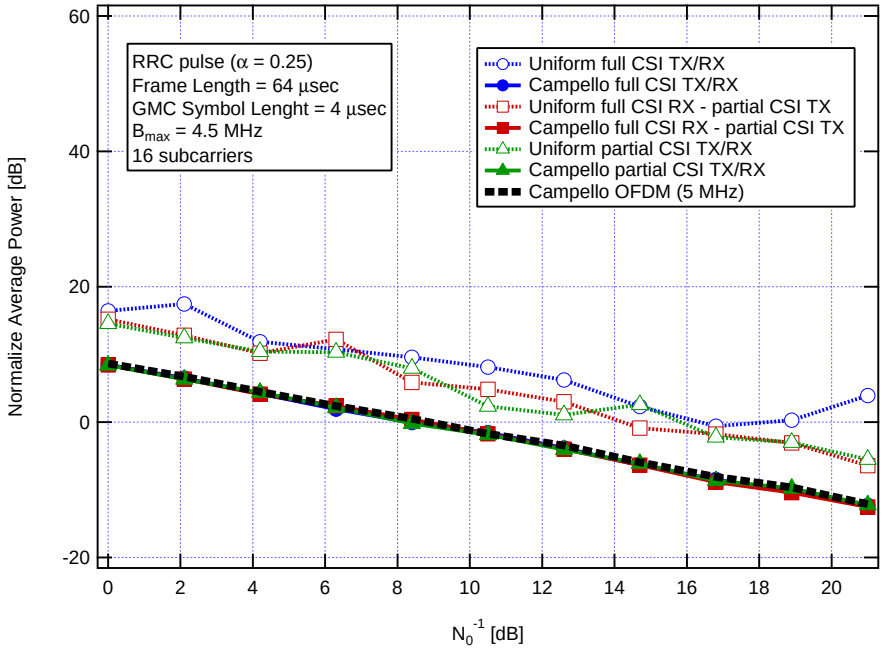

(b)

Figure 6.13: Normalized average transmitted power and BER when the available bandwidth is $B_{\max} = 4.5$ MHz and comparison with OFDM performances - *RRC pulse*

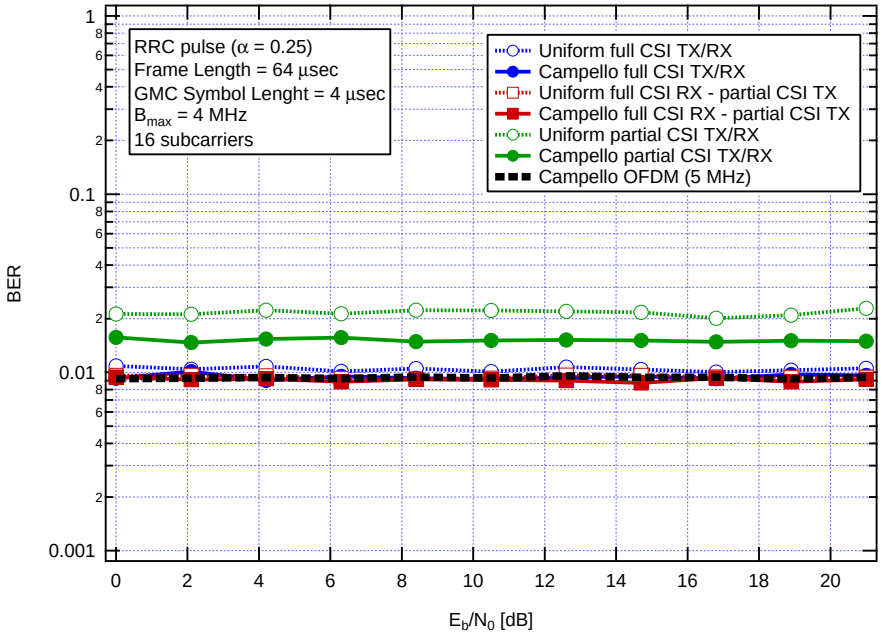

(a)

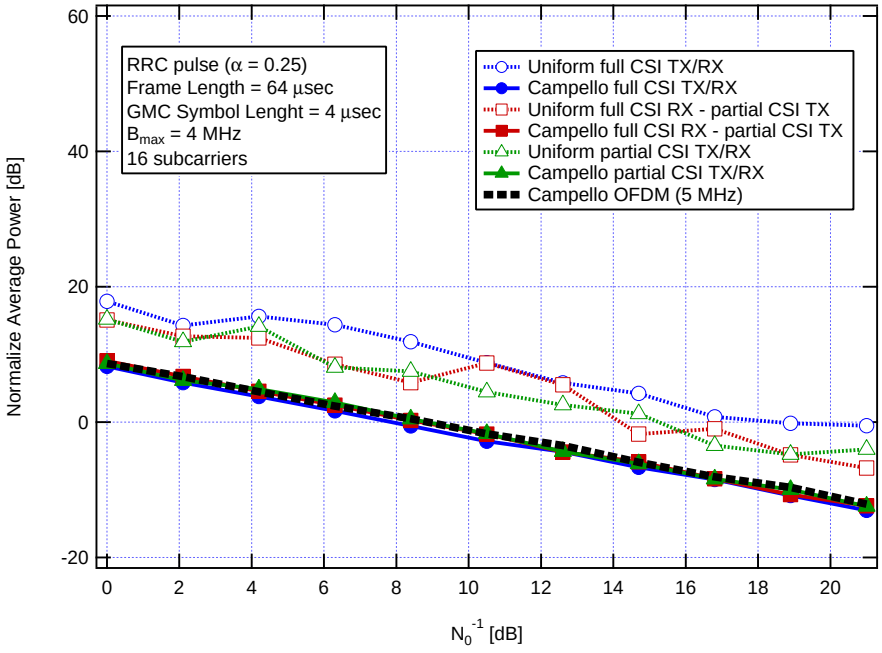

(b)

Figure 6.14: Normalized average transmitted power and BER when the available bandwidth is $B_{\max} = 4$ MHz and comparison with OFDM performances - *RRC pulse*

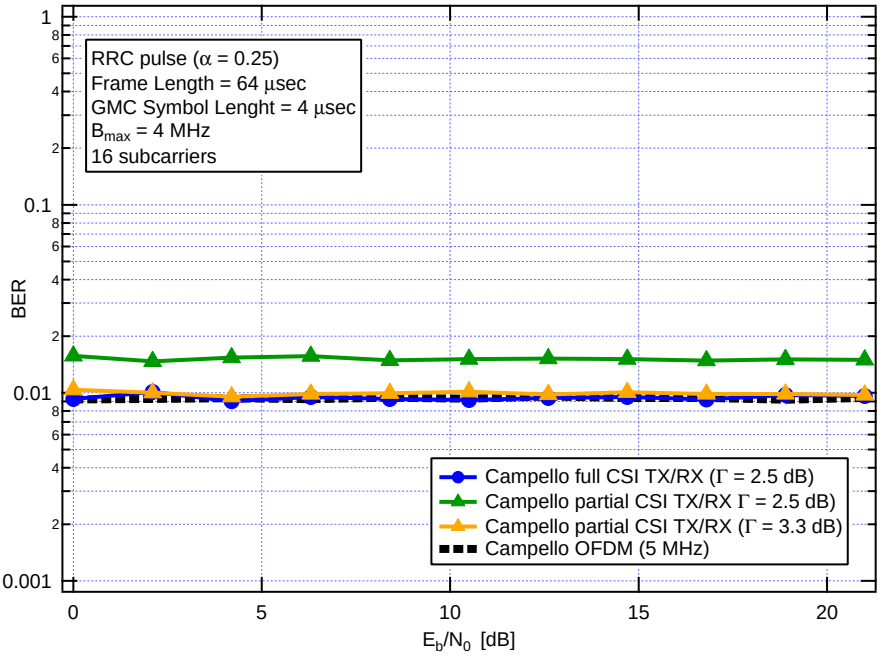

(a)

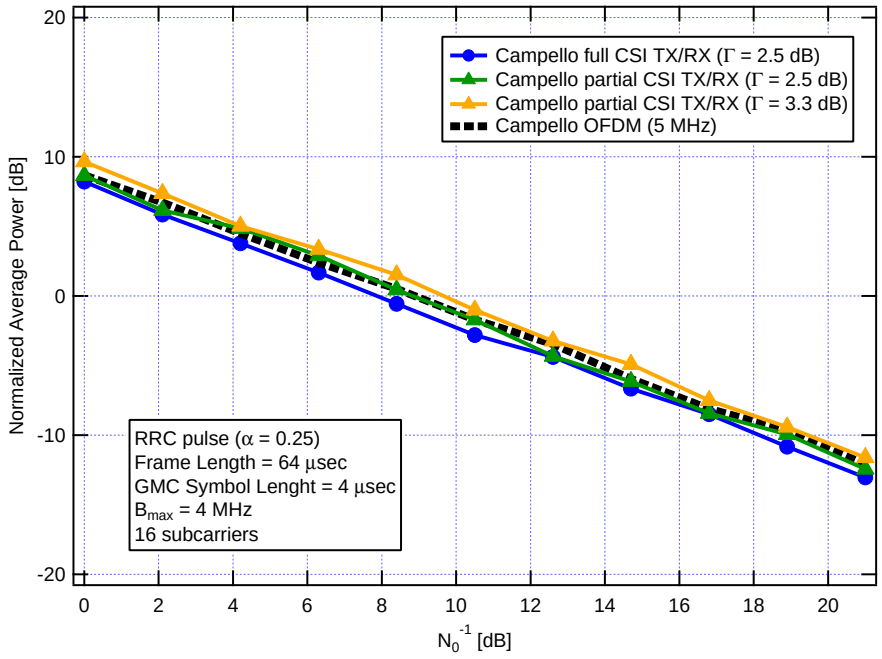

(b)

Figure 6.15: SNR gap increase - *RRC pulse*

Chapter 7

Conclusion

In this thesis, we have provided a general overview about generalized multicarrier systems based on a filterbank structure. The main aspects discussed and the results obtained in this work are:

- The complexity of the system is significantly decreased when the efficient polyphase implementation is employed. Moreover a fast algorithm to find the dual prototype pulse is presented. The pulse shaping and the overlapping among the subcarriers give newer degrees of freedom than the OFDM modulation scheme. These degrees of freedom can be exploited in the design of the system in order to improve the spectral efficiency and increase the input/output mutual information.

- A new equivalent channel model is introduced in order to describe jointly the transmitter filterbank, the frequency-selective channel and the receiver filterbank. The model results well-suited and it allows to apply a joint transceiver design that adds a linear precoder at the transmitter and a LMMSE equalizer at the receiver. The joint design allows to optimize different function objective as the mutual information. The capacity-achieving design diagonalizes the model and it allocates the transmitted power according to the well-known water-filling solution. In this case the optimum solution minimizes the MSE. It has been showed as a NOFDM system can reach a better spectral efficiency than the canonical CP-OFDM system because the presence of the cyclic prefix cannot allow to decrease the signaling interval.

- The use of efficient end effective AMC algorithms is discussed in order to further increase the achievable rates. The diagonalization of the GMC channel allows to apply AMC algorithms originally designated to orthogonal multicarrier systems as Hughes-Hartogs algorithm and the Campello algorithm.

- In a cognitive radio scenario the filterbank-based system shows a better ability to adapt its transmissions than the traditional CP-OFDM system thanks to the ability of shrinking the subcarriers according to the available bandwidth. The OFDM systems cannot shrink the subcarriers because of the orthogonality constraint. Moreover a NOFDM system does not suffers frequency synchronization errors as the OFDM system where a bad frequency synchronization can produce high level of interferences with other users. It has been showed as the well-localized pulses like the Gaussian pulse allows to decrease or to avoid the interferences with the transmissions of the primary users. Finally some approximations on the channel state information knowledge of the transmitter and the receiver is discussed and the relative performances are presented. In this cases the loss of performances can be compensate increasing the transmitted power.

7.1 Future work

There exist a number of areas for future work related to what has been presented in this thesis.

- A fast algorithm have to be studied in order to decrease the computational complexity of the joint transceiver design. The joint design presented in this thesis is based on the perfect knowledge of the channel impulse response and in a time-varying scenario the precoder and the equalizer have to be re-calculated every frame according to the current channel state. Exploiting the Toeplitz block structure of the equivalent model matrix and the approximations presented in the thesis, the research of a fast procedure can be studied.
- It is possible to study the joint transceiver design in order to optimize other objective function as the BER [88] or the SINR [59]. In these case the objective function results a Schur convex and the optimum solution is achieved by adding a further rotation matrix at the transmitter and by a different power allocation. Moreover the majorization theory allows to study and optimize the nonlinear transceiver employing, for example, a DFE equalizer [89], [90].
- Other bit and power loading algorithms can be implemented and discussed exploiting the diagonalized structure as the Fisher-Huber and the Chow algorithm. Moreover the performances can be studied with bit and power loading algorithm modified [91] and adapted to the TF analysis and recently developed in order to be directly applicable on the not diagonalized model.
- In a cognitive scenario, other algorithms can be develop in order to improve the performances and the sharing of the frequency spectrum with primary users. It can be

exploit the several degrees of freedom given by the filterbank-based system.

Bibliography

[1] T. Kurt, M. Siala, and A. Yongaçoglu, "Multi-carrier signal shaping employing hermite functions," in *Proc. European Signal Processing Conference*, (Antalya, Turkey), EUSIPCO, Sep. 2005.

[2] R. Haas and J. C. Belfiore, "Mutliple carrier transmission with time-frequency well-localized impulses," *IEEE Second Symposium on Communications and Vehicular Technology in the Benelux*, pp. 187–193, 1994.

[3] IST-027960 URANUS Deliverable 3.1, *GMCR transceivers for air interfaces in single-mode operation*, Jan. 2007.

[4] R. Rajbanshi, *OFDM-based cognitive radio for DSA networks*. Ph.d dissertation, University of Kansas, Lawrence, KS, USA, May 2007.

[5] H. Arslan, H. A. Mahmoud, and T. Yücek, "OFDM for cognitive radio: Merits and challenges," in *Cognitive Radio, Software Defined Radio and Adaptive Wireless Systems*, ch. 11, pp. 325–353, Springer Netherlands, 2007.

[6] W. Kozek and A. F. Molisch, "Nonorthogonal pulseshapes for multicarrier communications in doubly dispersive channels," *IEEE Journal on Selected Areas in Communications*, vol. 16, pp. 1579–1589, Oct. 1998.

[7] R. W. Chang, "Synthesis of band-limited orthogonal signals for multichannel data transmissions," *Bell Systems Technical Journal*, vol. 45, pp. 1775–1796, 1966.

[8] J. A. C. Bingham, "Multicarrier modulation for data transmission: An idea whose time has come," *IEEE Commun. Mag.*, pp. 5–14, May 1990.

[9] A. Vahlin and N. Holte, "Optimal finite duration pulses for OFDM," *IEEE Transactions on Communications*, vol. 44, pp. 10–14, 1995.

[10] R. Haas and J. C. Belfiore, "A time-frequency well-localized pulse for multiple carrier transmission," *Wireless Personal Communications*, vol. 5, pp. 1–18, 1997.

[11] G. Cherubini, E. Eleftheriou, and S. Ölçer, "Filtered multitone modulation for very high-speed digital subscriber lines," *IEEE journal on selected area in communications*, vol. 20, pp. 1016–1028, Jun. 2002.

[12] ETSI EN 301 958, *Digital Video Broadcasting (DVB): Interaction channel for Digital Terrestrial Television (RCT) incorporating Multiple Access OFDM*, Mar. 2002.

[13] W. T. Webb and R. Steele, "Variable rate QAM for mobile radio," *IEEE Transactions on Communications*, pp. 2223–2230, Jul. 1995.

[14] T. M. Cover and J. A. Thomas, *Elements of Information Theory*. New York: Wiley, 1991.

[15] J. Hagenauer, "Rate-compatible punctured convolutional codes (RCPC codes) and their applications," *IEEE Transactions on Communications*, vol. 36, pp. 389–400, Apr. 1988.

[16] Wikipedia, "Cognitive radio — Wikipedia, the free encyclopedia." `http://en.wikipedia.org/wiki/Cognitive_radio`.

[17] J. Mitola and G. Q. Maguire, "Cognitive radio: making software radios more personal," *IEEE Personal Communications*, vol. 6, pp. 13–18, Aug. 1999.

[18] T. A. Weiss and F. K. Jondral, "Spectrum pooling: an innovative strategy for the enhancement of spectrum efficiency," *IEEE Communications Magazine*, vol. 42, pp. 8–14, Mar. 2004.

[19] J. Hillenbrand, T. A. Weiss, and F. K. Jondral, "Calculation of detection and false alarm probabilities in spectrum pooling systems," *IEEE Communications Letters*, vol. 49, pp. 349–351, Apr. 2004.

[20] R. V. Prasad, P. Pawelczak, J. A. Hoffmeyer, and H. D. Berger, "Cognitive functionality in next generation wireless networks: Standardization efforts," *IEEE Communications Magazine*, Apr. 2008.

[21] C. Heil and D. Walnut, "Continuous and discrete wavelet transforms," *SIAM Review*, vol. 32, pp. 628–666, 1989.

[22] I. Daubechies, "The wavelet transform, time-frequency localization and signal analysis," *IEEE Trans. Information Theory*, vol. 36, pp. 961–1005, Sept. 1990.

[23] W. MathWorld, "L2-Funciton — Wolfram MathWorld." `http://mathworld.wolfram.com/L2-Function.html`.

[24] O. Christensen, *An Introduction to Frames and Riesz Bases*. Birkhauser, 2002.

[25] S. Qian and D. Chen, "Joint time frequency analysis," *Signal Processing Mag.*, pp. 52–67, Mar. 1999.

[26] J. M. Morris and Y. Lu, "Discrete Gabor expansion of discrete time signals in $l^2(\mathrm{Z})$ via frame theory," *Signal Processing Mag.*, vol. 40, pp. 155–181, 1994.

[27] H. Bölcskei and F. Hlawatsch, "Equivalence of DFT filter banks and gabor expansions," *Proc. SPIE*, vol. 2569, 1995.

[28] Z. Cvetkovic and M. Vetterli, "Oversampled filter banks," *IEEE Trans. Signal Processing*, vol. 46, pp. 1245–1255, May 1998.

[29] P. P. Vaidyanathan, *Multirate Systems and Filter Banks*. Prentice-Hall, 1993.

[30] J. Wexler and S. Raz, "Discrete Gabor expansion," *Signal Processing Mag.*, vol. 21, no. 3, pp. 207–220, 1990.

[31] H. G. Feightinger and T. Strohmer, *Gabor Analysis and Algorithms: Theory and Applications*. Birkhauser, 1998.

[32] Y. S. Choi, P. J. Voltz, and F. A. Cassara, "On channel estimation and detection for multicarrier signals in fast and selective Rayleigh fading channels," *IEEE Trans. Commun.*, vol. 49, pp. 1375–1387, 2001.

[33] H. Sari, G. Karam, and I. Jeanclaude, "Transmission techniques for digital terestial TV broadcasting," *IEEE Commun. Magazine*, pp. 100–109, Feb. 1995.

[34] G. Cherubini, E. Eleftheriau, S. Ölçer, and J. M. Cioffi, "Filter bank modulation techniques for very high-speed digital subscriber lines," *IEEE Commun. Magazine*, vol. 38, pp. 98–104, May 2000.

[35] M. G. Bellanger, G. Bonnerot, and M. Coudreuse, "Digital filtering by polyhase network: Application to sample-rate alteration and filter banks," *IEEE Trans. Acoustics, Speech, and Signal Processing*, vol. 24, pp. 109–114, Apr. 1976.

[36] A. Scaglione, S. Barbarossa, and G. B. Giannakis, "Filterbank transceivers optimizing information rate in block transmissions over dispersive channels," *IEEE Transaction on Information Theory*, vol. 45, pp. 1019–1032, Apr. 1999.

[37] S. Li, "Discrete multi-Gabor expansions," *IEEE Transaction on Information Theory*, vol. 45, pp. 1954–1967, Sep. 1999.

[38] "DMT: Cyclic prefix." `http://cnx.org/content/m11762/latest/`.

[39] R. Hleiss, P. Duhamel, and M. Charbit, "Oversampled OFDM systems," in *Proc. Int. Conf. on DSP*, (Santorini, Greece), pp. 329–332, July 1996.

[40] M. Sandell, *Design and analysis of estimators for multicarrier modulation and ultrasonic imaging*. PhD thesis, Lulea Univ. Technol., Lulea, Sweden, 1996.

[41] IST-027960 URANUS Deliverable 3.1, *User-defined air interfaces based on a generalized multicarrier representation*, Aug. 2008.

[42] P. Prinz, "Calculating the dual Gabor window for general sampling sets," *IEEE Transactions on Signal Processing*, vol. 44, pp. 2078–2082, Aug. 1996.

[43] F. Gardner, "Interpolation in digital modems: Part I: Fundamentals," *IEEE Trans. Commun.*, vol. 41, pp. 501–507, Mar. 1993.

[44] S. Qian and D. Chen, "Discrete Gabor transform," *IEEE Trans. Signal Processing*, vol. 41, pp. 2429–2439, Jul. 1993.

[45] S. Qian, "Optimal biorthogonal analysis window function for discrete Gabor transform," *IEEE Transactions on Special Processing*, vol. 42, pp. 694–697, Mar. 1994.

[46] L. Auslander, I. C. Gertner, and R. Tolimieri, "The discrete Zak transform application to time-frequency analysis and synthesis of nonstationary signals," *IEEE Trans. Signal Processing*, vol. 39, no. 4, 1991.

[47] T. Genossar and M. Porat, "Can one evaluate the Gabor expansion using Gabor's iterative algorithm?," *IEEE Trans. Signal Processing*, vol. 40, pp. 1852–1861, Aug. 1992.

[48] S. L. Campbell and C. D. M. Jr., *Generalized Inverses of Linear Transforms*. New York Dover, 1991.

[49] O. Christensen, *Atomic decomposition via projective group representations*. Rocky Mountain J. Math, to appear.

[50] H. G. Feichtinger, O. Christensen, and T. Strohmer, "A group-theoretical approach to gabor analysis," *Opt. Eng.*, vol. 34, pp. 1697–1704, 1995.

[51] J. G. Proakis, *Digital Communications*. Mc-Graw Hill, 4th ed., 2002.

[52] Wikipedia, "Raised-cosine filter — Wikipedia, the free encyclopedia." `http://en.wikipedia.org/wiki/Raised-cosine_filter`.

[53] Wikipedia, "Root-raised-cosine filter — Wikipedia, the free encyclopedia." `http://en.wikipedia.org/wiki/Root-raised-cosine_filter`.

[54] Wikipedia, "Hermite polynomials — Wikipedia, the free encyclopedia." `http://en.wikipedia.org/wiki/Hermite_polynomials`.

[55] ICT-211887 PHYDYAS Deliverable 5.1, *Prototype filter and structure optimization*, Jan. 2009.

[56] G. Matz, D. Schafhuber, K. Gröchenig, M. Hartmann, and F. Hlawatsch, "Analysis, optimization, and implementation of low-interference wireless multicarrier systems," *IEEE Transactions on Wireless Communications*, vol. 6, pp. 1921–1931, May 2007.

[57] K. Gröchenig, *Foundations of Time-Frequency Analysis*. Boston: Birkhäuser, 2001.

[58] N. Al-Dhahir and J. M. Cioffi, "Block transmission over dispersive channels: Transmit filter optimization and realization and MMSE-DFE receiver performance," *IEEE Trans. Inform. Theory*, vol. 42, pp. 137–160, Jan. 1996.

[59] D. P. Palomar, J. M. Cioffi, and M. A. Lagunas, "Joint tx-rx beamforming design for multicarrier MIMO channels: A unified framework for convex optimization," *IEEE Transactions on Signal Processing*, vol. 51, pp. 2381–2401, Sep. 2003.

[60] A. W. Marshall and I. Olkin, *Inequalities: Theory of Majorization and Its Applications*. New York: Academic, 1979.

[61] J. M. Cioffi and G. D. Forney, *Communications, Computation, Control and Signal Processing*, ch. 4. Generalized decision-feedback equalization for packet transmission with ISI and Gaussian noise. MA: Kluwer: Eds. Boston, 1997.

[62] P. Viswanath and V. Anantharam, "Optimal sequences and sum capacity of synchronous CDMA systems," *IEEE Trans. Inform. Theory*, vol. 45, pp. 1984–1991, Sep. 1999.

[63] J. Yang and S. Roy, "Joint transmitter-receiver optimization for multiinput multi-output systems with decision feedback," *IEEE Trans. Inform. Theory*, vol. 40, pp. 1334–1347, Sep. 1994.

[64] A. Lozano, A. Tulino, and S. Verdu, "Optimum power allocation for parallel Gaussian channels with arbitrary input distributions," *IEEE Transaction on Information Theory*, vol. 52, no. 7, 2006.

[65] R. Hoshyar, S. H. Jamali, and A. R. S. Bahai, "Turbo coding performance in OFDM packet transmission," *Proc. VTC 2000*, vol. 2, pp. 805–810, May 2000.

[66] E. Malkamki and H. Leib, "Coded diversity on block-fading channels," *IEEE Trans. Inform. Theory*, vol. 45, pp. 771–781, Mar. 1992.

[67] E. Malkamki and H. Leib, "Rate 1/n convolutional codes with interleaving depth of n over a block fading rician channel," in *Proc. IEEE Veh. Technol. Conf.*, (Phonix, AZ), pp. 2002–2006, May 1997.

[68] R. Knop and P. A. Humblet, "Maximizing diversity on block fading channels," in *Proc. IEEE Int. Conf. Commun. '97*, (Montreal, Quebec, Canada), pp. 647–651, Jun. 1997.

[69] B. Devillers, J. Louveaux, and L. Vandendorpe, "Bit and power allocation for goodput optimization in coded parallel subchannels with ARQ," *IEEE Transactions on Signal Processing*, Aug. 2008.

[70] D. Hughes-Hartogs, "Ensemble modem structure for imperfect transmission media." U.S. Patents Nos. 4,679,227 (July 1987), 4,731,816 (March 1988), and 4,833,706 (May 1989).

[71] J. Campello, "Optimal discrete bit loading for multicarrier modulation systems," in *Proc. Int. Symp. Information Theory (ISIT'98)*, (Cambridge, MA), p. 193, Aug. 1998.

[72] J. Campello, "Practical bit loading for DMT," in *Proc. Int. Conf. Communications (ICC'99)*, vol. 56, (Vancouver, BC, Canada), pp. 801–805, Jun. 1999.

[73] W. Bednorz, *Advances in Greedy Algorithms*. I-Tech, 2008.

[74] P. S. Chow, J. M. Cioffi, and J. A. C. Bingham, "A practical discrete multitone transceiver loading algorithm for data transmission over spectrally shaped channels," *IEEE Transactions on Communications*, vol. 43, pp. 773–775, Feb./Mar./Apr. 1995.

[75] A. Lozano, A. M. Tulino, and S. Verdu, "Mercury/waterfilling for fixed wireless OFDM systems," in *Proc. IEEE Radio and Wireless Symp. (RWS'06)*, (San Diego, CA), pp. 211–214, Jan. 2006.

[76] D. Guo, S. Shamai, and S. Verdu, "Mutual information and minimum mean-square error in Gaussian channels," *IEEE Trans. Inf. Theory*, vol. 51, pp. 1261–1283, Apr. 2005.

[77] M. McHenry, "NSF spectrum occupancy measurements," Technical report, The Shared Spectrum Company, Aug. 2005. `http://www.sharedspectrum.com/?section=nsf_measurements`.

[78] T. A. Weiss, J. Hillenbrand, and F. K. Jondral, "A diversity approach for the detection of idle spectral resources in spectrum pooling systems," in *Proc. 48th Int. Scientific Colloquium*, (Ilmenau, Germany), pp. 37–38, Sep. 2003.

[79] A. M. Wyglinski, "Effects of bit allocation on non-contiguous multicarrier-based cognitive radio transceivers," in *Proc. IEEE Veh. Technol. Conf.*, Sep. 2006.

[80] T. Weiss, A. Krohn, F. Capar, I. Martoyo, and F. Jondral, "Synchronization algorithms and preamble concepts for spectrum pooling systems," *IST Mobile & Wireless Telecommunications Summit*, Jun. 2003.

[81] T. A. Weiss, J. Hillenbrand, A. Krohn, and F. K. Jondral, "Mutual interference in OFDM-based spectrum pooling systems," in *Proc. IEEE Veh. Technol. Conf.*, vol. 4, 2004.

[82] C. Muschallik, "Improving an OFDM reception using an adaptive Nyquist windowing," *IEEE Trans. Consumer Electron.*, vol. 42, pp. 259–269, Aug. 1996.

[83] S. H. Muller-Weinfurtner, "Optimum Nyquist windowing in OFDM receivers," *IEEE Trans. Commun.*, vol. 49, pp. 417–420, Mar. 2001.

[84] H. Yamaguchi, "Active interference cancellation technique for MB-OFDM cognitive radio," in *Proc. IEEE European Microwave Conf.*, vol. 2, (Amsterdam, the Netherlands), pp. 1105–1108, Oct. 2004.

[85] S. Brandes, I. Cosovic, and M. Schnell, "Sidelobe suppression in OFDM systems by insertion of cancellation carriers," in *Proc. IEEE Veh. Technol. Conf.*, vol. 1, (Dallas, TX), pp. 152–156, Sep. 2005.

[86] I. Cosovic, S. Brandes, and M. Schnell, "A technique for sidelobe suppression in OFDM systems," in *Proc. IEEE Global Telecommunications Conf. (Globecom)*, vol. 1, (St. Louis, MO), pp. 204–208, Nov./Dec. 2005.

[87] I. Cosovic, S. Brandes, and M. Schnell, "Subcarrier weighting: a method for sidelobe suppression in OFDM systems," *IEEE Commun. Lett.*, vol. 10, pp. 444–446, Jun. 2006.

[88] L. G. Ordonez, D. P. Palomar, A. Pagès-Zamora, and J. R. Fonollosa, "Minimum BER linear MIMO transceivers with adaptive number of substreams," *IEEE Transactions On Signal Processing*, vol. 57, pp. 2336–2353, Jun. 2009.

[89] A. A. D'Amico and M. Morelli, "Joint Tx-Rx MMSE design for MIMO multicarrier systems with Tomlinson-Harashima precoding," *IEEE Transactions On Wireless Communications*, vol. 7, pp. 3118–3127, Aug. 2008.

[90] S. Bergman, D. P. Palomar, and B. Ottersten, "Joint bit allocation and precoding for MIMO systems with decision feedback detection," *IEEE Transactions On Signal Processing*, vol. 57, pp. 3118–3127, Nov. 2009.

[91] A. Kliks and H. Bogucka, "New adaptive bit and power loading policies for generalized multicarrier transmission," in *Proc. 17th European Signal Processing Conference*, (Glasgow, Scotland), pp. 1888–1892, EUSIPCO, Aug. 2009.